A comprehensive study of the orientation mechanisms of montmorillonite in a LLDPE polymer matrix using multi-nano-layer polymer co-extrusion: from orientation quantification to polymer-filler structure-property relationships

Dissertation zur Erlangung des akademischen Grades Doktor der Naturwissenschaften

(Dr. rer. nat.)

vorgelegt von

Noémie RIVOLLIER

Freie Universität Berlin

IPC

HZB Helmholtz Zentrum Berlin

CUSTOM-ART
DISRUPTIVE KESTERITE-BASED

Eingereicht am Fachbereich Geowissenschaften der

Freien Universität Berlin

Angefertigt an dem Französischen Technischen Zentrum für Kunststoffe und Verdundwerkstoffe (IPC) in Zusammenarbeit mit dem Helmholtz-Zentrum Berlin für Materialien und Energie GmbH im Rahmen des Europäischen Projektes H2020 CUSTOM-ART.

Die Arbeit ist in englischer Sprache verfasst.

Berlin, Oktober 2024

ZUSAMMENFASSUNG

Die Entwicklung einer flexiblen Photovoltaik-Technologie mit niedrigen Produktionskosten ist entscheidend für die Ausweitung des Zugangs zur Solarenergie und die Förderung ihrer breiten Nutzung. Eines der Ziele des Projekts CUSTOM-ART (unter der Zuschussvereinbarung Nr. 952982) ist die Entwicklung von Ultra-Barriere-Filmen zum Schutz von Photovoltaik-Zellen unter Verwendung gängiger, erschwinglicher Kunststoffmaterialien. Um dies zu erreichen, basiert die gewählte Strategie auf dem Einsatz der Co-Extrusionstechnologie für mehrschichtige Polymerfolien, die darauf abzielt, 2D-Montmorillonit-Nanofüllstoffe, die in einer Polyethylenmatrix dispergiert sind, zu orientieren, um Folien mit einem hohen Grad an Tortuosität herzustellen. Daher konzentriert sich diese Studie auf die Charakterisierung der Orientierung von Montmorillonit durch systematische Textur-Röntgenbeugungsanalyse. Die Ergebnisse zeigen, dass die Orientierung von Montmorillonit mit der Multinano-Liegen-Co-Extrusionstechnologie einen begrenzten Effekt hat, wenn sich das Polyethylen bei der Herstellung der Filme im geschmolzenen Zustand befindet. Die Orientierung wird jedoch durch eine biaxiale Dehnungsnachbehandlung der Folien, die bei einer Temperatur unterhalb des Schmelzpunkts des Polyethylens durchgeführt wird, erheblich verbessert. Dies wirft die Frage nach dem Einfluss der Matrix und der Beziehung zwischen Montmorillonit und Polyethylen auf die Montmorillonitorientierung auf. Weitere Untersuchungen der Kristallisation der Polyethylenphase ergaben, dass diese um die Montmorillonit-Nanofüllstoffe herum stattfindet, was eine bevorzugte Ausrichtung der Polyethylenkristalle ermöglicht, ohne die Kristallisationsgeschwindigkeit des Polyethylens zu beeinflussen. Folglich beeinflusst die Art und Weise, wie das Polyethylen kristallisiert, die Ausrichtung des Montmorillonits. Trotz dieser Unterschiede in der Ausrichtung wurde jedoch keine signifikante Verbesserung der Wasserbarriereeigenschaften der Filme beobachtet. Obwohl der Film eine kontrollierte Nanostruktur aufweist, find nur 35 % (einschließlich der Montmorillonit- und Polyethylenanteile) des Films kristallin, was deren Fähigkeit, die Wasserdiffusion durch den Film zu beeinflussen, einschränken könnte.

ABSTRACT

The development of flexible photovoltaic technology with low production costs is crucial for expanding access to solar energy and promoting its widespread adoption. One of the objectives of the CUSTOM-ART project (under grant agreement no. 952982) is to develop ultra-barrier films to protect photovoltaic cells using common, affordable plastic materials. To achieve this, the strategy adopted is based on the use of multi-nano-layer (MNL) polymer film co-extrusion technology aimed at orienting 2D montmorillonite nano-fillers dispersed in a poly(ethylene) matrix to produce films with a high degree of tortuosity. Therefore, this study focuses on characterizing the orientation of montmorillonite by systematic texture X-ray diffraction analysis. The results indicate that the orientation of montmorillonite with the MNL co-extrusion technology has a limited effect when the poly(ethylene) is in the molten state. However, the orientation is significantly improved with a biaxial stretching post-treatment of the films, which is performed at a temperature below the melting point of poly(ethylene). This raises the question of the influence of the matrix and the relationship between montmorillonite and poly(ethylene) on montmorillonite orientation. Further investigation of the crystallization of the poly(ethylene) phase revealed that it occurs around montmorillonite nano-fillers, allowing preferential orientation of poly(ethylene) crystals without affecting the rate of poly(ethylene) crystallinity. Consequently, the way poly(ethylene) crystallizes affects the orientation of montmorillonite. However, despite these variations in orientation, no significant improvement in the water barrier properties of the films was observed. Although the film has a controlled nanostructure, only 35% (including both montmorillonite and poly(ethylene) contributions) of the film consists of crystals, which may limit their ability to influence water diffusion through the films.

TABLE OF CONTENTS

LIST OF FIGURES

21

LIST OF TABLES

LIST OF ABREVIATIONS

2D	Two – dimensional
Al	Aluminum
ALD	Atomic Layer Deposition
BNNS	Boron nitride nano-sheets
C20A	Cloisite 20A®
Ca	Calcium
$CaCO_3$	Calcite
CNa^+	Cloisite Na$^+$ ®
CRMs	Critical Raw Material compounds
CZTS	Cu_2ZnSnS_4
CZTSe	$Cu_2ZnSnSe_4$
CZTSSe	$Cu_2ZnSn(S,Se)_4$
DR	Draw ratio
DSC	Dynamic scanning calorimetry
EAA	Ethylene Acrylic Acid Copolymer
ED	Extrusion direction
EVA	Ethylene Vinyl Acetate
Fe	Iron
FeS_2	Pyrite
h-BN	Boron nitride nano-sheets
HDPE	High Density Poly(Ethylene)
IB	Integral Breadth
ICP-AES	Inductively Coupled Plasma – Atomic Emission Spectroscopy
IEA	International energy agency
KMI	Keller-Machin I
KMII	Keller-Machin II
LDHs	Layered Double Hydroxides
LDPE	Low Density Poly(Ethylene)
LLDPE	Linear Low Density Poly(Ethylene)
LLDPE-g-MA	Linear Low Density Poly(Ethylene) graft Maleic Anhydride
LME	Layer Multiplying Element
MD	Machine Direction

Mg	Magnesium
MMT	Montmorillonite
MNL	Multi-nano Layer
Na	Sodium
OMMT	Organo-modified Montmorillonite
PA	Poly(Amide)
PBSA	Poly(Butylene Succinate-co-Butylene Adipate)
PC	Poly(Carbonate)
PCL	Poly(Caprolactone)
PE	Poly(Ethylene)
PECVD	Plasma-Enhanced Chemical Vapor Deposition
PEO	Poly(Ethylene Oxide)
PET	Poly(Ethylene Terephthalate)
PLA	Poly(Lactic Acid)
PMMA	Poly(Methacrylate Methyl Acrylique)
PP	Poly(Propylene)
PS	Poly(Styrene)
PU	Poly(Urethane)
PV	Photovoltaic
PVA	Poly(Vinyl Alcohol)
PVD	Physical Vapor Deposition
PVDF	Poly(Vinylidene Fluoride)
SEM	Scanning Electronic Microscopy
Si	Silicon
SiO_2	Quartz
SME	Specific Mechanical Energy
T_c	Crystallization Temperature
TD	Transverse Direction
TEM	Transmission Electronic Microscopy
T_f	Melting Temperature
T_g	Glass transition Temperature
WAXS	Wide Angle X-ray Scattering
WVTR	Water Vapor Transmission Rate
XRD	X-ray Diffraction

1. CHAPTER 1: INTRODUCTION

Energy production and consumption account for approximately 60% of greenhouse gas emissions (**Bouich et al., 2023**). Therefore, a rapid and effective transition to renewable energies is crucial in combating climate change. Geothermal, hydroelectric, wind, and solar power are emerging as clean, sustainable, and abundant alternatives with no harmful emissions (**IEA., 2023**). The proportion of renewable energy is constantly increasing (**IEA website**). The International Energy Agency (IEA) predicts that renewable energy will account for approximately 33.5% of total energy production in 2024, with photovoltaic (PV) cells contributing 6.7% (**Figure 1-1**).
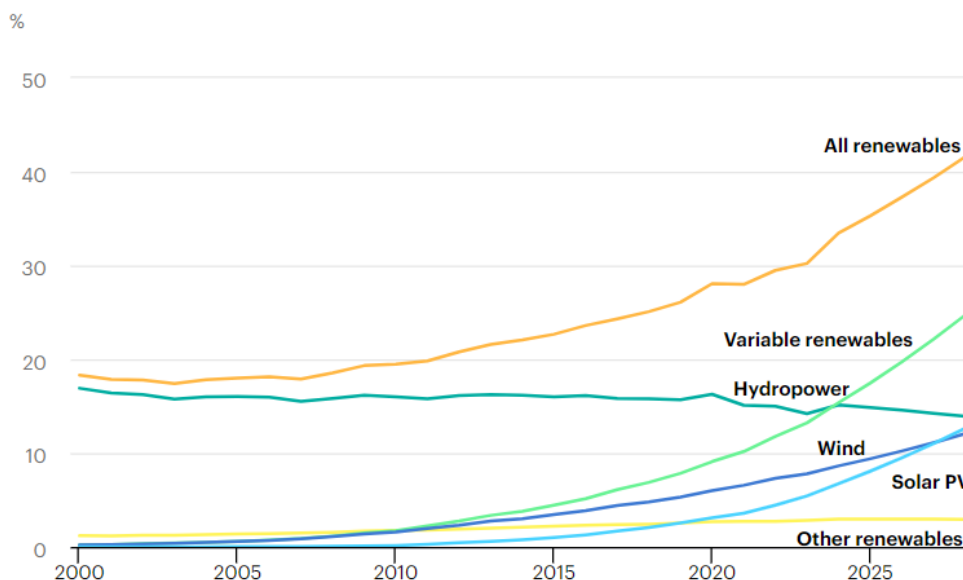
Figure 1-1 : Evolution of the proportion of the renewable energies over the years (IEA website).

PV cells are categorized into different generations (**Figure 1-2**). The first generation is primarily silicon-based and has a conversion efficiency actual world record comprised between 21.2 and 27.6% according to the type of silicon-based solar cell (**Green at al., 2023**; **NREL**). However, it is expensive due to the raw material used. Later generations introduced thin-film technologies, which reduced material usage and production costs. The third generation of solar cells includes halide perovskite-based cells, which have a conversion

efficiency actual world record of 26% (**Green at al., 2023**; **NREL**) or PVs based on organic or inorganic compounds. However, these cells are prone to stability issues when exposed to UV, oxygen, and humidity (**Dada & Popoola., 2023**).
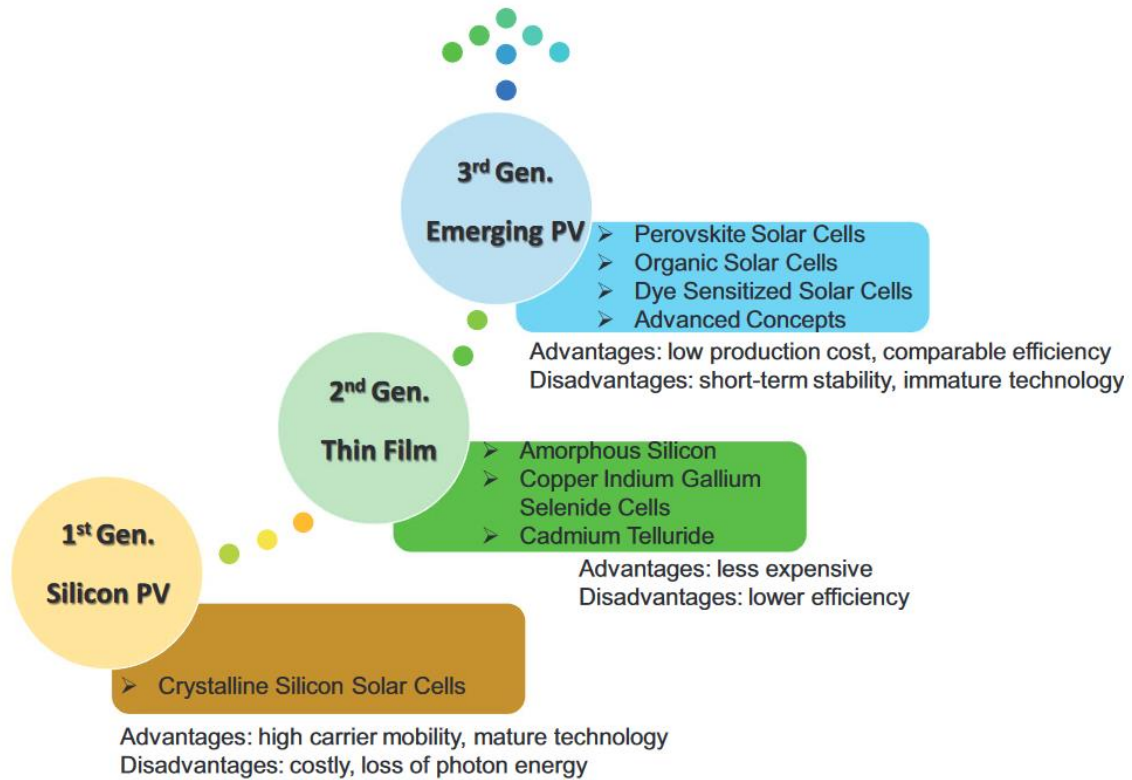
Figure 1-2 : Scheme of the different PV cells types classified according to their generations (Pham et al., 2020).

Among inorganic thin-film PV cell technologies, some employ critical raw material compounds (CRMs) such as indium, gallium, and tellurium, which have been classified as such by the European Commission (**European Commission., 2017**). Therefore, it is essential to find alternatives that use materials that are less toxic and more abundant on Earth. Kesterites, a family of materials including compounds such as $Cu_2ZnSnSe_4$ (CZTSe), Cu_2ZnSnS_4 (CZTS), and the corresponding solid solution $Cu_2ZnSn(S,Se)_4$ (CZTSSe), represent a potentially attractive solution (**Giraldo et al., 2019**). They have achieved the highest photovoltaic conversion efficiencies among emerging CRM-free technologies, with the actual world record efficiency of 14.9% (**Green at al., 2023**; **NREL**). Thus, kesterites seem to be the most relevant and promising option for large-scale deployment of photovoltaics without critical raw materials to date.

In this context, the CUSTOM-ART project, which is funded by the Horizon H2020 research program under Grant agreement n°952982, aimed at developing customized thin film technologies based on kesterites for architectural and active urban furniture applications. The goals of the project were numerous: enhancing the efficiency of kesterites-based cells, extending their lifespan to over 35 years, evaluating their end-of-life, and confirming the recyclability of cells and modules, all while maintaining a cost of less than 75€·m^{-2}. To produce this kind of kesterites-based PVs, it is recommended to use flexible substrates and encapsulation solution both based on polymer films. Moreover, producing films with ultra-barrier properties, particularly with regard to water permeability, is crucial for promoting durability of over 35 years. The water permeability should be of the order of 1·10^{-5} g·m^{-2}·day^{-1}.

Considerable research has been conducted to create polymer-based ultra-barrier films for flexible electronics. Some of these films use ethylene vinyl alcohol (EVA) copolymers, with or without the addition of inorganic fillers (**Gaddam et al., 2021**). Others combine a polymer film base with inorganic deposits on the surface, such as poly(ethylene terephthalate) (PET) with inorganic particles like Al_2O_3 or SiO_x (**Ahmad et al., 2013**). These deposits are typically achieved through techniques such as plasma-enhanced chemical vapor deposition (PECVD), atomic layer deposition (ALD), or physical vapor deposition (PVD) which are time and energy consuming. Multilayer films may also be used, consisting of several polymers, including technical polymers such as poly(imide) or perfluorinated polymers. All of these configurations can achieve the required permeability levels, with water vapor transmission rates (WVTR) ranging from 1·10^{-2} to 1·10^{-7} g·m^{-2}·day^{-1}, depending on the components used (**Ahmad et al., 2013**). However, these configurations require different and successive manufacturing processes, resulting in higher production costs for the film. For example, the supplier 3M offers barrier films with a permeability of less than 6·10^{-5} g·m^{-2}·day^{-1} (**3M™ Ultra Barrier Solar Film 512**), based on a multilayer configuration including PET and a barrier layer, with a production cost exceeding 70€·m^{-2}.

CHAPTER 1: INTRODUCTION

To ensure cost-effectiveness in producing ultra-barrier films, it is necessary to explore more affordable alternatives. Ideally, one would adopt a single process approach instead of multiple separate processes to manufacture multilayer films. We have chosen the principle of multi-nano-layer co-extrusion (MNL), which allows to produce a film with several thousands of layers and nominal thicknesses of up to a few nanometers in a single step.

The objective of this work was to identify an economical polymer matrix with good water-barrier properties and satisfactory transparency. To achieve this, poly(ethylene) (PE) was chosen due to its flexibility and cost-effectiveness. Compared to other polymers (**Figure 1-3**) such as poly(styrene) (PS), poly(propylene) (PP), and PET, PE offers the best value for water protection. In addition, PE is known for its flexibility, which makes it one of the most versatile polymers available.

POLYMER	$WVTR^a$ $(g/m^2/day)$ $(37.8\text{-}40°C)$	OTR^c $(cm^3$ $(STP)/m^2/day)$ $(20\text{-}23°C)$
Polyethylene	1.2-5.9	70-550
Polypropylene (PP)	1.5-5.9	93-300
Polystyrene (PS)	7.9-40	200-540
Poly(ethylene terephthalate) (PET)	3.9-17	1.8-7.7
Poly(ethersulfone) (PES)	14^b	0.04^b
PEN	7.3^b	3.0^b
Polyimide	0.4-21	0.04-17
15nm Al/ PET	0.18	0.2-2.9
SiO_x/PET		0.007-0.03
ORMOCER/PET		0.07
OLED requirement (estimate)	1×10^{-6}	$1 \times 10^{-5} - 1 \times 10^{-3}$

^{a} Calculated assuming 100μm polymer film
^{b} Temperature not given
^{c} Calculated assuming a 100μm polymer film and 0.2 atm O_2 pressure gradient

Figure 1-3 : List of some polymers coatings/barriers and their respective WVTR and OTR values (Lewis & Weaver., 2004).

To enhance the barrier properties of PE and achieve our goal of $1\cdot10^{-5}$ $g\cdot m^{-2}\cdot day^{-1}$ for water vapor transmission rate, we have introduced 2D inorganic fillers into the material to decrease diffusion within the films. Montmorillonite was selected from the available 2D inorganic fillers for this purpose. Unlike other fillers such as graphene or MoS_2,

montmorillonite is electrically non-conductive, which ensures that it does not interfere with the operation of PV modules. Furthermore, while boron nitrides are promising candidates, their high cost and difficulty in large-scale exfoliation into the polymer matrix make them less attractive. In contrast, montmorillonite is advantageous due to its low cost and ease of exfoliation in PE. By combining the addition of 2D fillers with the creation of nano-layers a few tens of nanometers thick, we aim at controlling the orientation of the inorganic 2D fillers parallel to the surface of the film. This optimal orientation of nanofillers could significantly reduce water vapor diffusion by several orders of magnitude.

The objective of this thesis is to analyze the effect of the multi-nano-layer co-extrusion process on the orientation of montmorillonite nano-fillers (MMT) in a PE matrix. Additionally, it aims at assessing the impact of this orientation on the barrier properties of the films obtained. The objective of this study is to comprehend the parameters that affect the barrier properties of films in a multi-nano-layer architecture and to overcome the scientific and technical challenges in achieving very low WVTR levels ($1 \cdot 10^{-5}$ g·m^{-2}·day^{-1}).

This thesis is structured as follows:

Chapter 1 provides a review of the current state of nano-composites, including their manufacturing and their barrier properties. It details also the multi-nano-layer co-extrusion technique and its applications. It also discusses the properties and structure of the PE which is the polymer matrix used for barrier films.

Chapter 2 presents the experimental parameters used to fabricate nano-composites and films, as well as all the characterization methods employed to analyze film microstructures.

Chapter 3 discusses the exfoliation of montmorillonite in LLDPE to produce a nanocomposite. It also covers the characterization of this exfoliation and the morphology of the blends.

Chapter 4 focuses on the orientation of montmorillonite in mono and multi-nano-layer films. It investigates the process parameters that favor the best possible orientation of

montmorillonite and examines the correlation between this orientation and the final barrier properties of the films.

Chapter 5 discusses the crystallization of LLDPE in the presence of montmorillonite and with a multi-nano-layer structure. It analyzes the resulting morphologies and their correlation with barrier properties.

Chapter 6 focuses on improving montmorillonite orientation through a bi-axial stretching process and explores its correlation with the barrier properties of the resulting films.

Chapter 7 provides a comprehensive conclusion to the study, analyzing the factors that affect the barrier properties of the obtained films and suggesting solutions to overcome the identified technical obstacles. Additionally, it explores potential applications of this work in fields beyond those related to gas barrier properties.

2. CHAPTER 2: STATE OF THE ART

INTRODUCTION

An overview of the key points and topics from the different scientific domains covered in the thesis will be summarized in this chapter. Starting with the definition of the nanocomposites and their specific properties, focusing specifically on layered silicates and, therefore, montmorillonite, which is the nano-filler under study. Then, the multi-nano-layer co-extrusion process will be explained, highlighting its efficacy in regulating polymer crystallization and its application in 2D filler-based nano-composites. Finally, a particular attention will be paid to the crystallization of poly(ethylene), which is the polymer matrix chosen for this work. Indeed, poly(ethylene) is a material that can develop different crystallization morphologies depending on the process parameters used and can affect the final properties of the materials.

2.1 POLYMER NANO-COMPOSITES WITH 2D MATERIALS

Composites are defined as the blend of two materials of different natures with the aim of obtaining a material exhibiting superior properties through the combination of the initial characteristics of both materials (**Chawla., 2012**). Polymer-based composites can incorporate reinforcement into two types of matrix: thermosets and thermoplastics. Thermosets are a type of polymer that includes materials like poly(urethane) (PU) and polyesters. Thermoplastics, such as poly(ethylene), poly(propylene), and poly(amide) (PA), are commonly used. Two types of composites are then distinguished based on the size of the reinforcement: long or short fibers microcomposites, characterized by reinforcements on the order of micrometers such as fibers (of 6-25 mm length for long fiber and 0.7-1 mm length for short fibers) or particles, and nanocomposites, with reinforcements approaching the nanometer scale (**Gloaguen & Lefebvre., 2007**).

2.1.1 General concept

As mentioned earlier, polymer-based nanocomposites are characterized by the size of the dispersed fillers. Indeed, the nanometric size of the fillers offers several advantages, such as a significant increase in interfacial surface area and a reduction, at an equivalent volumetric fraction of reinforcement, in the distances between particles (**Gloaguen & Lefebvre., 2007**).

There are several geometries of nano-fillers illustrated in **Figure 2-1** below:

Name	Shape
Sphere	
Platelet	
Cylinder	

Figure 2-1 : Shapes of nanoparticles (Sobamowo & Yinus., 2019).

As shown in **Figure 2-1**, the nanoparticles can be presented in different shapes. For example, the silica particles are nano-spheres with a diameter between 30 and 150 nm, carbon nanotubes are cylinders with a diameter range of 0.5 to 30 nm (according to multi-walls or single wall) and a length of 10 to 50 µm, and nano-silicate sheets are platelets with a length between 50 and 500 nm and a thickness of 1 nm (**Gloaguen &Lefebvre., 2007; Fu et al., 2019**).

A particular interest lies in a family of 2D nano-fillers, namely platelets or sheets. Due to their low thickness and lengths of up to several hundreds of nanometers, these fillers have a form factor ranging from 50 to 2000 for platelet-type reinforcements (**Gloaguen &**

Lefebvre., 2007). Among the 2D inorganic platelet fillers, various materials are found, such as graphite, boron nitride (h-BN), chalcogenides like MoS_2, layered silicates, or layered double hydroxides (LDHs) (**Nicolosi et al., 2013**).

2D fillers present in polymer nanocomposites are widely used in various applications. Their use aims primarily at improving the mechanical properties of polymer matrices (**Tjong., 2006**). By forming interfaces with the matrix in which they are dispersed, these fillers create reinforcement that increases the matrix strength, especially concerning its Young's modulus (**Kojima et al., 1993a and b; Ji et al., 2002**). In the work of **Kojima et al., 1993a**, the authors show that with a complete exfoliation, there is a 100% increase in the Young's modulus compared to the raw matrix, whereas with partial exfoliation, the observed increase is only 50%. This enhancement can be explained by the creation of numerous interfaces.

Additionally, they can improve the thermal and electrical conductivity within a material, due to their ability to orient anisotropically in the plane (thickness) (**Shen et al., 2021**). As described in **Figure 2-2**, due to their shape, these fillers also play a role in introducing tortuosity within the material, serving as a physical barrier.
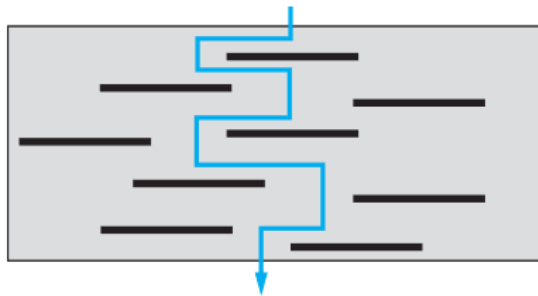
Figure 2-2 : Tortuous pathway created by nano-fillers (Gloaguen & Lefebvre., 2007).

Indeed, this configuration slows down diffusion within the nanocomposite, leading to improvements in certain properties such as flame retardancy, aiming to reduce the flammability of materials (**Porter et al., 2000; Gilman et al., 2000**). In some cases, as demonstrated by **Gilman., 1999** in a Silicate-Nylon 6 system, this allows a significant reduction,

in the range of 50 to 75%, in the propagation of combustion by promoting slower diffusion of combustion heat within the material.

Following the same logic, this type of nanocomposites are used for barrier applications to reduce gas diffusion and decrease the permeability of the matrices used (**Gloaguen & Lefebvre., 2007; Tan & Thomas., 2006**). **Yano et al., 1997** observed a reduction of 90% in water permeability compared to the matrix alone with the addition of 2wt% montmorillonite in poly(imide). This is also the case for **Xie et al., 2015**, who observed the reduction in oxygen permeability with the addition of only 0.02 vol% boron nitride nano-sheets (BNNs) in PET, and a 70% reduction with the addition of 3 vol% BNNS compared to the pure PET matrix. Finally, due to their size, this type of nano-filler does impact the optical properties of materials. This characteristic is due to the fact that when the particle size is approximately one-tenth of the light wavelength, the diffusion phenomenon is reduced. They preserve the transparency of the material, making it non-opaque, with a transmission kept at more than 90% (**Althues et al., 2007**).

2.1.1 The montmorillonite

Montmorillonite is a natural lamellar clay belonging to the silicate family, specifically the smectites (**Manas-Zloczower., 1994**). It is characterized by the stacking of multiple layers, giving it a distinctive multi-scale structure (**Figure 2-3**). Commercial clays typically consist of agglomerates with a size of approximately 10 µm, composed of aggregates that are assemblies of several tactoids. These tactoids, in turn, consist of around ten individual layers. The individual layers of montmorillonite possess interesting properties due to their thickness of approximately 0.96 nm and lengths that can extend to several hundreds of nanometers (**Vaia et al., 1995**).
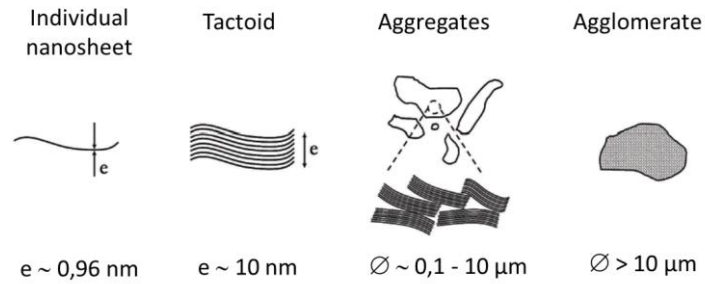
Figure 2-3 : Multi-scale structure of the smectites like Montmorillonite. Adapted from Domenech., 2012.

A montmorillonite layer has chemical formula $Si_4O_{10}(Al_{(2-X)}R_X^{2+})(OH)_2CE_nnH_2O$ with R a cation and CE the exchangeable cation in between TOT layers, as described by **Caillère et al., 1982**, with the following crystallographic model (**Figure 2-4**):
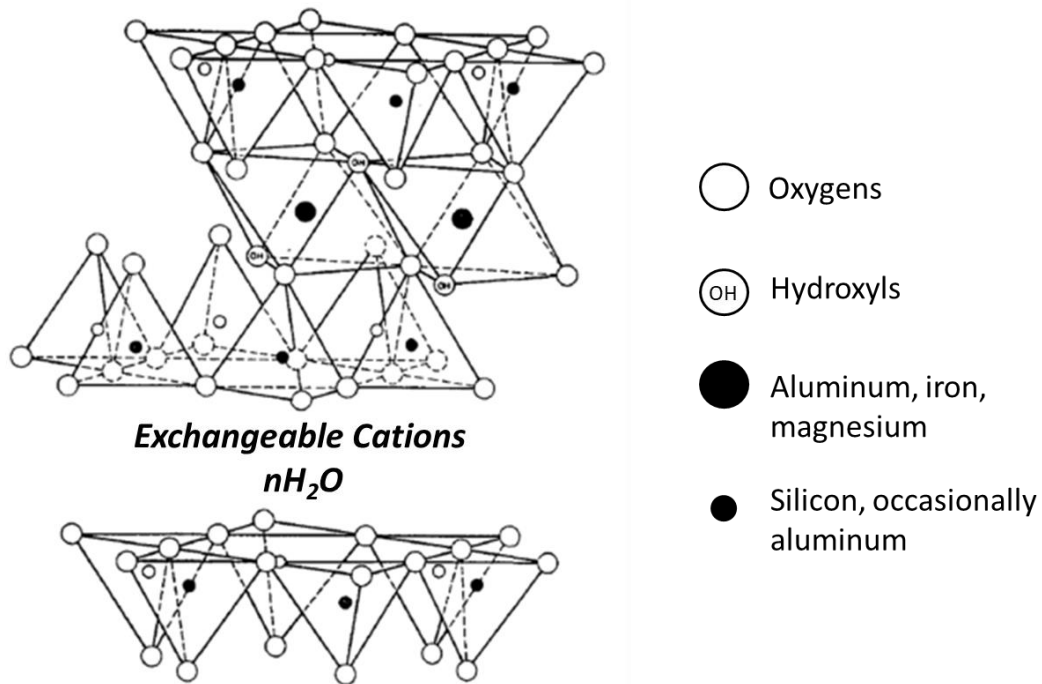
Figure 2-4 : Crystallographic model of a montmorillonite layer (Pusch & Karnland., 1996).

Montmorillonite is composed of a central octahedral layer sandwiched between two parallel tetrahedral layers, forming a unit layer known as 'tetrahedral-octahedral-tetrahedral'

(TOT), as illustrated in **Figure 2-4**. Montmorillonite has the peculiarity of having high isomorphic substitutions at the octahedral sites, notably the replacement of an Al^{3+} cation by a Mg^{2+} cation. This results in an excess of negative charges within the montmorillonite layers, promoting the presence of compensating ions such as Na^+ and Ca^{2+} between the layers, as well as the presence of water (**Caillère et al., 1982**).

By leveraging the ability of montmorillonite to accommodate compensating ions between its layers, companies have developed organomodified montmorillonites by replacing Na^+ ions with quaternary ammonium ions bearing a long aliphatic chain (**Fujiwara & Sakamoto., 1976**). This approach aims to overcome the hydrophilic nature of montmorillonite, primarily attributed to the presence of hydroxyl groups in the octahedral layer, hindering optimal compatibility with nonpolar organic polymer chains. Additionally, it allows for an increase in the space between the layers and reduces van der Waals interactions, promoting better exfoliation.

2.1.3 The exfoliation of 2D nano-materials

Commercial montmorillonite (MMT) particles are composed of a stack of nano-layers. Thus, the principle of exfoliation is to break the interactions between these layers to obtain dispersed individual nano-layers in the polymer matrix. In the context of polymer-based nanocomposites, there are several ways to exfoliate montmorillonite (**Zhu et al., 2019**). Most of these methods depend on the type of final application as well as the properties of the polymer matrices used.

Among these methods, there is the solution mixing. The principle is to mix the polymer and montmorillonite in a solvent in which the polymer is soluble and in which montmorillonite can swell. It will allow to promote its exfoliation and the intercalation of polymer chains between its layers (**Figure 2-5**). Thus, after the solvent is evaporated, the nanocomposite is obtained. This method is widely used for water-soluble polymers such as poly(vinyl alcohol) (PVA), Poly(ethylene oxide) (PEO) (**Greenland., 1963; Yeun et al., 2006; Zhao et al., 1989**).

However, this method is more complex to implement on a large scale as it involves a significant amount of solvent.
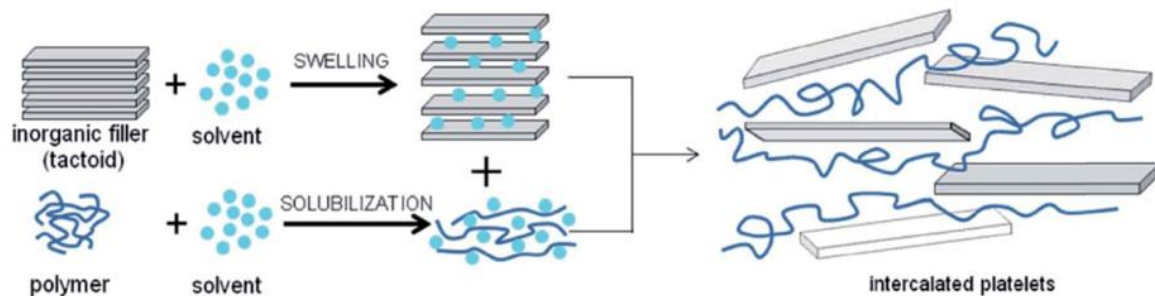
Figure 2-5 : Scheme of solution mixing exfoliation (Cui et al., 2015).

There is also *in situ* polymerization, which involves the mixture of montmorillonite and monomers in a solvent where both are miscible (**Figure 2-6**). In this way, the solvent has the ability to swell the montmorillonite, facilitating the insertion of monomers between the nano-layers of montmorillonite before polymerization. This method is applicable to various types of polymers of different natures, such as poly(amide) or amorphous polymers like poly(styrene) (**Akelah & Moet., 1996; Doh & Cho., 1998**), as well as polyolefin such as poly(propylene) (**Ma & Hu., 2001**) and poly(ethylene) (**Alexandre & Dubois., 2000**).
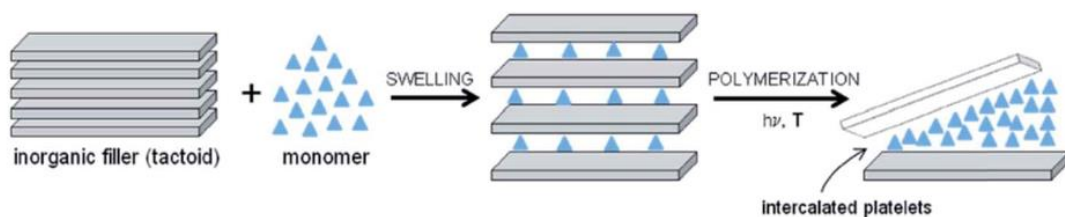
Figure 2-6 : Scheme of exfoliation by *in situ* polymerization (Cui et al., 2015).

Finally, melt extrusion exfoliation (**Figure 2-7**) represents an advantageous approach for the dispersion of fillers such as montmorillonite, especially when subsequent processing of the blends through extrusion is anticipated. Moreover, this process is conducive to continuous

41

exfoliation, facilitating large-scale production. The objective is to melt the polymer material through a twin-screw extruder, incorporating montmorillonite into it. The rotation of the screws generates shear forces on both the polymer matrix and the montmorillonite fillers, promoting the shear necessary for montmorillonite exfoliation. Additionally, polymer chains also have the ability to diffuse into the interlayer space of montmorillonite, thereby promoting intercalation and subsequent exfoliation.
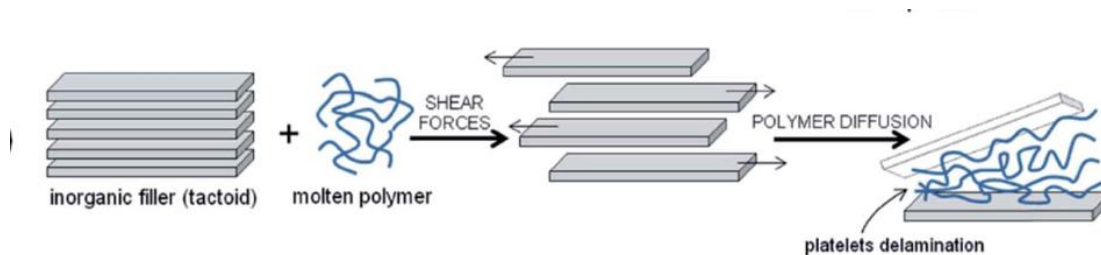
Figure 2-7 : Scheme of exfoliation by melt extrusion (Cui et al., 2015).

Several parameters can influence the melt extrusion exfoliation of montmorillonite. More in-depth studies have been conducted, notably by **Domenech et al., 2012 and Vergnes., 2019** on poly(propylene)-montmorillonite systems. The following parameters emerge from these studies:

- Increasing the screw rotation speed results in a decrease in both the number and size of agglomerates, as evidenced by the works of **Modesti et al., 2005**, **Lertwimolnun & Vergnes., 2007**, and **Domenech et al., 2012.** This increase in speed also promotes enhanced nano-dispersion and better filler exfoliation, as demonstrated by **Domenech et al., 2012**. In their study, these researchers characterized exfoliation based on melt yield stress and confirmed, with an equivalent formulation that increasing the screw rotation speed leads to an increase in this parameter.

- The extrusion feed rate also plays a significant role, as demonstrated by **Ryu & Chang., 2005**, who found more effective exfoliation of LLDPE/organo-modified montmorillonite (OMMT) at an extrusion feed rate of 3 kg·h^{-1} compared to 9 kg·h^{-1}.

Other studies have also indicated that at low feed rates, the improvement in exfoliation applies to both the size of agglomerates and nano-dispersion (**Domenech et al., 2012; Lertwimolnun & Vergnes., 2006**). This observation can be explained by the increased residence time, thus promoting the exfoliation process.

- Extrusion temperature and the molecular weight of the matrix are also parameters that impact montmorillonite exfoliation, although their effect remains relatively minor compared to the extrusion feed rate and screw rotation. In reality, the last two contribute to increasing the matrix viscosity, thus promoting an increase in stress applied to montmorillonite and facilitating its exfoliation. This has been illustrated, for example, by **Modesti et al., 2015**, who observed better exfoliation at a temperature of 180°C compared to 210°C. Similarly, studies such as those by **Normand et al., 2017** and **Shah & Paul., 2004** have demonstrated more effective exfoliation in a matrix with a higher molecular weight, unlike a matrix with a lower molecular weight.

Another parameter that can be used to combine the influence of most of the previously detailed parameters, is the specific mechanical energy (SME) as described in the following equation (2.1):

$$SME = \frac{\alpha \times C \times N}{Q} \qquad (2.1)$$

Where 'α' is a constant dependent on the motor power, maximum screw rotation speed, and maximum extruder torque; 'C' is the measured torque during extrusion; 'N' is the screw rotation speed, and 'Q' is the extrusion feed rate. **Domenech et al., 2012, 2013** were among the first to demonstrate that this parameter is correlated with an increase in the exfoliation rate. Indeed, an increase in energy input to the system results in an enhancement of exfoliation.

2.1.4 The characterization – case of the exfoliation by extrusion

Several methods can be employed to characterize the state of montmorillonite exfoliation in a polymer matrix, including X-ray diffraction (XRD), transmission electron microscopy (TEM), and rheology, particularly the study of material behavior at low frequency (**Biwas & Ray., 2001, Cassagnau., 2008**).

The most commonly used method is X-ray diffraction (**Figure 2-8**). Indeed, 2D materials, such as montmorillonite, are characterized by layers stacked along a specific lattice plane. In the case of montmorillonite, stacking occurs along the c-axis of the unit cell, with the (00l) planes defining these stacks. X-ray diffraction enables the determination of distances between atoms constituting the crystal structure, as these interatomic distances are on the order of the wavelength of X-rays.
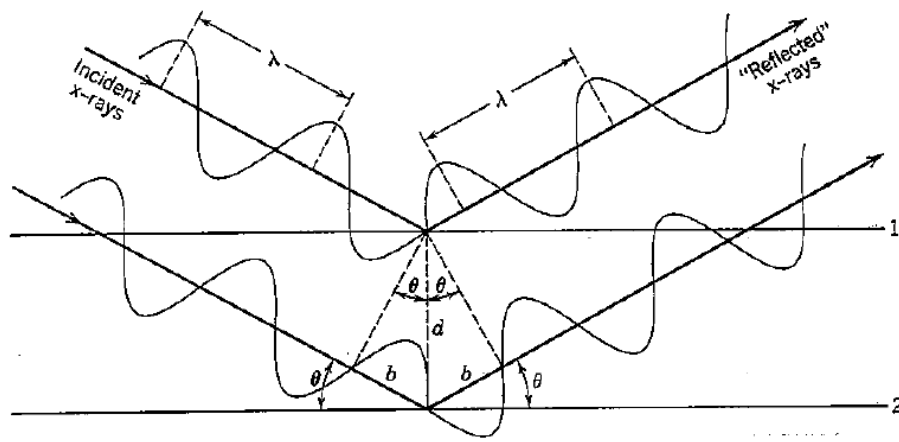
Figure 2-8 : Geometry of the Bragg reflexion analogy (Alexander., 1971).

Thus, irradiating the surface of a sample with a beam of X-rays at an incident angle 'θ' induces diffraction phenomena manifesting in certain directions. Each Bragg peak measured at a diffraction angle 'θ' follows Bragg's law (2.2), allowing the determination of interplanar distances for a given lattice plane:

$$2d_{hkl} \sin \theta = n\lambda \qquad\qquad (2.2)$$

Here, 'd_{hkl}' is the interplanar distance under study, and h,k,l are the Miller indices of the lattice plane. 'θ' is the diffraction angle, 'n' is the order of reflection, and 'λ' is the wavelength of the X-ray radiation used.

By studying Bragg peaks corresponding to lattice planes (00l), one can determine the interplanar distance along the c-axis. In the case of polymer chain intercalation between the layers, there is an increase in the 'd_{001}' distance, leading to a shift of the Bragg diffraction peak towards smaller angles compared to pure montmorillonite (**Figure 2-9**). In the scenario of complete exfoliation, the diffraction conditions are no longer satisfied, resulting in the disappearance of Bragg peaks (**Figure 2-9**) (**Gloaguen & Lefebvre., 2007**).
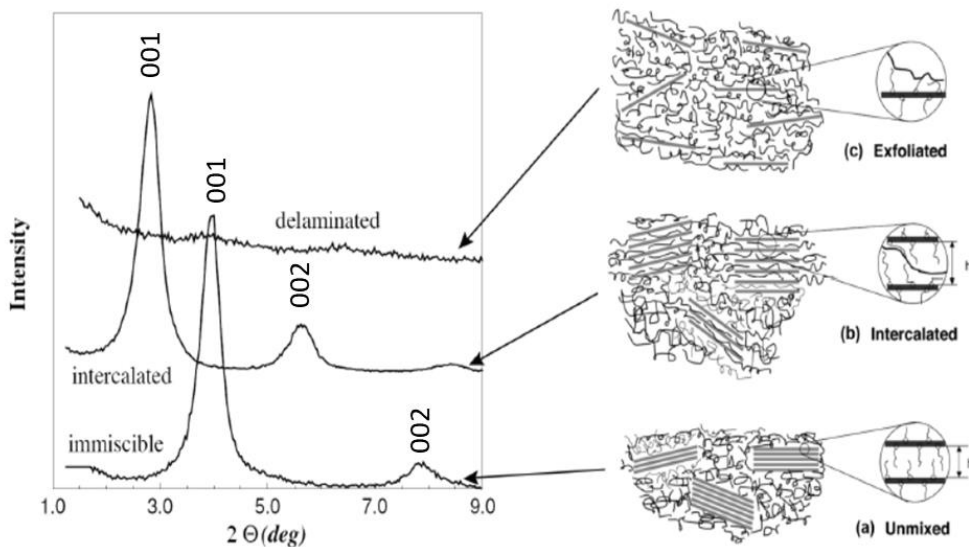
Figure 2-9 : XRD pattern from exfoliated, intercalated and immiscible MMT- polymer blends (Domenech., 2012).

There is also TEM for this purpose, which provides a direct observation of the morphology and dispersion state of fillers in a sample. Transmission electron microscopy is chosen for its ability to achieve high magnifications and to observe morphologies on a scale of a few nanometers, thus allowing the observation of exfoliation and dispersion of MMT

nano-layers in the polymer matrix. An example of possible morphologies is presented in **Figure 2-10** below:
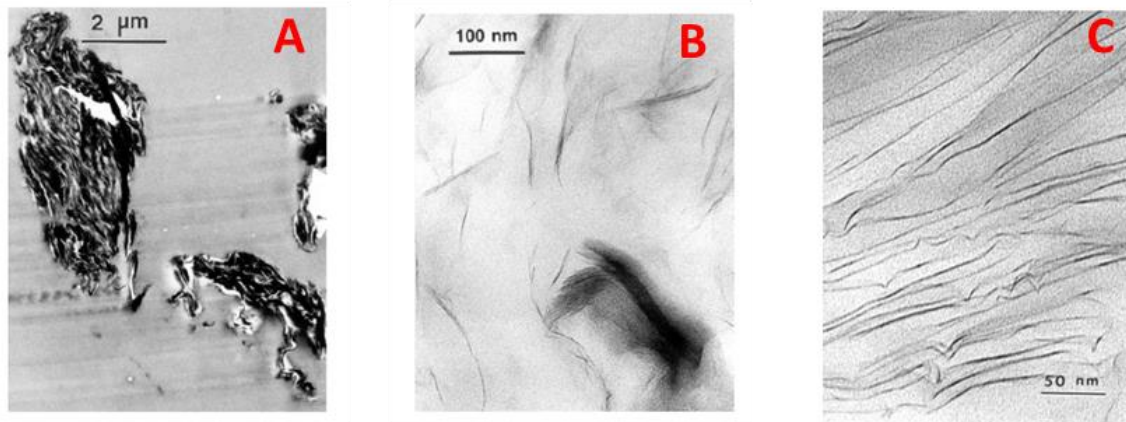
Figure 2-10 : TEM images of MMT dispersed in a polymer matrix, different morphologies are presented. A) Non exfoliated (Morgan & Guilman., 2003).

Morgan & Guilman., 2003 conducted a study demonstrating that TEM is the preferred method for identifying the presence of mixed intercalated and exfoliated montmorillonite (**Figure 2-10**). XRD has limitations in identifying certain morphologies. The Bragg peak is still present because of the intercalated montmorillonite, but its intensity decreases as some montmorillonite nanosheets are exfoliated. Therefore, TEM is necessary to confirm these hypotheses. However, in cases of complete exfoliation, XRD remains the preferred method because it can directly identify Bragg peaks that disappear in this scenario.

However, it is important to note that transmission electron microscopy provides a local analysis of montmorillonite exfoliation. For this reason, rheology serves as a complementary method for characterizing montmorillonite exfoliation as a whole by measuring the mechanical behavior of the nanocomposite (**Figure 2-11**).

Indeed, the presence of individual platelets, combined with the reduction in the number of layers in tactoids, promotes enhanced interactions and leads to the formation of a percolated network. This percolated network can be clearly observed through a small-amplitude oscillatory shear measurement with the appearance of a plateau for the elastic modulus G' at low frequency (**Figure 2-11a**) (**Cassagnau., 2008**).
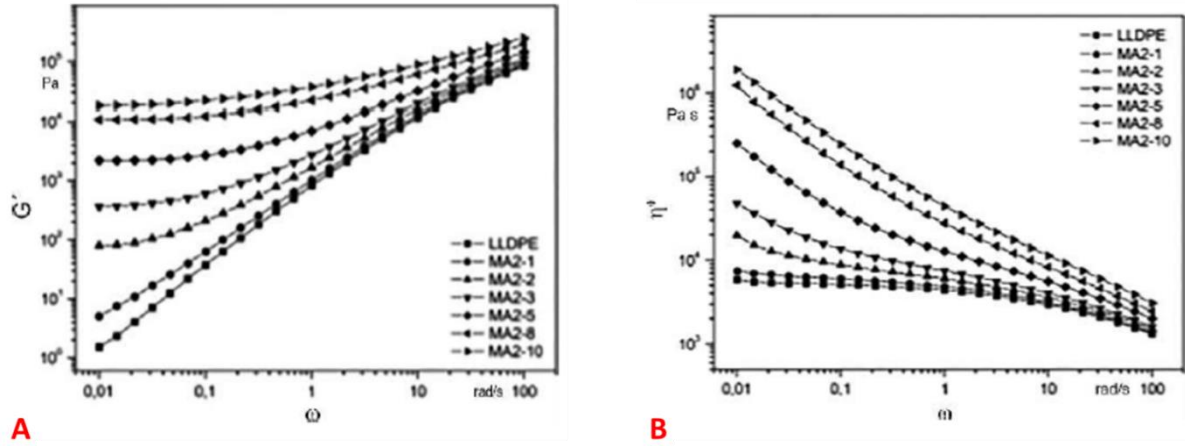
Figure 2-11 : a) Frequency dependence of the storage modulus (G') of the nanocomposite series prepared with an increase amount of MMT b) Frequency dependence of the dynamic viscosity (η*) of the nanocomposite series prepared with an increase amount of MMT; (Durmus et al., 2007).

This phenomenon is also reflected in an increase in the complex viscosity (η*) at low frequency (**Figure 2-11b**). This variation can be modeled by the Carreau-Yasuda equation (2.3) with a yield stress (**Lertwimolnun & Vergnes., 2005**).

$$\eta^*(\omega) = \frac{\sigma_0}{\omega} + \eta_0[1 + (\lambda\omega)^a]^{\frac{n-1}{a}} \tag{2.3}$$

Here, 'η*' is the complex viscosity, 'σ_0' the melt yield stress, 'ω' the angular frequency, 'η_0' the Newtonian viscosity, 'λ' is the characteristic relaxation time, 'a' is the Yasuda parameter, and 'n' is the shear-thinning index.

Thus, **Vergnes., 2011** demonstrated for the first time that the yield stress parameter was a crucial factor in accurately describing the increase in the level of exfoliation (at an equivalent concentration) and, more generally, the enhancement of interactions between nano-fillers (**Figure 2-12**).
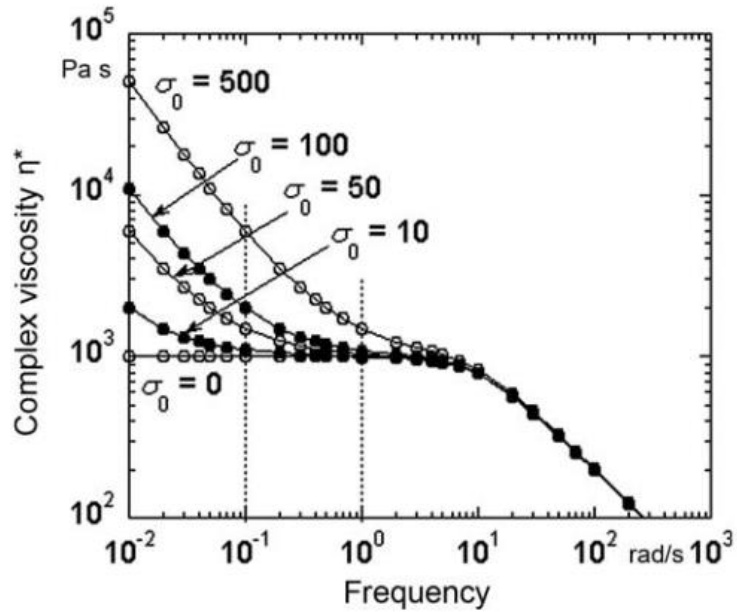
Figure 2-12 : Modelisation of complex viscosity curves for different values of yield stress 'σ₀' (Vergnes., 2011).

The use of this parameter has been widely adopted and validated in the studies by **Normand et al., 2017**; **Domenech et al., 2012,2013**; **Khosrokhavar et al.,2016**, and **Watzeels et al., 2013** on the characterization of montmorillonite exfoliation.

2.1.5 The application to barrier films

As mentioned earlier, in the context of an application involving barrier properties, the goals of adding 2D nano-fillers are: to increase the diffusion path of gases through the polymer matrix and to orient these nano-fillers to achieve a charge orientation parallel to the sample's surface.

Nielson., 1967 developed a model for predicting the permeability of nanocomposite-type materials by introducing the concept of tortuosity into its modeling. The relative permeability of the nanocomposite is defined by the following equation (2.4):

$$P_{Relative} = \frac{P_{nanocomposite}}{P_{Matrix}} = \frac{\phi_{Matrix}}{\tau} \qquad (2.4)$$

Where 'P' is the permeability, 'ϕ_{Matrix}' is the volumetric fraction of the matrix, and 'τ' is the tortuosity factor. The tortuosity factor is defined by the equation (2.5) and the following parameters:

$$\tau = 1 + \frac{L}{2W}\phi_{Filler} \tag{2.5}$$

With 'L' being the length of the filler, 'W' the thickness of the filler, and 'ϕ_{Filler}' the volumetric fraction of the filler.

At a high 'L/D' ratio, corresponding to the aspect ratio of the filler (length and diameter), permeability is significantly reduced, hence the interest in 2D nano-fillers. However, in this model, the orientation of the fillers is not taken into account. That is why **Bharadwaj., 2001** introduced a parameter characterizing the orientation of the filler, the order parameter '*S*' calculated by the following equation (2.6) (**Chandrasekhar., 1992**):

$$S = \frac{1}{2}(3cos^2\theta - 1) \tag{2.6}$$

 Where 'θ' corresponds to the angle between the normal direction of the 2D nano-filler and the surface of the sample, as shown in **Figure 2-13**:

- S = 0: the fillers are randomly oriented;
- S = −0.5: the fillers are perpendicular to the surface or 'edge-on';
- S = 1: the fillers are parallel to the surface or 'in-plane';
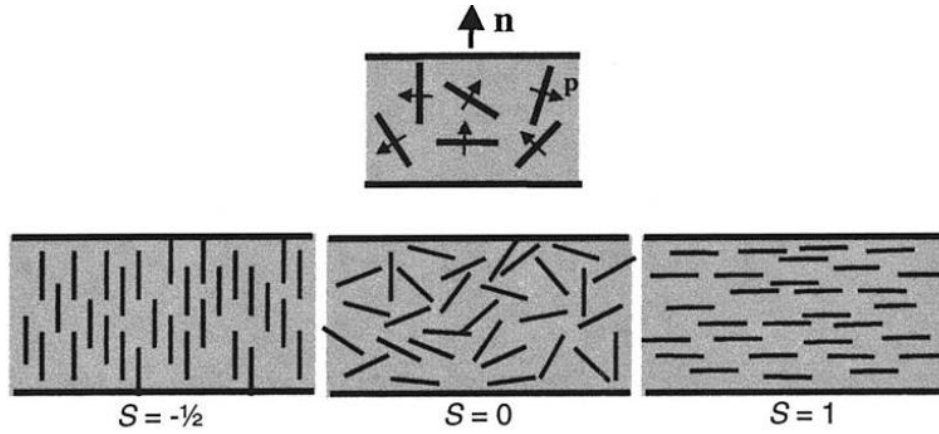
Figure 2-13 : Scheme of the nano-fillers orientation according to the corresponding orientation parameter S value, (Bharadwaj., 2001).

Thus, the following permeability equation (2.7) can be obtained:

$$P_{Relative} = \frac{1 - \phi_{Filler}}{1 + \frac{L}{2W} \phi_{Filler} \left(\frac{2}{3}\right)\left(S + \frac{1}{2}\right)} \tag{2.7}$$

Then, as shown in **Figure 2-14**, the closer the order parameter 'S' approaches 1, indicating a more 'in-plane' filler orientation, the more the relative permeability is reduced, regardless of the length of the filler. This clearly demonstrates that the orientation of the fillers has an impact on permeability.
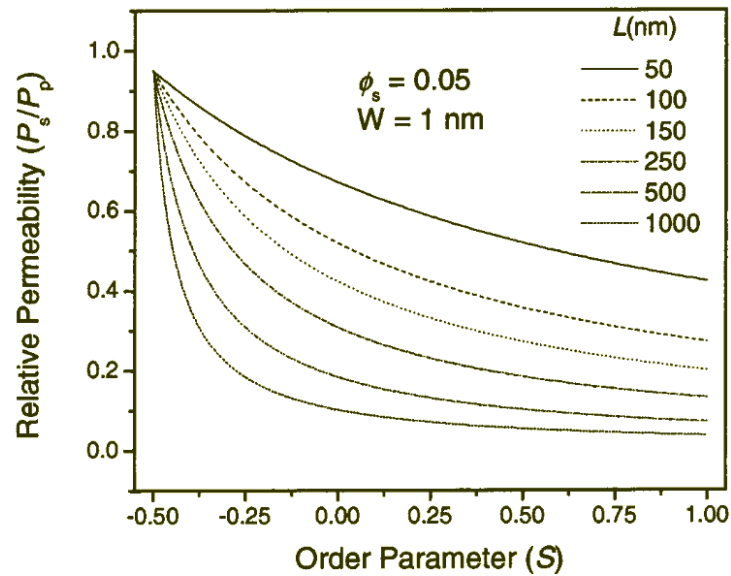
Figure 2-14 : Effect of sheet orientation on the relative permeability in exfoliated nanocomposites at a volume fraction of 0.05 and 1 nm width (Bharadwaj., 2001).

Various studies have been conducted in the field of polymer-based nanocomposites, including the incorporation of montmorillonite (**Cui et al., 2015; Tan & Thomas., 2016**). In most studies, the orientation of the 2D nano-filler is taken into account in the modeling to determine which model corresponds best to the measured permeability values at different filler concentrations. For example, the studies of **Alix et al., 2012, and Li et al., 2018,** demonstrated that an increase in the montmorillonite content leads to a decrease in permeability. By using the Nielson model combined with **Bharadwaj., 2001** modeling, which incorporates orientation factors, researchers have shown that with an S=1 value, the models tend to approximate the observed variations. However, these models do not always agree. Several hypotheses have been highlighted, as described in the work of **Tenn et al., 2013**, where other parameters such as gas sorption, effects of fillers percolation, and the level of crystallinity in the matrix play a role in diffusion and are not necessarily considered by these models. Moreover, the determination of the orientation of the fillers is not quantitative, relying solely on observations in microscopy rather than quantification through other methods such as X-ray diffraction (**Bartzczak et al., 2014**).

2.2 MULTI-NANO LAYER POLYMER CO-EXTRUSION TECHNOLOGY

Cast extrusion is a widely used industrial process to manufacture polymer films for various applications. In recent years, techniques have been developed to create multi-layer films and even multi-nano-layer films. These methods allow the combination of polymers of different natures and manipulation of the final material's properties. We will introduce the concepts of monolayer and multi-nano-layer cast film extrusion. Furthermore, we will examine in more detail the work done on the incorporation of two-dimensional nanomaterials and on barrier properties in a multi-nano-layer system.

2.2.1 Cast film extrusion

The production of plastic films, especially those intended for food packaging, relies on the flat film extrusion process. This process involves melting polymer pellets through a heating barrel equipped with a single screw. The screw's role is to convey the molten material to the exit, where a flat die shapes the material into a film (**Figure 2-15**). The flat die applies stress to the molten material, generating additional shear forces to facilitate flow and ensure uniform filling, resulting in the formation of a uniform film (**Silagi., 2005**).
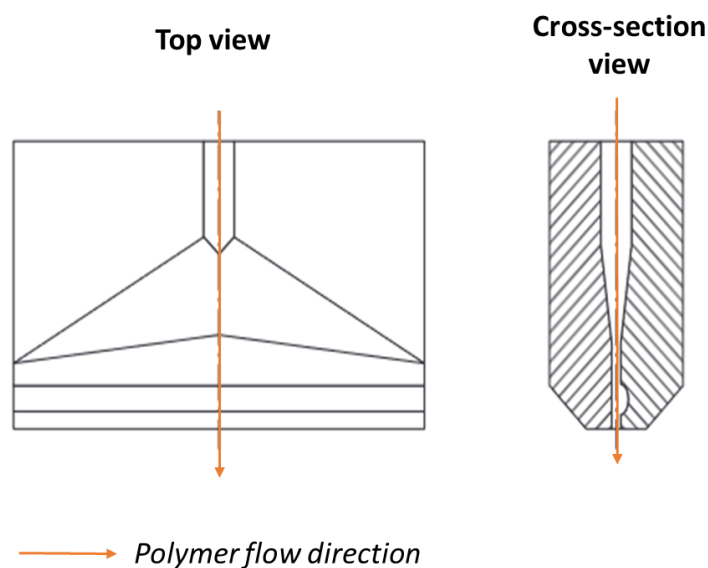
Figure 2-15 : Scheme of the interior of a flat die known as a 'fish tail', adapted from Silagi., 2005.

Subsequently, the film is cooled-down on chill rolls whose temperature and speed are adaptable (**Figure 2-16**). Adjusting the temperature allows for quenching the molten material, thereby controlling its crystallization. Furthermore, adjusting the rolling speed enables stretching of the material in the molten state, influencing the conformation of molecular chains and also the material's crystallization.
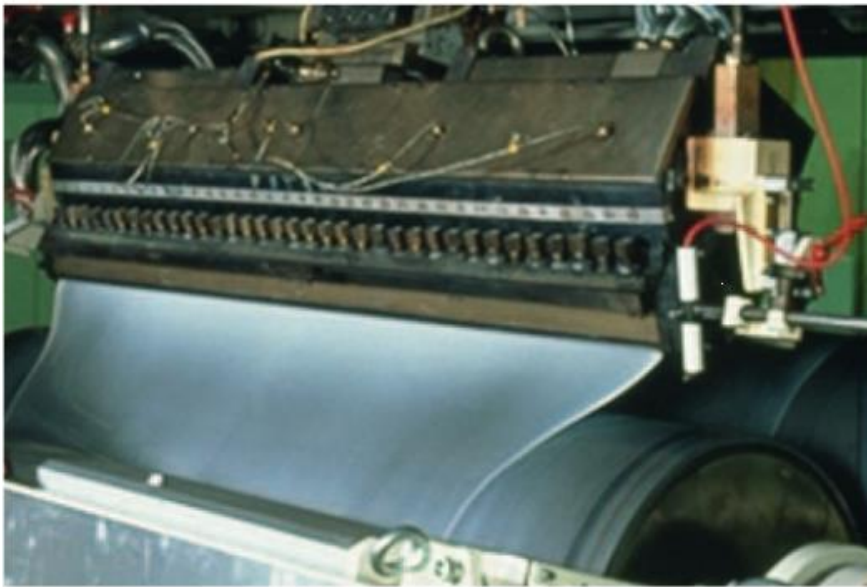
Figure 2-16 : Cooling of the melted polymer film at the exit of the flat die on the chill roll, (Silagi., 2005).

In this stage, is possible to control the film's thickness as well. On one hand, by adjusting the opening of the flat die's lips according to the requirements. On the other hand, by the adjusting the rolling speed of the chill-rolls (**Figure 2-17**). Indeed, reducing the film's thickness is possible by applying a stretching on the molten material. However, it should be noted that this process can lead to lateral constriction phenomena of the material, reducing the width of the film as shown in **Figure 2-16**.
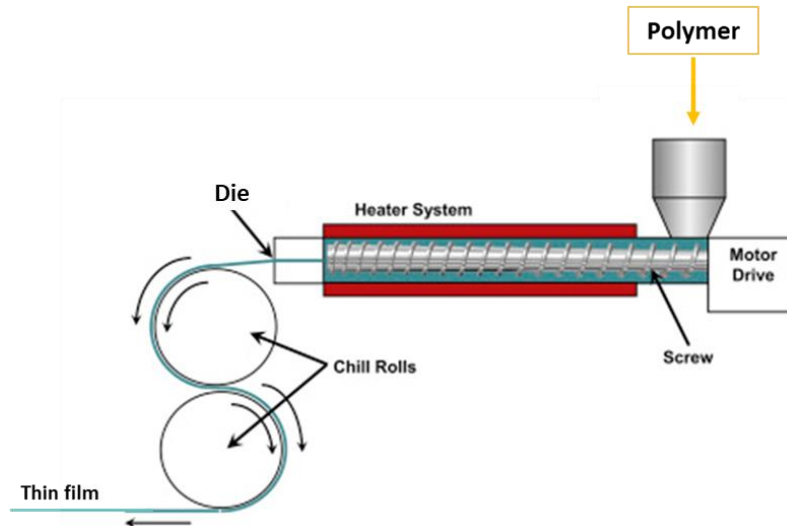
Figure 2-17 : Scheme of cast extrusion line, adapted from McKeen., 2015.

2.2.2 Cast film co-extrusion

While maintaining the same cast film production process, it is possible to move towards a slightly more complex film architecture by increasing the number of layers of the films, combining 1 to 3 different polymers. This enables the production of a film with distinct properties associated with the combination of these materials. To accomplish this, a co-extrusion block, referred to as a feed block, is used. It comprises channels that combine the streams from multiple extruders into a single stream before passing through the flat die (**Figure 2-18**) (**Agassant & Demay., 2022**).

Cross-section view
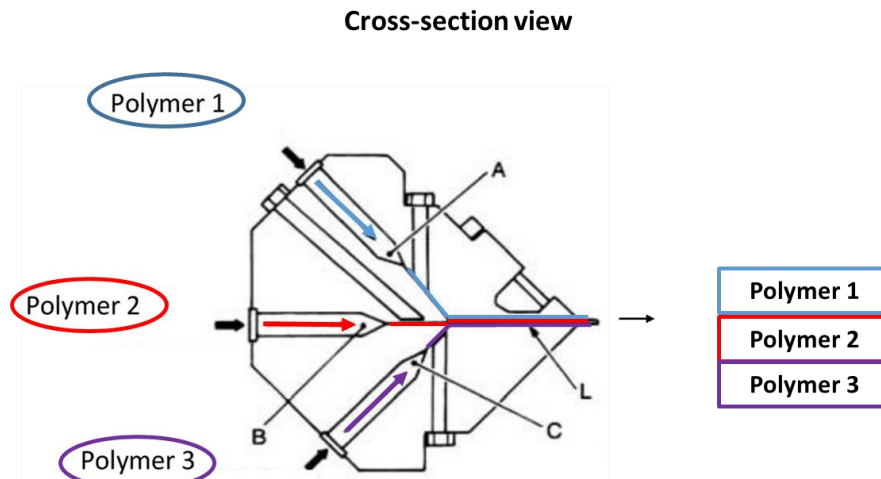
Figure 2-18 : Multi-channel co-extrusion block, adapted from Agassant & Demay., 2022.

Some requirements are necessary for the co-extrusion process. Indeed, the viscosity ratio between the different combined polymers must be respected, ideally with a ratio of 1. Beyond 1, this indicates a significant viscosity mismatch between the materials, potentially resulting in the encapsulation phenomenon. This occurrence is favored by the material with the lower viscosity, leading to the encapsulation of the more viscous one, as shown in **Figure 2-19**.
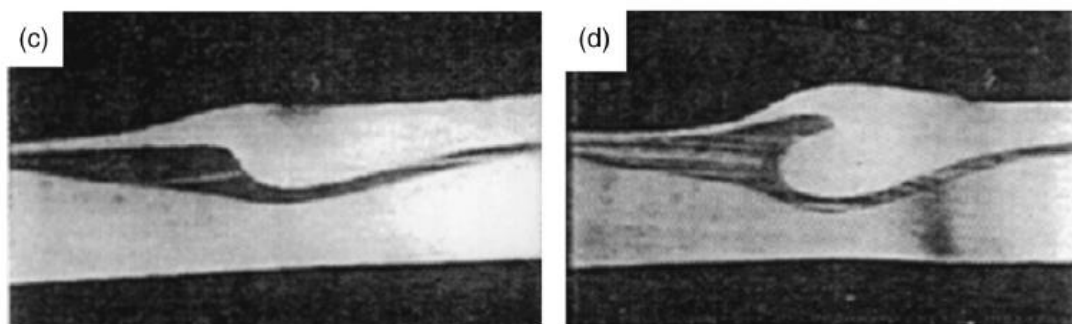
Figure 2-19 : Picture of encapsulation phenomenon during co-extrusion (Langhe et al., 2016).

Furthermore, it is preferable to use a combination of two materials that are chemically or physically compatible. The goal is to achieve good adhesion between the two polymer phases to avoid any delamination issues between them. This adhesion is primarily created by the

presence of an interphase between the polymer layers, which is on the order of a few nanometers and consists of a combination of the two coexisting phases (**Lu et al., 2021**).

2.2.3 The multi-nano layer polymer co-extrusion (MNL)

The multi-nano-layer co-extrusion technique allows the combination of extruder flows from 2 up to 3 polymers of different or identical natures via a co-extrusion feedblock, as explained earlier. Then, by passing this flow through multiplier elements, it is possible to obtain a film with up to several thousand layers in a single step (**Figure 2-20**).
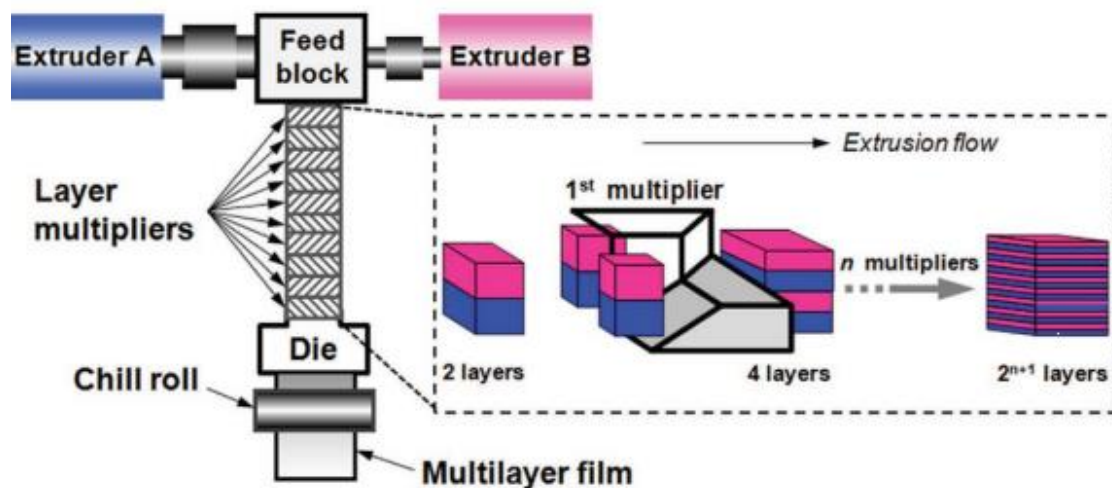
Figure 2-20 : Scheme of a multi-nano layer co-extrusion line (Lu et al., 2020).

Indeed, during the 1960s-70s, Dow Chemical developed and patented various technologies to increase the number of layers, by split and recombine the molten polymer flows **(Schrenck., 1975; Schrenck et al., 1971; Nissel., 1976**).
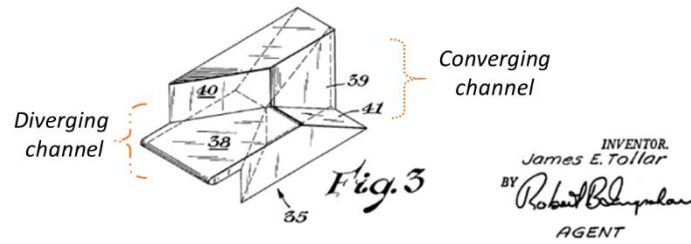
Figure 2-21 : Scheme of a layer multiplier element (LME) developed by Tollar (Tollar., 1966).

The most widely used and commercialized technology is the one developed by **Tollar., 1966** (**Figure 2-21**), known as the 'interface generator' and more commonly referred to a 'layer multiplier element' (LME) in scientific literature. In the case of combining the flow of 2 polymers (**Figure 2-22**), it involves vertically splitting the polymer flow into two. Each of the two flows is first compressed vertically by passing through the converging channel of the multiplier element, and then laterally stretched by the diverging channel before being recombined at the output of the multiplier element. Thus, the different dimensions of the channels induce a pressure delta (between the entrance and the exit of the LME) on the molten material flow, promoting more or less significant shear on the material (**Zang et al., 2019**). The sudden deformations experienced by the molten material during this multiplication are assimilated to bi-axial stretching of the molten material.
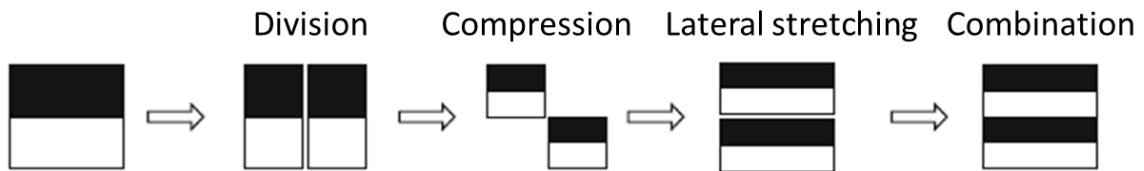
Figure 2-22 : Transformation and deformation undergone by the polymer flow in the multiplier elements, (Sollogoub., 2018).

The multiplier elements are installed in a block allowing the alignment of up to 12 LMEs successively. The final number of layers generated depends on both the number of layers at

the output of the co-extrusion block and the number of multiplier elements. The final number of layers can be calculated using the following equation (2.8):

$$N = 2^{n+1} \qquad (2.8)$$

With 'N' the number of layers, 'n' being the number of multiplier elements. It is therefore possible to design a film from 2 up to 8, 32, or 4096 layers, as shown in **Figure 2-23** below.
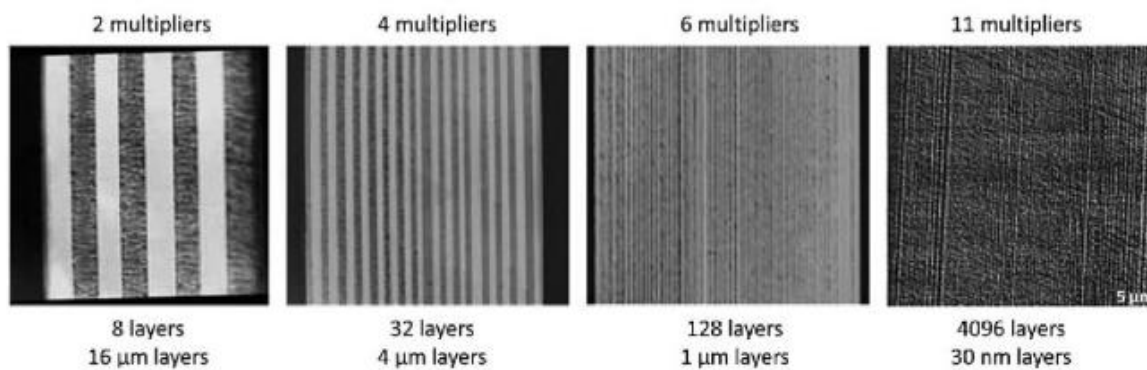
Figure 2-23 : Multi-nano-layer films Poly(carbonate) (PC)/ Poly(methacrylate methyl acrylique)(PMMA), A-B configuration, 50/50 vol% phase ratio, film thickness 127 μm (Langhe et al., 2016).

For most of the research dealing with MNL technology, the main objective is to achieve the lowest possible nominal layer thickness, in order to promote various phenomena as:

- Control of polymer crystallization through confinement effect. (**Carr et al., 2012**)
- Orientation of dispersed fillers in one of the layers. (**Gao et al., 2018; Decker et al., 2015**)
- Promoting adhesion, compatibility between two more or less miscible phases to create an interphase. (**Lu et al., 2020, 2021**)
- To promote co-extrusion in some cases with highly mismatched viscosities (viscosity ratio up to 2) without generating defects. (**Li et al., 2024**)

Several parameters can be varied during film fabrication to minimize the nominal layer thickness:

- Equivalent film thickness:
  - ○ Increase the number of multiplier elements and thus the number of layers. (**Langhe et al., 2016; Zhang et al., 2014c**)
  - ○ Variation of the volumetric proportion of each phase by adjusting the extruder feed rates. (**Zhang et al., 2014a; Langhe et al., 2016**)
- Equivalent number of layers and equivalent phase volume:
  - ○ Reduction of the total film thickness by stretching during cooling or by decreasing the opening of the flat die. (**Jin et al., 2004**)

All these parameters can be combined in order to obtain the nominal layer thickness, as described in equation (2.9):

$$h_{individual\ layer\ A\ or\ B} = \gamma_{A\ or\ B} \times \frac{h_{film}}{2^{n+1} + 1} \qquad (2.9)$$

Where 'h' is the thickness of the overall film, 'ϒ' is the proportion of phase A or B, and 'n' is the number of multiplying elements.

However, it is important to keep in mind that below a certain layer thickness, around 10 nm, instabilities occur due to an increase in the interfacial tension of polymer chains. This leads to the creation of layer breaks that can alter the final properties of the films (**Figure 2-24**) (**Bironeau et al., 2017).**
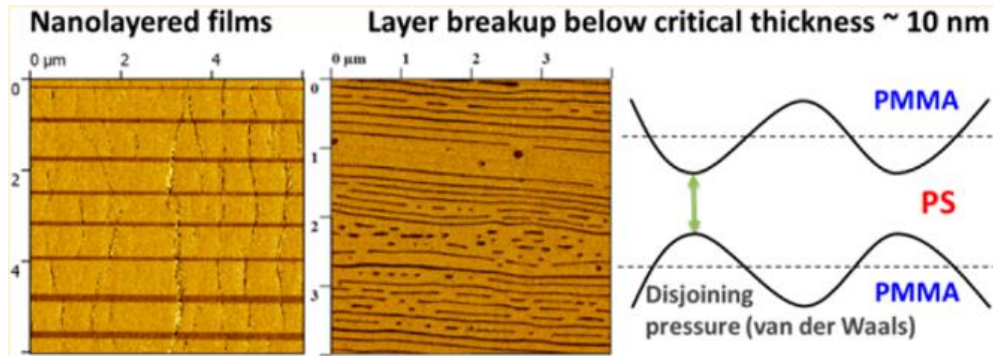
Figure 2-24 : Images of layer break up in MNL film with PMMA/PS (Bironeau et al., 2017).

The control of the layer architecture provided by the MNL configuration allows adjusting the film's properties for various applications, such as dielectric properties (**Lu et al., 2020; Mackey et al., 2011**). For optical properties, aiming to increase the transmission of films compared to conventional blends, **Zeng et al., 2020** have demonstrated that they could go from 61.8% light transmittance for a blend to 89.4% for a multi-nano layer architecture on a poly(propylene carbonate) / thermoplastic poly(urethane) system. Some other studies focus on improving mechanical properties, such as **Burt et al., 2012** or **Li et al., 2014,** or **Cabrera et al., 2021**. However, the majority of the research is concentrated on enhancing barrier properties, either by combining several materials with complementary barrier effects, such as poly(butylene succinate-co-butylene adipate) (PBSA) with poly(lactic acid) (PLA), or PE with polyamide in the works of **Messin et al., 2020b** or **Lozay et al., 2021**. Or alternatively, by promoting control over polymer crystallization to influence orientation and increase crystallinity, thereby blocking gas diffusion (**Carr et al., 2017**).

2.2.4 The control of the polymer crystallization

As mentioned earlier, most of the work relies on the combination of two polymers of different natures. Indeed, when combining an amorphous polymer 'A' with a semi-crystalline polymer 'B', or two semi-crystalline polymers 'A' and 'B' with distinct crystallization temperatures, this can lead to confinement-induced crystallization phenomena. In the case of MNL technology, the phenomenon was first demonstrated on poly(ethylene oxide) confined

by Ethylene acrylic acid copolymer (EAA) by **Wang et al., 2009a**, and then extensively studied on other materials such as PS/PMMA combinations; PMMA/poly(caprolactone) (PCL); PS/PEO; PC/poly(Vinylidene Fluoride) (PVDF); PS/PP; PS/HDPE; PS/PCL (**Carr et al., 2011**).

In general, the idea is that the glass transition temperature (T_g) of the amorphous polymer should be higher than the crystallization temperature (T_c) of the semi-crystalline phase. Thus, during cooling, the chains of the amorphous layer solidify prior to the crystallization of the chains in the semi-crystalline phase, exerting pressure on the chains of the semi-crystalline phase. This has the effect of constraining the orientation of the chains and, consequently, controlling their crystallization.
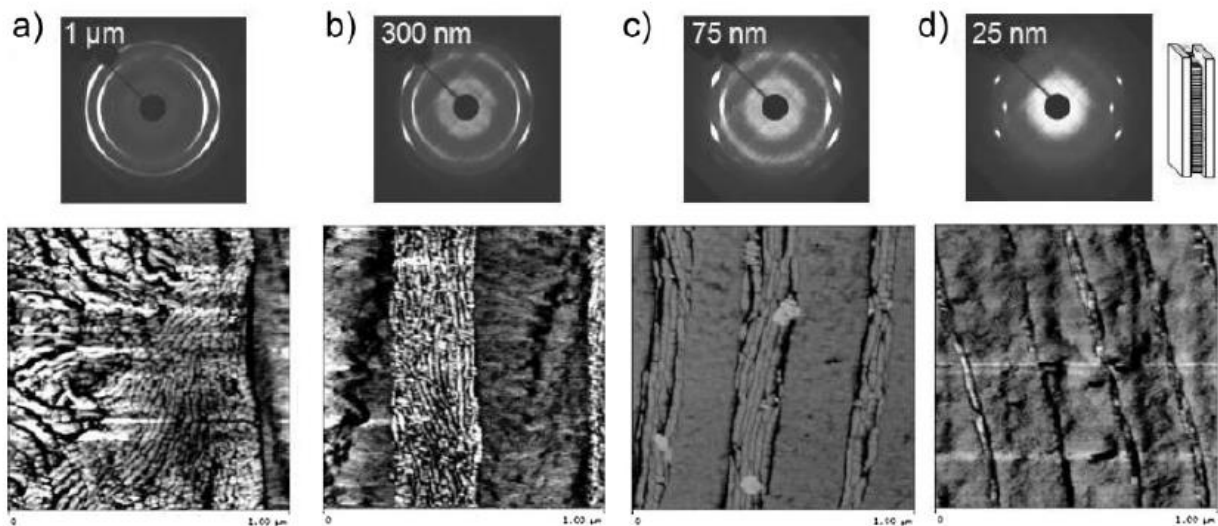
Figure 2-25 : 2D WAXS extrusion direction patterns and AFM cross-section images in PS/PEO layered film with nominal layer thickness of a) 1μm, b) 300nm, c) 75nm, and d) 25.nm (Pontig et al., 2010).

As illustrated in **Figure 2-25**, by reducing the thickness of the layers in the semi-crystalline part from 1 μm to 25 nm, a layer size similar to that of polymer chains is achieved. This modification promotes the transition from spherulitic crystallization to 2D crystallization of the chains in the form of oriented lamellae. This is confirmed by diffraction patterns, which demonstrate a shift from predominantly isotropic diffraction of PEO to increasingly fine localized diffraction poles, indicating a preferential orientation.

In **Figure 2-26**, a more in-depth study conducted by **Pontig., 2010**, showed in the case of a PCL/PS multilayer film that between 3000 and 100 nm layer thickness, there is an influence on the orientation of PCL crystals. From 100 nm onwards, PCL crystals begin to adopt an 'in-plane' crystal orientation with a lattice plane orientation parameter (110) tending towards 1.
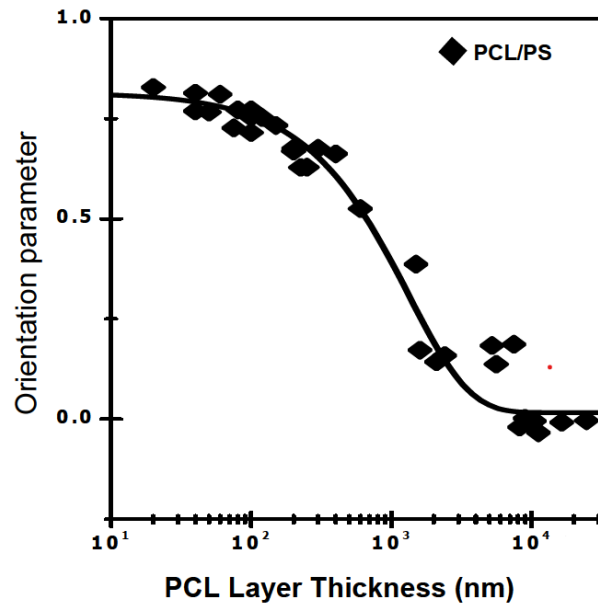
Figure 2-26 : Orientation parameter according to the PCL layer thickness (Pontig., 2010).

The objective of controlling the orientation of polymer crystals is to enable better control of the barrier properties of films. Indeed, taking the example of the work by **Wang et al., 2009b**, in **Figure 2-27**, they demonstrate that reducing the thickness of the layers leads to a decrease in the barrier properties of films by approximately 2 decades in the case of a PS/PEO system with a crystallinity in the range of 70% for the PEO (with a control crystallinity of 76%). This improvement is induced by controlling the orientation of PEO crystals parallel to the layers with an orientation factor that tends towards -0.5 (In this case the lattice plane which is used to characterize the 'in-plane' orientation of PEO crystals is the (120). When this lattice plane is oriented perpendicular to the film surface, it means that crystals are 'in-plane' oriented, therefore the orientation factor f_{120} tend to -0.5) (**Figure 2-27b**).
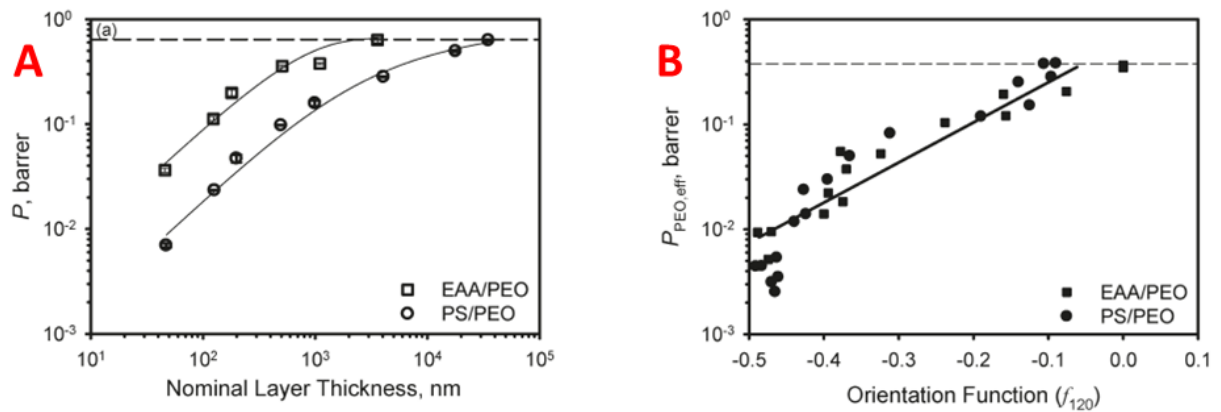
Figure 2-27 : A) Variation of the barrier properties according to the layers thicknesses B) Variation of the barrier properties according to the orientation factor (Wang et al., 2009b).

One way to control these orientation phenomena is recrystallization, which allows certain systems to transition from an 'on-edge' orientation, meaning crystallization perpendicular to the layers, to an 'in-plane' orientation, parallel to the layers.

Indeed, by heating the film to a temperature below the glass transition temperature (T_g) of the amorphous confined phase and above the T_g of the semi-crystalline polymer, it enables the semi-crystalline phase to reorient while being subjected to the confinement forces applied by the amorphous phase. Thus, with preliminary studies such as the works of **Wang et al., 2010**, finding an optimal temperature at which to freeze the system allows achieving an 'in-plane' orientation (**Figure 2-28**).
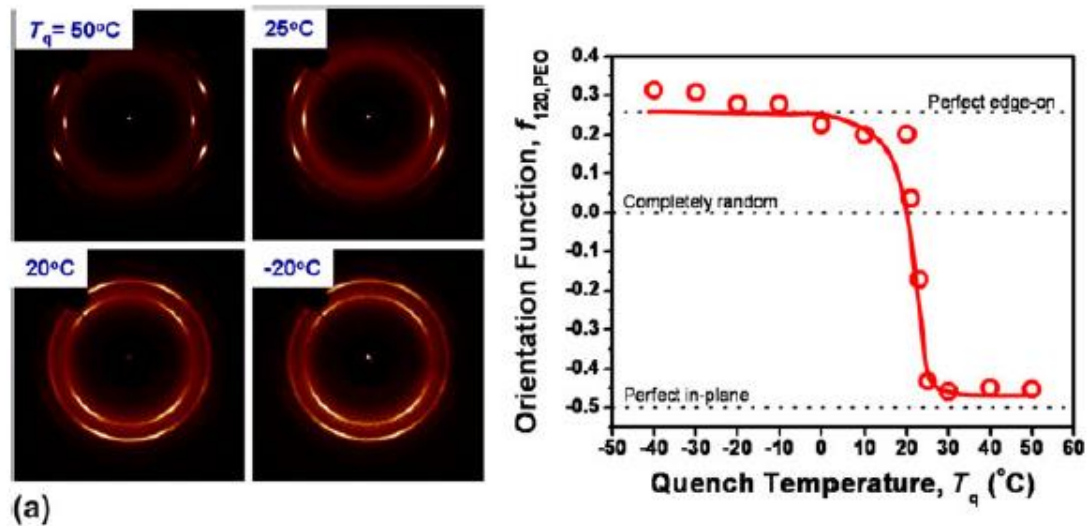
Figure 2-28 : ED WAXS pattern for PS/PEO nanolayered film with 75nm layer thickness of PEO quenched at various temperatures. Corresponding orientation function calculated according to the quenching temperature. Adapted from Carr et al., 2011.

Despite the significant effects brought about by this recrystallization method, it requires post-processing of films, which can be limiting in large-scale production of barrier films.

2.2.5 The addition of 2D fillers

Studies on the integration of 2D fillers in multi-nano-layer systems have revealed various contributions of these fillers to the final properties of films, as well as different methods for their orientation.

In the example of an LLDPE matrix with the addition of graphite particles in a ratio of 10:1, as studied by **Shi et al., 2019**, increasing the number of layers from 1 to 729 resulted in an elevation of the film crystallinity rate from 27% to 34% and an improvement in dielectric properties. The authors attribute these results to better filler orientation and increased compaction between the fillers. **Zhang et al., 2019** quantified the orientation of expanded graphene in a TPU matrix by analyzing the intensity of the 002 Bragg peak of graphene. The results demonstrated increased 'in-plane' filler orientation with a filler content increase from 5 to 15wt%, all within a multi-layer structure. **Li et al., 2014's** work showed an increase in the

mechanical properties of PMMA in the extrusion direction, indicating improved filler orientation in a PMMA/PMMA-graphene system with a 2wt% of fillers. Finally, simulations of graphene orientation during MNL co-extrusion conducted by **Shi et al., 2019** demonstrated that graphene orientation is not necessarily homogeneous based on layer position, with outer layers exhibiting better filler orientation than the core of the sample.

Regarding the incorporation of 2D fillers in multi-nano-layer systems to enhance film barrier properties, **Decker et al., 2015**, demonstrated a 63% improvement in oxygen barrier properties compared to a multi-nano-layer LDPE/LLDPE-g-MA system of 65 layers without fillers. The results were obtained after thermal annealing allowing polymer chain diffusion between LDPE and LLDPE-g-MA phases to concentrate MMT fillers in very thin layers and thus improve the barrier properties of the films (**Figure 2-29**).
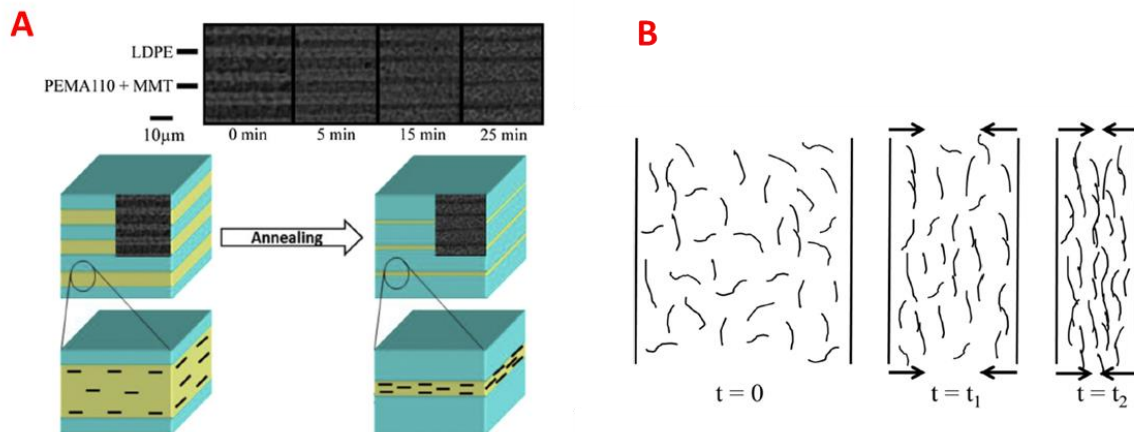
Figure 2-29 : A) Scheme of the effect of thermal annealing on the multilayered films morphologies. B) Modeling of the evolution of the fillers compacity in the layers due to the thermal annealing (Decker at al., 2015).

In this case, the authors did not investigate whether the thermal annealing improved the filler orientation or if the concentration of fillers was the sole factor affecting the barrier properties.

While remaining in a multi-nano-layer film architecture with a similar A and B matrix, the work of **Gao et al., 2018** demonstrated an improvement in barrier properties from 9 without fillers to 4 mg·mm·m^{-2}·day^{-1} in a PLA/PLA + 5wt% graphene nanoparticle system. The enhancement

is mainly due to the presence of fillers, which promotes an increase in the film's crystallinity from 0 to about 42%. Quantification of filler orientation determined through scanning electronic microscope (SEM) images of the films shows that reducing the thickness of filler-containing layers (by decreasing their proportion in the film) promotes their orientation. **Figure 2-30** shows that for a 90:10 configuration, the majority of fillers have an inclination angle between 0° and 10°. However, orientation is not directly related to the improvement in barrier properties but only to the percentage of crystallinity (**Figure 2-31**).
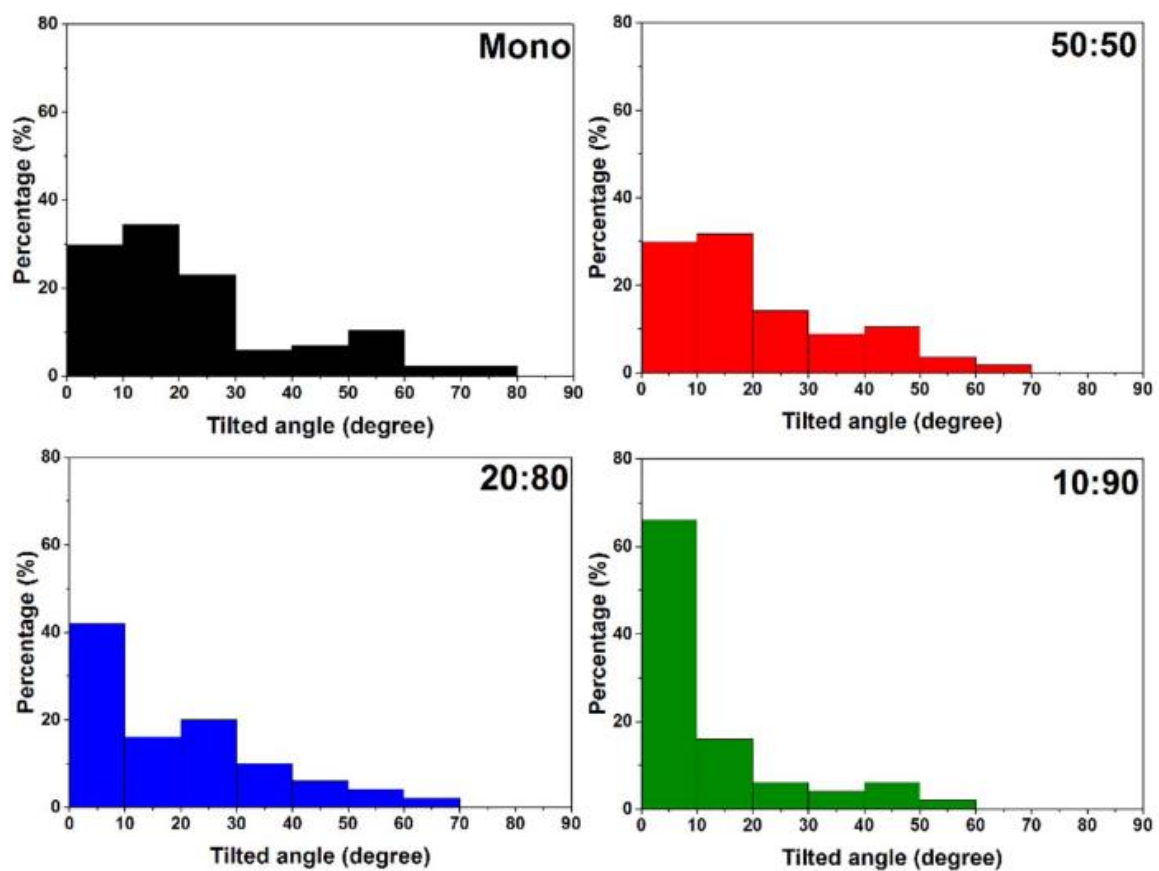
Figure 2-30 : Histograms of nano-platelet orientation in monolayer and multilayer PLA/GNP with different filled: unfilled ratios. Gao et al., 2018.
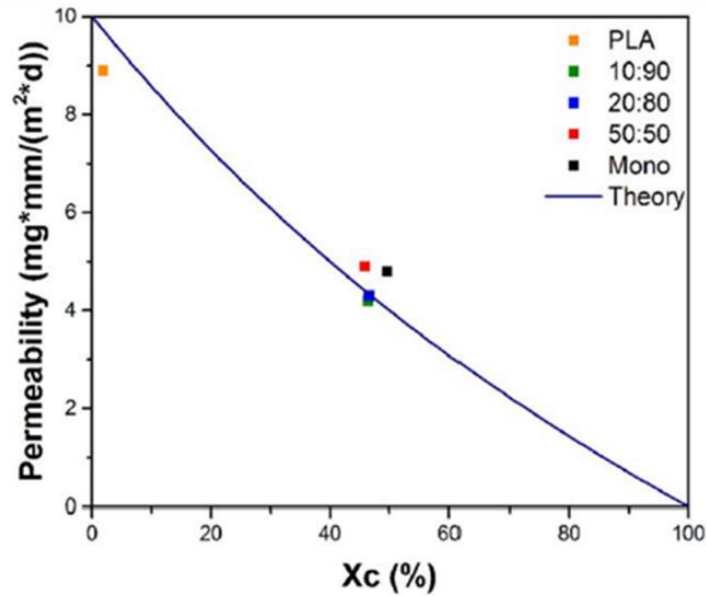
Figure 2-31 : Water vapor permeability as a function of polymer crystallinity. Gao et al., 2018.

Finally, research has been conducted to exploit a phase A different from B, with the aim of generating potential confinement effects favoring filler orientation and improving barrier properties. These studies were carried out by **Messin et al., 2020a** and **Lozay., 2020**. In their work, **Messin et al., 2020a** demonstrated an improvement in water barrier properties, illustrated in **Figure 2-32**, by introducing 2 to 5wt% of montmorillonite into PBSA in a multi-nano-layer system consisting of 2049 layers, compared to PBSA alone. The combination of the multi-nano-layer structure and the addition of filler resulted in a 58% improvement factor. Intermediate results clearly indicate that the barrier property enhancement is attributable to the synergistic effect of both factors. Furthermore, **Messin et al., 2020b**'s earlier work revealed a confinement effect of PBSA by PLA, thus controlling the orientation of PBSA. Additionally, they associated the filler effect with its improved orientation, although this enhancement was not quantified in their work.

Figure 2-32 : Comparison of the experimental and predicted permeability of PBSA under monolayer and multilayer films. IF1: calculated from neat PBSA – effect of loading. IF2: calculated from PBSA – effect of multilayer. IF3: calculated from neat PBSA – effect of leading and multilayer (Messin et al., 2020a).

Lozay., 2020's work based on a multi-nano-layer system of PA6/PE-g-MA/LLDPE in which montmorillonite has been dispersed in PA6 on one hand and in LLDPE on the other hand. In LLDPE, no improvement in water permeability is observed, whereas in PA6, there is a twofold improvement compared to its unfilled equivalent. This observation is attributed to the effect of better exfoliation and dispersion of the fillers.

2.3 THE POLY(ETHYLENE)

Poly(ethylene) with the chemical formula $(C_2H_4)_n$, where 'n' represents the degree of polymerization, is a widely known polymer commonly used in the packaging industry. Its synthesis was patented for the first time in 1939 by **Fawcett et al., 1939**. It is cost-effective and exhibits good mechanical properties as well as water barrier capabilities. Derived from the polymerization of ethylene monomers, its architecture varies based on the type of polymerization employed (**Peacock., 2000**). There are three main types: high-density poly(ethylene) (HDPE) with linear, unbranched chains; low-density poly(ethylene) (LDPE) with long branches along the main chain; and linear low-density poly(ethylene) (LLDPE) with short branches (**Peacock., 2000**). In this section, we will focus more on the behavior of LLDPE.

2.3.1 The linear low-density poly(ethylene)

The molecules of LLDPE are composed of long linear chains with short branches, which can include ethyl to hexyl groups, as illustrated below (**Figure 2-33**):
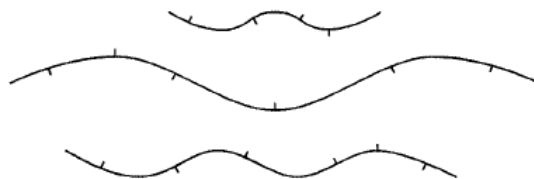
Figure 2-33 : Linear low-density polyethylene (Peacok., 2000).

LLDPE is a semi-crystalline polymer, meaning that a fraction of its chains, when perfectly arranged, tends to crystallize, while the rest of the chains remain disordered, forming the amorphous part. Generally, the crystallinity of LLDPE can vary between 22% and 55%, according to **Peacock., 2000**. LLDPE is also known to have a relatively low glass transition

69

temperature, at -110°C, providing it with flexibility and significant chain mobility even at low temperatures.

In the molten state, LLDPE can crystallize into various crystal structures depending on the crystallization conditions. In most cases, crystallization occurs in the orthorhombic form (**Figure 2-34**), with crystallographic $\vec{c}$ axis being the chain axis and the crystallographic $\vec{b}$ axis being the crystal growth axis, forming crystalline lamellae with a thickness of up to 10nm (**Peacock., 2000**). The main Bragg peaks characterizing LLDPE are the one corresponding to (110), (200) and (020) lattice planes, while the lattice plane (002) is not identifiable in the case of LLDPE due to its low crystallinity (**Lindenmeyer & Lustig., 1965**).
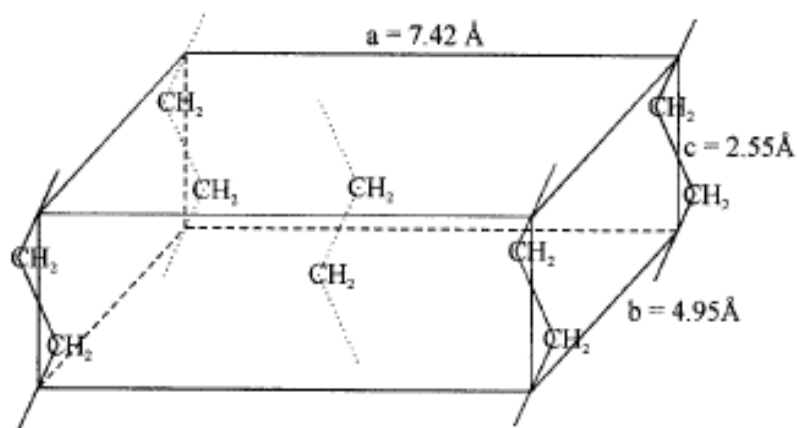
Figure 2-34 : LLDPE orthorhombic structure (Peacock., 2000).

Under elongation conditions, LLDPE can crystallize into the monoclinic structure (**Figure 2-35**) with the crystallographic $\vec{c}$ axis always along the chain axis. This is a metastable crystalline phase that is only achieved under strong cold deformation or during crystallization at very low temperatures. This phase transforms into the orthorhombic phase just below its melting point, 110°C (**Seto et al., 1968**). This transformation is also referred to as martensitic deformation (**Bowden & Young., 1974**).
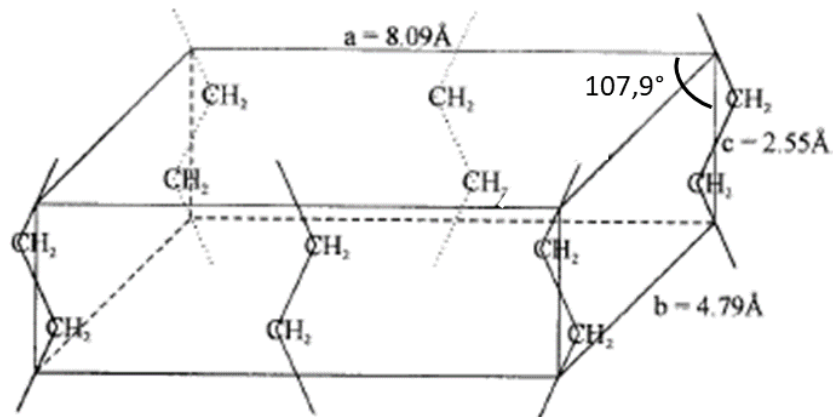
Figure 2-35 : LLDPE monoclinic structure (Peacock., 2000).

The lattice plane studied to characterize this transformation are the (001), (200), and (201). Indeed, their corresponding Bragg peaks are not identified usually in the orthorhombic phase. In **Figure 2-36**, they are present along with those belonging to the orthorhombic phase. The results show a significant overlap of diffraction peaks (**Wang et al., 2019**).
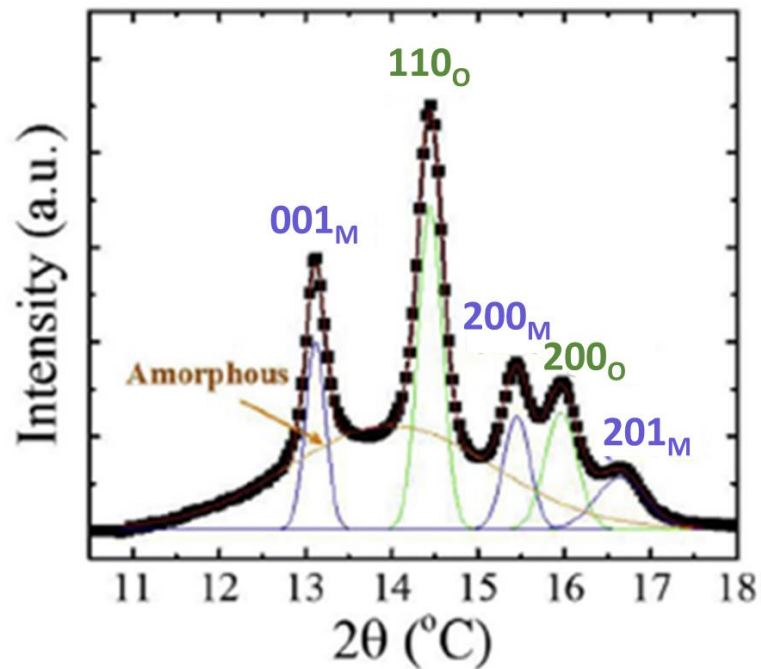
Figure 2-36 : XRD pattern of polyethylene sample containing both monoclinic and orthorhombic phases (Wang et al., 2019).

Finally, under very high pressure, LLDPE can crystallize into a hexagonal form. This transformation is highly uncommon in the molten state and is most often achieved at the laboratory scale, in solution (**Peacock., 2000**).

2.3.2 Factors affecting the crystallization of the linear low-density poly(ethylene) and poly(ethylene)

In the molten state, crystal growth initiates from a nucleus, from which the crystal growth continues. Nucleation can occur either from the melted polymer itself or at the surface of an external agent (**Haudin., 2015**). Various crystallization modes are observed, whether they occur statically or under shear.

In the current case, we are interested in the effect of processing conditions on the crystallization of LLDPE. In the cast extrusion process, the flow of molten polymer undergoes stretching as the polymer chains are drawn into the air, followed by unconstrained crystallization of the polymer chains on the chill-roll (**Haudin., 2015**).

Several stages and conditions can then influence the crystallization of LLDPE in this particular case:

- **The flow:**

    o Kinetic effect

The flow leads to an increase in the equilibrium temperature of the crystalline-liquid thermodynamic state (governed by the enthalpy-entropy ratio of fusion per unit volume) and accelerates the kinetics of nucleation, growth, and overall crystallization (**Figure 2-37**). Indeed, the flow induces a reduction in the fusion entropy due to chain orientation, resulting in this temperature increase (**Monasse., 1995; Haudin., 2015**).
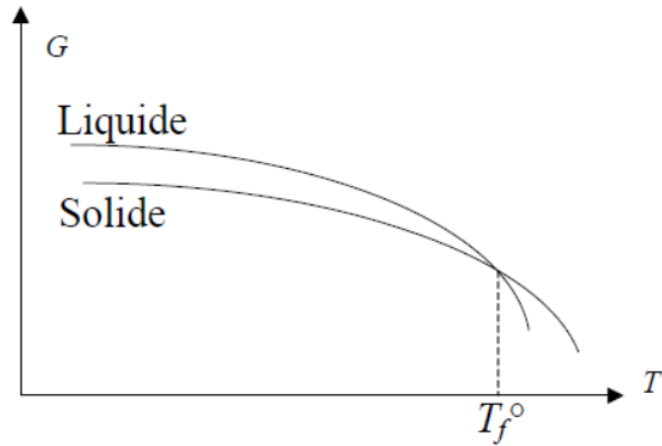
Figure 2-37 : Free enthalpy of a solid and its corresponding liquid as a function of temperature (Bustos., 2004).

Several studies have demonstrated that flow increases the number of nuclei as well as the germination rate per unit volume (**Tribout et al., 1996; Monasse., 1995**).

This is evidenced in the research conducted by **Monasse., 1995**, as outlined below:
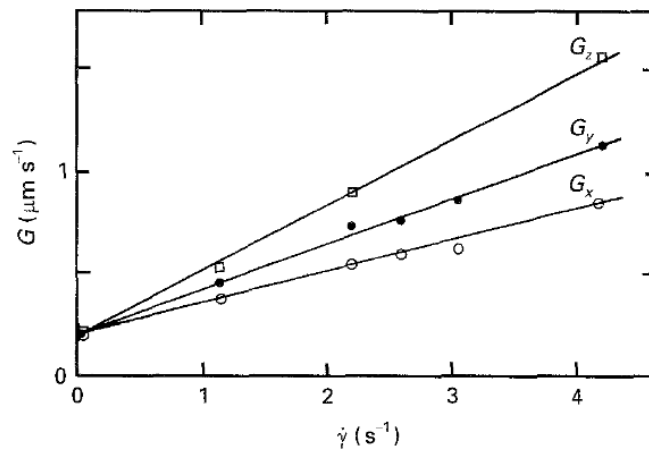
Figure 2-38 : Growth rate measurement of G_x, G_Y, G_Z as function of the shear rate (Monasse., 1995).

It shows that the growth rate 'G' of spherulites increases linearly with the increase in shear rate 'γ' (**Figure 2-38**). Furthermore, in his work, **Monasse., 1995** distinguishes different growth rates in the X, Y, and Z directions (corresponding respectively to the shear direction, transverse

73

direction, and normal direction) of the sample. It indicates an anisotropic orientation effect that can be explained by the chain orientation relative to the lamellae growth front (Y direction), taking into account the local flow.

Therefore, the flow also affects the morphology of the crystals.

o   Morphologic effect

In the molten state, poly(ethylene) molecules, and polymers in general, adopt a configuration of random coils. When subjected to elongational flow, the macromolecules undergo stretching, untangling, and tend to align in the direction of the flow (**Figure 2-39**) (**Peter et al., 2013**).

Figure 2-39 : Scheme of chains extension during the flow. i. Random coil, ii. Oriented chains by extension, iii. Pre-oriented chains have crystallized, adapted from Keller & Kolnaar., 2006.

As mentioned earlier, in combination with chain elongation, shear also increases the number of nuclei, thereby reducing the size of crystal morphologies. It facilitates the alignment of nuclei parallel to the direction of extrusion and induces anisotropic crystal growth. Different crystallization models can manifest depending on the shear level, ranging from spherulitic growth under static conditions to the formation of disks, cylindrites, or fibrils under very high stresses (these states will be detailed later).

In the case of cast extrusion, crystallization occurs after the flow; thus, it is necessary to consider not only the intensity of the flow but also the timing and duration of its application. These parameters will influence the partial or total relaxation of macromolecule orientation between the end of the flow and the onset of crystallization.

Bustos et al., 2006 notably demonstrated, using poly(ethylene), that the application of a 30-second pre-shearing (it corresponds to the application of a stress on the polymer melt) leads to an acceleration of crystallization compared to a sample that did not undergo pre-shearing. They also showed that the intensity of the pre-shearing plays a role in crystallization. In further studies, **Bustos., 2004** demonstrated that the effect of pre-shearing is observed when the relaxation time of polymer chains is long, thereby promoting an acceleration of orientation. Thus, it is the ability of chain segments to maintain the orientation specified by pre-shearing that dictates the increase in crystallization kinetics. Indeed, **Pople et al., 1999** showed through their work on the crystallization of molten poly(ethylene) that, from a critical shear rate of about $1s^{-1}$, oriented structures can be generated. However, as the molecular weight of the polymers increases, crystallization in the form of shish-kebab-like structures is favored. This has also been observed in the studies of **Lagasse & Maxwell., 1976**.

- **Cooling rate:**

Indeed, the cooling rate indirectly influences the relaxation time of polymer chains. The faster the cooling, the less time polymer chains have to relax if they are already oriented. Thus, more oriented structures can be obtained (**Bourg et al., 2019**).

Furthermore, as the cooling rate increases, the crystallinity decreases because less time is allowed for the system to crystallize and for the propagation of crystallization (**Haudin., 2015**).

- **Surface effect:**

Observable effects on the thermostated chill-roll and in the presence of fillers in the polymer blend are subject to competition between nucleation at the surface of the rolls and/or fillers and nucleation at the core of the molten polymer. This phenomenon can result in surface inactivity and nucleation from the molten polymer. There might be partial surface activity with the growth, for instance, of half-spherulites from these surfaces (**Haudin., 2015**). Alternatively, there could be strong surface activity leading to the formation of trans-crystalline growth zones from these surfaces. In the case of poly(ethylene), this phenomenon can occur for blends of poly(ethylene). For example, **Kestenbach et al., 1999** observed trans-crystallization of HDPE on the surface of ultra-high molecular weight poly(ethylene) fibers.

2.3.3 Linear low-density poly(ethylene) crystallization models

Under low flow and shear conditions, LLDPE and poly(ethylene) in general tend to crystallize in the form of spherulites. These result from the growth of crystalline lamellae without a preferred direction from a single nucleus (**Keith & Padden., 1963**). They can grow either straight or twisted upon themselves, forming twists along the crystallographic $\vec{b}$-axis of the crystal system (**Figure 2-40**). The space between the lamellae is composed of amorphous chains.
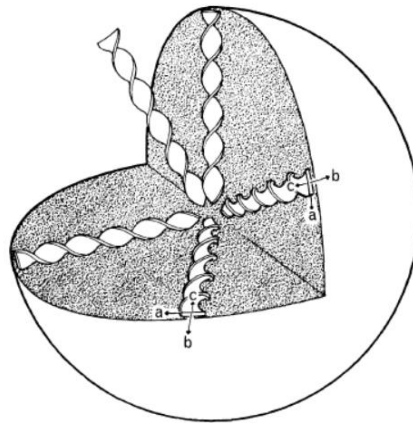
Figure 2-40 : Scheme of a spherulite with twisted lamellas, adapted from Keller & Kolnaar., 2006.

However, when the chains are subjected to a higher flow and therefore higher shear conditions, they crystallize in the form of cylindrites, also known as shish-kebabs (**Hobbs et al., 2001**). The shish-kebabs are composed of a central fibril, the 'shish', formed first by the crystallization of macromolecular chains aligned in the direction of the flow. From this fibril, germs arise, forming crystalline disks that grow radially around the fibril (**Figure 2-41**). These are what is call the 'kebabs' (**Hosier et al., 1995**).
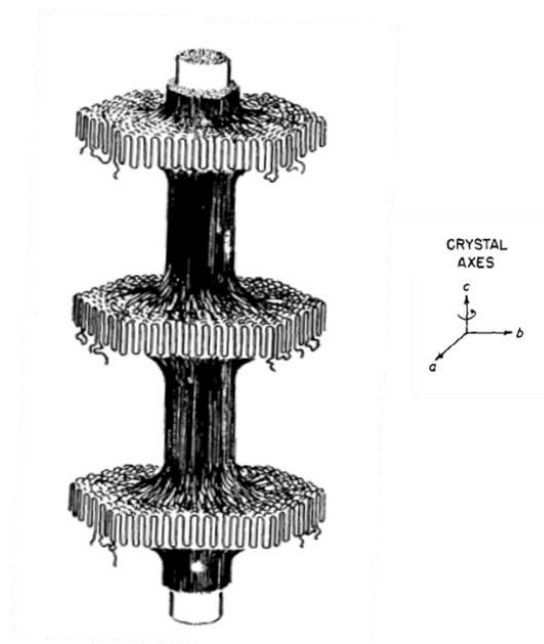
Figure 2-41 : Scheme of shish-kebab structure, adapted from Keller & Kolnaar., 2006.

In 1967, **Keller & Machin., 1967** suggested models to characterize these superstructures, resulting in the Keller Machin I model (KMI) (**Figure 2-42a**) for crystallization under low stress conditions, and the Keller Machin II model (KMII) (**Figure 2-42b**) for crystallization under high stress conditions.
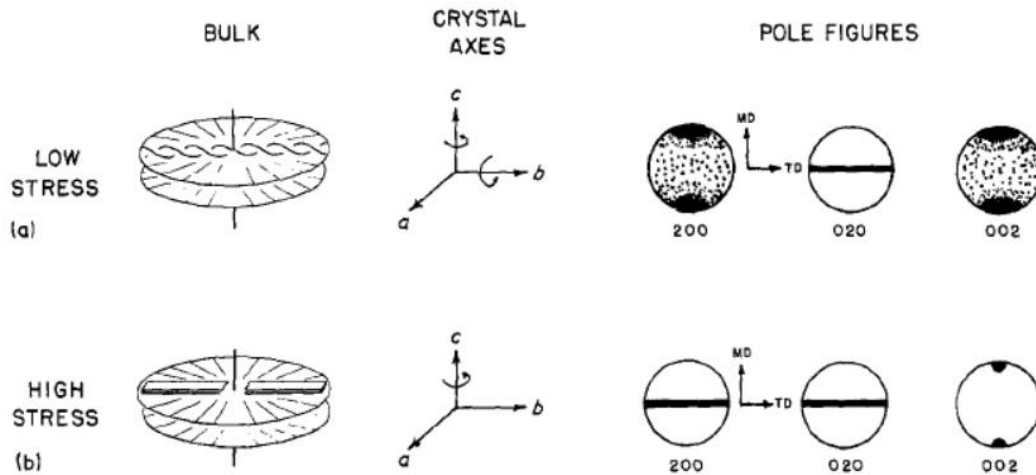
Figure 2-42 : a) KMI Model in bulk. Cylindrical structure with twisted lamellas. Scheme of 200, 020 and 002 pole figures for KMI model. B) KMII model in bulk. Cylindrical structure with straight lamellas. Scheme of 200, 020 and 002 pole figures for KMII model (Adams et al., 1986).

In the KMI model, the lamellae grow in a twisted way, but only in the direction perpendicular to the extrusion. On the pole figures, diffraction along the TD-ND axis for the lamellae's growth axis $\vec{b}$ is observed. Additionally, there is predominantly diffraction along the machine direction (MD) axis for crystallographic $\vec{a}$ axis. Considering that the lamellae grow perpendicular to the direction of extrusion (MD), it is not intuitive that crystallographic $\vec{a}$ axis diffracts in the MD direction. **Nagasawa et al., 1973** proposed a model where lamellae growth begins with crystallographic $\vec{c}$ axis perpendicular to the fiber axis, and then gradually twist around their growth crystallographic $\vec{b}$ axis. Thus, the overall orientation of this type of structure is calculated by integrating the orientation in infinitesimally small rings whose diameter increases as they move away from the fibril. In **Figure 2-43**, it can be observed that in ring A, crystallographic $\vec{c}$ axis is oriented parallel to the extrusion direction, while in ring B, it is the crystallographic $\vec{a}$ axis that is oriented parallel to the extrusion direction. As the diameter of

ring B is larger than that of ring A, the crystallographic $\vec{a}$ axis is preferentially oriented in the extrusion direction for lamellae of that size.
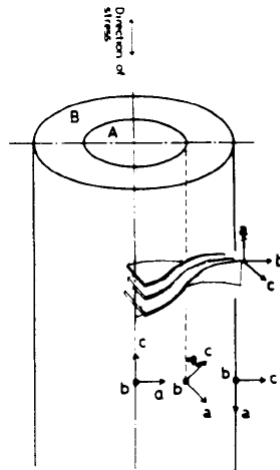
Figure 2-43 : Scheme of the intermediate orientations of crystallographic $\vec{a}$ and $\vec{c}$ axes when there are folded crystals. Representation of the circle of diameter A et B (Keller & Kolnaar., 1993).

They examined the evolution of the orientation factor of crystallographic $\vec{a}$ axis in the extrusion direction in relation to the twist angle of the lamellae, which is linked to their size (the longer the lamellae, the greater the twist angle). Their study revealed that as the diameter of the structure increases, a preferential orientation of crystallographic $\vec{a}$ axis in the flow direction is observed. On the other hand, for shorter lamellae, there is a tendency toward the orientation of crystallographic $\vec{c}$ axis in the flow direction.

In the KMII model, the same type of structure is maintained; however, the lamellae are no longer twisted. Thus, there is a rotation around the crystallographic $\vec{c}$ axis of the chains, which is in the direction of flow, resulting in the diffraction of lattice planes associated to crystallographic $\vec{a}$ and $\vec{b}$ axes along the TD-ND axis, with crystallographic $\vec{b}$ axis remaining the growth axis of the lamellae.

Finally, these two models can be found in a thin film configuration when growth is constrained in two dimensions (**Adams et al., 1986**) (**Figure 2-44**), where this time the growth of lamellae does not occur in the form of disks but only in the transverse direction to extrusion (TD).
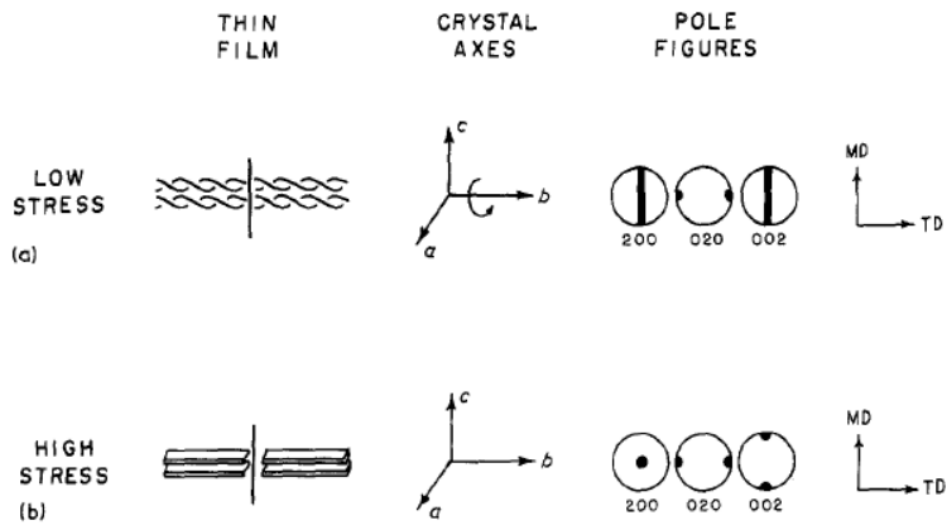
Figure 2-44 : a) KMI Model in thin films. Twisted lamellas structure. Scheme of 200, 020 and 002 pole figures for KMI model. B) KMII Model in thin films. Straight lamellas structure. Scheme of 200, 020 and 002 pole figures for KMII model (Adams et al., 1986).

In the context of the KMI model, crystallographic $\vec{a}$ and $\vec{c}$ axes undergo rotation and diffraction along the MD-ND axis, while the crystallographic $\vec{b}$ axis diffracts in the TD direction. For the KMII model, a fixed orientation of the axes is observed, with crystallographic $\vec{c}$ axis in the flow direction, crystallographic $\vec{a}$ axis in the normal direction, and crystallographic $\vec{b}$ axis in the transverse direction.

Based on these studies, orientation factors are extracted from pole figures to quantify this orientation and determine if the measurements performed in pole figures correspond well to the KMI or KMII models. These parameters can be arranged in Desper and Stein triangles (**Desper & Stein., 1966**) or White-Spruiell triangles for bi-axial stretching (**White & Spruiell., 1981**) to visualize the position of the axes relative to the sample directions. This aspect will be detailed in the experimental section.

2.3.4 Examples of poly(ethylene) crystallization under different conditions

Poly(ethylene) crystallization has been extensively studied over the last decades, revealing that oriented crystallization modes of LLDPE and the poly(ethylene) in general, can be achieved in various configurations.

In particular, several studies have demonstrated the formation of highly oriented structures in LLDPE, especially during biaxial stretching in processes like blown film extrusion. This has been observed in the works of **Ajii et al., 2005**; **Chen et al., 2005; Lindenmeyer & Lustig.**, **1965**; **Desper., 1969**; or **Pazur & Prud'homme., 1995**. In most cases, increasing the draw ratio (DR) has an impact on this orientation. For example, **Zhang et al., 2004** demonstrated that, in the case of LLDPE, increasing the DR (the ratio of the thickness of the extrudate as it exits the die to the final film thickness) during the blown film extrusion process leads to increased nucleation structures and crystallization of LLDPE similar to the Keller-Machin models.

Preferential orientations are also observed in poly(ethylene) in multi-nano layer configurations associated with an amorphous polymer, thereby promoting confinement-induced crystallization. This has been detailed previously in the section dedicated to MNL. Research conducted by **Zhang et al., 2014a,b,c** on HDPE/PC, HDPE/HPO, and LLDPE/EVOH systems revealed a specific orientation of PE lamellae, where the crystallographic $\vec{a}$ axis is perpendicular to the layers, and the crystallographic $\vec{c}$-chain axis is aligned in the extrusion direction. A specific example from **Zhang et al., 2014c**, on LLDPE confinement, is presented in **Figure 2-45** :
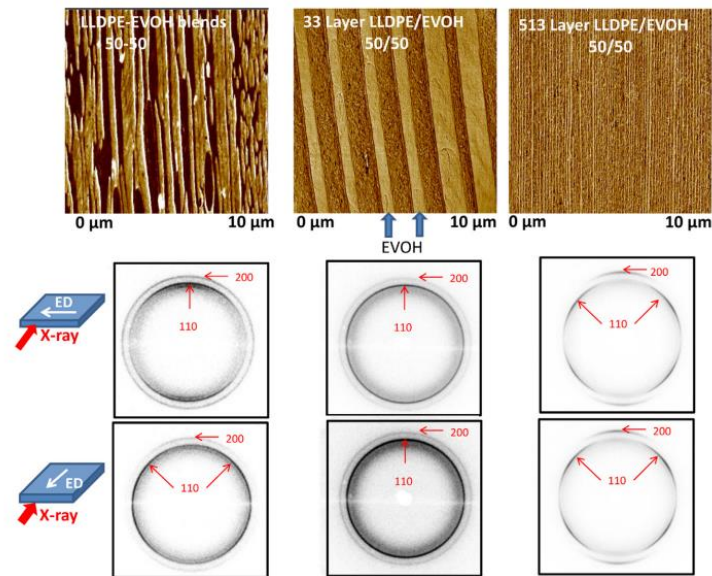
Figure 2-45 : Comparison of LLDPE-EVOH blend and multi-nano layered films. Layered structure image by AFM. WAXS patterns of the samples (Zhang et al., 2014c).

It is observed that in a conventional blend of LLDPE and EVOH, no confinement effect is present. However, transitioning to an MNL configuration with the number of layers increasing from 33 layers (layer thickness of 790 nm) to 513 layers (layer thickness of 40 nm), a transition is observed. It goes from an isotropic orientation of (200) and (100) lattice planes to a preferential orientation of LLDPE, marked by the appearance of diffraction poles of those lattice planes in the wide angle X-ray scattering (WAXS) images. The position of these diffraction poles suggests an 'edge-on' orientation of the lamellae. The works of **Bernal-Lara et al., 2005, 2006**, on HDPE confinement in an HDPE/PS system, also showed an 'edge-on' orientation of PE lamellae with the reduction of layer thickness but also indicated that confinement at a few nanometers avoids the formation of twisted lamellae.

Finally, the crystallization of poly(ethylene) can also be influenced by the presence of 2D nano-fillers. Research by **Gopatumar et al., 2002**, demonstrated that the presence of nanoscale exfoliated fillers increases local interactions between the polymer and fillers, impacting crystallization. Indeed, this promotes the formation of more nucleation sites but simultaneously restricts crystal growth and crystallinity. In other words, it influences the mobility of polymer chains and restricts crystal growth in a two-dimensional configuration.

Conversely, research by **Xu et al., 2005**, highlighted a disparity in LLDPE crystallization in the presence of MMT depending on the morphology, whether it is exfoliated or intercalated. In their study, they observed three-dimensional crystal growth with complete exfoliation, while two-dimensional crystallization was observed in the case of intercalation, with crystal growth between the layers of montmorillonite, as illustrated in **Figure 2-46** below:
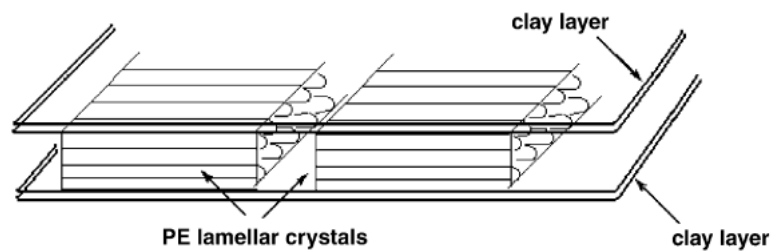
Figure 2-46 : Scheme of the crystallization of PE in-between clay layers in an intercalated morphology (Xu et al., 2005).

Furthermore, a decrease in the activation energy of crystallization has been observed in the case of an intercalated morphology compared to crystallization under an exfoliated morphology.

Additional research on the influence of the presence of MMT fillers on the crystallization of polyolefin other than poly(ethylene) has revealed that the presence of these fillers promotes a preferential orientation of polymer crystals. This is notably the case for poly(propylene), as demonstrated in the works of **Wang et al., 2005**. However, to our knowledge, similar effects on poly(ethylene) have not been reported.

CONCLUSION

This chapter emphasizes the importance of montmorillonite exfoliation in determining the ultimate properties of the nanocomposite material. It also highlights the critical role of filler orientation in influencing the barrier properties of the samples. Furthermore, it underscores the predominant use of multi-nano layer architecture for controlling polymer crystallization in barrier applications.

However, the addition of nano-fillers to multi-nano layer systems has not been extensively studied in comparison to crystallization control. Although some studies have shown slight improvements in barrier properties, there has been limited focus on quantifying the orientation of these nano-additives within multi-nano layer systems.

Additionally, the crystallization of LLDPE is affected by various factors. Poly(ethylene) can crystallize under the influence of flow and 2D confinement, depending on process conditions. This can result in the formation of oriented lamellae in an 'edge-on' configuration.

This highlights the technological challenges that need to be addressed in our study and the corresponding solutions. Indeed, the following sections will focus on the factors that influence the orientation of montmorillonite exfoliation, as well as the quantification of its orientation. Additionally, the impact of multi-nano layer architecture on this orientation will be evaluated. Finally, the influence of montmorillonite on the behavior and crystallization of LLDPE will be also investigated.

3. CHAPTER 3: EXPERIMENTAL SECTION

INTRODUCTION

This chapter details the methods used to analyze the morphology of multi-nano layered films, the orientation of montmorillonite, the crystallization of LLDPE, and the final properties of the films. It also includes information on the materials used in the film's extrusion and the processing conditions employed.

3.1   METHODS OF CHARACTERIZATION

3.1.1 X-ray diffraction (XRD)

3.1.1.1 XRD applying Bragg-Brentano geometry

The laboratory X-Ray diffractometer Bruker D8 from the X-ray CoreLab at the Helmholtz-Zentrum Berlin (HZB) was used for the measurements. The Bragg-Brentano configuration was used (**Figure 3-1**). It employs a para-focusing geometry composed of a divergent primary beam and a diffracted (re)focusing beam with the detector and X-ray tube moving symmetrically.
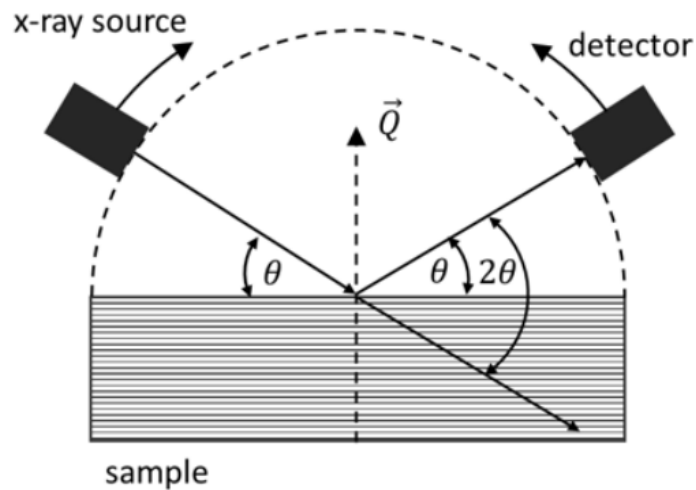
Figure 3-1 : Scheme of a Bragg-Brentano set up XRD measurement, adapted from Jamning., 2020.

During the measurements, the sample position remain fixed and planar. Measurements were taken over a 2θ range from 0° to 70° with a 0.0158° step size. To prevent the primary beam from hitting the detector, a beam knife was used for measurements at small angles.

The wavelength of the X-ray radiation source purposefully employed is $CuK_{\alpha 1}$ = 1.5406 Å, with the X-ray tube being operated at a voltage of 40 kV and a current of 40 mA.

3.1.1.2 Texture XRD

Texture analysis was performed in reflection mode using a PANalytical MRD X-ray diffractometer from the X-ray Corelab at HZB. The diffractometer is equipped with an Eulerian cradle that enables two-axis scans along ϕ and χ. The wavelength of the X-ray radiation source used is $CuK_{\alpha 1}$ = 1.5406 Å, the X-ray tube being operated at a voltage of 40 kV and a current of 40 mA.

The film samples were mounted on a 5 x 5 cm^2 glass substrate to ensure uniform flatness, reducing measurement errors caused by uneven sample surfaces.

The intensity distribution for a specific 2Θ angle corresponding to the studied lattice plane was recorded along both φ and χ with an increment of 5° x 5°, ranging from 0° to 360° and 0° to 85°, respectively. The values of φ and χ are plotted on a pole figure graph (**Figure 3-2**).
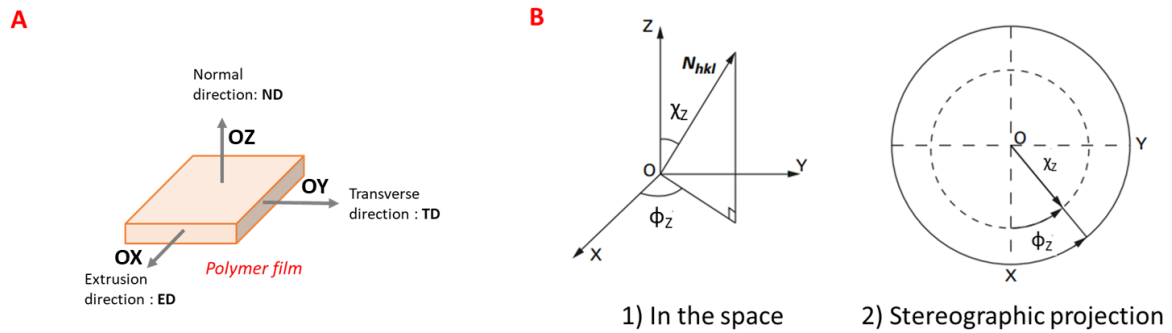
Figure 3-2 : a) Scheme of the directions in a polymer film. b) Scheme of the position of the normal of a lattice plane in space compared to χ and φ angles, and its representation on stereographic projection. Scheme adapted from Haudin., 2015.

Pole figures are a stereographic projection of the normal of the studied lattice planes (N_{hkl}) in a coordinate system OXYZ where the sample directions are associated to:

- OX = Extrusion direction (ED)
- OY = Transverse direction (TD)
- OZ = Normal direction (ND)

The samples were positioned to ensure that the extrusion direction and transverse direction of the films were always aligned with the OX, OY, and OZ directions.

The OXY plane of the sample has been chosen as the projection for the pole figures. The angles 'φ' and 'χ' measured during texture analysis correspond to the following angles:

- X: The angle between the normal of the plane N_{hkl} and the OZ direction.
- Φ: The angle between the projection of N_{hkl} onto the OXY plane and the OX axis.

Since texture measurements were performed only in reflection, the reliability of results beyond χ angles of 60° may be questionable. To address this concern, we conducted a texture analysis on one of the samples using a texture diffractometer capable of operating in both reflection and transmission modes (at the Center for Material Forming (CEMEF) Mines Paris). This instrument covers a range of χ angles from 0 to 60° in reflection mode, from 60° to 70° in transmission and reflection mode, and from 70° to 90° in transmission mode only. The measurements were compared and found to be in significant agreement. The positions of the diffraction peaks were consistent in both cases, as shown in **Figure 3-3**, confirming the validity of the results obtained using only the reflection mode.
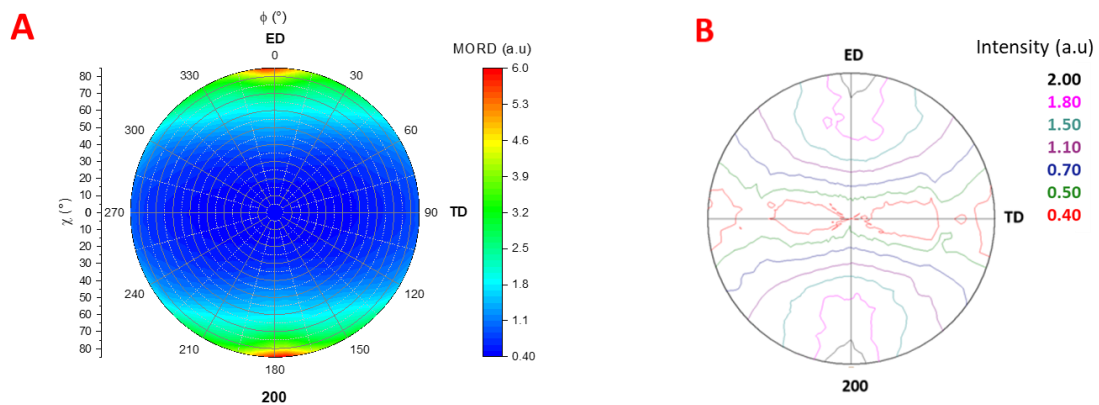
Figure 3-3 : Pole figures of the (200) lattice plane of the LLDPE in the sample A=B_1025L_18. A) Acquisition in reflection mode only. B) Acquisition in both reflection and transmission mode.

Finally, this study utilizes pole figures to i) determine the orientation of montmorillonite nano-fillers relative to the film surface by measuring the pole figure of the lattice plane (001) or (002) of montmorillonite; and ii) study the orientation of LLDPE polymer crystals with respect to different directions of the polymer film.

3.1.1.2.1 The integral breadth

When analyzing the pole figures of the lattice planes (002) or (001) of montmorillonite, the diffracted intensity is primarily concentrated at the center of the pole figure (**Figure 3-4a**), where the maximum is at angles χ around 0°. To characterize this distribution along χ angles, we averaged the intensities measured along the ɸ axis for each χ increment and plotted the results in the graph below **Figure 3-4b**.
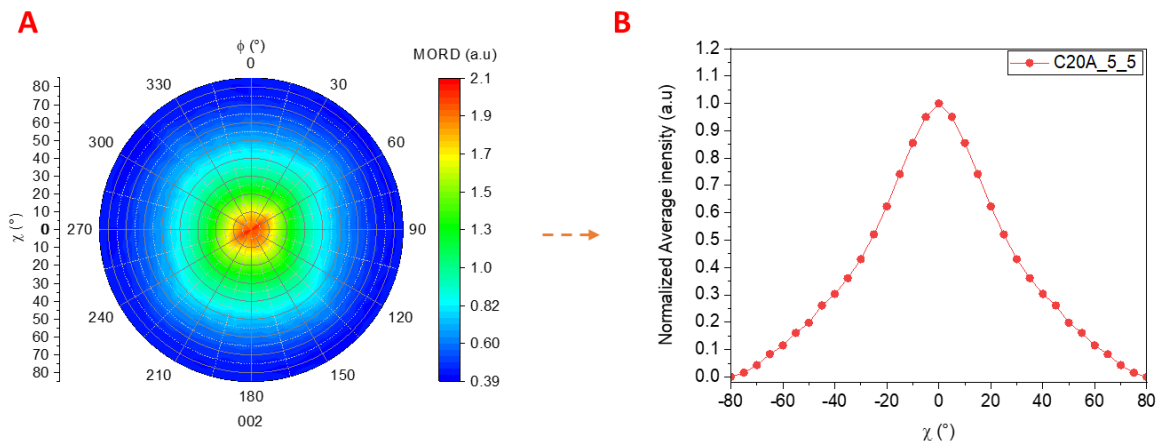
Figure 3-4 : a) Pole figure of the (002) MMT lattice plane for a sample containing 5wt% of C20A MMT. b) Extracted average intensity measured on all the ɸ range according to χ.

In order to quantify the intensity distribution around χ = 0° (**Figure 3-4b**), we aimed to use a parameter that would quantify the width of the peak and thus the distribution around χ = 0°. This parameter is the integral breadth (IB), which is calculated as follows:

$$IB = \frac{Peak\ area}{Peak\ height} \qquad (3.1)$$

The IB value represents the width of a rectangle with the same area and height as the peak (**Figure 3-4b**). A lower IB value indicates a narrower distribution around $\chi = 0°$, which corresponds to a better 'in-plane' orientation of montmorillonite.

3.1.1.2.2 The orientation factor

It is possible to quantify the orientation of polymer crystals in a sample by calculating orientation factors. The principle is to determine the average orientation of the N_{hkl} normal of the studied plane based on the OX, OY, and OZ (respectively ED, TD, ND) directions of the pole figure (**Figure 3-2b**). To do this, the average value of the square of the cosine of the angle $\chi_{j,i}$ between a crystallographic axis $\vec{j}$ ($\vec{j}=\vec{a}, \vec{b}, \vec{c}$) and an axis 'i' of the OXYZ reference frame of the film (i=ED, TD, ND) is calculated using the following equations (3.2 to 3.4):

$$< cos^2\chi_{hkl,ND} > = \frac{\int_0^{2\pi} \int_0^{2\pi} I(\chi, \phi) cos^2\chi \sin\chi \, d\chi \, d\phi}{\int_0^{2\pi} \int_0^{2\pi} I(\chi, \phi) \sin\chi \, d\chi \, d\phi} \qquad (3.2)$$

$$< cos^2\chi_{hkl,ED} > = \frac{\int_0^{2\pi} \int_0^{2\pi} I(\chi, \phi) \sin^3\chi \, cos^2\phi \, d\chi \, d\phi}{\int_0^{2\pi} \int_0^{2\pi} I(\chi, \phi) \sin\chi \, d\chi \, d\phi} \qquad (3.3)$$

$$< cos^2\chi_{hkl,TD} > = \frac{\int_0^{2\pi} \int_0^{2\pi} I(\chi, \phi) \sin^3\chi \, sin^2\phi \, d\chi \, d\phi}{\int_0^{2\pi} \int_0^{2\pi} I(\chi, \phi) \sin\chi \, d\chi \, d\phi} \qquad (3.4)$$

The intensity values for a given position of χ and ϕ are represented by $I(\chi,\phi)$, with ϕ corresponding to the measurement angles of χ and β to the measurement angles of ϕ.

Additionally, in the case of LLDPE, which has an orthorhombic lattice, the sum of the squared cosines calculated for each direction 'i' (ED, TD, ND) for a given value of crystallographic axis $\vec{j}$ satisfies the following orthogonality relationship (3.5):

$$\sum_i <cos^2\chi_{hkl,i}> = <cos^2\chi_{hkl,ED}> + <cos^2\chi_{hkl,TD}> + <cos^2\chi_{hkl,ED}> = 1 \qquad (3.5)$$

Thanks to this relation, it is possible to deduce the orientation of the crystallographic $\vec{c}$-axis in the case of LLDPE.

The $cos^2\chi_{j,i}$ values can be represented in an equilateral orientation triangle by Desper Stein (**Figure 3-5**) (**Desper & Stein., 1966**) to identify whether there are isotropic orientations, uniaxial orientations of axes, or to identify superstructures such as those of Keller/Machin I and II detailed in the part **2.3.3 Linear low-density poly(ethylene) crystallization models**.
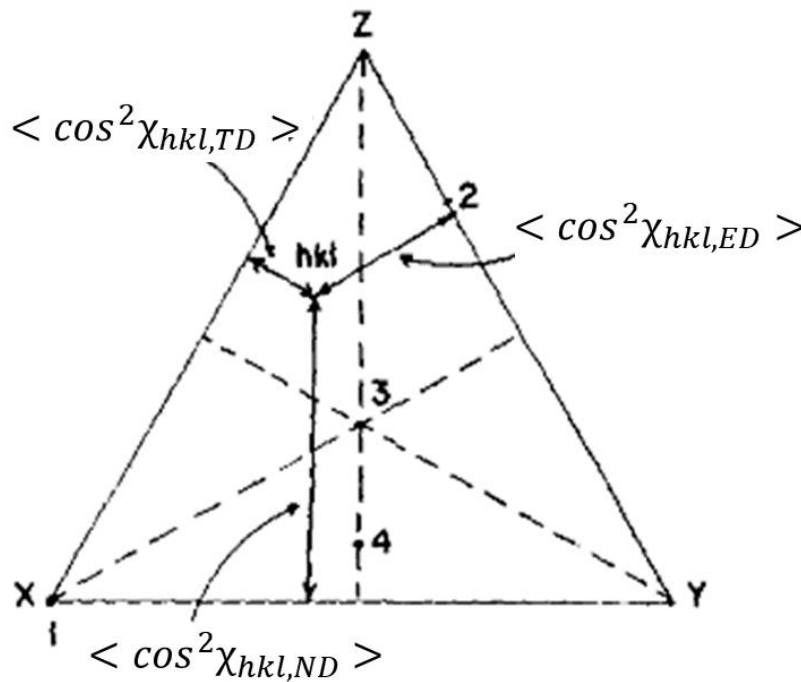
Figure 3-5 : Desper-Stein triangle, adapted from Desper & Stein., 1966.

The point hlk in **Figure 3-5** represents the average orientation of the axis $\vec{j}$ ($\vec{a}$, $\vec{b}$, or $\vec{c}$), with the distances between this point and the three sides of the triangle corresponding to the $\cos^2\chi_{j,i}$ values determined for the three directions 'i' (ED, TD, and ND), respectively X, Y, Z in **Figure 3-5**. Several positions of the hkl point are noteworthy:

- If hkl is located on a point X, Y, or Z, it means that the directions of crystallographic $\vec{j}$ axis are parallel to the corresponding direction.
- If hkl is located on YZ, XZ, or XY, all directions of crystallographic $\vec{j}$ axis are perpendicular to ED, TD, and ND respectively.
- If hkl is located on the XC, YA, ZB axis, it indicates a uniaxial orientation along the directions of ED, TD, and ND respectively.
- If hkl is located at point 3, it represents an isotropic orientation of crystallographic $\vec{j}$ axis.

3.1.2 Rheology

3.1.2.1 Rotational rheometry

Rheology allows characterizing the flow of material, particularly the relationships between material deformation and the behavior it undergoes (**Figure 3-6**).
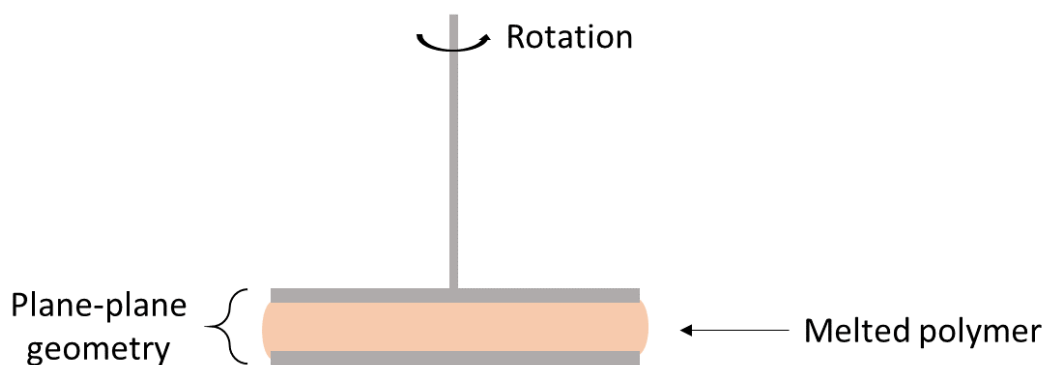
Figure 3-6 : Scheme of a rotational rheological measurement set up.

The measurements were carried out on a stress-controlled rheometer, the AR2000ex from TA Instruments, with a 25 mm diameter parallel-plate geometry. Strain sweep measurements were performed first to determine the linear viscoelastic domain of the samples. The frequency was set at 1Hz, and the strain range from 0.01 to 100% at 170°C. Subsequently, frequency sweep measurements were conducted to determine the variation of the complex viscosity 'η*' as a function of angular frequency 'ω'. For this measurement, the strain was fixed at 0.08% (determined from the strain sweep measurement), and the angular frequency ranged from 0.08 to 628 rad·s⁻¹, all at 170°C. The behavior of the storage modulus IG'I and loss modulus IG''I corresponding to the elastic and viscous behavior of the material, respectively, can also be extracted from these measurements.

The complex viscosity curves are then fitted using the Carreau-Yasuda model via the following equation (3.6):

$$\eta^*(\omega) = \frac{\sigma_0}{\omega} + \eta_0[1 + (\lambda\omega)^a]^{\frac{n-1}{a}} \tag{3.6}$$

With 'η*' corresponding to the complex viscosity, 'σ_0' the melt yield stress, 'ω' the angular frequency, 'η_0'' the Newtonian viscosity, 'λ' the characteristic relaxation time, 'a' the Yasuda parameter and 'n' the shear-thinning index.

3.1.2.2 Capillary rheometry

Viscosity measurements were conducted using an INSTRON CEAST SR 60 capillary rheometer to determine viscosity as a function of shear rate at a given temperature. The procedure involves filling the sheath with polymer granules, heating it to the required temperature, and then moving the piston downwards to push the molten polymer through the capillary, which has a smaller diameter than that of the sheath (**Figure 3-7**).

This increases the stress applied to the polymer. As the piston moves downward, it generates greater shear on the material, resulting in an increase in speed. The stress applied by the piston to the molten polymer is measured by the pressure sensor. This pressure change is then correlated to viscosity and related to piston speed, allowing to plot curves showing viscosity versus shear rate.
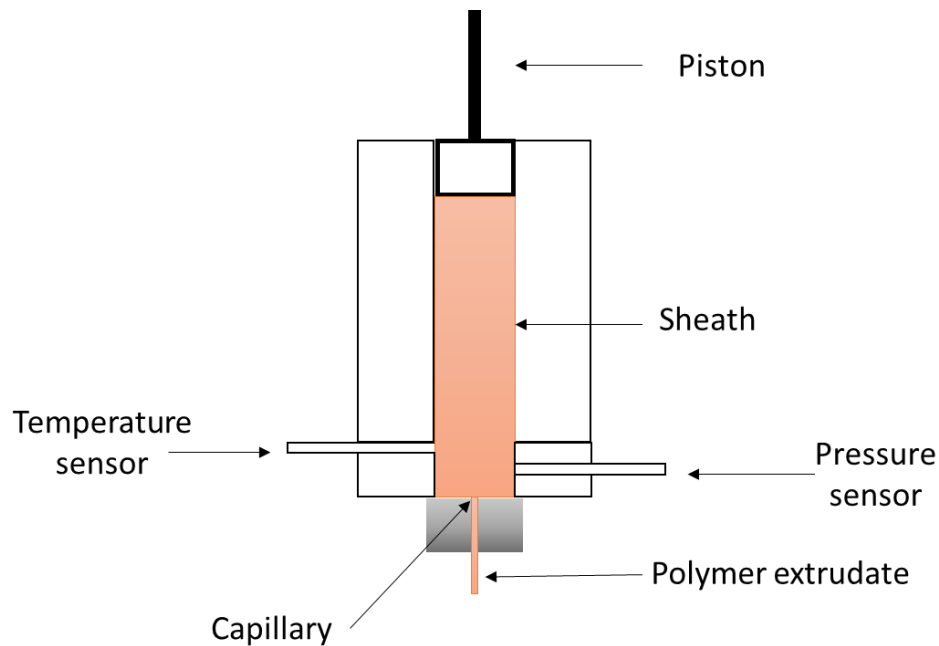
Figure 3-7 : Scheme of a capillary rheological measurement set up.

The capillary length is 30 mm with a 1 mm diameter. The sheath has a diameter of 15 mm. The piston speed varied from 0.02 to 6.66 mm·s^{-1}.

3.1.3 Microscopy

3.1.3.1 Optical microscope

A VHX-7000 (Keyence Company) optical microscope was used for this study. Observations were conducted on 10 μm thick samples. These samples are cross-sections

prepared using a microtome and then placed between two glass slides. When observing the dispersion of montmorillonite particles, the cutting was performed on extrudates. For the films, the cutting was done along the cross-section of the film in the direction of the extrusion. The films had a thickness greater than 500 μm to facilitate the cutting.

Observations were carried out in transmission mode in both bright field and polarized light.

3.1.3.2 Transmission electronic microscope

The TEM measurements were carried out at the Technological Center of Microstructures at Claude Bernard University in Lyon. The equipment used was a JEOL 1400 Flash microscope. The measurements were conducted at 120 kV using various magnifications. The samples were prepared using ultra-cryo microtome where both knife and sample are cooled by liquid nitrogen at -130°C to obtain 30 nm thick lamellae. The observed samples consisted of cross-sections of extrudates and films.

3.1.4 Differential scanning calorimetry

DSC is a thermal analysis technique that measures the differences in heat exchange between a sample under analysis and a reference. It allows determining characteristic temperatures of polymers such as the glass transition temperature, crystallization temperature (T_c), and melting temperature (T_m). Thus, by determining the enthalpy of the melting peak, it is possible to calculate the crystallinity of the sample with the following equation (3.7):

$$X_c = \%_{Polymer} \times \frac{\Delta H_m}{\Delta H_m^{\infty}} \qquad (3.7)$$

Where $'X_c'$ is the percentage of crystallinity, '%$_{Polymer}$' is the polymer fraction in the sample, $'\Delta H_m'$ is the enthalpy of the melting peak, and $'\Delta H_m^\infty{}'$ is the enthalpy of the melting peak for 100% crystalline poly(ethylene), which is equivalent to 289 J·mol^{-1} (**Small et al., 2003**).

Also, lamellae thickness at the melting temperature can be determined, as shown by **Feng., 2004** who demonstrated a correlation between the melting temperature of polymer crystals and lamellar structure. It is important to note that only the maximum melting peak temperature correlates with lamellae thickness (**Hohne., 2002**).

To determine lamellae thickness at the melting temperature, we used the simplified Gibbs-Thomson and Wunderlich equation (3.8) (**Hohne., 2002**).

$$l = \frac{2\sigma_e T_m^\circ}{\Delta H^\circ \rho_c (T_m^\circ - T_m)} \tag{3.8}$$

Where 'l' represents the thickness of the lamellae, 'T$_m$' is the melting temperature (in K), 'σ' is the basal surface free energy (90 erg·cm^{-2} for LLDPE), $'\Delta H^\circ{}'$ is the heat of melting of 100% crystalline LLDPE (289 J·g^{-1}), 'ρ' indicates the density of the crystalline phase (0.995 g·cm^{-3} for LLDPE), and 'T$_f$°' represents the melting temperature of 100% crystalline LLDPE (418.7 °K).

The measurements were performed on a TA Instruments Q100. The samples were heated from 20 to 200°C with a heating rate of 10°C·min^{-1}.

3.1.5 Barrier properties measurements

Permeability to water vapor was measured using the PERMATRAN® model W3/34 (Mocon, USA). The principle involves placing the film to be analyzed in a controlled chamber at 38°C and 100% relative humidity, divided into two distinct sections (**Figure 3-8**). The lower

part of the film is exposed to a constant flow of water vapor that continuously fills this section of the chamber, while the upper part is traversed by a stream of dry N_2.

As water vapor diffuses through the sample, it reaches the upper part of the chamber. A detector, positioned at the exit of the chamber, is capable of detecting humid N_2. It measures the flow of water vapor that has passed through the sample over time. When the measured flux value reaches a steady state, the test is considered complete, and the flux value at this plateau corresponds to the water vapor permeability of the sample, expressed in $g \cdot m^{-2} \cdot day^{-1}$.
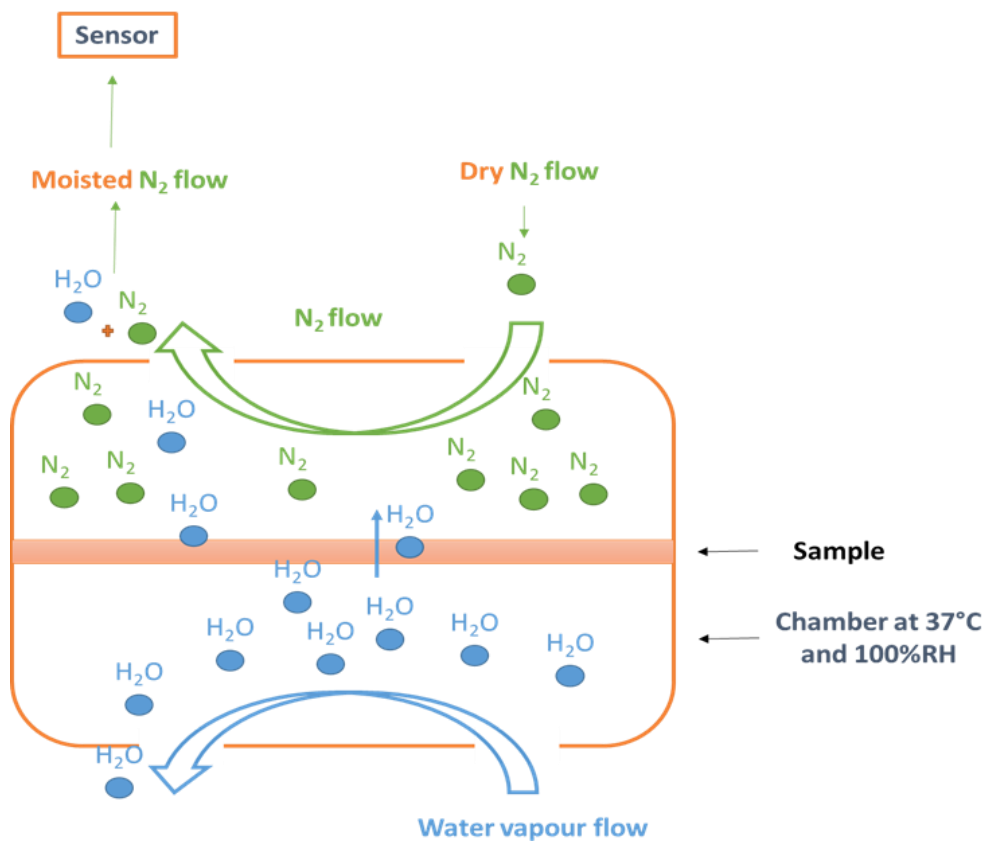
Figure 3-8 : Scheme of the set-up of the permeability test to measure the WVTR.

In order to eliminate the influence of the sample thickness and obtain the intrinsic permeability properties of the sample, the flux value is normalized with respect to the thickness of the sample. Permeability is thus expressed in $g \cdot cm \cdot m^{-3} \cdot day^{-1}$.

3.2 MATERIALS PROPERTIES

3.2.1 The montmorillonite

We have chosen to work with the following montmorillonites:

3.2.1.1 Cloisite Na+

Cloisite Na$^+$ (CNa$^+$) was purchased from BYK Company, it originates from bentonite. It is important to mention that this CNa$^+$ MMT is not an organomodified montmorillonite, since it only has Na$^+$ cations between its TOT layers. The Cloisite Na$^+$ exhibits the following characteristics (**Table 3-1**):

Table 3-1 : Cloisite Na+ properties according to its technical data sheet from the supplier.

Density	2.86 g·cm^{-3}
Lamellar d-spacing (d$_{001}$)	1.17 nm
Particle size	< 25 μm

3.2.1.2 Cloisite 20A

Cloisite 20A (C20A) was purchased from BYK Company. It also originates from bentonite; however, it underwent chemical post-treatment to replace the compensating ion with a quaternary ammonium salt containing 2 methyl groups and 2 aliphatic chains of 16 to 18 carbons, as indicated in **Figure 3-9**.
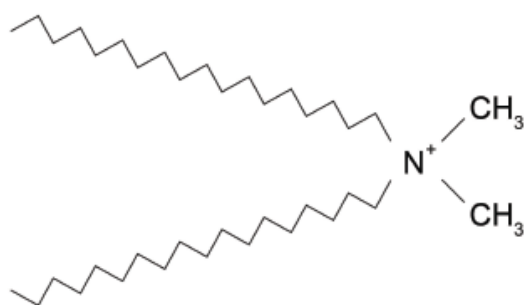
Figure 3-9 : Morphology of the quaternary ammonium salt in between MMT nano-sheets in C20A MMT. Adaptation from Domenech., 2012.

Thus, Cloisite 20A exhibits the following characteristics (**Table 3-2**):

Table 3-2 : Cloisite C20A properties according to its technical data sheet from the supplier.

Density	1.80 g·cm^{-3}
Lamellar d-spacing (d$_{001}$)	2.7 nm
Particle size	< 10 µm

Since montmorillonite originates from bentonites, it may contain traces of other materials such as quartz (SiO_2), calcite ($CaCO_3$), or pyrite (FeS_2). To determine the composition of the MMT and identify any side materials, we quantified some elements of the MMT using Inductively Coupled Plasma – Atomic Emission Spectroscopy (ICP-AES) by an external laboratory. Only the C20A Montmorillonite was analysed because it is the one used throughout this work. **Table 3-3** presents the results of the quantification.

Table 3-3 : Concentration of chemical elements present in the C20A MMT determined by ICP-AES.

Element	Concentration (mg·kg⁻¹)	wt%
Aluminium (Al)	7,442.2 ± 852.5	**0.74**
Calcium (Ca)	543.2 ± 39.1	**0.05**
Iron (Fe)	21,234 ± 529	**2.12**
Magnesium (Mg)	677.6 ± 99.4	**0.07**
Sodium (Na)	557.2 ± 265.0	**0.06**
Silicon (Si)	193,040 ± 5,126	**19.30**

Silicon represents 19.3% of the main constituent by weight, which is consistent with its major presence in montmorillonite's TOT structure. The other identified components may be associated with the cations present in montmorillonite's octahedral sites. However, the presence of calcium and iron may suggest the existence of calcite or pyrite in smaller quantities. Calcite shows two predominant Bragg peaks at 23.1° and 29.4° in the 2θ range of 20° to 35°. Pyrite, on the other hand, exhibits Bragg peaks at 23.5°, 33°, and 37°. However, the XRD pattern of MMT C20A (**Figure 3-11**) does not reveal any of the main Bragg peaks of these compounds, indicating their absence.

Finally, the unquantified residual mass is probably composed of oxygen, carbon, and nitrogen present in the quaternary ammonium salt.

3.2.1 The linear low-density poly(ethylene)

The LLDPE used for this work is DOWLEX 2645 from Dow Chemical. It has the following characteristics and properties (**Table 3-4**):

Table 3-4 : DOWLEX 2645 properties: *Taken from the technical data sheet, ‡ determined by DSC measurements, ×Cabrera., 2020.

Melt index (190°C · 2.16kg^{-1})*	0.85 g·10 min^{-1}
Density *	0.918 g·cm^{-3}
Melting point determined (T_m)‡	1st peak: 108°C
	2nd peak: 120°C
Temperature of crystallization (T_c) ‡	102 °C
Glass transition temperature (T_g)*	~ -110°C
Molecular weight (M_w)^x	108,780 g·mol^{-1}

According to the work conducted by **Cabrera., 2020**, the two melting peaks are attributed to the crystallization of short chains of LLDPE for the first peak, and the melting of long chains for the second one.

A copolymer based on LLDPE was also used for this work. It is a linear low-density poly(ethylene) grafted with maleic anhydride (LLDPE-g-MA) supplied by SK Polymer Company, referenced as OREVAC 18341® (**Figure 3-10).**
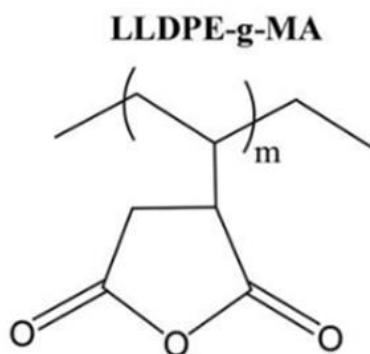
Figure 3-10 : Structure of LLDPE-g-MA copolymer.

It has the following characteristics and properties (**Table 3-5**):

Table 3-5 : OREVAC 18341 properties: *Taken from the technical data sheet, ǂ determined by DSC measurements.

Melt index (190°C · 2.16kg^{-1})*	1.5 g·10 min^{-1}
Density *	0.918 g·cm^{-3}
Melting point determined (T_m)ǂ	121°C
Temperature of crystallization (T_c) ǂ	105°C

3.2.2 XRD characterization

3.2.2.1 The montmorillonites

The X-ray diffraction patterns of the C20A and CNa$^+$ MMT powder were measured to identify the Bragg peak positions of their main lattice planes. The results are displayed in **Figure 3-11**.
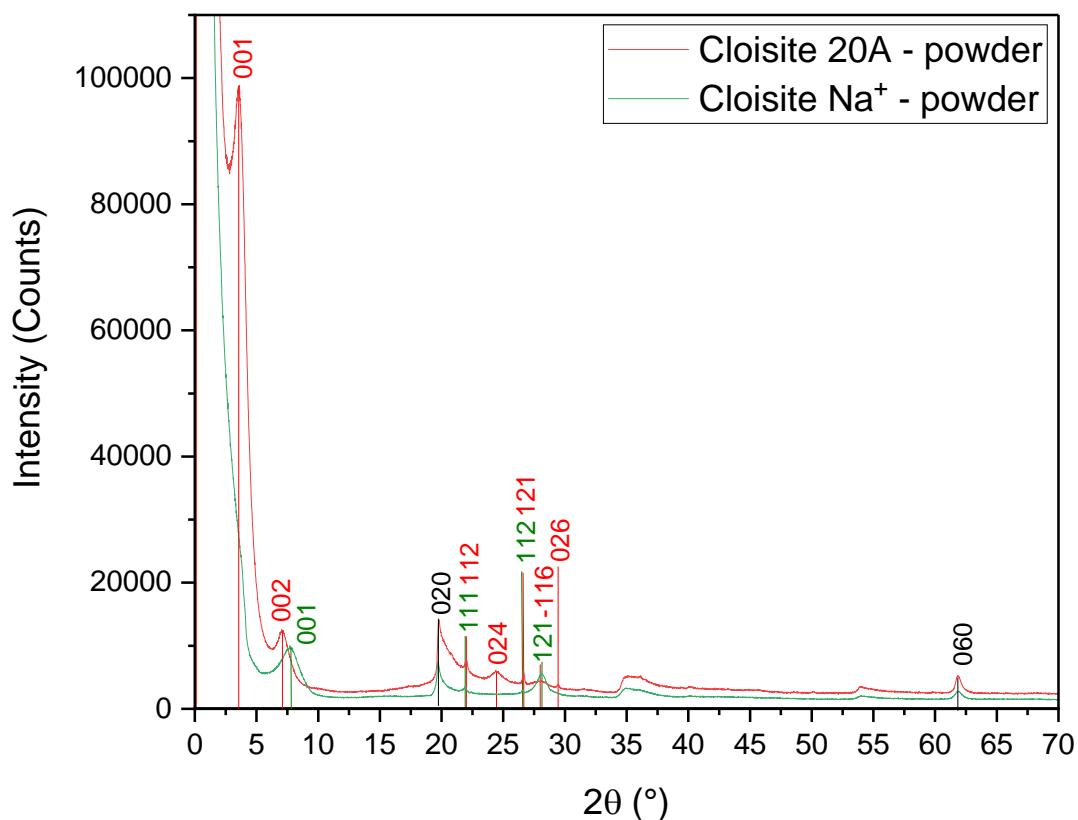
Figure 3-11 : Bragg Brentano XRD pattern of the Cloisite 20A and Cloisite Na⁺.

In **Figure 3-11** indexing the MMT Bragg peaks is challenging due to their broad and indistinct shape, which corresponds to the weak periodicity in the montmorillonite crystals and a high concentration of stacking faults (**Rits et al., 1984**). As a result, refining it using methods such as Rietveld refinement is not possible. Thus, we attempted to index it manually using the following method and with some assumptions to be made.

The c parameter for each MMT sample can be determined by analyzing the positions of the Bragg peaks 001 and 002 (**Figure 3-11**). The value of c for C20A MMT is 23.86 Å, while for CNa⁺ it is 11.41 Å. **Yapar et al., 2009** found that the Bragg peak at $2\theta = 61.8°$ corresponds to the (060) lattice plane, which gives the value of b = 8.9 Å for both MMT samples. Additionally, the Bragg peak at $2\theta = 19.8°$ corresponds to the 020 reflection. The a parameter value is set to a = 5.1 Å, as per the literature, due to the absence of clear h00 Bragg peaks. The

β value is determined as β = 94.48° for both MMT based on the c value and the 001 and 002 Bragg peaks.

Using the Checkcell software, we have calculated the reflections based on the given unit cell parameters and the C2/m space group. Then associated the Bragg peaks with their respective reflections. However, in **Figure 3-11** the Bragg peak at 2θ = 28° could not be associated with any lattice plane. Stacking fault are likely the cause of the visible Bragg peak that should have been extinguished. When calculating reflections with a P2 space group, there is no extinction, and this Bragg peak is associated with the (121) lattice plane. The same methodology was applied to the C20A MMT indexation, which identified a shift in the 121 and 112 Bragg peaks due to an increase in the c value. The 111 Bragg peak is not observed because it should be located near the broad 020 Bragg peak. New Bragg reflections appear due to the increase in the c value. These Bragg peaks were not identifiable for the CNa^+ MMT and located at higher 2θ angles.

The summary of all Bragg reflections is presented in **Table 3-6**.

Table 3-6 : Cloisite Na⁺ and C20A Bragg peak and their corresponding 2θ positions indexed on the Figure 3-11.

Cloisite Na⁺		Cloisite 20A	
Bragg peak position 2θ (°)	hkl	Bragg peak position 2θ (°)	hkl
7.75	001	3.66	001
19.80	020	7.14	002
21.88	111	19.81	020
26.53	112	21.98	112
28.08	121	24.46	024
61.83	060	26.61	121
		28.03	-116
		29.41	026
		61.82	060

However, for this study, the 001 and 002 Bragg peaks are the most important and reliable. Below, **Table 3-7** is summarizing the crystallographic data and information extracted from the XRD patterns in **Figure 3-11:**

Table 3-7 : Crystallographic data of the Cloisite Na$^+$ and Cloisite 20A, *taken from Tsipursky & Drits., 1984.

	Cloisite Na$^+$	Cloisite 20A
Space group	C2/m	
Crystal system	Monoclinic	
a from literature*	5.16 Å	
b measured	8.98 Å	
c measured	11.41 Å	23.86 Å
β	94.48°	
001 Bragg peak position	7.74°	3.7°
002 Bragg peak position	/	7.2°

3.2.2.2 The linear low-density poly(ethylene)

The LLDPE sample were also characterized by X-ray diffraction, as shown in **Figure 3-12**.
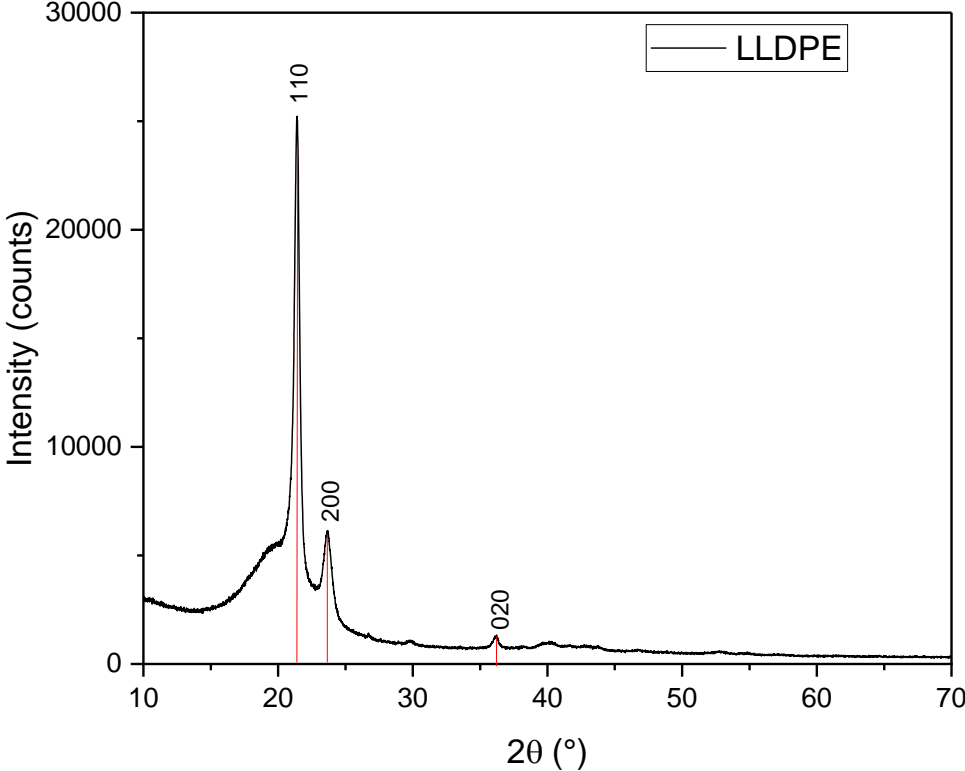
Figure 3-12 : Bragg Brentano XRD pattern of the LLDPE.

The positions of the Bragg peaks corresponding to the lattice planes (110), (200), and (020) were determined and gathered in **Table 3-8**.

Table 3-8 : Crystallographic data of the LLDPE.

	LLDPE
Space groupe	Pnam
Crystal system	Orthorhombic
a measured	7.50 Å
b measured	4.97 Å
c theoretical	2.55 Å
110 Bragg peak position	21.4°
200 Bragg peak position	23.7°
020 Bragg peak position	36.1°

Upon this work, the orientation of the LLDPE (110), (200) and (020) lattice planes in a polymer film was characterized through XRD texture measurements.

To have a better understanding of the pole figures, **Figure 3-13** presents the theoretical pole figures for a perfect 'in-plane' orientation of 2D LLDPE lamellas crystals.
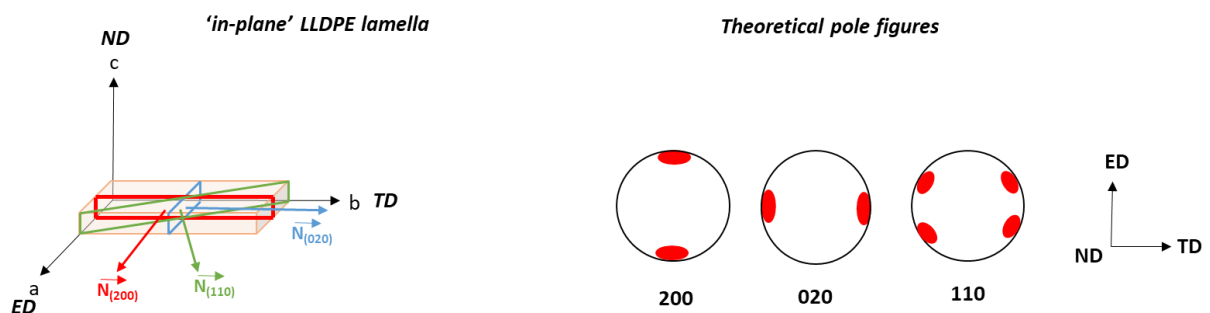
Figure 3-13 : Scheme of an 'in-plane' oriented 2D LLDPE lamellas and its corresponding theoretical pole figures.

In this case the crystallographic $\vec{a}$ axis is oriented in the ED, while the crystallographic $\vec{b}$ axis is oriented in the TD. As a result, the 200 pole figure displays two high density diffraction poles in the ED, and the 020 pole figure displays two high density diffraction poles in the TD. The (110) lattice plane is dependent on both the crystallographic $\vec{a}$ and $\vec{b}$ axes, resulting in diffraction in the ED-TD plane and two symmetry axes for the diffraction poles. The diffraction poles are located at a position of ϕ = ± 57° compared to the ED axis on the pole figure and ϕ = ± 33° compared to the TD axis, as the (110) lattice plane intersects the crystallographic $\vec{b}$ axis at an angle of 33° and the crystallographic $\vec{a}$ axis at an angle of 57° (angle values determined by trigonometry rules using the unit-cell parameters). The χ value for all diffraction poles is 90°, as all lattice planes are perpendicular to the ND.

The **Figure 3-14** presents the theoretical pole figures for a perfect 'edge-on' orientation of 2D LLDPE lamellas crystals.
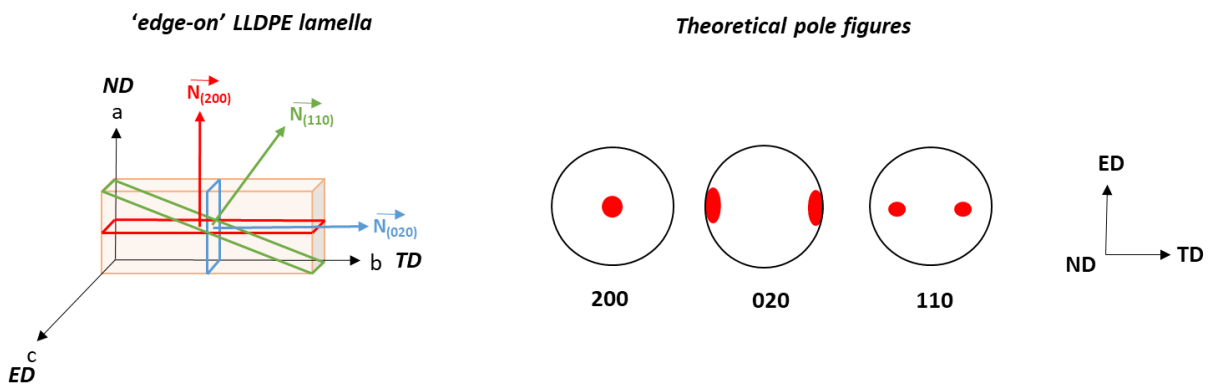
Figure 3-14 : Scheme of an 'edge-on' oriented 2D LLDPE lamellas and its corresponding theoretical pole figures.

When LLDPE lamellas are oriented 'edge-on', the crystallographic $\vec{a}$ axis is in the ND and the crystallographic $\vec{b}$ axis is in the TD. This causes one highest density diffraction pole to appear at the center of the 200 pole figure in the ND, and two diffraction poles to appear in the TD of the 020 pole figure. The (110) lattice plane is still dependent on both the crystallographic $\vec{a}$ and $\vec{b}$ axes, resulting in diffraction in the ND-TD plane. The diffraction poles are located on the TD-ND axis, specifically on the TD at a position of ϕ = 90° and 270°. Each diffraction pole is centered on this axis and positioned at both χ = 57° compared to the ND and

$\chi = 33°$ compared to the TD axis. Therefore, in this case, there are only two high density diffraction poles.

3.3 COMPOUNDS AND POLYMER FILMS MANUFACTURING

3.3.1 Blend's compounding and mechanical exfoliation

3.3.1.1 Blend composition

To improve the exfoliation of montmorillonite in LLDPE, LLDPE-g-MA was added as a compatibilist. The presence of the polar maleic anhydride group promotes physical interactions between the compatibilist and the montmorillonite layers, reducing Van der Waals interactions between the nano-sheets of montmorillonite and making exfoliation easier. **Domenech., 2012** conducted a detailed study on the exfoliation of montmorillonite by melt extrusion with a polyolefin. The study found that the optimal ratio of LLDPE-g-MA to MMT for achieving optimal exfoliation conditions is 2:1, with the rest being supplemented by LLDPE. Additionally, the study showed that using a master batch followed by subsequent dilution by melt extrusion allows for better exfoliation.

In this work, a master batch containing 20wt% of montmorillonite was prepared and then diluted to achieve concentrations of 15, 10, and 5wt% of montmorillonite. Blends with both Cloisite 20A and Cloisite Na⁺ MMT were investigated.

3.3.1.1 Exfoliation by twin-screw extrusion

As explained in the previous chapter, achieving a high level of montmorillonite exfoliation depends heavily on the twin-screw extrusion conditions. For this study, a ZSK 18 MEGAlab contra-rotating twin-screw extruder from Coperion was used, as shown in **Figure 3-15a**. The LLDPE and LLDPE-g-MA were introduced in zone 1 of the extruder, while the

montmorillonite was added in zone 4 (**Figure 3-16**). The blends produced by the extruder die was then passed through a cold-water bath for the quenching process. Afterward, they were cut into pellets (**Figure 3-15b**).
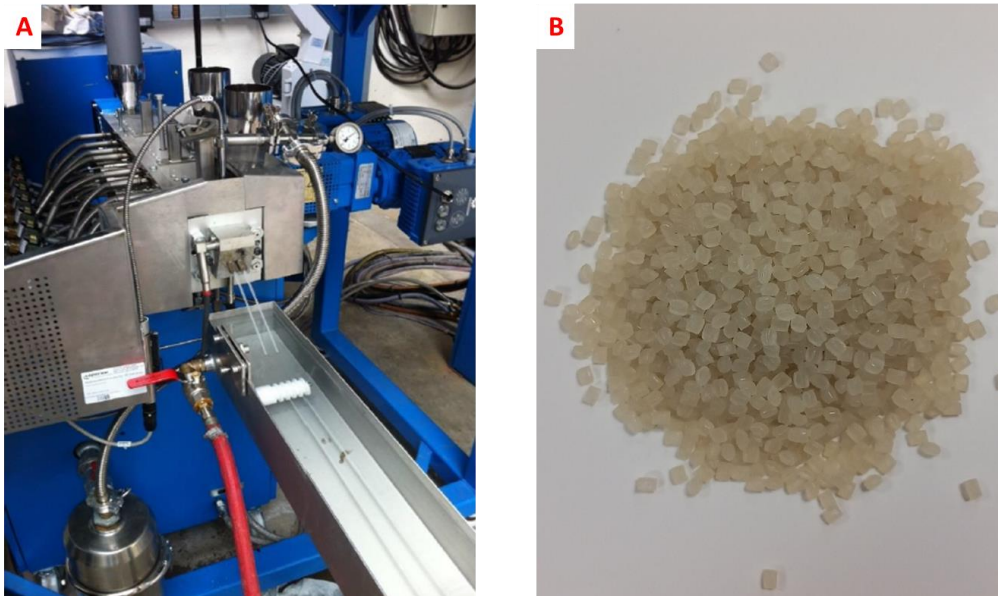
Figure 3-15 : a) ZSK18 Twin screw extruder, extrudate cool down into cold water bath. b) Pellets of the extrudate compound.

- **The screw profile:**

A high shear profile was chosen for the mixing extrusion process (**Figure 3-16**). The kneading elements first allow the breaking of the montmorillonite agglomerates and subsequently, throughout the conveying zone, promote the erosion of tactoids to obtain dispersed nano-sheets in the LLDPE matrix.
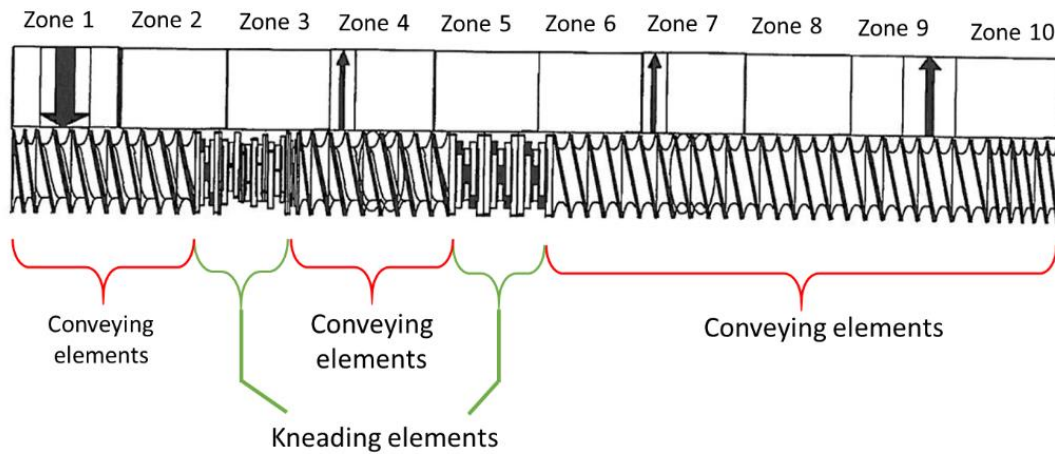
Figure 3-16 : Scheme of the screws profile and heating zones.

- **The extrusion temperature:**

The chosen working temperature is 190°C or lower to maintain a sufficiently viscous matrix. Previous studies have shown that a more viscous matrix applies greater stress on the nano-layers, promoting their exfoliation (**Vergnes., 2019**).

Table 3-9 details the temperature profile used for twin-screw extrusion.

Table 3-9 : Temperature profile in the twin-screw extruder.

HEATING ZONES TEMPERATURES									
ZONE 1	ZONE 2	ZONE 3	ZONE 4	ZONE 5	ZONE 6	ZONE 7	ZONE 8	ZONE 9	ZONE 10
170°C	190°C	190°C	190°C	185°C	185°C	185°C	180°C	180°C	170°C

- **The screw speed and the feed rate:**

Based on the conclusions and observations from the work made by **Domenech., 2012 and Vergnes., 2019**, the extruder feed rate was varied to optimize the exfoliation of our systems. This previous work has shown that the residence time is the most influencing parameter impacting the exfoliation optimization: the longer the residence time, the better the exfoliation state. Therefore, as both the screw speed and feed rate impact the residence time, with the feed rate having a greater influence, it was decided to vary the latter. These trials allow us to evaluate and determine the optimal feed rate for achieving the exfoliation of montmorillonite.

The screw speed was set at 500 rpm since previous studies conducted by **Domenech et al., 2012** demonstrate that in their system, beyond 500 rpm, the exfoliation was no longer improved. Therefore, the system undergoes heating due to the high shear on the material.

In **Table 3-10** and **Table 3-11**, a summary of the manufactured blends is provided:

Table 3-10 : List of the manufactured blends with the CNa$^+$ MMT with their compositions and varying process parameters.

NAME	CNa$^+$ CONTENT (wt%)	FEED RATE (kg·h^{-1})
CNa_20_5	20	5
CNa_5_0.5	5	0.5
CNa_5_1	5	1
CNa_5_3	5	3
CNa_5_5	5	5
CNa_5_10	5	10

Table 3-11 : List of the manufactured blends with the C20A MMT with their compositions and varying process parameters.

NAME	C20A CONTENT (wt%)	FEED RATE (kg·h^{-1})
C20A_20_5	20	5
C20A_5_0.5	5	0.5
C20A_5_1	5	1
C20A_5_3	5	3
C20A_5_5	5	5
C20A_5_10	5	10
C20A_10_5	10	5
C20A_15_5	15	5

3.3.2 Monolayer films

3.3.2.1 Compression molding

The compression molding allows the production of monolayer films by applying a vertical pressure to melted polymer pellets. For that, a Carver hydraulic press (**Figure 3-17a**) was used with the protocol outlined in **Table 3-12**. For each film, a mass of 2g of pellets was placed between 2 steel plates covered with non-stick Teflon sheets.

Table 3-12 : Compression molding protocol steps.

STEPS	TIME	TEMPERATURE	PRESSURE	COMMENTS
1	3 min	195 °C	700 LB	Pre-heating to melt polymer pellets
2	5 min	195 °C	6000 LB	Formation of the films
3	2 min	Cooling at room temperature	Between 2 cold steel plates	Controlled cooling of the polymer films

Figure 3-17 : a) Carver hydraulic press. b) Film made by compression molding with the C20A_5_5 blend.

With this amount of material, the films obtained have a thickness between 150 µm and 250 µm. The summary of the films obtained are described in **Table 3-10** and **Table 3-11.**

3.3.2.2 Cast extrusion

The principle is the same as detailed in the **2.2.1 Cast film extrusion** part. For this work, a E45 single-screw extruder with an L/D =25 (Collins Company) was used, connected to a 350 mm flat die and a winding system including the chill roll, both from Scamex Company (**Figure 3-18**). A screw profile with only conveying elements was used.
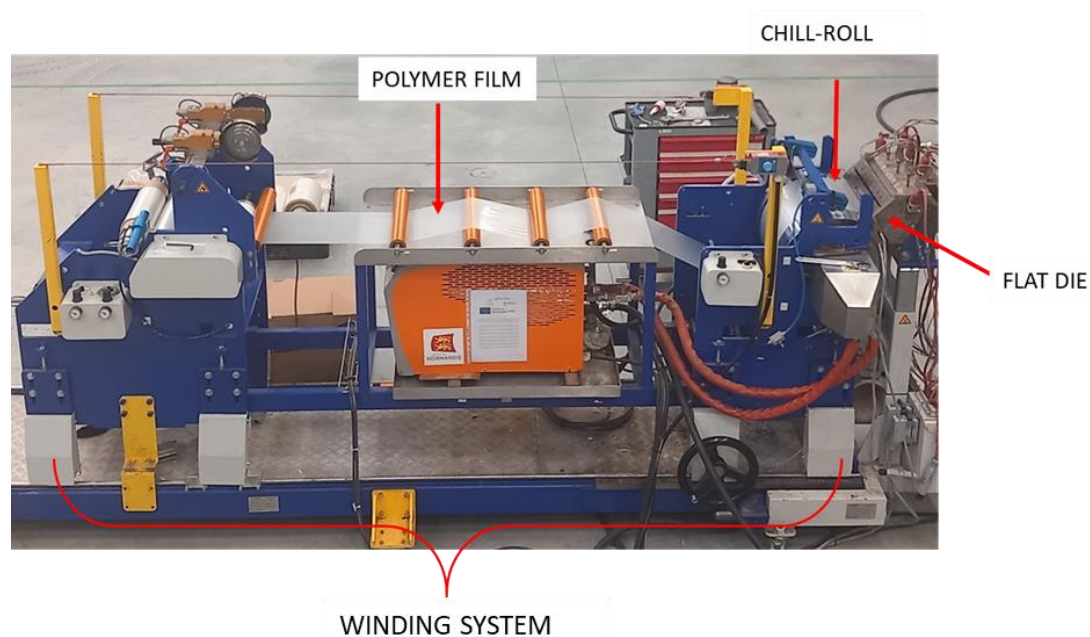
Figure 3-18 : Picture of the cast extrusion line at IPC.

Monolayer films were extruded with some of the blends listed in **Table 3-11**. All films were manufactured at a feed rate of 5 Kg·h^{-1}, a screw speed of 15 rpm, using a flat die opening of 400 µm to limit the force applied by the flat die on the melted polymer and a chill-roll at 90°C.

Table 3-13 presents the list of monolayer films that have been manufactured, along with some of their corresponding processing details.

Table 3-13 : Temperature profile used for the monolayer cast extrusion.

NAME	BLEND	EXTRUSION TEMPERATURE	ROLLING SPEED (m·min^{-1})	DRAW RATIO	FILM THICKNESS (µm)
1L_0	LLDPE	180 °C	3	6	100
			5	11	60
			8	18	40
			10	23	30
1L_5	C20A_5_5	210 °C	3	6	100
1L_20	C20A_20_5	250 °C	2	5	250

The process conditions differ depending on the blend due to the increase in the concentration of montmorillonite, which impacts their processability.

The draw ratio was calculated using the equation (3.9) from **Silagy., 2005**:

$$Dr = \frac{U_f}{U_0} = \frac{U_f \, \rho_0 \, e_0 L_0}{Q_m} \tag{3.9}$$

'U_f' represents the rolling speed, 'ρ_0' the polymer density, 'e_0' the thickness of the polymer melt at the exit of the flat die, 'L_0' the width of the polymer let at the exit of the die and 'Q_m' the extrusion feed rate.

3.3.3 Multi-nano layer films

For the production of multi-nano layer films, we used the co-extrusion line shown in **Figure 3-19**, which allows for semi-industrial scale film production. The IPC MNL line includes a co-extrusion block (or feedblock) that allows the connection of two single-screw extruders, E45 and E30 (Collins Company), each with L/D=25. We work with an A-B-A configuration at the output of the co-extrusion block, where the flow of three layers enters the MNL line (Nordson Company) with multiplier elements. For this study, 3 to 9 multiplier elements were used, corresponding to 17 and 1025 layers, respectively (calculated using equation 2.9 in **2.2.3 The multi-nano layer polymer co-extrusion (MNL)** part). Finally, similar to monolayer films, a 350 mm wide flat die was connected to the output of the line to form and cool the film.
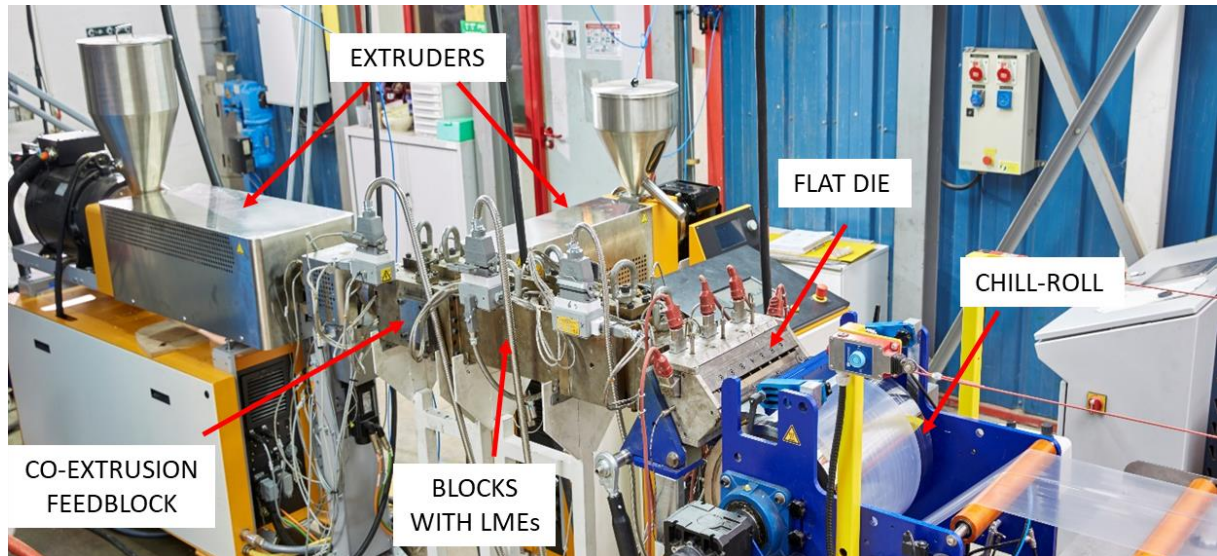
Figure 3-19 : Photo of the multi-nano layer co-extrusion line at IPC.

Several film architectures were manufactured by varying both the number of layers and the nature of phases A and B, as shown in **Figure 3-20**, while maintaining a volumetric flow of 50:50.
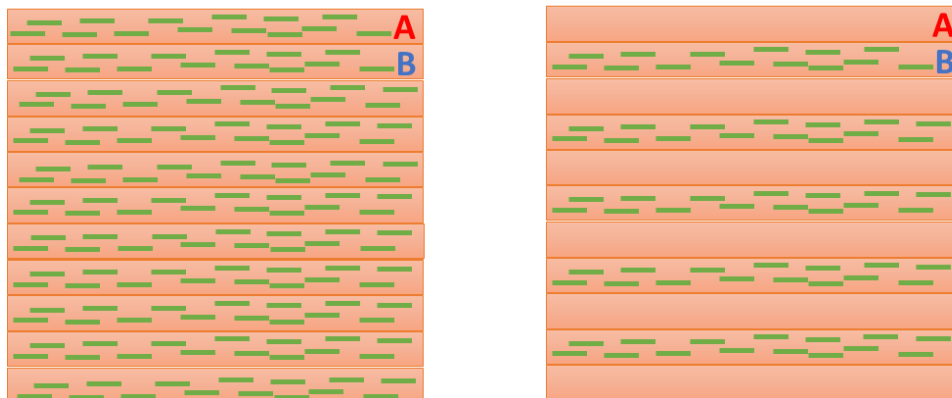
Figure 3-20 : Scheme of the different architectures of the produced MNL films. The green lines represent the MMT nano-sheets.

Regarding the process conditions, viscosity measurements for both phase A (LLDPE alone) and phase B (C20A_5_5 blend) were manufactured by varying the temperature profile. As mentioned in **2.2.3 The multi-nano layer polymer co-extrusion (MNL)** part, to minimize

layer defects, it is essential to ensure a viscosity ratio between the two phases as close to 1 as possible. In **Figure 3-21**, measurements taken at 200°C show that at a shear rate between 200 and 3000 s⁻¹, the viscosities are equivalent. For lower shear rates, the viscosity ratio is a maximum of 1.44, which is still acceptable for co-extrusion.
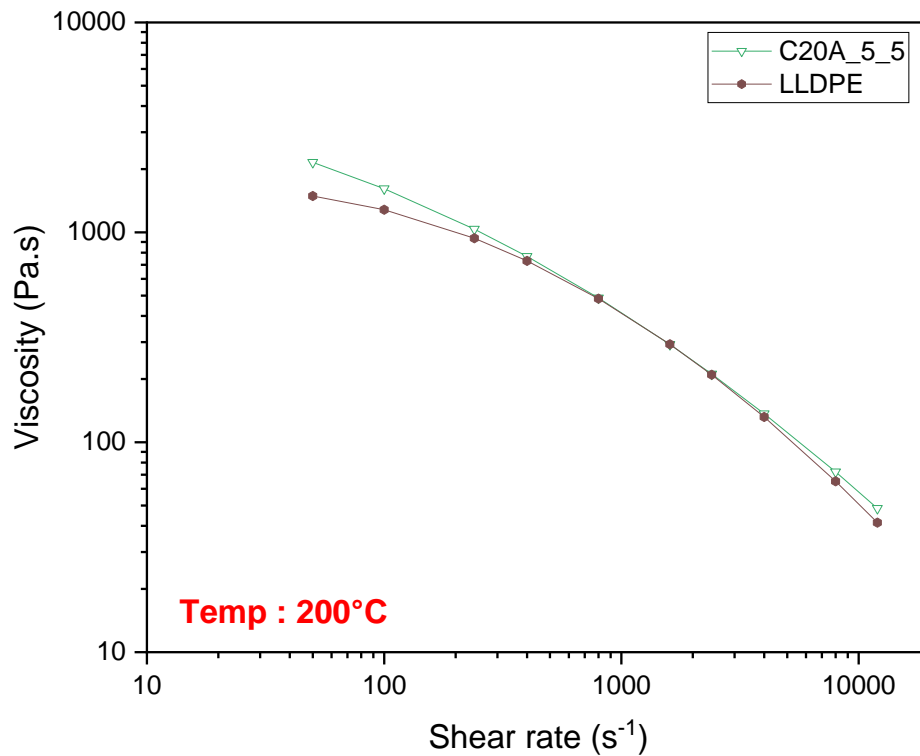
Figure 3-21 : Flow curves of the phases A and B determined by capillary rheometer at 200°C.

Thus, the temperature was set at 200°C in both extruders, the feed block, the MNL line, and the flat die. The feed rate of both extruders was fixed at 2.5 kg·h⁻¹, resulting in an overall feed rate of 5 kg·h⁻¹ in the MNL line. The flat die opening was set at 400 µm. The chill-roll temperature was set at 90°C, and the rolling speed varied from 3 to 10 m·min⁻¹.

CHAPTER 3: EXPERIMENTAL SECTION

The list of films produced is described in **Table 3-14**.

Table 3-14 : List of the manufactured films with their architectures and compositions.

ARCHITECTURE	NUMBER OF LME	NUMBER OF LAYERS	DRAW RATIO	FILM THICKNESS (µm)	OMMT CONTENT IN THE FILM
A: C20A_5_5 **B**: C20A_5_5 **Samples names:** A=B_number of layers_draw ratio	3	17			
	6	129	6	100	
	8	513			
	9	1025	0	~ 600	5 wt% OMMT
			6	100	
			11	60	
			18	40	
			23	30	
A: LLDPE **B**: C20A_5_5 **Samples names:** A≠B_number of layers_draw ratio	3	17	0	~ 600	
	6	129	0	~ 600	
	8	513			
	9	1025	0	~ 600	2,5 wt% OMMT
			6	100	
			11	60	
			18	40	
			23	30	
A: LLDPE **B**: LLDPE **Samples names:** LLDPE_1025L_draw ratio	9	1025	6	100	
			11	60	
			18	40	0 wt% OMMT
			23	30	

Some photographs of the manufactured films are shown in **Figure 3-22**, demonstrating that transparent and defect-free films were obtained.
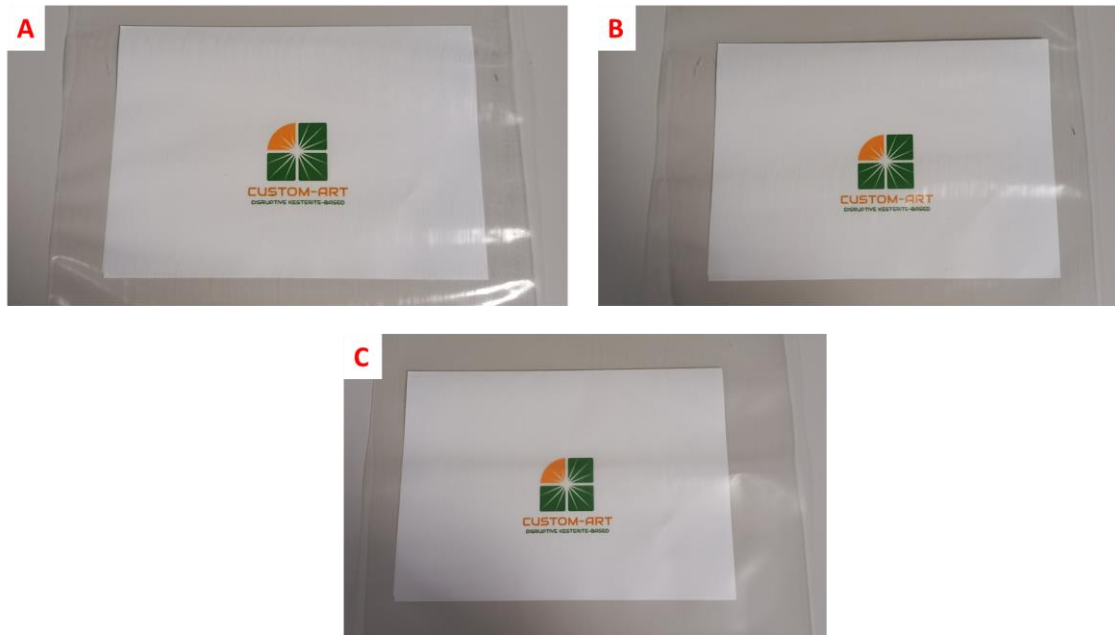
Figure 3-22 : Picture of some manufactured films. A: LLDPE_1025L_3; B: A≠B_1025L_3; C: A=B_1025L_3.

3.3.4 Bi-axial stretching

3.3.4.1 Principle and equipment

A custom-built apparatus, called ETIFI, developed by the Center for Material Forming (CEMEF) of Mines Paris was used, as shown in **Figure 3-23a**. It allows the bi-axial stretching of polymer films while simultaneously tracking changes in mechanical properties throughout the stretching process. The equipment consists of four independent motorized arms, each coupled with a force and displacement transducer. A cross-shaped sample (**Figure 3-23a and b**) was placed between the jaws of each arm, with ovens positioned on either side of the sample. The portion undergoing deformation at the center of the cross has dimensions of 24 x 24 mm^2. The sample was heated just below the complete crystallite melting temperature to preserve the mechanical strength of the film during deformation. Temperature control was achieved using an infra-red pyrometer that was pre-calibrated based on the material used and its emissivity. During the stretching test, the oven was removed, and the cross head velocity remained constant and pre-set. After the test, the sample was rapidly cooled down using a

compressed air gun to rapidly freeze the microstructures generated during bi-axial stretching for characterization.
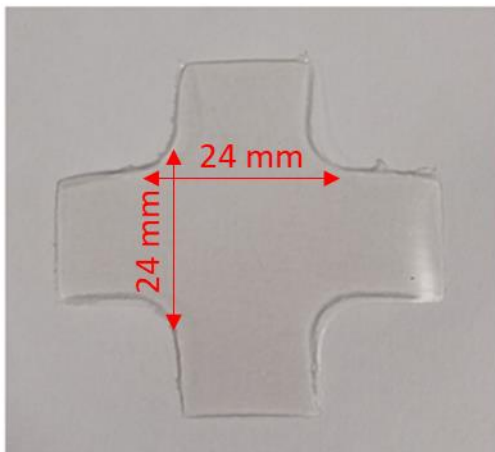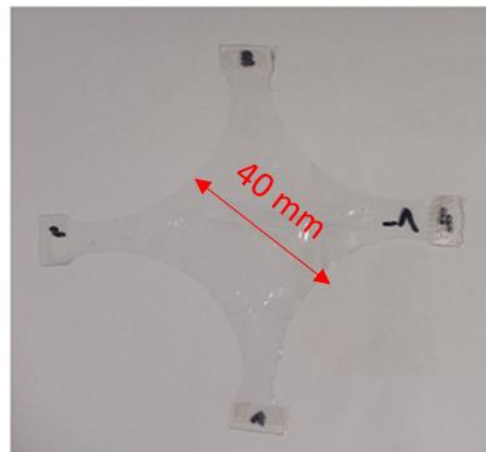
Figure 3-23 : A) ETIFI equipment with the sample display in the jaws of each arms. B) Pictures of the film before bi-axial stretching. C) Pictures of the film after bi-axial stretching.

3.3.4.2 Trials conditions

Five film architectures were tested, each undergoing a DSC beforehand to determine the working temperature, which should be below the melting temperature as mentioned above. The drawing speed was set at 1 mm·s^{-1} on each arms for all films, and the drawing time was determined on a case-by-case basis during an initial trial based on their breaking point. Therefore, the drawing time was set just before the breaking point. The detailed parameters are displayed in **Table 3-15**.

The study investigated the behavior of the samples based on the proportion of crystallites that melted at the chosen working temperatures of 90°C and 105°C.

Table 3-15 : Bi-axial stretching parameters and results for each samples.

	BI-AXIAL STRETCHING PARAMETERS					
SAMPLES	TEMPERATURE	STRETCHING SPEED	DURATION	INITIAL THICKNESS	FINAL THICKNESS	DEFORMA-TION
1L_0	90 °C		34 s	100 µm	17 µm	7 x 7
1L_0	105 °C		10 s	100 µm	12 µm	4 x 4
1L_5	90 °C		35 s	100 µm	15 µm	7 x 7
1L_5	105 °C		40 s	100 µm	5 µm	12 x 12
1L_20	90 °C	1 mm·s^{-1}	14 s	250 µm	38 µm	4 x 4
1L_20	105 °C		10 s	250 µm	50 µm	3 x 3
LLDPE_ 1025L_3	90 °C		37 s	100 µm	9 µm	7 x 7
LLDPE_ 1025L_3	105 °C		13 s	100 µm	21 µm	4 x 4
A=B_ 1025L_3	90 °C		37 s	100 µm	10 µm	7 x 7
A=B_ 1025L_3	105 °C		35 s	100 µm	3 µm	10 x 10

The deformation in **Table 3-15** is calculated by measuring 2 mm x 2 mm squares on the sample before stretching and comparing them to the size of the squares after stretching.

In order to calculate and plot the engineering stress-strain curves, it was necessary to determine the two entities through calculation using the measured data from force and displacement transducer. Deformation was assumed to be uniform along the material's diagonal.

The deformation is calculated as follows (3.10):

$$\varepsilon = \ln \left(\frac{l(t)}{l_0} \right) \tag{3.10}$$

With 'l' is the length of the sample at time t involving the two arms displacement in one direction and 'l_0' as the initial length of the sample, which is 24 mm.

The engineering stress is calculated based on the force sensor data as follows (3.11):

$$\sigma = \frac{\sqrt{2} \times F_n}{l_0 \ \times \ e_0 \times e^{-\varepsilon}} \tag{3.11}$$

With 'F_n' representing the force from the force sensor on motorized arm 'n', 'l_0' the initial length of the sample, 'e_0' the initial thickness of the sample and 'ε' the deformation calculated from equation (3.10).

Then the engineering stress-strain curves can be plotted as in **Figure 3-24**.
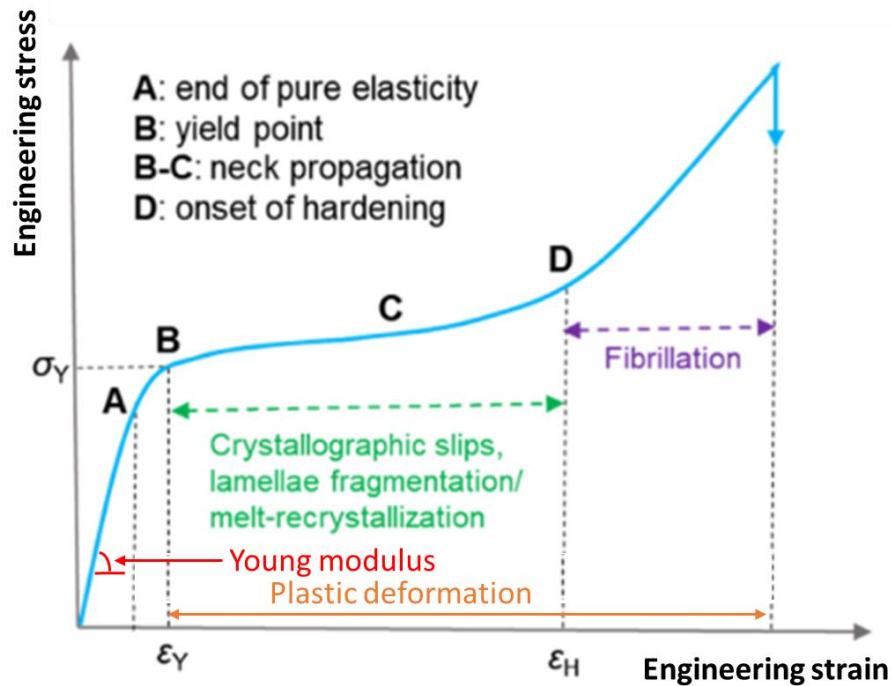
Figure 3-24 : A typical true stress-strain curve of a semi-crystalline polymer, adapted from Xu et al., 2023.

From this curve, several points are important to identify and understand:

- The **Young modulus**, which is calculated from the slope of the pure elastic domain at low strain. It gives information about the intrinsic properties of the material such the stiffness.

- The **Yield point**, which corresponds to the beginning of the plastic deformation. After this point is reached the deformation is considered as irreversible.

- The **necking propagation**, which correspond to the plateau after the yield point. During necking propagation crystals lamellae deformations occurs, like crystallographic slips, or lamellae fragmentation.

- The **strain - hardening** phase after the plateau, which correspond to a structuration of the material through the formation of fibrillar crystals.

4. CHAPTER 4: THE MECHANICAL EXFOLIATION OF THE MONTMORILLONITE

INTRODUCTION

The first phase of this study involves the exfoliation of montmorillonite. As detailed in section **3.3.1**Blend's compounding and mechanical exfoliation**,** commercial montmorillonite is initially in powder form, composed of aggregates, which are clusters of montmorillonite tactoids. Therefore, an exfoliation step is necessary to disperse nano-sheets in the LLDPE polymer matrix. For this procedure the melt exfoliation method was chosen using twin-screw extrusion (detailed in section **3.3.1.1**). This process allows in a single step the exfoliation of the filler, mixing with the polymer matrix, and obtaining pellets of this blend for further processing.

Therefore, in this chapter, the focus is on the optimization of the twin-screw extrusion parameters to promote optimal exfoliation of both CNa^+ and C20A montmorillonites. Furthermore, the exfoliation process will be characterized to select the blend that will be used in the subsequent stages of this thesis.

4.1 THE EXFOLIATION OF THE TWO MONTMORILLONITES

We initiated our work by seeking to define the optimal processing conditions for the exfoliation of the two selected types of montmorillonites, namely Cloisite 20A and Cloisite Na^+. To achieve this, we adjusted various extrusion parameters while measuring the energy supplied to the system, aiming to correlate it with the levels of exfoliation achieved. The objective was to obtain blends with 5wt% of exfoliated montmorillonite dispersed in an LLDPE matrix, using LLDPE-g-MA as a compatibilist to improve the adhesion between them.

4.1.1 Selection of the processing conditions

To determine the optimal processing conditions, the previous research conducted by **Domenech., 2001**; **Domenech et al., 2012**; and **Vergnes., 2019**, were used as a reference on the favorable conditions for montmorillonite exfoliation. Their work demonstrated that i) the Specific Mechanical Energy (SME) expressed in kWh·t^{-1} (**Domenech et al., 2013**) linked all the processing parameters that can affect the exfoliation, and that ii) the higher the SME value, the better the exfoliation. The SME is expressed by the following equation (4.1):

$$SME = \frac{\alpha \times C \times N}{Q} \tag{4.1}$$

Where 'C' is the torque measured during extrusion in Nm, 'N' is the screw rotation speed in rpm, 'Q' is the extrusion feed rate in kg·h^{-1}, and 'α' is a constant in kW·Nm^{-1}·rpm^{-1}, which describes the properties of the used extruder via the following equation (4.2) (**Domenech et al., 2013**):

$$\alpha = \frac{P_{motor}}{\tau_{max} \times N_{max}} = \frac{11.7}{38 \times 1200} = 2.6 \cdot 10^{-4} \, kW \cdot Nm^{-1} \cdot rpm^{-1} \tag{4.2}$$

With 'P_{motor}', the power of the extruder motor in kW, 'τ_{max}' the maximum value of the motor torque in Nm, and 'N_{max}' the maximum screw rotation speed in rpm.

In the context of our study on montmorillonite exfoliation and the search for optimal process conditions, we decided to vary the extrusion feed rate. This decision was based on the findings of **Domenech et al., 2012**, which demonstrated that the specific mechanical energy was maximized at low feed rates. Additionally, the residence time is also influenced by the feed rate and screw rotation speed, with a more significant proportion attributed to the feed rate. Since residence time also promotes exfoliation through erosion, we chose to vary this parameter as well.

Regarding the exfoliation process temperature, we deliberately went for slightly lower values (190°C) than the recommended processing temperatures (200-210°C), in order to maintain a high viscosity. This approach allows us to play with the torque values during extrusion, since the latter contributes to increase the mechanical energy supplied to the system, thereby promoting montmorillonite exfoliation.

We started by preparing master batches with 20wt% of montmorillonite. Then, these concentrated blends were subsequently diluted to obtain blends with 5wt% montmorillonite concentration. Therefore, the processing parameters as the extrusion feed rate, were varied only with the diluted blends (with 5wt% of montmorillonite).

4.1.2 Specific mechanical energy monitoring

During the exfoliation of 5wt% montmorillonite blends, we calculated the values of the specific mechanical energy (Equation 4.1) for each compound made with both C20A and CNa$^+$ montmorillonites. The recorded parameters and the calculated energy are shown in **Table 4-1** and **Table 4-2**.

Table 4-1 : Parameters monitored during the exfoliation step by twin-screw extrusion for blends with the CNa$^+$ MMT.

BLEND	SCREW SPEED (N) (rpm)	FEED RATE (Q) (kg·h^{-1})	TORQUE (C) (Nm)	SME (kWh·t^{-1})
CNa_5_0.5		0.5	4.2	1,087
CNa_5_1	500	1	6.1	790
CNa_5_3		3	13.7	593
CNa_5_5		5	17.1	445
CNa_5_10		10	28.5	371

Table 4-2 : Parameters monitored during the exfoliation step by twin-screw extrusion for blends with the C20A MMT.

BLEND	SCREW SPEED (N) (rpm)	FEED RATE (Q) (kg·h⁻¹)	TORQUE (C) (Nm)	SME (kWh·t⁻¹)
C20A_5_0.5		0.5	4.2	1,087
C20A _5_1		1	5.7	741
C20A_5_3	500	3	13.3	576
C20A_5_5		5	16.7	435
C20A_5_10		10	28.1	366

It can be observed that under equivalent process conditions, the torque values slightly vary depending on the type of montmorillonite used in the blends. The variation is about -0.4 Nm for the blends with C20A MMT compared to the blends with CNa⁺ one, and for all feed rates comprised between 1 and 10 kg·h⁻¹.
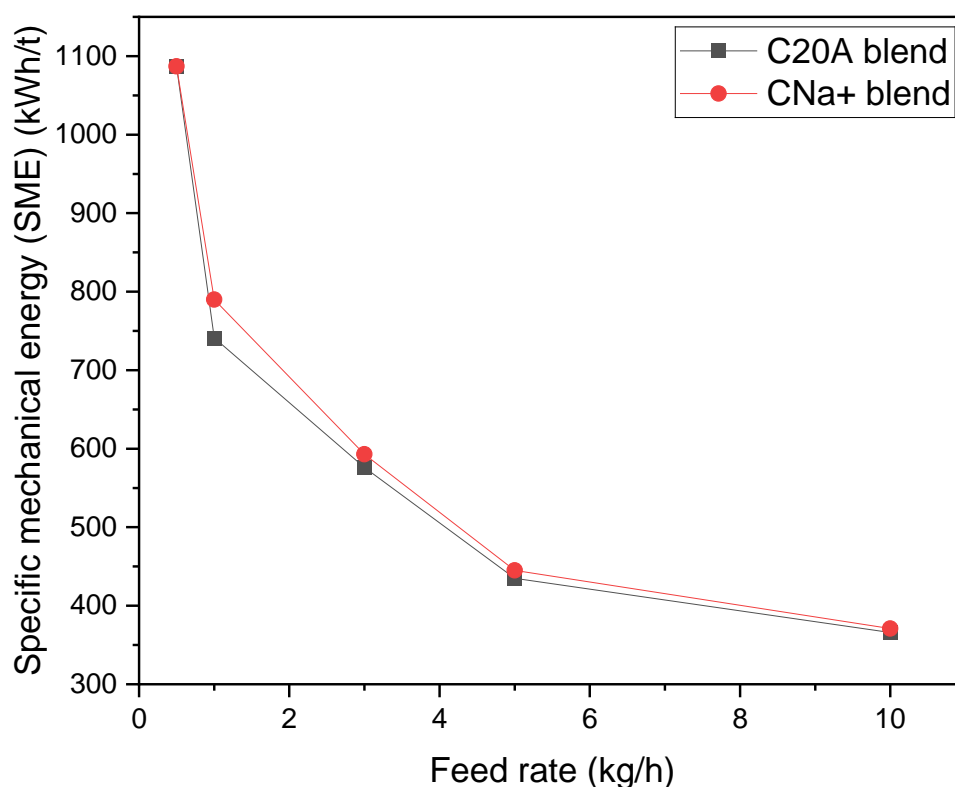
Figure 4-1 : Specific mechanical energy measured during the extrusion process versus the corresponding feed rate used for the exfoliation. Both CNa+ and C20A blends are represented.

Indeed, in **Figure 4-1**, it can be noted that as the extrusion feed rate increases, the specific mechanical energy supplied to the system decreases, and the variations are similar regardless of the type of montmorillonite used. These results are consistent with the works of **Domenech et al., 2012 and 2013**, and **Vergnes., 2019** which have shown in the case of a poly(propylene) - MMT blend a reduction of the SME from 1,087 kWh·t^{-1} to 224 kWh·t^{-1} with a feed rate variation from 3 to 20 kg·h^{-1} at screw speed of 500rpm.

After the extrusion process, a compression molding step was conducted in order to obtain thin films. These films were used to study the quality of montmorillonite dispersion. The obtained films are presented in **Figure 4-2** below:
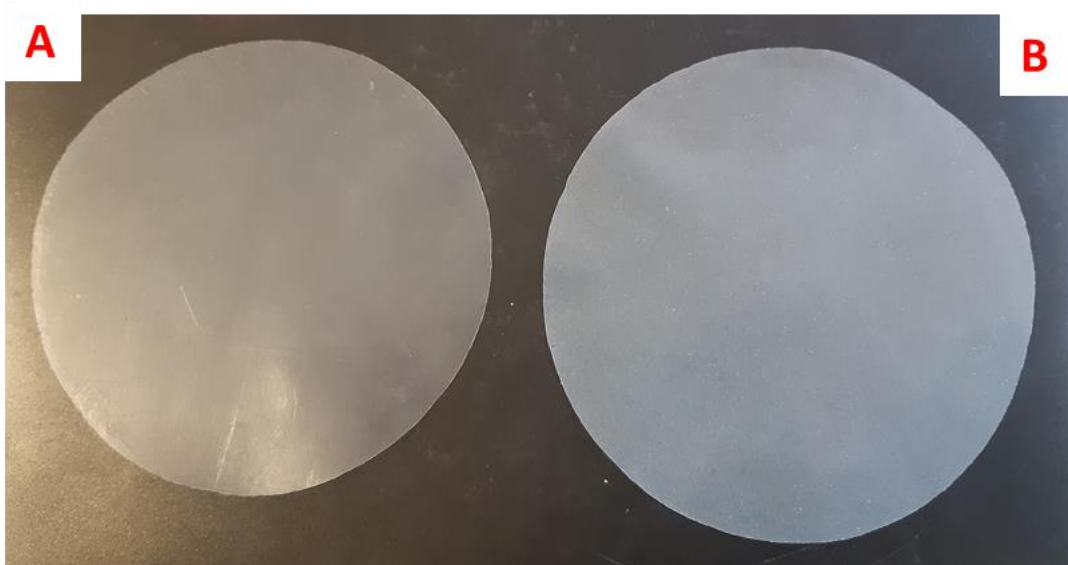
Figure 4-2 : Image of the films made by compression molding from a) C20A_5_5 blend and b) CNa_5_5 blend.

As observed, the film made with the mixture containing CNa$^+$ (**Figure 4-2b**) appears whiter than the film made with C20A MMT (**Figure 4-2a**). The white appearance of the film with CNa$^+$ is due to the presence of micrometer-sized particles that diffract light and are visible to the naked eye. In contrast, the film made with C20A MMT does not show visible particles, suggesting that the particles are smaller in size and do not diffract light, resulting in a colorless appearance. However, one advantage of nano-fillers over micro-fillers is their smaller size, which has little effect on the optical properties of the matrix in which they are dispersed

(**Althues et al., 2007**). This observation suggests better exfoliation of C20A montmorillonite than CNa⁺ montmorillonite.

4.2   EXFOLIATION CHARACTERIZATION

In this section, the objective is to characterize the degree of exfoliation of the blends previously prepared. To achieve the most accurate characterization possible, we used different techniques, including X-ray diffraction, rheology, and both optical microscopy and transmission electronic microscopy.

4.2.1 X-ray diffraction

We conducted measurements on Bragg peak's positions of the (001) lattice plane CNa⁺ MMT and both (001) and (002) lattice plane for the C20A MMT. The main objective is to observe any disappearance of these peaks in the case of complete exfoliation or a shift of the peaks towards smaller 2θ angles, which would indicate an increase in the interlayer distance indicating polymer chain intercalation between the layers.
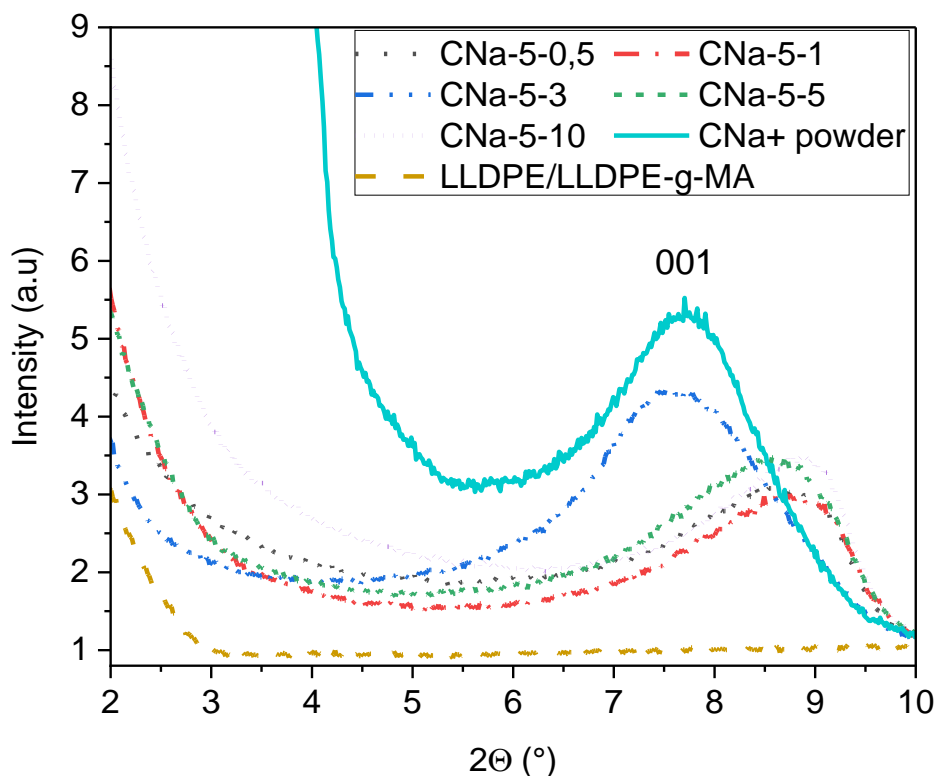
Figure 4-3 : BBXRD patterns of the blends made with 5wt% of CNa⁺ MMT with various feed rates (Rivollier et al.,2024).

Figure 4-3 presents the XRD patterns of blends made with CNa⁺ MMT, varying the extrusion feed rate, as well as a blend of LLDPE/LLDPE-g-MA without MMT. The intensity is normalized by the minimum recorded value for each sample. It is notable that the polymer matrix alone (LLPDE/LLDPE-g-MA) does not exhibit any diffraction peak at 2θ angles below 10°, emphasizing that, in the blends, the diffraction peaks come exclusively from montmorillonite. The XRD patterns reveal the persistence of the 001 Bragg peak of CNa⁺ MMT, regardless of the process conditions, suggesting either no exfoliation or incomplete exfoliation (**Rivollier et al., 2024**).

However, in the case of blends produced at feed rate of 0.5, 1, 5, and 10 kg·h⁻¹, a shift of the peaks towards higher 2θ angles is observed, around 8.5° compared to the powder alone, which shows a peak at 7.74°. This indicates a decrease in the interlayer distance, with a shift of approximately 170 pm (**Table 4-3**). We hypothesize that this could result from the

disappearance of Na^+ ions between the layers of the MMT, since the diameter of this ion is around 200 pm (**Yoon et al., 2003; Rivollier et al., 2024**).

Table 4-3 : Bragg peak positions determined by manual single peak fit from BBXRD patterns in Figure 4-3, and their corresponding interlayer spacing calculated with Bragg's law.

SAMPLE	FEED RATE ($kg \cdot h^{-1}$)	$2\theta - 001$	d_{001}
CNA^+ Powder	/	7.74°	1.14 nm
CNa_5_0.5	0.5	8.65°	1.02 nm
CNa_5_1	1	8.71°	1.01 nm
CNa_5_3	3	7.71°	1.14 nm
CNa_5_5	5	8.53°	1.03 nm
CNa_5_10	10	8.26°	1.07 nm

In the case of blends with C20A MMT, a similar observation can be made. Indeed, in **Figure 4-4**, we can observe the presence of the 001 and 002 Bragg peaks of C20A MMT regardless of the extrusion feed rate. Thus, there is no complete exfoliation observed. The intensity is also normalized by the minimum recorded value for each sample. However, a shift of the Bragg peaks towards smaller 2θ angles can be noted, at 3.3° and 6.7°, compared to the powder alone, whose (001) and (002) lattice planes diffract at angles 2θ = 3.66° and 7.15°, respectively (**Table 4-4**)(**Rivollier et al., 2024**). This shift resembles polymer chain intercalation between the layers of MMT instead of or in the presence of the organomodified ion, thereby increasing the interlayer distance (**Środoń., 2006; Guo et al., 2020**).
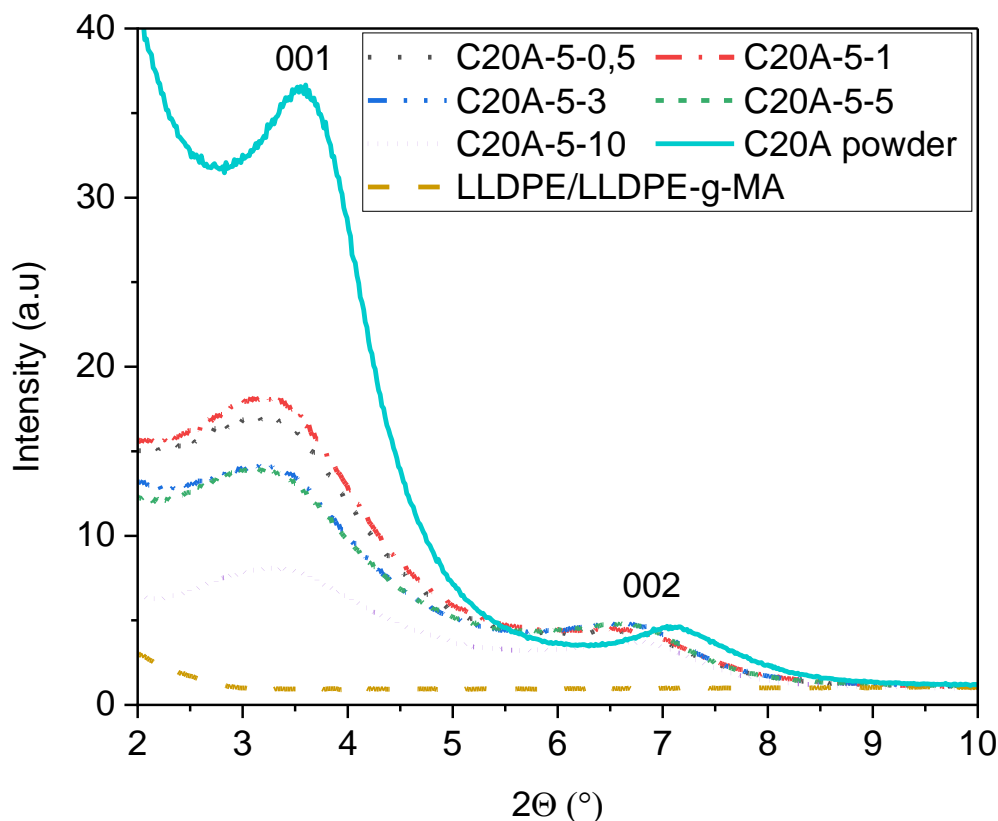
Figure 4-4 : BBXRD patterns of the blends made with 5wt% of C20A MMT with various feed rates (Rivollier et al., 2024).

Table 4-4 : Bragg peak positions determined by manual single fit peaks from BBXRD patterns in Figure 4-4, and their corresponding interlayer spacing calculated with Bragg's law.

SAMPLE	FEED RATE (kg·h^{-1})	$2\theta - 001$	d_{001}	$2\theta - 002$	d_{002}
C20A Powder	/	3.66°	2.41 nm	7.15°	1.24 nm
C20A_5_0.5	0.5	3.34°	2.64 nm	6.73°	1.31 nm
C20A_5_1	1	3.35°	2.64 nm	6.74°	1.31 nm
C20A_5_3	3	3.34°	2.64 nm	6.70°	1.32 nm
C20A_5_5	5	3.31°	2.68 nm	6.69°	1.32 nm
C20A_5_10	10	3.37°	2.62 nm	6.77°	1.30 nm

Intensity variations are observed on the 001 Bragg peaks of the C20A MMT as the extrusion feed rate changes. It may seem that these variations are caused by a decrease in the

number of MMT nano-sheet stacks, which could be related to an increase in exfoliation and therefore fewer diffracting (00l) lattice planes (**Środoń., 2006; Zeng et al., 2005**). However, the lack of changes in intensity on the 002 Bragg peak is inconsistent. Since (001) and (002) lattice planes belong to the same family, a decrease in the intensity of the 001 Bragg peak should lead to a corresponding decrease in the intensities of the 002, 003, and 00l Bragg peaks. Therefore, the intensity variation cannot be attributed to variations in the level of exfoliation. Instead, these intensity variations are caused by a too high contribution of the direct beam at angles less than $2\theta = 5°$, which affects the intensity of the diffraction pattern at small angles (**Rivollier et al., 2024**). Finally, the width of the Bragg peaks could give information on the level of exfoliation. It has been noted that the peaks of mixtures are wider than those of montmorillonite alone. This is because the fewer the layers stacked, the less significant the diffracted beam, resulting in a weaker signal (**Morgan & Gilman, 2003**). However, quantifying this information is difficult due to the contribution of the direct beam.

Finally, it can be concluded that the systems with C20A and CNa$^+$ are not completely exfoliated because neither the 001 nor the 002 Bragg peaks disappear. However, it is not possible to draw conclusions about potential differences in exfoliation among all samples. Therefore, additional characterizations using other methods are necessary (**Rivollier et al., 2024**).

4.2.2 Rheology

Rheological measurements were performed with the blends obtained after the extrusion exfoliation step. The blends analyzed are those previously characterized by XRD and the master batch blends containing 20wt% MMT for both C20A and CNa$^+$. Dynamic Frequency Sweep tests were realized, where the complex viscosity 'η^*' is measured as a function of the angular frequency 'ω'. The results are shown in **Figure 4-5** and **Figure 4-6** for each type of montmorillonite. All curves were fitted using the Carreau-Yasuda model (**Equation 3.6**) to determine the melt yield stress 'σ_o', which is an indicator of the level of montmorillonite

exfoliation (**Vergnes., 2011**). The fitted results were also integrated into the graphs (**Figure 4-5** and **Figure 4-6**), and the melt yield stress values are presented in **Table 4-5** and **Table 4-6.** Since the polymer matrix initially has a significant melt yield stress value, we deliberately chose to compare the obtained melt yield stress with relative values of 'σ_0' (blend/matrix), aiming to specifically evaluate the impact of the presence of the filler. The parameters derived from the fitting with Carreau-Yasuda model are grouped in the appendix (**Table A-1-1** ; **Table A-1-2**).

Figure 4-5 : Dynamic frequency sweep measurements showing the impact of the feed rate upon the complex viscosity η*variation on CNa$^+$ MMT blends. Addition of the corresponding Carreau-Yasuda fit.

Table 4-5 : Melt yield stress ('σ₀') values determined by the Carreau-Yasuda fit for each blends with CNa⁺ MMT, and relative melt yield stress values associated (Rivollier et al., 2024).

SAMPLE	σ_0 compound (Pa)	σ_0 compound / σ_0 matrix
CNa_20_5	1,659	6.57
CNa_5_0.5	899	3.56
CNa_5_1	633	2.51
CNa_5_3	725	2.87
CNa_5_5	281	1.11
CNa_5_10	231	0.92
LLDPE_LLDPE-g-MA	253	1

Figure 4-5 and **Figure 4-6** show that, regardless of the type of montmorillonite and the filler content, the addition of fillers increases the complex viscosity of the compounds compared to that of the polymer matrix alone over the entire frequency range. This observation is consistent, given that MMT is an inorganic material with mechanical properties significantly superior to those of LLDPE (**Rivollier et al., 2024**).

Figure 4-5 reveals differences in viscosity at low frequencies for various 5 wt% CNa⁺ based compounds. In **Table 4-5**, the melt yield stress values 'σ₀' decrease significantly with increasing feed rates, from 899 to 231 Pa when increasing the feed rate from 0.5 to 10 kg·h⁻¹(**Rivollier et al., 2024**). According to **Vergnes., 2019**, this drop suggests that the exfoliation state of CNa⁺ decreases with increasing feed rate, mainly due to the decrease in specific mechanical energy provided by the process, as shown in the part **4.1.2**.

In the case of C20A-based compounds (**Figure 4-6**), no significant variation in viscosity is observed for blends with 5% MMT prepared at various feed rates. The values for calculated melt yield stress listed in **Table 4-6** are relatively close to each other, with 'σ₀' ranging from 1,500 to 1,800 Pa. The C20A blends exhibit a variation of only 20% with an increase in feed rate, compared to CNa⁺ which shows a variation of 70% under the same conditions. This suggests that C20A based compounds have reached their maximum exfoliation state regardless of the feed rate. Through chain intercalation between the nano-layers, interactions are reduced, requiring less process energy to achieve a good level of exfoliation (**Rivollier et**

al., 2024). Therefore, it is assumed that the minimal specific mechanical energy provided by the highest feed rate is already sufficient to exfoliate montmorillonite.
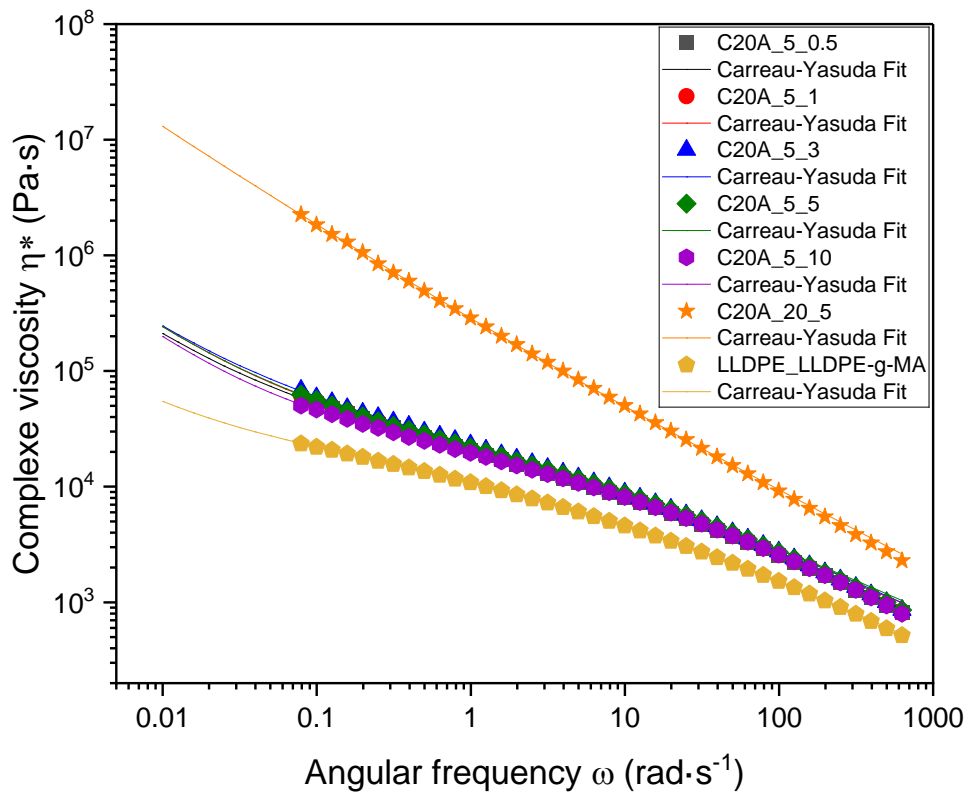
Figure 4-6 : Dynamic frequency sweep measurements showing the impact of the feed rate upon the complex viscosity η^* variation on C20A MMT blends. Addition of the corresponding Carreau-Yasuda fit.

Table 4-6 : Melt yield stress ('σ_0') values determined by the Carreau-Yasuda fit for each blends with C20A MMT, and relative melt yield stress values associated (Rivollier et al., 2024).

SAMPLE	σ_0 compound (Pa)	σ_0 compound / σ_0 matrix
C20A_20_5	107,980	427.63
C20A_5_0,5	1,530	6.06
C20A_5_1	1,890	7.49
C20A_5_3	1,741	6.89
C20A_5_5	1,823	7.22
C20A_5_10	1,612	6.39
LLDPE_LLDPE-g-MA	253	1

The melt yield stress values 'σ$_0$' of C20A compounds (**Table 4-6**), with a concentration of 5wt% are at least twice as high as those of CNa$^+$ compounds prepared under the same conditions. This difference can be attributed to the fact that higher exfoliation states generate more significant mechanical interactions between the nano-sheets and the matrix. This hypothesis is reinforced by the 'σ$_0$' value obtained for the 20wt% C20A MMT compound, which is approximately 67 times higher than that calculated for the 20wt% CNa$^+$ MMT compound. Thus, it can be concluded that compounds with CNa$^+$ MMT are probably not completely exfoliated, while those with C20A MMT are likely almost entirely exfoliated (**Rivollier et al., 2024**).

In summary, extracting the melt yield stress parameter from complex viscosity measurements provides indications about the level of MMT exfoliation. This method provides much more detailed information compared to the X-ray diffraction patterns discussed earlier, which do not allow for an in-depth analysis of the state of the 2D material integrated into the polymer matrix (**Rivollier et al., 2024**).

4.2.3 Microscopy

Optical microscopy observations were conducted in order to confirm the conclusions drawn from the rheological analysis of the montmorillonite exfoliation state. These observations focused on both blends containing 20wt% and 5wt% of montmorillonite concentration, as displayed in **Figure 4-7** and **Figure 4-8**.
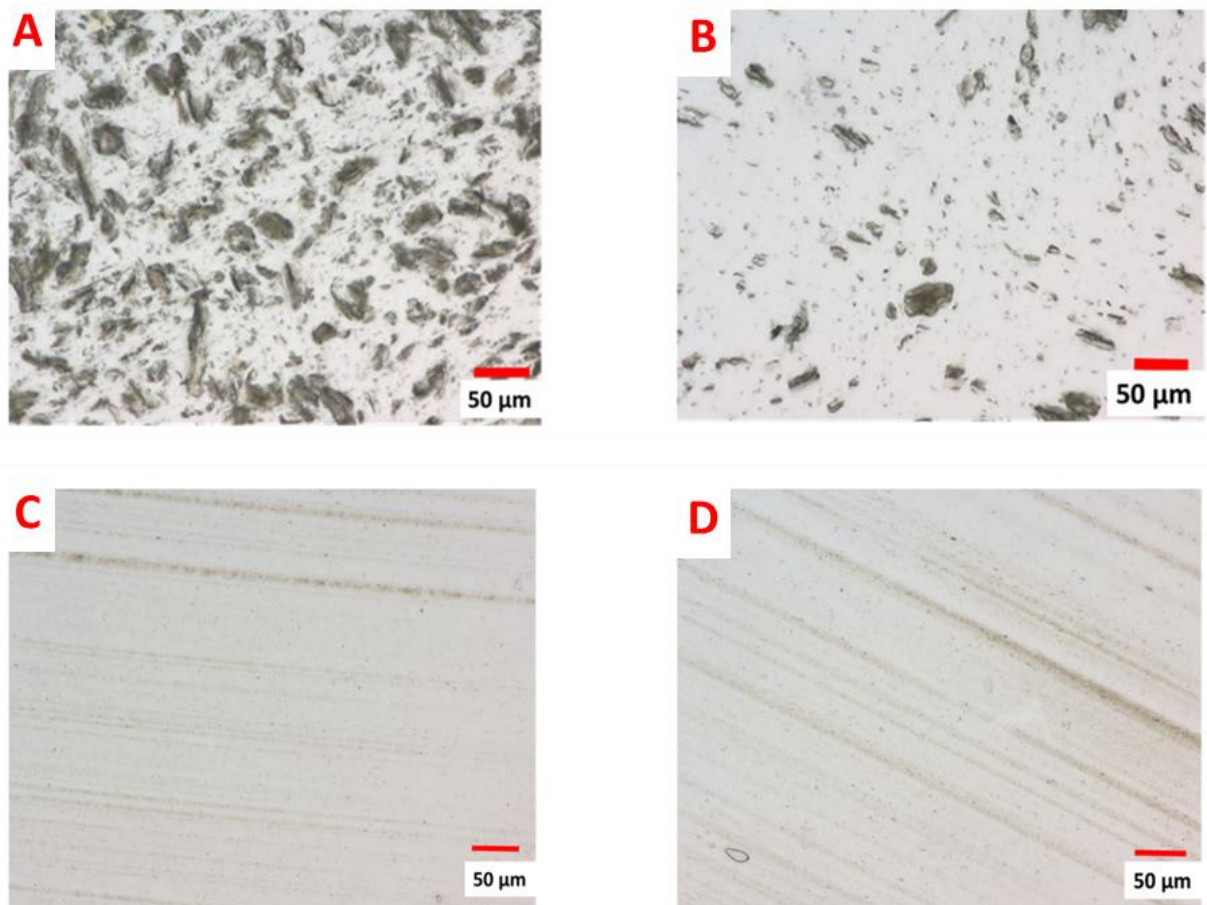
Figure 4-7 : Optical microscope images of extrudate cross-sections in transmission mode. A) CNa_20_5 blend B) CNa_5_5 C) C20A_20_5 blend D) C20A_5_5 blend (Rivollier et al., 2024).

The optical microscope images of the compounds (derived from extrudates obtained at the extrusion die), presented in **Figure 4-7a and b**, indicate that the CNa^+ MMT particles do not appear to be exfoliated but rather exist in the form of tactoid aggregates. However, **Figure 4-7c and d** demonstrate that the C20A MMT mixtures exhibit a finer dispersion of MMT particles, which are not visible under an optical microscope magnification (**Rivollier et al., 2024**). The lines in the images correspond to the marks made by the knife used to prepare the samples and do not represent a layered structure. This suggests a better exfoliation for C20A MMT compared to the CNa^+ one (**Rivollier et al., 2024**).
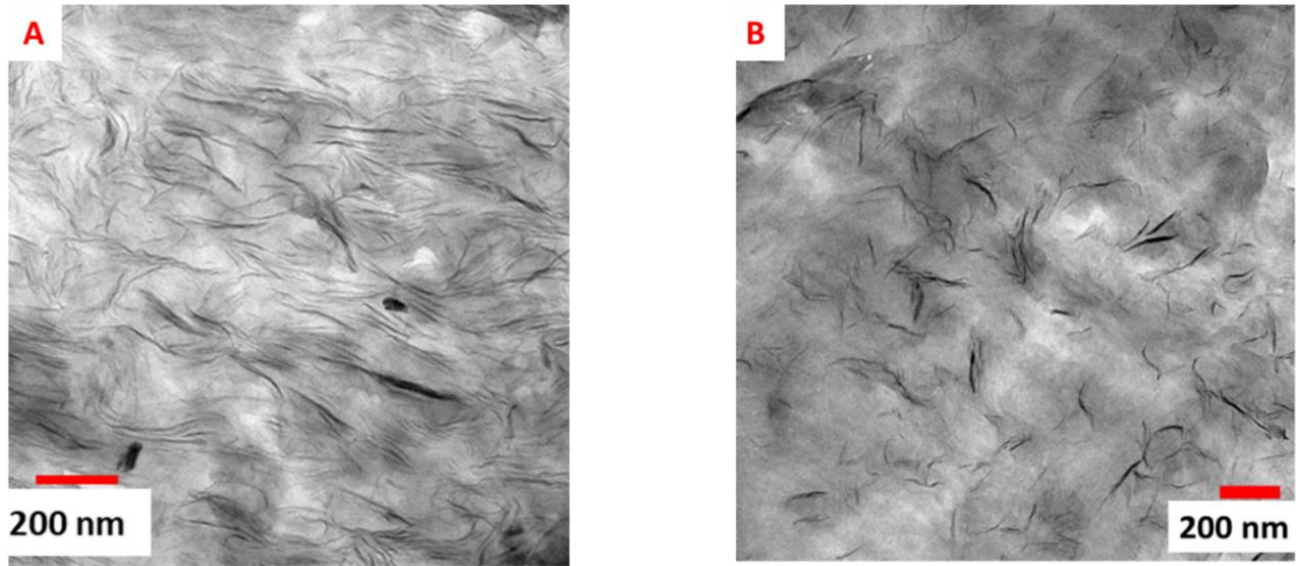
Figure 4-8 : TEM images of strand cross-sections. A) C20A_20_5 blend B) C20A_5_5 (Rivollier et al., 2024).

Therefore, to be able to identify any exfoliation of the C20A MMT, more powerful microscopic analysis was performed, such as TEM. **Figure 4-8** suggest that the majority of montmorillonites are exfoliated in the compounds with 5 and 20wt% C20A MMT, respectively. Although some nano-sheets stackings are still visible, their total thickness is in order of nanometers, representing a significant difference compared to the situation observed in **Figure 4-7a and b**. These observations confirm the previously established conclusion from complex viscosity measurements: compounds with CNa^+ MMT are not exfoliated, while those with C20A MMT are predominantly exfoliated, with nano-sheets ranging from 200 nm in length to 1 to 10 nm in thickness (**Rivollier et al., 2024**).

Furthermore, TEM analyses were conducted on three blends with C20A subjected to feed rates of 0.5, 5 and 10 $kg·h^{-1}$. The goal was to detect any notable differences in exfoliation between these flow rates. The results are presented in **Figure 4-9**, **Figure 4-10** and **Figure 4-11**.
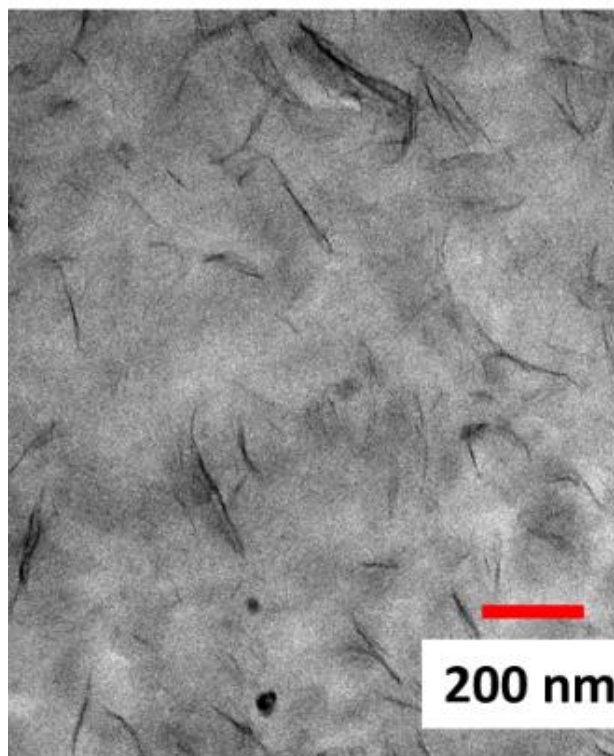
Figure 4-9 : TEM image of strand cross-sections of C20A_5 blend at a feed rate of 0.5 kg·h⁻¹.
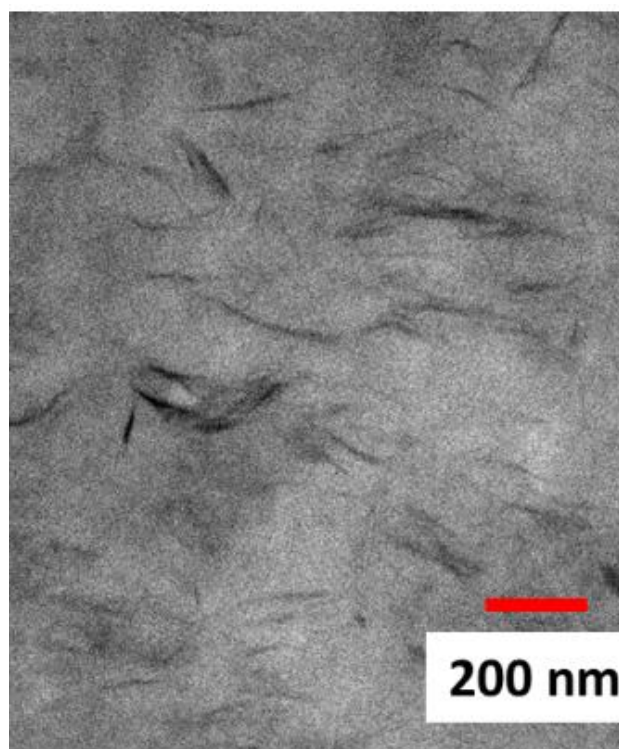
Figure 4-10 : TEM image of strand cross-sections of C20A_5 blend at a feed rate of 5 kg·h⁻¹.
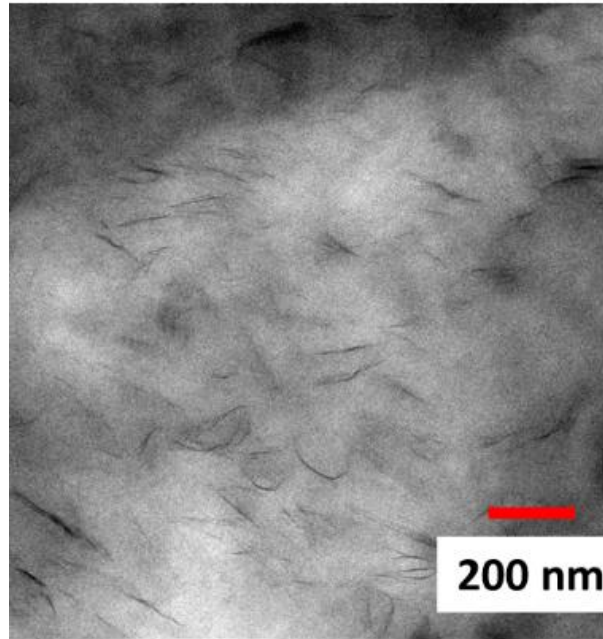
Figure 4-11 : TEM image of strand cross-sections of C20A_5 blend at a feed rate of 10 kg·h^{-1}.

Figure 4-9, Figure 4-10 and **Figure 4-11** show that the degree of exfoliation in the blends is not significantly different. This confirms the rheological observations indicating that, regardless of the extrusion feed rate, in the case of C20A, the maximum level of exfoliation is already achieved under these conditions.

In this section, we have observed that the three characterization techniques provide access to different but relatively complementary information, especially in the case of partially exfoliated morphology.

4.3   BLEND'S MORPHOLOGY ORIENTATION

In this section, correlations between the previous observations will be established in order to confirm the hypothesis regarding the blend's morphology obtained after the exfoliation of the two types of montmorillonites.

The objective is to establish a correlation between the morphology of the blend and the montmorillonite's capability to orient itself. This correlation will guide the selection of the blend for the subsequent phases of this thesis.

4.3.1 Conclusions about the blends morphologies

The summary of results from all characterization techniques, described in this chapter, has allowed us to obtain a more detailed and comprehensive analysis about the morphology induced in our systems. The results are described in **Table 4-7** below:

Table 4-7 : Summary of results from the characterization techniques described in this chapter: conclusions about blend's morphology described in part B.

METHOD OF CHARACTERISATION AND STUDIED PARAMETERS	C20A MMT BLEND	CNa⁺ MMT BLEND
X-ray diffraction (001 and 002 Bragg peaks)	Shift toward smaller 2θ angles **No complete exfoliation – intercalated morphology**	Shift toward higher 2θ angles **No complete exfoliation**
Rheology (relative σ_0 value)	6 – 7.5 range with 5wt% MMT 427 with 20wt% MMT **A lot of interactions MMT – Polymer matrix : High level of exfoliation**	0.9 - 3.6 range with 5wt% MMT 6.5 with 20wt% MMT **Few interactions MMT – Polymer matrix : Low level of exfoliation**
Microscopy	Exfoliated nano-sheets + stacks of few MMT nano-sheets **Exfoliated – intercalated morphology**	Micro-aggregates + tactoids **No exfoliated morphology**

Thus, we can confirm that in case of blends with C20A MMT, we predominantly have an exfoliated/intercalated morphology (**Figure 4-12a**). Meanwhile, in blends with CNa$^+$ MMT, the presence of micro-particles/tactoids persists (**Figure 4-12b**).
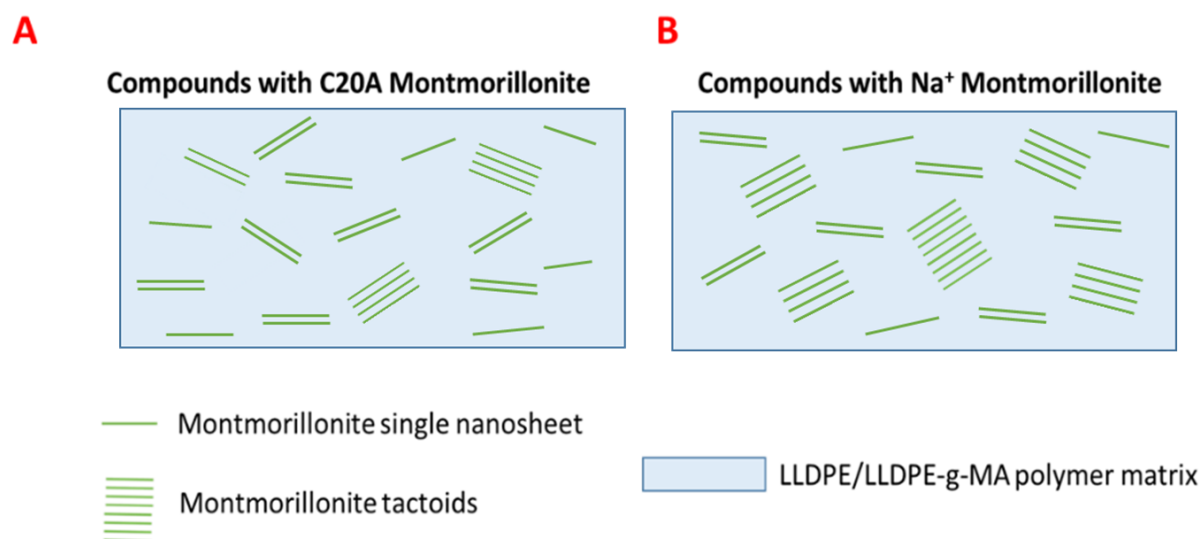
Figure 4-12 : Scheme of the blend morphologies. A) 5wt% C20A MMT blend B) 5wt% CNa$^+$ MMT blend.

Indeed, previous works such as those by **Morgan & Gilman., 2003**, and **Kim et al., 2007**, have also noted a combination of intercalated and exfoliated structures. This observation is particularly understandable given the initial physicochemical properties of the components, with polar montmorillonite and a predominantly non-polar polymer matrix. Indeed, when the matrix is polar (**Alix et al., 2012**; **Fornes et al., 2004**), the nano-sheets have a strong affinity for it, which promotes the exfoliation of montmorillonite. This results in favorable interactions between the matrix and the filler, allowing polymer chains to be intercalated between the MMT nano-sheets and ultimately leading to exfoliation. Intercalating polymer chains between MMT nano-sheets is challenging for LLDPE due to its non-polar nature.

However, C20A MMT has a quaternary ammonium salt present between its nano-sheets, which increases the space between the layers by 2.38 nm. As C20A MMT is also non-polar, it has an affinity with LLDPE chains, allowing them to intercalate between MMT nano-sheets. This process promotes both polymer chain intercalation and MMT exfoliation. This

phenomenon was not observed with Na$^+$ montmorillonite because the space between the MMT nano-sheets is much smaller, measuring only 1.4 nm, and the affinities between LLDPE and the Na$^+$ ion are low. Therefore, these parameters do not lead to intercalated/exfoliated morphologies.

4.3.2 Impact of the exfoliation on the montmorillonite orientation

First, the impact of mixture morphology (exfoliated/intercalated versus non-exfoliated) on montmorillonite orientation was studied. To this end, two thin films obtained by compression molding were measured, one containing 5wt% of CNa$^+$, and the other 5wt% of C20A. As mentioned earlier, the blend with C20A is exfoliated, while the one with CNa$^+$ is not.

Texture analyses on the 001 Bragg peak of CNa$^+$ and the 002 Bragg peak of C20A are represented in **Figure 4-13** and **Figure 4-14**, respectively. In case of the montmorillonite C20A, we chose to measure the 002 Bragg peak instead of the 001. This decision is based on the fact that 002 Bragg peak is located at a $2\theta = 7.15°$, whereas 001 is at $2\theta = 3.66°$. At 2θ angles less than 5°, the contribution of the direct beam to the diffraction signal is too large, which disturbs the measurement. On top of it, the beam footprint becomes even larger at smaller 2θ which leads to more over-irradiation. Thus, to obtain more accurate measurements, we selected 002 Bragg peak which diffracts at a 2θ angle greater than 5°.
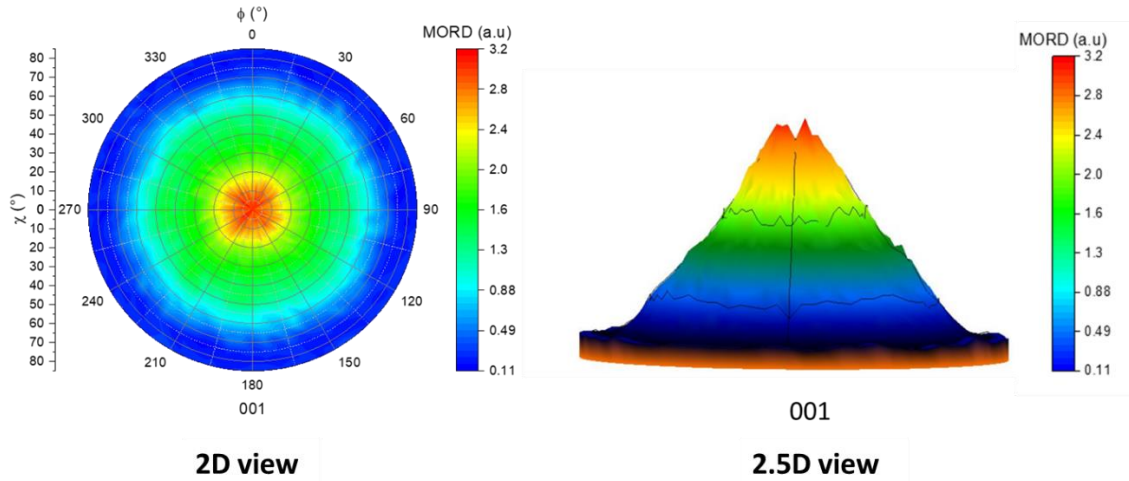
Figure 4-13 : 2D and 2.5D views of the pole figure of the (001) lattice plane of the MMT in the CNa_5_5 blend.
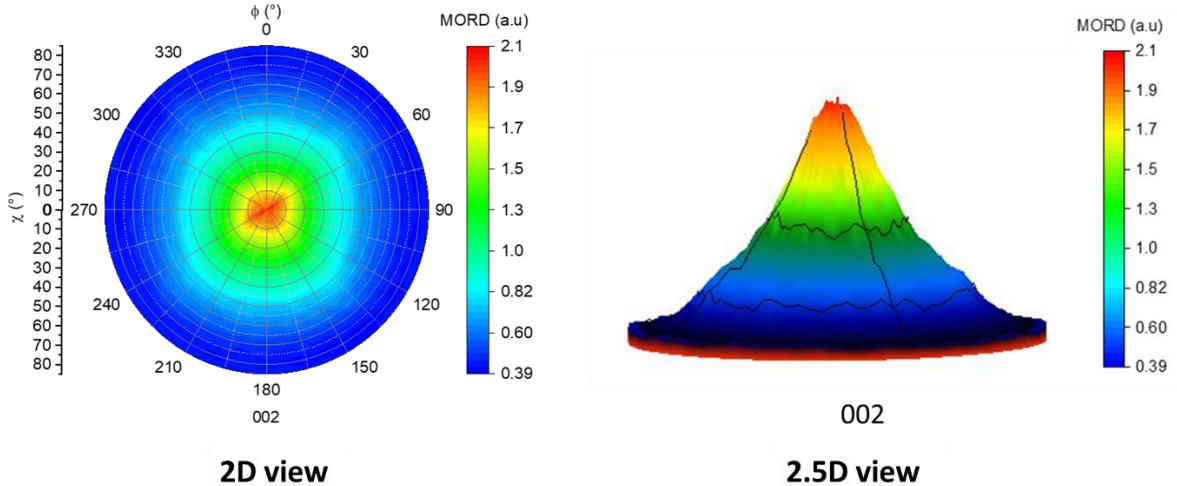
Figure 4-14 : 2D and 2.5D views of the pole figure of the (002) lattice plane of the MMT in the C20A_5_5 blend.

A maximum of diffraction in red color is identified at the center of the pole figure in both **Figure 4-13** and **Figure 4-14**. This suggests that most of the diffraction occurs for montmorillonite layers exhibiting an orientation of their (001) and (002) lattice planes with an 90° - χ angle between 0 and 10° relative to the film's normal (**Rivollier et al., 2024**). In other words, most nano-sheets of montmorillonite are arranged 'in-plane' in both films. However, it is worth noting that **Figure 4-13** exhibits a wider diffraction intensity distribution than **Figure 4-14**, which is even more evident when observing the 2.5D view of pole figures. This observation suggests that the (001) lattice plane of CNa$^+$ nano-sheets can be positioned in

significant amounts with angles 90°- χ of up to 60° relative to the film's normal, while 90° - χ does not exceed 40° in significant amounts in the case of C20A MMT. Thus, it can be inferred that CNa⁺ montmorillonite nano-layers exhibit less 'in-plane' alignment compared to those of C20A MMT. These results significantly highlight the influence of the exfoliation state on the overall orientation of MMT within the compounds. Due to their two-dimensional shape, exfoliated MMT nano-sheets tend to align more in the direction of the flow of molten polymer (**Alix et al., 2012**). In contrast, when MMT is in the tactoid state, it has a lower aspect ratio and is less influenced by the flow of molten polymer (**Rivollier et al., 2024**).

Based on the results and work presented in this chapter, we have chosen to continue the studies with the blends containing C20A, since they present a sufficient level of exfoliation. Additionally, regarding the processing conditions of these blends by extrusion, we have chosen to carry out the exfoliation at a feed rate of 5 kg·h^{-1}. Since the feed rate does not have a significant influence on the level of exfoliation in the case of C20A MMT, we have decided to go for an intermediate feed rate that can be adapted to large-scale productions in a relatively short time frame (**Rivollier et al., 2024**).

5. CHAPTER 5: ORIENTATION OF THE MONTMORILLONITE THROUGH THE PROCESS: FROM MONOLAYER TO MULTI-NANO LAYER SYSTEM

INTRODUCTION

In the previous chapter, we examined how the exfoliated morphology of montmorillonite promotes its orientation parallel to the film's surface. In this section, the main goal is to determine the processing parameters that influence the optimal 'in-plane' orientation of montmorillonite, starting from an exfoliated morphology. We started by working with a monolayer configuration to understand the behavior in a 'simpler' system. Then, we evaluate the impact of multi-nano layer architecture on the orientation of fillers. The study examined the influence of nano-fillers concentration, processing technique, layer thickness, and drawing speed on the orientation of montmorillonite.

5.1 MONTMORILLONITE ORIENTATION IN A MONOLAYER SYSTEM

Following the exfoliation of MMT, our objective is to align the 2D nano-sheets parallel to the film surface. Due to their 2D plate-like morphology, MMT nano-sheets naturally align themselves in the flow direction during the manufacturing process (**Alix et al., 2012**). Moreover, our previous findings indicate a tendency for a more pronounced 'in-plane' orientation after MMT exfoliation. However, it is expected that additional factors could further enhance this orientation. Therefore, we investigated various parameters that could impact the alignment of MMT nano-sheets in monolayer films, including MMT concentration and the polymer film manufacturing process.

5.1.1 Influence of the MMT concentration in the films

We started by investigating the influence of MMT concentration in the blends. Films with concentrations of 5, 10, 15, and 20wt% of C20A MMT were fabricated by compression molding process. The orientation of MMT in these films was characterized using the pole figure measurement method, and the results are presented in **Figure 5-1**.

5wt% MMT   **10wt% MMT**

15wt% MMT   **20wt% MMT**
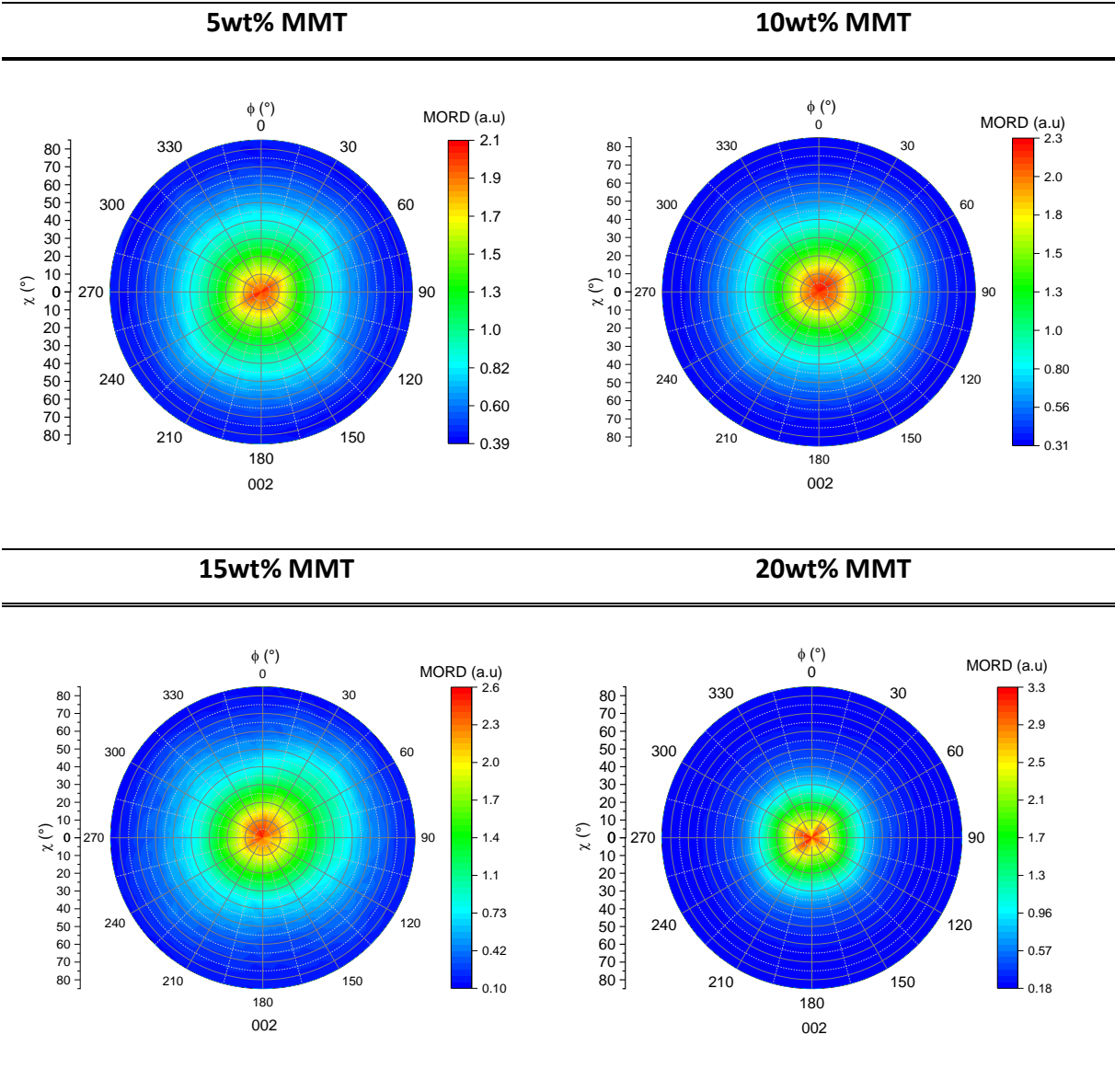
Figure 5-1 : MMT 002 pole figure measurements, progressing from left to right and top to bottom: C20A_5_5; C20A_10_5; C20A_15_5; C20A_20_5 blends (Rivollier et al., 2024).

The 002 MMT pole figures of films containing 5, 10, and 15% by weight appear to be relatively similar. Diffraction is primarily observed at the center of the pole figure and up to χ angles of 40°. However, in the case of the mixture containing 20% by weight of montmorillonite, the diffraction signal seems to be concentrated between values of χ ranging from 0 to a maximum of 30° (**Rivollier et al., 2024**). To quantify this difference, we calculated the average of the measured intensities for all ϕ values at a given χ value, as illustrated in **Figure 5-2**. The integral breadths of these curves were extracted and compiled in **Table 5-1**.
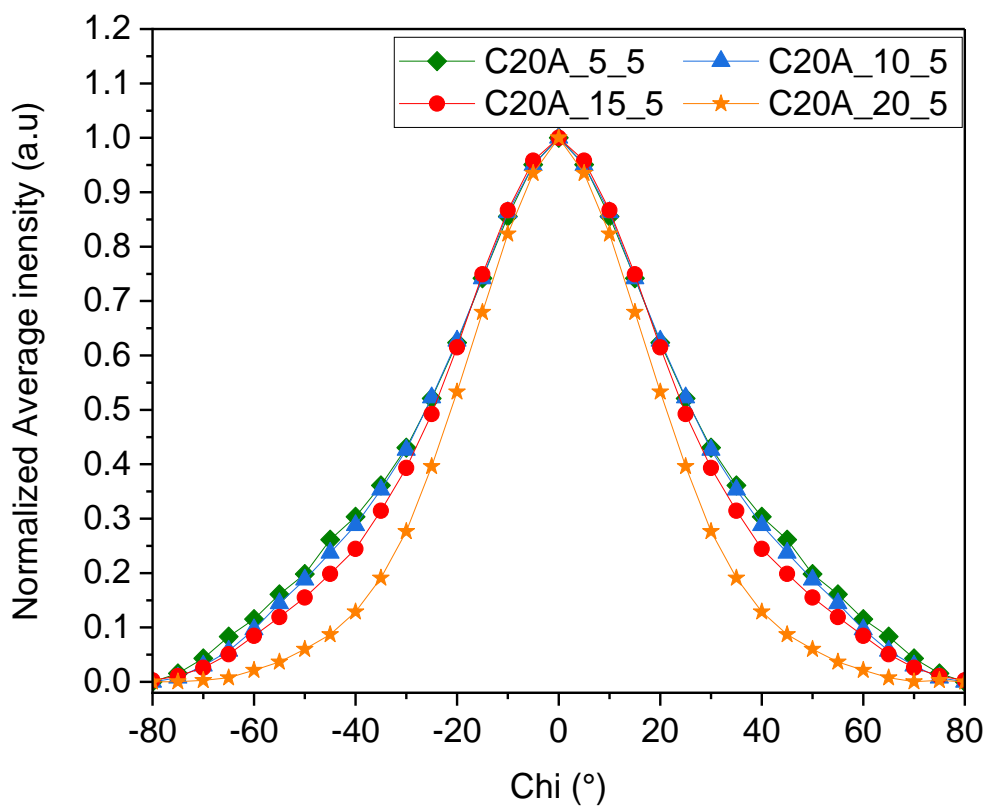
Figure 5-2 : Average intensity over Φ versus χ calculated from the 002 MMT pole figures displayed in Figure 5-1 (Rivollier et al., 2024).

Table 5-1 : Calculated integral breadths of the curves shown in Figure 5-2.

BLEND	MMT CONCENTRATION (wt%)	INTEGRAL BREADTH (°)
C20A_5_5	5	64 ± 2
C20A_10_5	10	63 ± 2
C20A_15_5	15	59 ± 1
C20A_20_5	20	43 ± 0.5

The integral breadth values confirm that the filler orientation remains quite similar between 5 and 10wt%, with integral breadths of 64 ± 2° and 63°± 2°, respectively. However, at 15wt% and 20wt%, the orientation improves with integral breadth of 59°± 1° and 43° ± 0.5°, respectively (**Rivollier et al., 2024**). Therefore, we can conclude that after reaching a certain threshold of MMT concentration (between 15 and 20wt%), the 'in-plane' orientation of MMT nano-sheets is significantly enhanced (**Rivollier et al., 2024**).

This effect can be explained by the observations made in rheology. **Figure 5-3** shows the evolution of the complex viscosity and Carreau-Yasuda fits model for blends containing 0, 5, 10, 15, and 20wt% of montmorillonite. And the **Figure 5-4** shows the evolution of the storage modulus IG'I which characterized the elastic component on the blend.
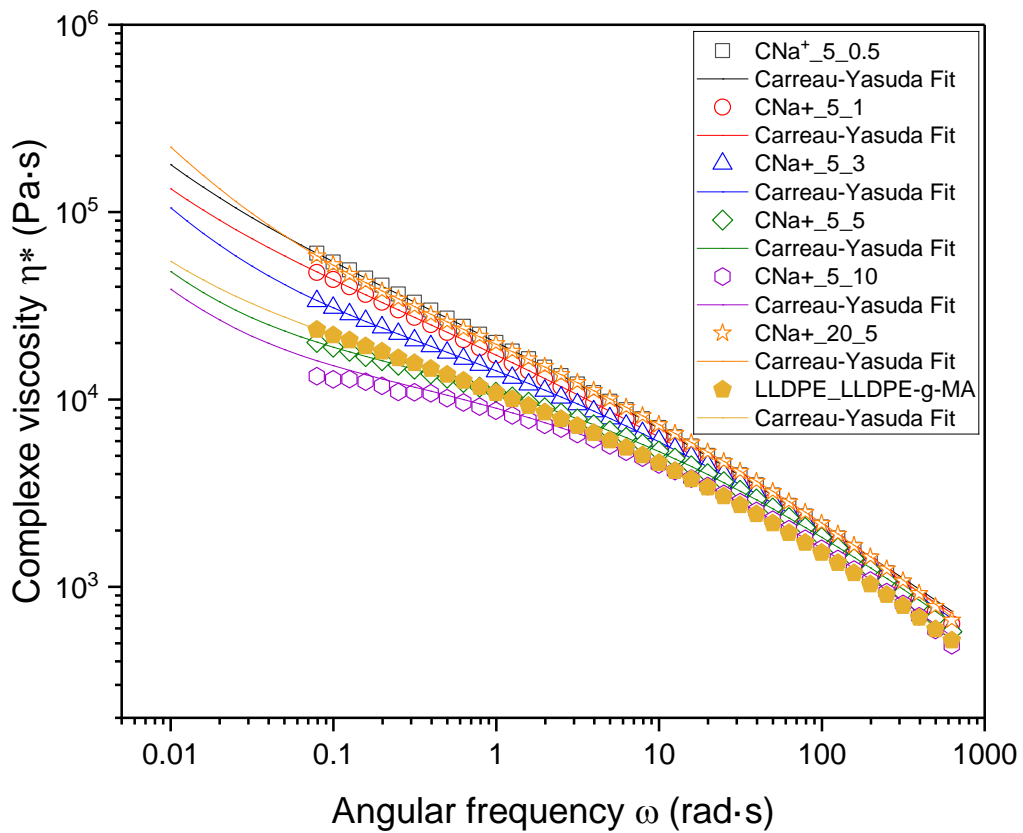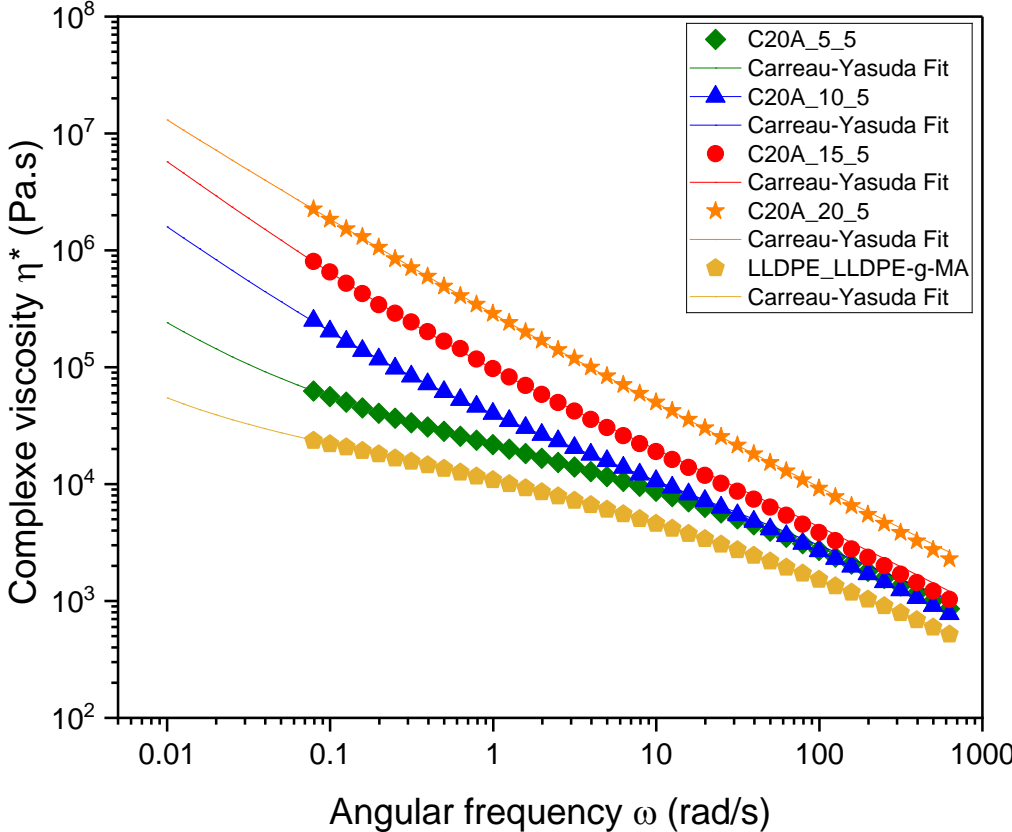
Figure 5-3 : Dynamic frequency sweep measurements showing the impact of the MMT concentration upon the complex viscosity η* variation. Addition of the corresponding Carreau-Yasuda fit.
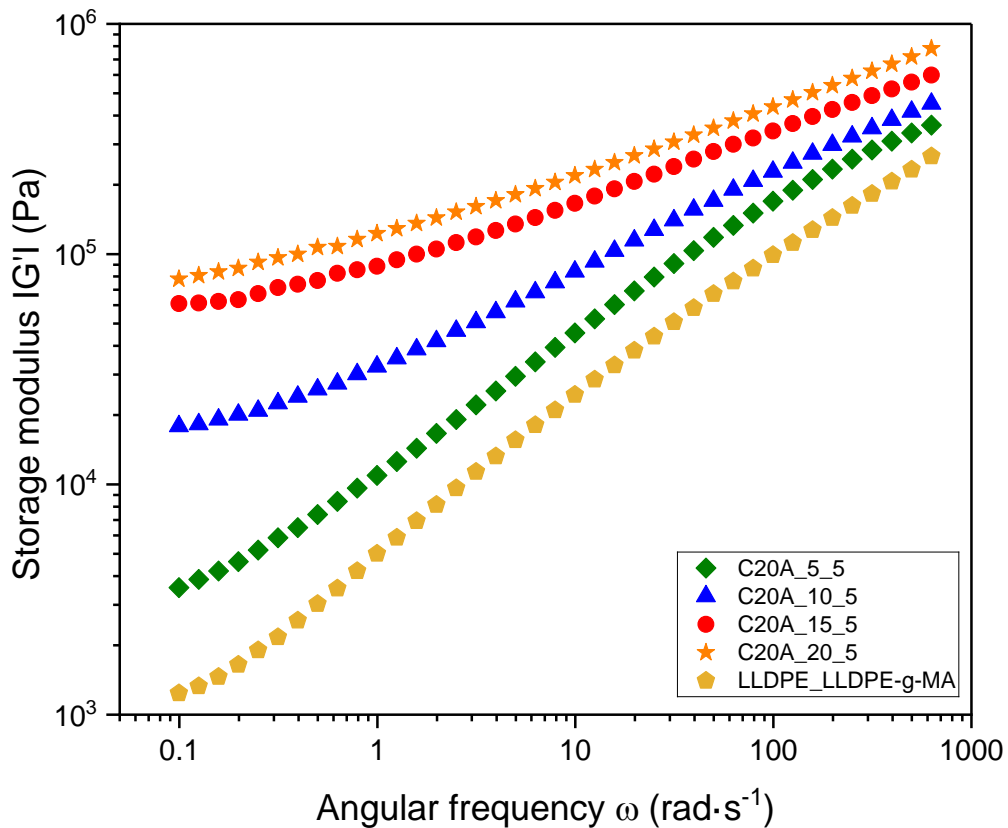
Figure 5-4 : Dynamic frequency sweep measurements showing the impact of the MMT concentration upon the storage modulus│G'│variation.

An increase in the complex viscosity η* is noted with the increase in MMT concentration (**Figure 5-3**), and in the **Figure 5-4,** the appearance of a plateau at low angular frequency is observed when the concentration of MMT increased to 10, 15 and 20wt%. Those two phenomena indicate a behavior similar to a solid-like behavior. A solid-like behavior is a material which has the behavior of a solid at low deformation or low frequency and which is able to flow under high deformation or high frequency. The observed solid-like behavior is even more pronounced with the increase of the MMT concentration. Indeed, when the concentration increases from 10 to 20wt%, the η* increases at low frequency (**Figure 5-3**) as well as the IG'I value at the plateau (**Figure 5-4**). Furthermore, the nonlinear increase of η* at low frequencies becomes immediately obvious with the increase in MMT concentration. Indeed, in the case of a linear increase, the value of η* at low frequency of the blend with

10wt% of MMT should be twice the one of the blend with 5wt% of MMT. However, if we compare the η^* at 0.1rad·s^{-1} of the C20A_5_5 (55,824 Pa·s) with the one of the C20A_10_5 (203,032 Pa·s) this is not the case. Therefore, we look deeper onto those variations with the melt yield stress (**Figure 5-5**).
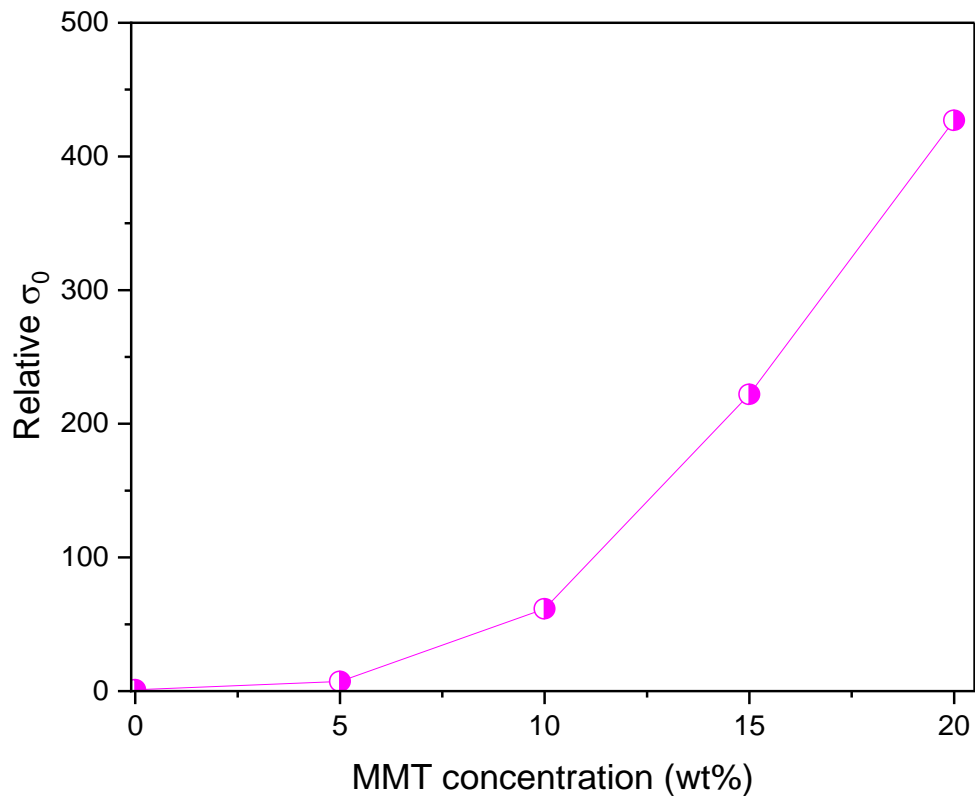
Figure 5-5 : Relative melt yield stress values extracted from Carreau-Yasuda modelisation upon the MMT concentration.

The relative values of melt yield stress extracted for each of the curves plotted in **Figure 5-3** reveal a nonlinear evolution of this parameter as a function of MMT concentration. In the case of the presence of polymer-particles interactions only, the σ_0 variation would have been proportional to the concentration increase. However, here (**Figure 5-5**) this is not the case, there is no linear increase, which suggests the presence of particle-particle interactions in addition to polymer-particle interactions. The works of **Ren et al., 2000** and **Solomon et al., 2001**, have already demonstrated the emergence of a pseudo-solid behavior in poly(propylene)/MMT nanocomposites starting from a concentration of 6wt%. They

associated this behavior with the formation of a 3D network between MMT layers, implying the creation of particle-particle interactions. This is consistent with our observation which suggest the presence of a beginning of a non-linear variation of the melt yield stress for concentration comprising between 5 and 10wt% MMT.

This hypothesis is further supported by TEM images of the degree of exfoliation in the extrudates, presented in **Figure 4-8a**. The latter clearly indicates that the fillers are much closer to each other for the samples with 20%wt MMT than the ones with 5%wt MMT concentration which is normal because the concentration increases. It is possible that these 'clusters' and interactions likely promote an 'in-plane' orientation through self-assembly mechanisms as the MMT concentration increases.

5.1.2 Influence of the manufacturing process

A second parameter that could influence the orientation of MMT within the polymer matrix is the manufacturing process used to produce films. Indeed, some studies have already demonstrated that, in the case of MMT (**Bartczak et al., 2014**) and 2D materials in general (**Moisan et al., 2017**), the manufacturing process has an impact on the improvement of the 'in-plane' orientation due to the forces generated by the process (**Schiessl et al., 2023**). **Bartczak et al., 2014**, showed that blow extrusion leads to better 'in-plane' orientation than compression molding. Regarding coating deposition, both slot die coating and spin coating provide better 'in-plane' orientation compared to drop casting or processes that do not involve shear forces (**Moisan et al., 2017; Schiessl et al., 2023**). Therefore, we conducted a comparison between the compression molding process and monolayer extrusion. In the first case, constant pressure is applied to the molten compound for a few minutes. In the second case (monolayer extrusion) forces are applied for only a few seconds as the molten material passes through the flat die, but it is also subjected to shear forces (**Hyvärinen et al., 2020; Silagy, 2005**).

Figure 5-6 and **Figure 5-7** show the normalized intensity of X-ray diffraction signals measured for the 002 MMT pole figure in the case of films manufactured by both processes

and at two different concentrations, namely 5 and 20wt% (as this is the best orientation achieved at this stage).
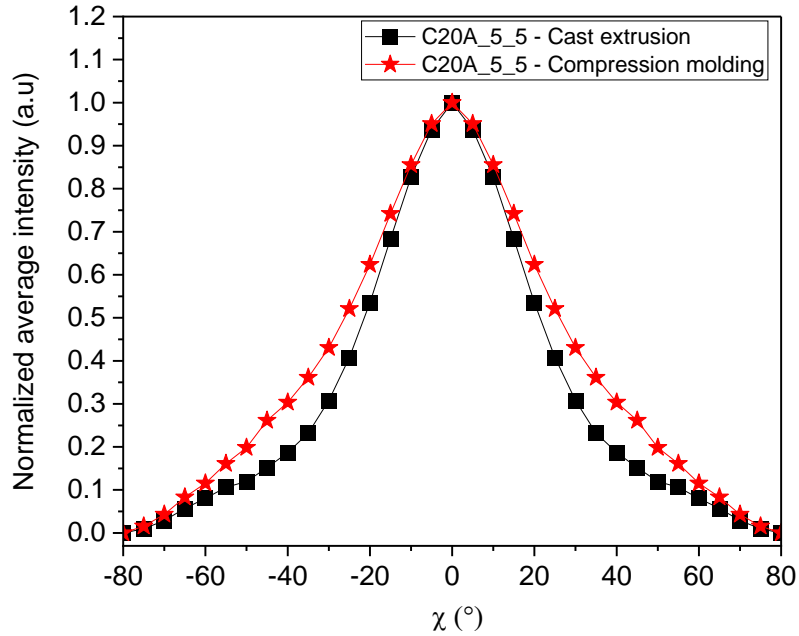
Figure 5-6 : Average intensity over Φ versus χ from 002 MMT pole figures for C20A_5_5 films made by cast extrusion and compression molding (Rivollier et al., 2024).
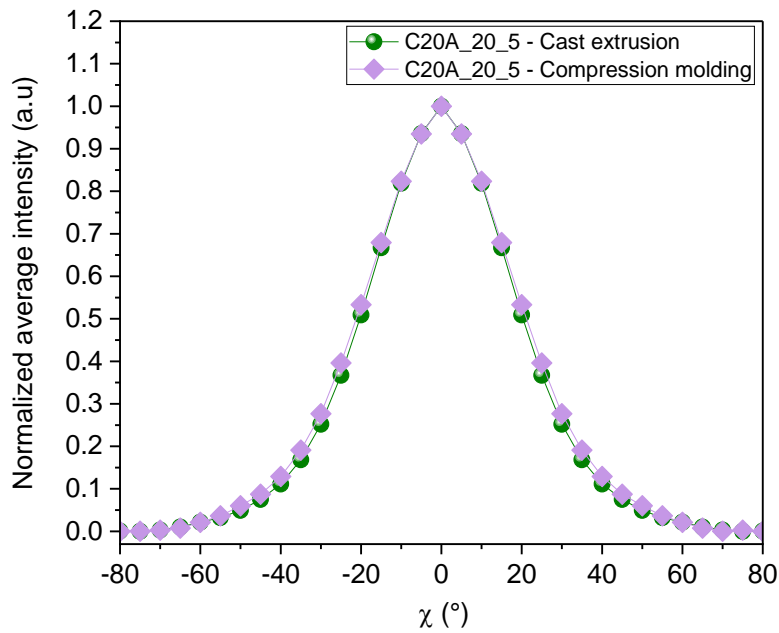
Figure 5-7 : Average intensity over Φ versus χ from 002 MMT pole figures for C20A_20_5 films made by cast extrusion and compression molding (Rivollier et al., 2024).

Table 5-2 reports the extracted integral breadth in each of these cases.

Table 5-2 : Calculated integral breadth values from Figure 5-6 and Figure 5-7 (Rivollier et al., 2024).

SAMPLE	PROCESS	INTEGRAL BREADTH (°)
C20A_5_5	Compression-molding	64 ± 2
	Cast extrusion	52 ± 1
C20A_20_5	Compression-molding	48 ± 0.5
	Cast extrusion	45 ± 0.5

One can observe in **Figure 5-6** that the 'in-plane' orientation is more pronounced in the film with 5wt% of MMT prepared by monolayer extrusion than in the one produced by compression molding. Indeed, there is a reduction in the integral breadth from 64°± 2° to 52°± 1° (**Rivollier et al., 2024**). This observation aligns with previous studies by **Alix et al., 2012** and **Bartczak et al., 2014**, which showed that during the extrusion process, MMT nano-sheets tend to align in the direction of the flow of the molten polymer. This phenomenon is primarily due to the shear forces present in the monolayer extrusion die (**Silagy., 2005**).

Interestingly, the influence of shear flow on 'in-plane' orientation seems to be reduced at a higher concentration of MMT, as the orientation of MMT appears similar with both processes at 20wt%, with integral breadths of 48°± 0.5° and 45° ± 0.5°. This is consistent with the rheological results obtained in **Figure 5-3**. Indeed, viscosity is significantly increased, leading to a loss of chain mobility due to numerous interactions between the charges and LLDPE as well as particle-particle interactions (**Rivollier et al., 2024**). Studies conducted by **Gupta et al., 2005**, or **Hyun et al., 2001**, have shown that in the case of charged nanocomposites, the Newtonian behavior (constant viscosity despite increasing shear rate) at low shear rates occurs, transitioning to pseudo-plastic flow behavior (material flows at high shear rate) at higher shear rates due to the orientation of nano-platelets in the flow direction. Thus, in our case, the shear rate may be insufficient to enhance the orientation of MMT in the monolayer extrusion process.

Hence, in this section, we have shown that both concentration of montmorillonite in the polymer matrix and the film manufacturing process has a significant impact on the 'in-

plane' orientation of MMT in monolayer film configurations. Therefore, we have investigated the impact of multi-nano layer co-extrusion, which represents a more complex film architecture, to further improve orientation. Based on our previous observations, we decided to work with a compound composed of 5wt% of C20A-type MMT due to its exfoliated structure and its ability to align through shear flow.

5.2 MONTMORILLONITE ORIENTATION IN A MULTI-NANO LAYER SYSTEM

In this section, we will examine how the reduction in layer thickness affects the orientation of montmorillonite. Indeed, when the number of layers increases with a constant film thickness, the individual thickness of each layer automatically decreases. Additionally, maintaining the constant number of layers while reducing the total film thickness through stretching also has the effect of decreasing the individual thickness of each layer. Finally, we will also explore the influence of layer composition on the orientation of MMT nano-fillers.

5.2.1 Influence of the number of layers

The objective was to compare the orientation of montmorillonite within films with a thickness of 100 μm ± 20μm, where the number of layers has been varied from 1 to 1025, consequently reducing the thickness of the individual layers. Initially, the characterization of the multi-nano layer structure was carried out to ensure the compliance of the film architecture.

5.2.1.1 Study of the multi-nano layer architecture morphology

To facilitate characterization, microscopic observations were performed on non-stretched thick films of 500 ± 50μm with a different layer architecture (A ≠ B). Verification of the theoretical layer thickness was conducted on a non-stretched film consisting of 17 layers (**Figure 5-8**).
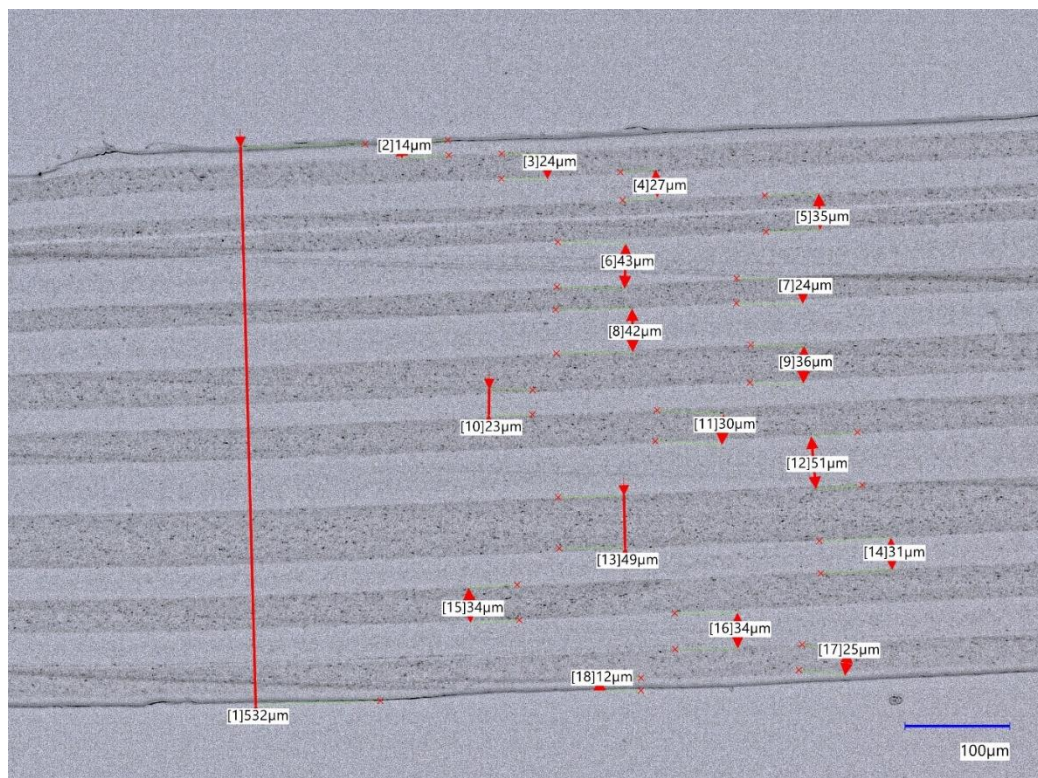
Figure 5-8 : Optical microscope observation in transmission mode of a 17 layers unstretched film cross-section. Dark layers are the ones containing the MMT.

The measured average thickness was determined to be 31.4 ± 10.4 μm. **Figure 5-9**, shows that most layers have a thickness close to the average and included in the calculated standard deviation, although the layers located at the ends of the film are notably thinner than the others. This difference is explained by the fact that the polymer flow A, located on the outer side in an A-B-A configuration, is split into two. Thus, with a 50:50 phase ratio between phases A and B, the upper layer of A represents half of the A flow, as well as the

lower layer of A. This explains why the outer layers have a thickness less than the central layers. Moreover, the comparison between the measured average value and the theoretical value of the layers shows similar results, with the theoretical value (calculated from Equation 2.9) being 31.3 µm.
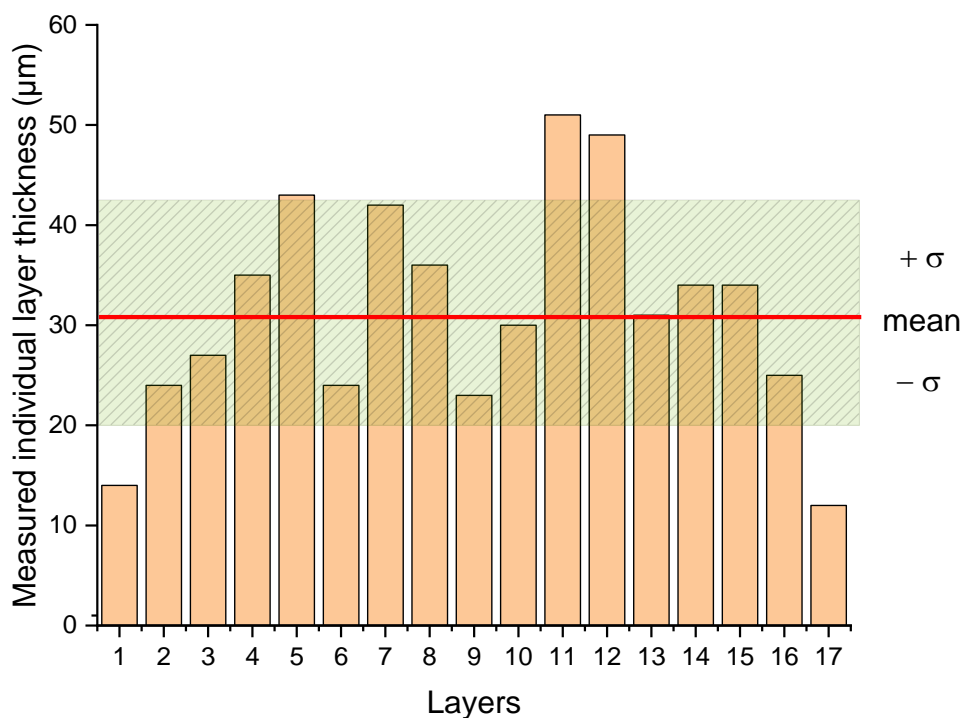
Figure 5-9 : Diagram gathering the measured individual layer thickness upon the layer position.

This suggests that the theoretical values are reliable compared to the average thicknesses of the processed films. The morphology of non-stretched films has also been characterized with higher numbers of layers, ranging from 512 to 1025 layers (**Figure 5-10**).
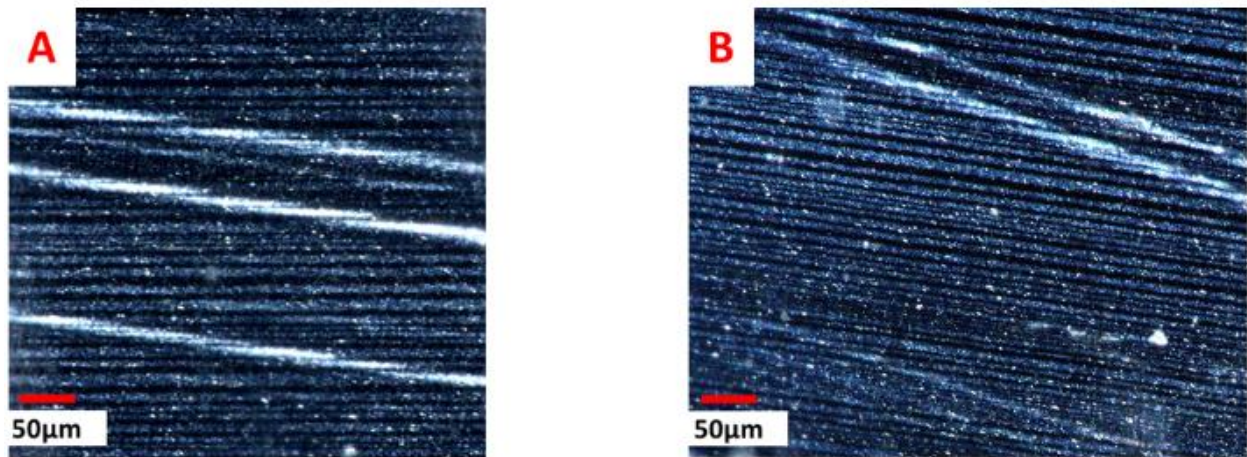
Figure 5-10 : Optical microscope observation in transmission mode under polarized light of films cross-sections. A) 512 Layer film B) 1025 Layers film (Rivollier et al., 2024).

In both **Figure 5-10a and b**, the presence of tilted white lines are knife traces from the sample preparation. In addition, as shown, an increase in the number of layers is observed, with the presence of well-defined layers. Therefore, we confirm that the increase in the number of multiplier elements effectively leads to an increase in the number of layers in our system.

5.2.1.2 Impact on the MMT orientation

The 002 MMT pole figures of 100µm thick films with 1, 17, 123, 512, and 1025 layers were measured, and the average intensities measured in ɸ for each χ value were plotted in **Figure 5-11** below.
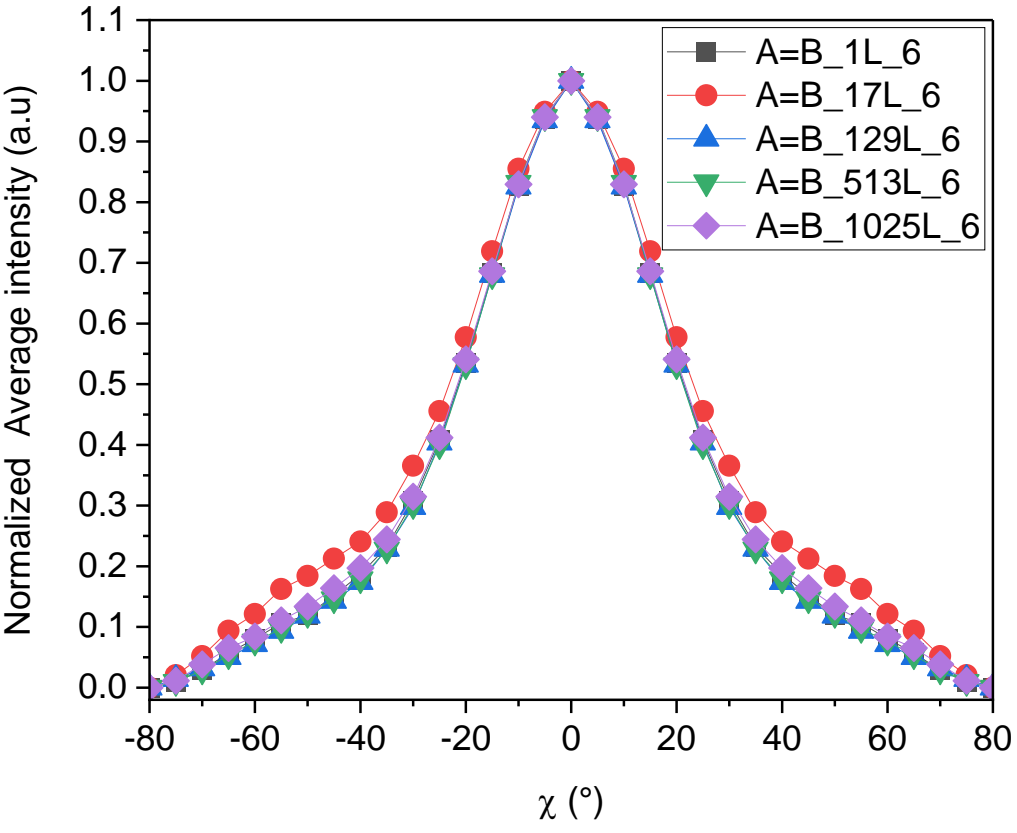
**Figure 5-11 : Average intensity over Φ versus χ from 002 MMT pole figures of each sample. Each film has an overall
thickness of 100 μm, while the number of layers in the film varies (Rivollier et al., 2024).**

It is observed that, regardless of the number of layers in the samples, the curves do all
overlap. This indicates a similar orientation of montmorillonite in all cases studied. This is
supported by the integral breadth (IB) values extracted from these curves and grouped in
Table 5-3 below (**Rivollier et al., 2024**).

Table 5-3 : Individual layer thickness calculated based on the number of layers in a 100µm thick film and calculated integral breadth of the curves in Figure 5-11 (Rivollier et al., 2024).

SAMPLE	CALCULATED INDIVIDUAL THICKNESS	INTEGRAL BREADTH (°)
1L_5	100 µm	52 ± 1
A=B_17L_6	6 µm	58 ± 2
A=B_129L_6	775 nm	51 ± 1
A=B_513L_6	195 nm	52 ± 1
A=B_1025L_6	98 nm	53 ± 1

Indeed, except for the 17 layers sample, no variation in the integral breadth value is observed with the increase in the number of layers in the films (**Table 5-3**). These observations are surprising as we transition from a theoretical layer thickness of 100 µm to 98 nm, and yet, no change in the orientation of montmorillonite is observed (**Rivollier et al., 2024**). At this stage, several hypotheses can be considered. The first is that the layer thickness is not reduced enough to reach nano-sheet sizes, which can be several nanometers when stacked. Previous studies in confinement-induced crystallization via the MNL process have shown that this phenomenon occurs at layer thicknesses of around 30 – 40nm, specifically close to the size of polymer chain dimensions (**Carr et al., 2012**). Furthermore, as shown by **Figure 4-8**, montmorillonite nano-sheets exhibit high flexibility, posing a challenge for achieving orientation without reducing layer thickness (**Rivollier et al., 2024**).

Therefore, in the case of a film thickness of 100 µm, increasing the number of layers does not appear to be a sufficient measure to improve the orientation of montmorillonite. It is possible that the current layer thickness is still too large to promote a significant enhancement in orientation (**Rivollier et al., 2024**).

5.2.2 Influence of the layers architectures

Since the number of layers appears to have no impact on the orientation of MMT fillers, we decided to evaluate whether the influence of the film architecture have an impact

on the orientation. Hence, we compared the orientation of montmorillonite in a film containing 1025 layers with a film having an A = B architecture, where all layers contain MMT; and another having an A ≠ B architecture, where layer B contain MMT while layer A does not.

As shown in **Figure 5-12**, the average intensities measured in ɸ for each χ value, reveal a variation in the orientation of MMT depending on the architecture.
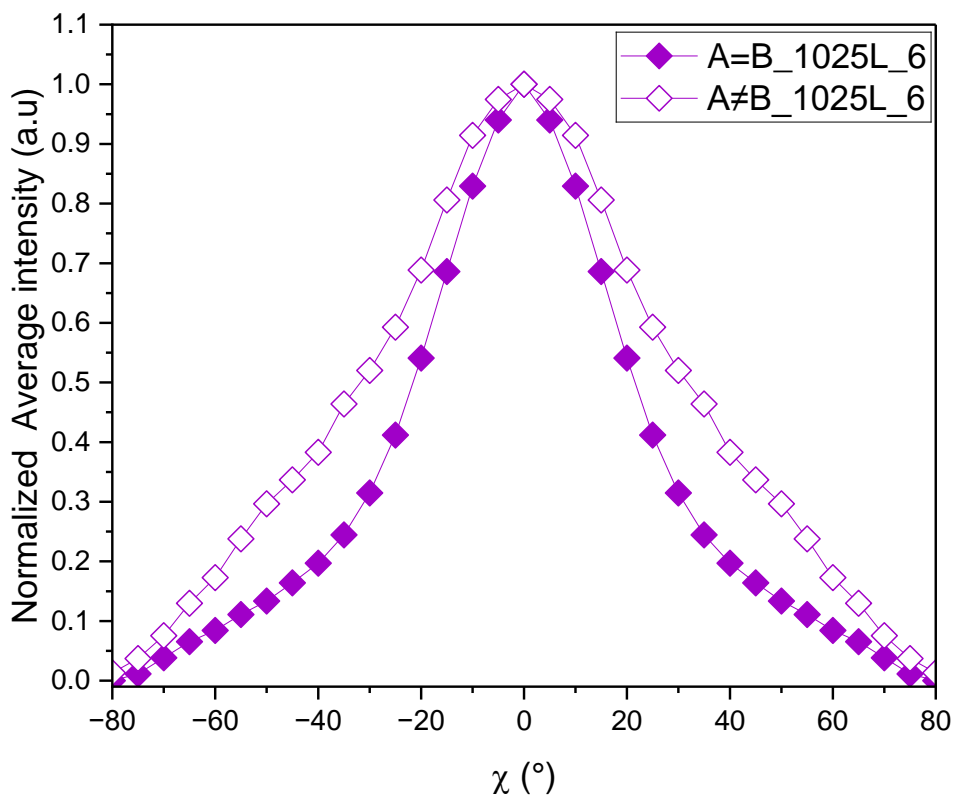
Figure 5-12 : Average intensity over Φ versus χ from 002 MMT pole figures of 1025 layers film with an A=B and A≠B architectures.

For an A ≠ B configuration, the diffraction intensity round χ = 0° is considerably broader than in the case where A is equal to B. This suggests a less pronounced in-plane orientation for the A ≠ B architecture. This observation is supported by the integral breadth values extracted from these curves and presented in **Table 5-4**.

Table 5-4 : Calculated integral breadth of curves in Figure 5-12.

SAMPLE	CALCULATED INDIVIDUAL THICKNESS	INTEGRAL BREADTH (°)
A≠B_1025L_6	98 nm	72 ± 3
A=B_1025L_6	98 nm	53 ± 1

The A ≠ B sample presents an integral breadth of 72° ± 3°, whereas the A = B sample has an integral breadth of 53°± 1°. An entropy-related hypothesis can be proposed to explain these variations. It is possible that the differences in orientation are linked to the fact that layers containing MMT in the A ≠ B sample are surrounded only by polymer without fillers, leading to greater entropy favoring potential filler disorientation. Indeed, **Decker et al., 2015** showed that in a multilayer system composed of LDPE/LDPE-g-MA + MMT, MMT fillers tend to migrate towards the interface with the layer devoid of MMT fillers. This highlights the mobility of fillers in such a configuration. This phenomenon of charge migration at interfaces is also observed in other materials and with different fillers (**Dai et al., 2019**; **Shi et al., 2023**). In contrast, in the scenario where A = B, the presence of fillers in each layer could promote a more homogeneous orientation of charges among them. Particle-particle interactions, as mentioned in the previous section, could also contribute to this orientation.

5.2.3 Influence of stretching

To significantly reduce the thickness of individual layers, another approach involves applying uniaxial stretching in the molten state during film manufacturing. This operation is performed by adjusting the rotation speed of the chill-roll positioned immediately after the die through which the molten polymer is extruded as a film. This stretching process causes a reduction in the total thickness of the film (**Hyvärinen et al., 2020**), thereby leading to a shrinkage in the thickness of individual layers (**Jin et al., 2004; Zhang et al., 2014**).

As mentioned in the section on the impact of the number of layers, the influences of MNL on crystal orientation become noticeable with a decrease in layer thickness of approximately 30 to 40 nm (**Carr et al., 2012**). To establish the possibility of a similar effect for

the MMT incorporated into the polymer matrix by reaching these individual layer thicknesses, we produced films composed of 1025 layers. These films were subjected to stretching at different speeds, resulting in various stretch ratios (DR) and a theoretical reduction in the individual layer thickness down to 29 nm (**Table 5-5**). We also compared the effect of A = B and A ≠ B architectures.

The average intensities measured in ɸ for each χ value extracted from the pole figures for each architecture are grouped in **Figure 5-13** and **Figure 5-14** below.
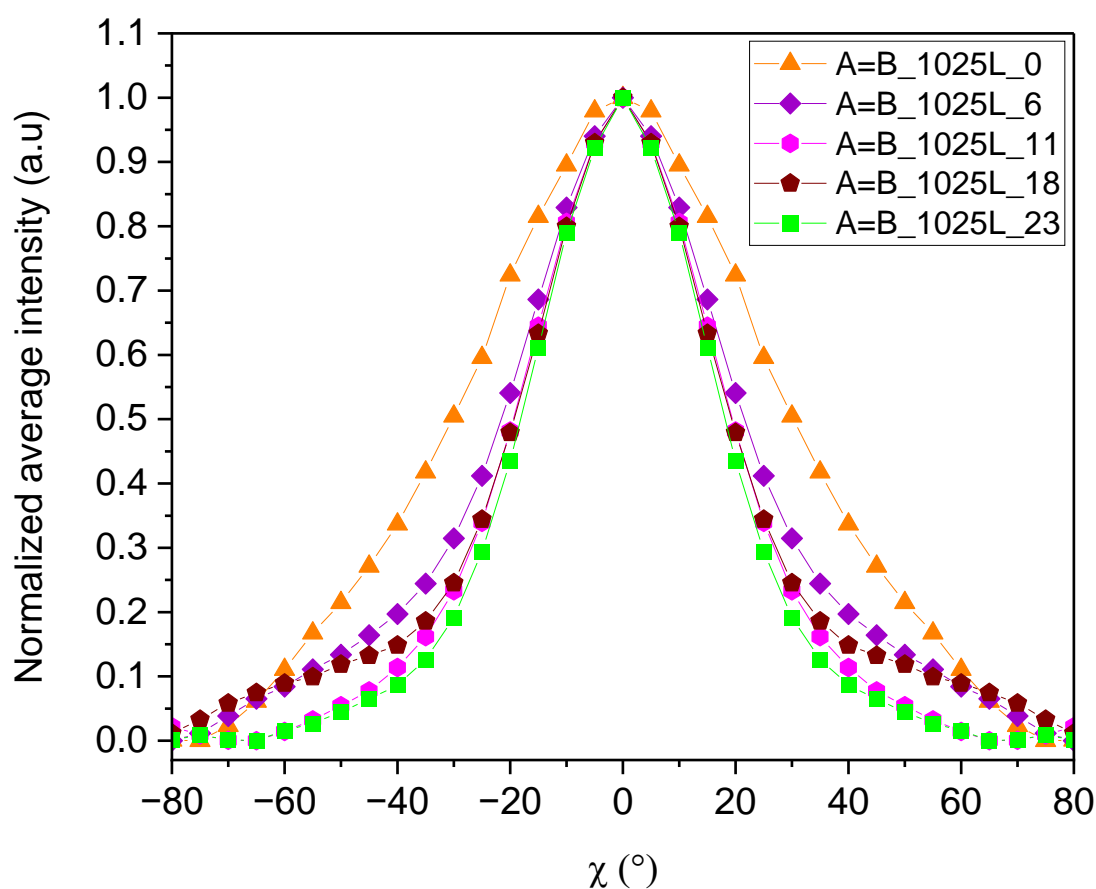
Figure 5-13 : Average intensity over Φ versus χ from 002 MMT pole figures of 1025 layers film with an A=B architecture for different draw ratios ranging from 0 to 23 (Rivollier et al., 2024).
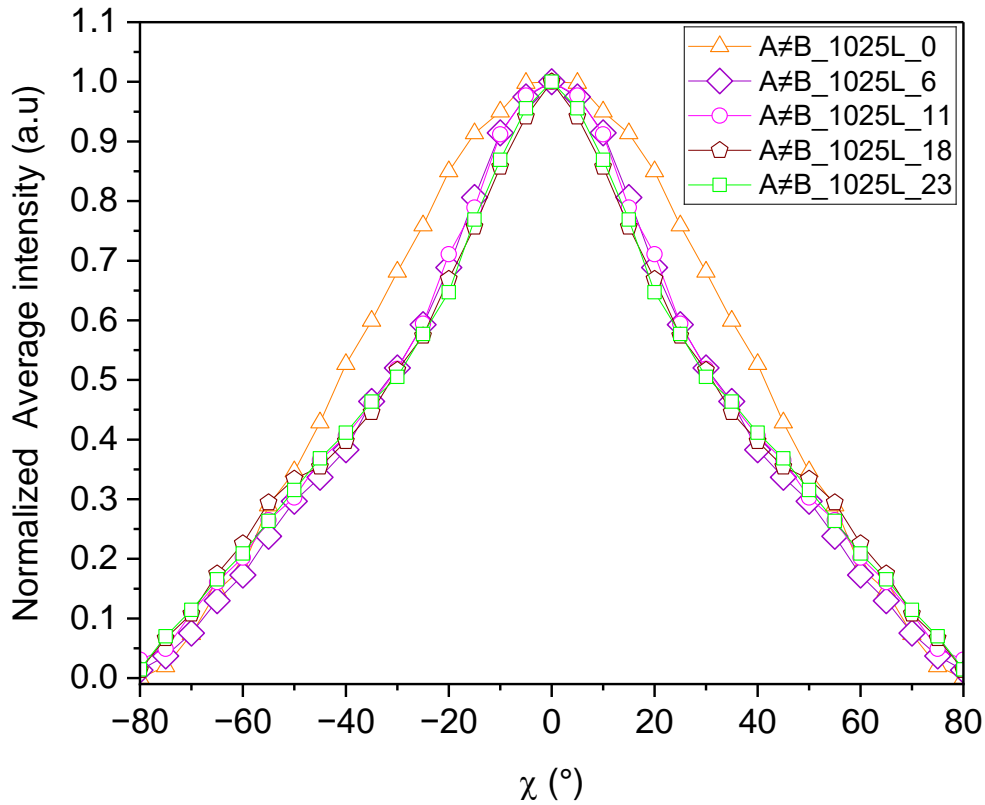
Figure 5-14 : Average intensity over Φ versus χ from 002 MMT pole figures of 1025 layers film with an A≠B architecture for different draw ratios ranging from 0 to 23.

In the case of both architectures, a similar behavior of MMT orientation in response to applied stretching during film processing is observed. Indeed, in both cases, there is an improvement in orientation between the non-stretched and stretched samples. However, at first glance, the increase in draw ratios does not seem to influence a lot the orientation (**Rivollier et al., 2024**).

CHAPTER 5: ORIENTATION OF THE MONTMORILLONITE THROUGH THE PROCESS: FROM MONOLAYER TO MULTI-NANO LAYER SYSTEM

The integral breadth values extracted from **Figure 5-13** and **Figure 5-14** are grouped in **Table 5-5** below.

Table 5-5 : Individual layer thickness calculated based on the film overall thickness in 1025 layers film, for A=B and A≠B architectures. Calculated integral breadth of curves in Figure 5-13 and Figure 5-14.

SAMPLE	DRAW RATIO (DR)	CALCULATED INDIVIDUAL THICKNESS (nm)	INTEGRAL BREADTH (°)
A=B_1025L_0	0	780	70 ± 2
A≠B_1025L_0			83 ± 3
A=B_1025L_6	6	98	53 ± 1
A≠B_1025L_6			72 ± 3
A=B_1025L_11	11	58	46 ± 1
A≠B_1025L_11			74 ± 3
A=B_1025L_18	18	39	50 ± 1
A≠B_1025L_18			73 ± 3
A=B_1025L_23	23	29	42 ± 0.5
A≠B_1025L_23			72 ± 3

The integral breadth values confirm the observations from the curves in **Figure 5-13** and **Figure 5-14**. When the draw ratio (DR) is greater than 0, a reduction in the value is observed, decreasing from 83° ± 3° to approximately 72° ± 3° for the A ≠ B architecture and from 70° ± 2° to around 40-50° ± 1° for the A = B architecture. Thus, for both architectures, a similar variation is observed with the draw ratio increase. However, in the case of the A=B architecture the 'in-plane' orientation of the MMT is better. Indeed, the entropic effect of the non-filled layer is again noted in the case of the A ≠ B architecture, at the expense of improving the orientation of montmorillonite.

Finally, in the case of the A = B configuration, the best improvement is observed with a DR of 23 and a theoretical layer thickness of 30 nm which achieved an integral breadth of 42° ± 0.5° (**Rivollier et al., 2024**).

Several mechanisms can be involved to explain the improvement in this orientation. Firstly, the small layer thickness may favor a confinement and thereby the orientation of montmorillonite, as orientation effects are observed for layer thickness values in the range of a few nanometers (**Carr et al., 2012; Wang et al., 2009; Rivollier et al., 2024**). Moreover, taking into account the finding that the most notable enhancement in MMT filler orientation arises simply from material stretching or deformation, a plausible hypothesis can be proposed. By stretching the molten material, we induced a deformation that promotes the elongation and unfolding of polymer chains, leading to the formation of more oriented morphology (**Keller & Kolnaar., 2006**; **Haudin., 2013**). By increasing the applied draw ratio on the films, we rapidly solidified these oriented morphologies, leaving them less time to relax, which can increase the confinement applied to MMT fillers and promote their orientation (**Rivollier et al., 2024**). To verify the theory of cooling, we performed thermal measurements during the cooling and drawing phases. This provided an overview of the temperature profile and its evolution. **Figure 5-15** below shows the resulting IR images. The color of the films on the chill-roll changes from green to blue as the DR increases. Green indicates temperatures below 100°C and blue indicates temperatures below 60°C. Thus, the higher the DR, the faster the films cool.
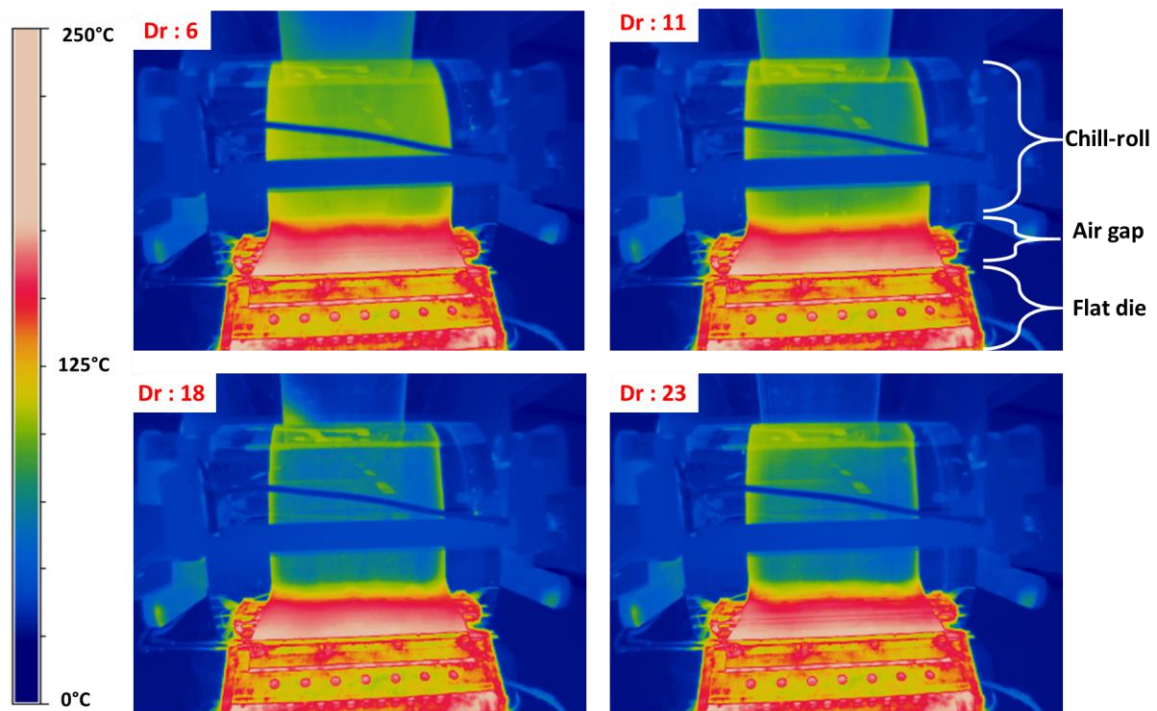
Figure 5-15 : IR images of the films during the stretching step on the chill-roll at DR of 6, 11, 18 and 23.

5.3   CONCLUSIONS AND CORRELATION WITH THE BARRIER PROPERTIES

In this section, we will establish a relationship between the integral breadth values and the water vapor barrier properties measured on the samples. Our goal is to understand how various parameters influence the water vapor barrier properties of the films. Finally, we will draw a conclusion on the synergy of all these parameters concerning nano-filler orientation and barrier properties.

5.3.1 Correlation of the orientations to the water barrier properties

The objective here is to correlate the integral breadth values obtained previously with the water permeability values of the samples. As a reminder, permeability corresponds to the ratio of the measured WVTR flux plateau value to the thickness of the sample. Thus, permeability values are representative of the intrinsic properties of the samples and allows the comparison of samples with different thicknesses.

5.3.1.1 The effect of the MMT concentration

H_2O permeability measurements were conducted on a monolayer film without MMT filler, as well as on monolayer films containing 5 and 20wt% of MMT manufactured by cast extrusion. The MMT free sample and the one with 5wt% MMT have a thickness of 100µm, while the sample with 20wt% MMT has a thickness of 200µm. The results are presented in **Figure 5-16** and **Table 5-6** below:
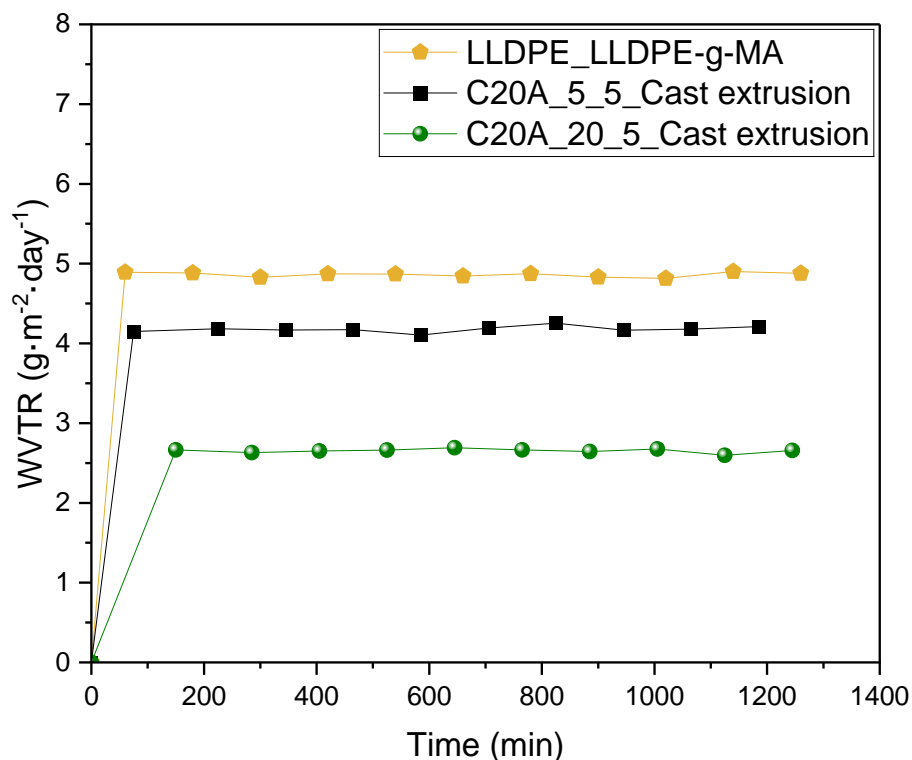
Figure 5-16 : Water vapor transmission rate upon the time, samples with a variation of MMT concentration.

Table 5-6 : Water permeability values extracted from measurements in Figure 5-16.

SAMPLE	MMT CONCENTRATION (wt%)	INTEGRAL BREADTH (°)	H_2O PERMEABILITY ($g \cdot cm \cdot m^{-2} \cdot day^{-1}$)
LLDPE_LLDPE-g-MA	0	/	$4.91 \cdot 10^{-2}$
C20A_5_5_Cast extrusion	5	52 ± 1	$4.89 \cdot 10^{-2}$
C20A_20_5_Cast extrusion	20	45 ± 0.5	$4.28 \cdot 10^{-2}$

It is noticeable that adding 5wt% of MMT only reduces water permeability by 0.4%, while adding 20wt% of fillers results in a 13% decrease in permeability. These results may seem surprising, as in the case of adding montmorillonite to PE, previous studies such as

172

Bumbudsanpharoke et al., 2017, who showed a relative decrease in permeability of 16% with the addition of 5wt% of MMT in LDPE, and a reduction of 26% with 10wt%, respectively. In our case, the concentration effect was observed but not as noticeable as the previous works (**Bumbudsanpharoke et al., 2017)**. While variations in permeability are observed due to differences in measured orientation, the permeability values obtained remain far from the target value of $1 \cdot 10^{-5}$ g·m^{-2}·day^{-1}.

5.3.1.2 The effect of the number of layers

Water permeability measurements were conducted on multi-nano-layer films with 5wt% of MMT, and with a number of layers varying from 1 to 1025 and a thickness of 100µm. The results are presented in **Figure 5-17** and **Table 5-7** below:
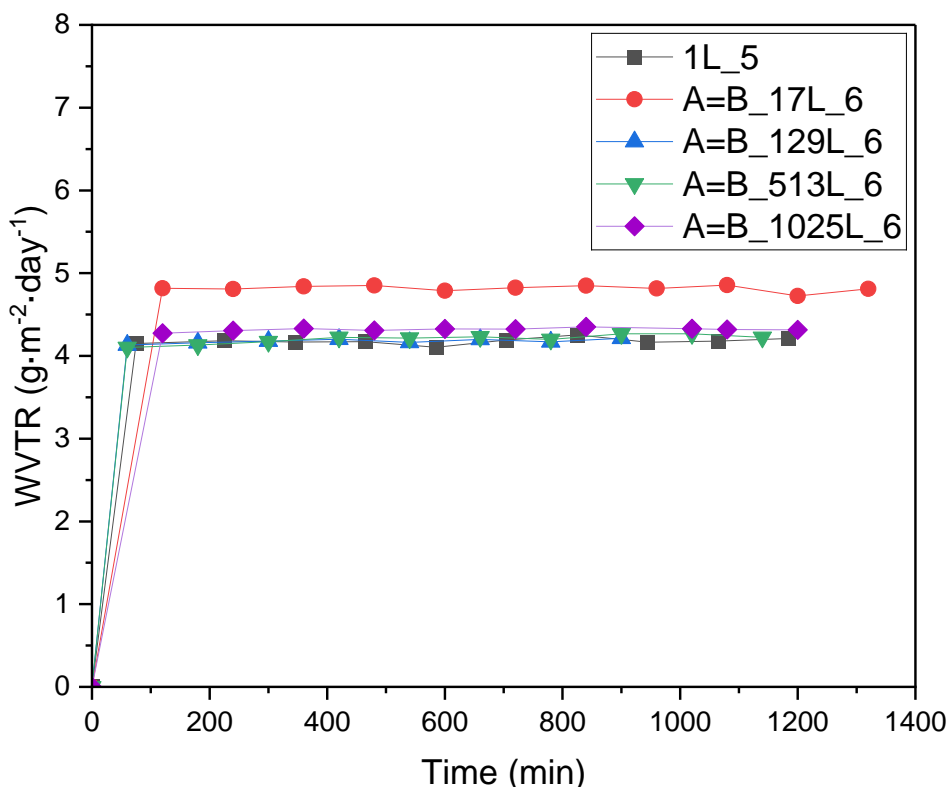
Figure 5-17 : Water vapor transmission rate upon the time, samples with a variation of the number of layers in a 100µm thick film.

Table 5-7 : Water permeability and diffusion coefficient values extracted from measurements in Figure 5-17.

SAMPLE	NUMBER OF LAYERS	INTEGRAL BREADTH (°)	H$_2$O PERMEABILITY (g·cm·m^{-2}·day^{-1})
1L_5	1	52 ± 1	4.89·10^{-2}
A=B_17L_6	17	58 ± 2	4.94·10^{-2}
A=B_129L_6	129	51 ± 1	4.10·10^{-2}
A=B_513L_6	513	52 ± 1	4.20·10^{-2}
A=B_1025L_6	1025	53 ± 1	4.33·10^{-2}

Regarding the increase in the number of layers in a film containing 5wt% of MMT, it is observed that the best reduction in permeability is approximately 16% compared to a monolayer film and also compared to a monolayer film without fillers. This result is observed for a film with 129 layers. It is interesting to note that the change in permeability does not necessarily seem to be related to the orientation of the montmorillonite, except for the film with 17 layers, which has a higher integral breadth value than the other films and has a permeability value higher than the others. However, it is important to consider that variations in permeability remain relatively minor and may fall within the margin of error of the machine. Finally, looking at the diffusion coefficient, an increase of 24% is observed with 129 and 513 layers compared to the single-layer film. There is a decrease of 23% and 37% for samples with 17 and 1025 layers, respectively. As the variations are relatively random depending on the number of layers in the samples, it is challenging to make hypotheses about the impact of the number of layers on water vapor diffusion in the samples.

5.3.1.3 The effect of the architecture

Permeability measurements for water vapor were conducted on 100μm thick multi-nano layer films with 1025 layers, one with an A≠B architecture and the other with an A=B architecture. The results are presented in **Figure 5-18** and **Table 5-8** below:
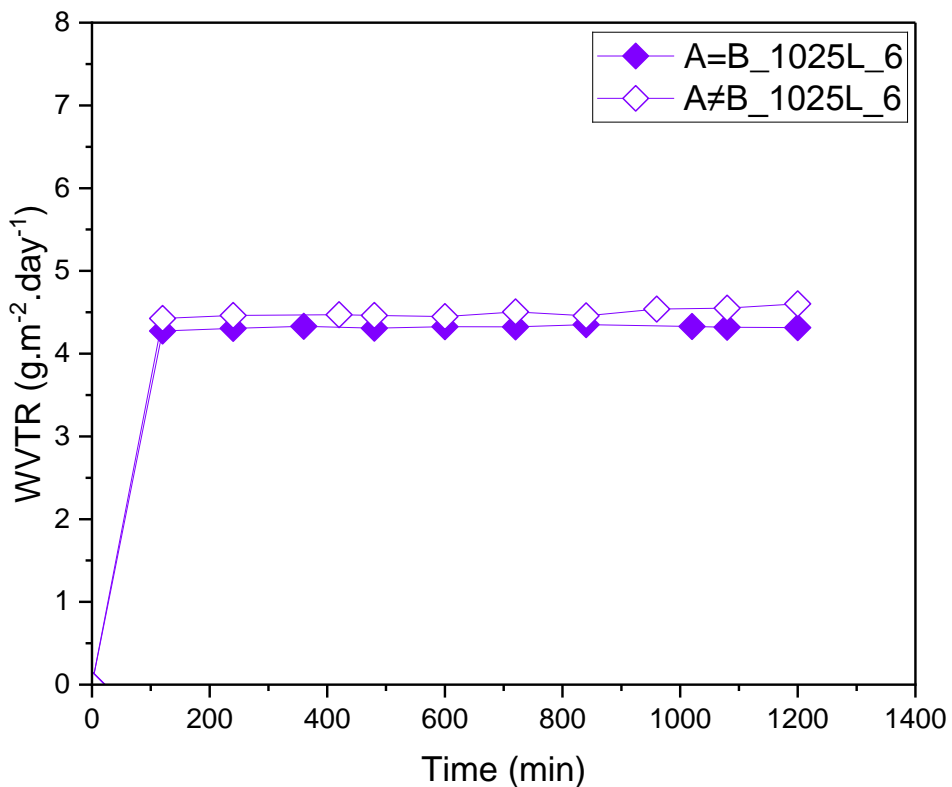
Figure 5-18 : Water vapor transmission rate upon the time, samples with 1025 layers, variation of the film architecture: A=B and A≠B.

Table 5-8 : Water permeability values extracted from measurements in Figure 5-18.

SAMPLE	NUMBER OF LAYERS	INTEGRAL BREADTH (°)	H_2O PERMEABILITY $(g \cdot cm \cdot m^{-2} \cdot day^{-1})$
A=B_1025L_6	1025	53 ± 1	$4.33 \cdot 10^{-2}$
A≠B_1025L_6	1025	72 ± 3	$4.91 \cdot 10^{-2}$

It can be observed that in the case of the A≠B architecture, the integral breadth is significantly higher than that of the A=B architecture. This is correlated with the permeability values, showing a 13% increase in permeability in the A≠B configuration compared to the A=B configuration. However, the A=B architecture sample contains twice as much MMT as the A≠B sample, which may also impact permeability. It is thus challenging to differentiate the impact of two factors, namely the improved orientation of the MMT and the higher concentration, on this enhancement.

5.3.1.4 The effect of stretching

Permeability measurements for films with 1025 multi-nano layers containing 5wt% MMT and subjected to various degrees of draw ratio at the melted state have been conducted. The films present different thicknesses from 100µm for the A=B_1025L_6 sample to 30µm for the A=B_10025L_23, with intermediates thickness of 60 and 40µm for the samples A=B_1025L_11 and 18. The results are presented in **Figure 5-19** and **Table 5-9** below:
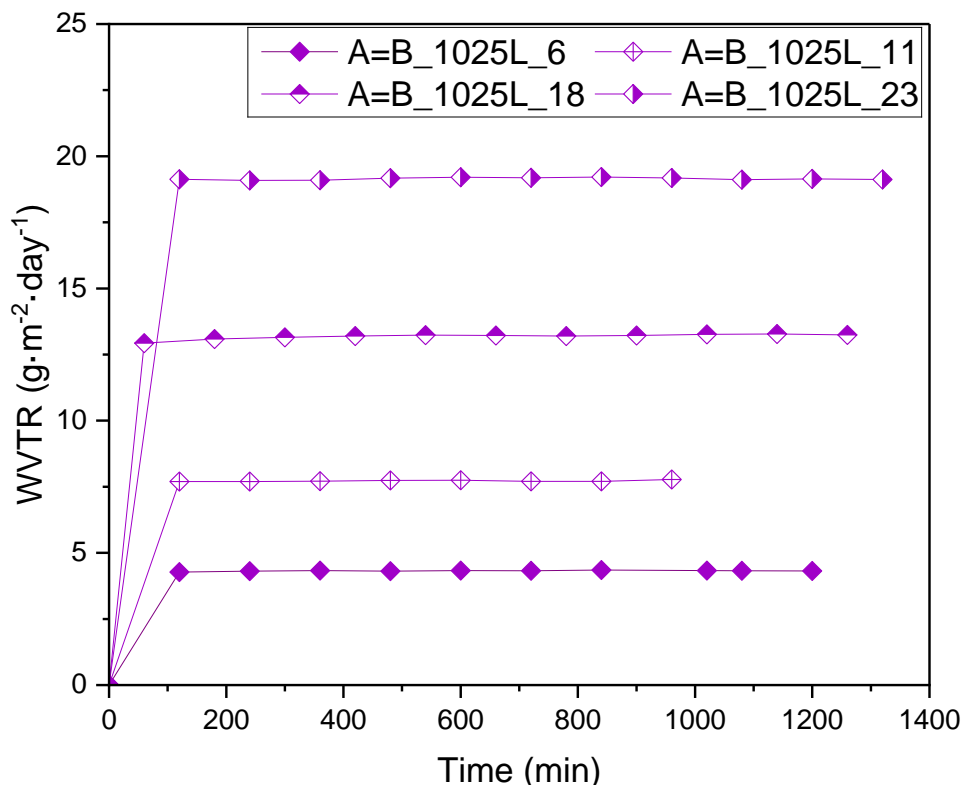
Figure 5-19 : Water vapor transmission rate upon the time, samples with 1025 layers and a variation of the draw ratio.

Table 5-9 : Water permeability values extracted from measurements in Figure 5-19.

SAMPLE	DRAW RATIO	INTEGRAL BREADTH (°)	H_2O PERMEABILITY $(g \cdot cm \cdot m^{-2} \cdot day^{-1})$
A=B_1025L_6	6	53 ± 1	$4.33 \cdot 10^{-2}$
A=B_1025L_11	11	46 ± 1	$4.66 \cdot 10^{-2}$
A=B_1025L_18	18	50 ± 1	$5.59 \cdot 10^{-2}$
A=B_1025L_23	23	42 ± 0.5	$5.97 \cdot 10^{-2}$

There is an improvement in the orientation of the MMT nano-fillers. However, surprisingly, the integral breadth parameter does not show a clear correlation with permeability variations. While a permeability decrease was expected due to the MMT orientation improvement. As the orientation of the fillers increases, water permeability also

increases. A 38% progression is noted between the reference film with a draw ratio of 6 and the film subjected to a draw ratio of 23, while the integral breadth decreases from 53° ± 1° to 42° ± 0.5°, respectively.

In light of these observations, one could hypothesize that the orientation of MMT is not the sole parameter influencing the water permeability of our films. Despite the improvement in the orientation of MMT, permeability seems to be altered, as clearly evidenced by the effect of the stretching ratio. This raises questions about the role of the polymer matrix. Indeed, during stretching, it is known that LLDPE may tend to deform and orient preferentially in certain directions of the film. **Zhang et al., 2014** demonstrated that, in the case of HDPE in MNL configuration, the orientation of LLDPE crystals influences oxygen barrier properties. A 50% reduction is observed when the crystals are in confined spherulites. However, when the crystals are in 'on-edge' lamellar form oriented, there is no improvement in barrier properties.

5.3.2 Conclusions about the factors affecting the orientation of the MMT

In this section we summarized the parameters that influence the orientation of MMT during the multi-nano layer co-extrusion process, as well as their impact on barrier properties. This summary is described in **Table 5-10**.

Table 5-10 : Regroupment of all the parameters improving or not the MMT orientation and water barrier properties.

(+++): Very good improvement; (++): Good improvement; (+): improvement; (-): no improvement.

PARAMETER	MMT ORIENTATION	H_2O BARRIER PROPERTIES
MMT Concentration	The increase of MMT concentration improves the 'in-plane' orientation (+++)	-13% H_2O permeability at the maximum. (+)
Manufacturing process	The presence of shear forces improves the 'in-plane' orientation (+)	Not investigated.
Number of layers	Does not improve the 'in-plane' orientation. (-)	-16% H_2O permeability at the maximum. (+)
Film architecture	The presence of MMT in all the layers gives a better 'in-plane' orientation. (++)	-13% H_2O permeability with MMT in all the layers. (+)
Film drawing	The increase of the stretching slightly improves the 'in-plane' orientation (+)	+ 38% H_2O permeability at the maximum DR. (-)

At the end of this investigation, it is surprising to note that it is not the multi-nano-layer architecture that provides the highest level of orientation for montmorillonite. In reality, factors such as the concentration of fillers, particle-particle interactions, and shear applied during the process primarily induce better in-plane orientation of MMT. Although effects on barrier properties have been observed, the improvements remain very modest, not exceeding 16% at most. This raises questions about the real significance of these variations. In some cases, these variations are correlated with changes in integral breadth, while in others, they are not, suggesting that the orientation of MMT may not be the only parameter influencing water permeability in our samples. The crystallization process of LLDPE can impact both orientation and barrier properties. Therefore, in the next chapter, we will examine the crystallization of LLDPE, how it crystallizes in our systems, and whether this can be correlated with the observed permeability variations.

6. CHAPTER 6: CRYSTALLIZATION OF THE LINEAR LOW-DENSITY POLY(ETHYLENE) IN MONOLAYER AND MULTI-NANO LAYER SYSTEMS IN PRESENCE OF MONTMORILLONITE

INTRODUCTION

As demonstrated in the previous chapter, none of the configurations used in the production of multi-nano-layer films succeeded in effectively orienting the MMT nano-fillers more than the simple cast extrusion. Although a slight improvement was observed by applying a high draw ratio to a film with 1025 layers, the variations in barrier properties do not consistently match the measured orientation of the fillers after the films have been drawn. Indeed, the 'in-plane' orientation of the MMT nano-fillers was improved, but the permeability of the films was not improved, in fact, it increased by 38%. This raises several questions: does the way LLDPE crystallize influence the orientation of MMT nano-sheets? Is the loss of barrier properties been influenced due to a particular crystallization of LLDPE, when fillers are better oriented? Given that LLDPE tends to crystallize under shear (**Haudin., 2015a**), it is possible that the crystallization of LLDPE changed during the film manufacturing process. Therefore, this chapter will focus on the crystallization of LLDPE in samples studied in the previous chapter. The effect of MMT concentration, sample architecture, and stretching on crystallization will be examined and a correlation between the morphologies and the final barrier properties obtained will be established. All the crystallization models of the LLDPE mentioned in the chapter are detailed in the appendix (**A.2 LLDPRE CRYSTALLIZATION MODELS – CHAPTER 6)** to help the understanding.

6.1   IMPACT OF THE PRESENCE OF THE MMT IN A MONOLAYER SYSTEM

Initially, we focused on the influence of the incorporation of MMT fillers in a monolayer film produced by cast extrusion process. Previous research has reported that the addition of fillers to the polymer melt stream leads to an increase in the local shear rate, thus promoting the flow of the polymer melt (**Jain et al., 2023**). Furthermore, as demonstrated in the previous chapter, MMT charges exhibit improved 'in-plane' orientation when exposed to flow compared to compression molding.

6.1.1 XRD texture analysis of linear low-density poly(ethylene) monolayers

Texture analyses on monolayer films made by cast extrusion with 0wt%, 5wt% and 20wt% MMT (under references 1L_0, 1L_5 and 1L_20) were performed by XRD and plotted in pole figures (**Figure 6-1**). These films have a thickness of 100µm, which corresponds to a draw ratio of 6. As a reminder, texture analysis was only performed on the 110, 200 and 020 Bragg peaks of LLDPE. As mentioned in **Chapter 3**, the 002 Bragg peak is not identifiable in the case of LLDPE, so there is no 002 pole figure. Finally, the samples were oriented to obtain the transverse direction (TD) of the film and the extrusion direction (ED) of the film always at the same positions on the pole figure.

The pole figures of the (110), (200), and (020) lattice planes for the MMT-free film (1L_0) (**Figure 6-1**) exhibit diffraction intensity predominantly localized at angles χ > 75° and across all ϕ values ranging from 0 to 360°. This indicates that the crystallographic $\vec{a}$ and $\vec{b}$ axes of the unit cell of LLDPE are oriented in a plane perpendicular to the film normal but randomly relative to the extrusion direction and transverse to the extrusion direction. According to the work of **Desper., 1969**, one can qualify this structure this as a fiber texture along the normal of the film.
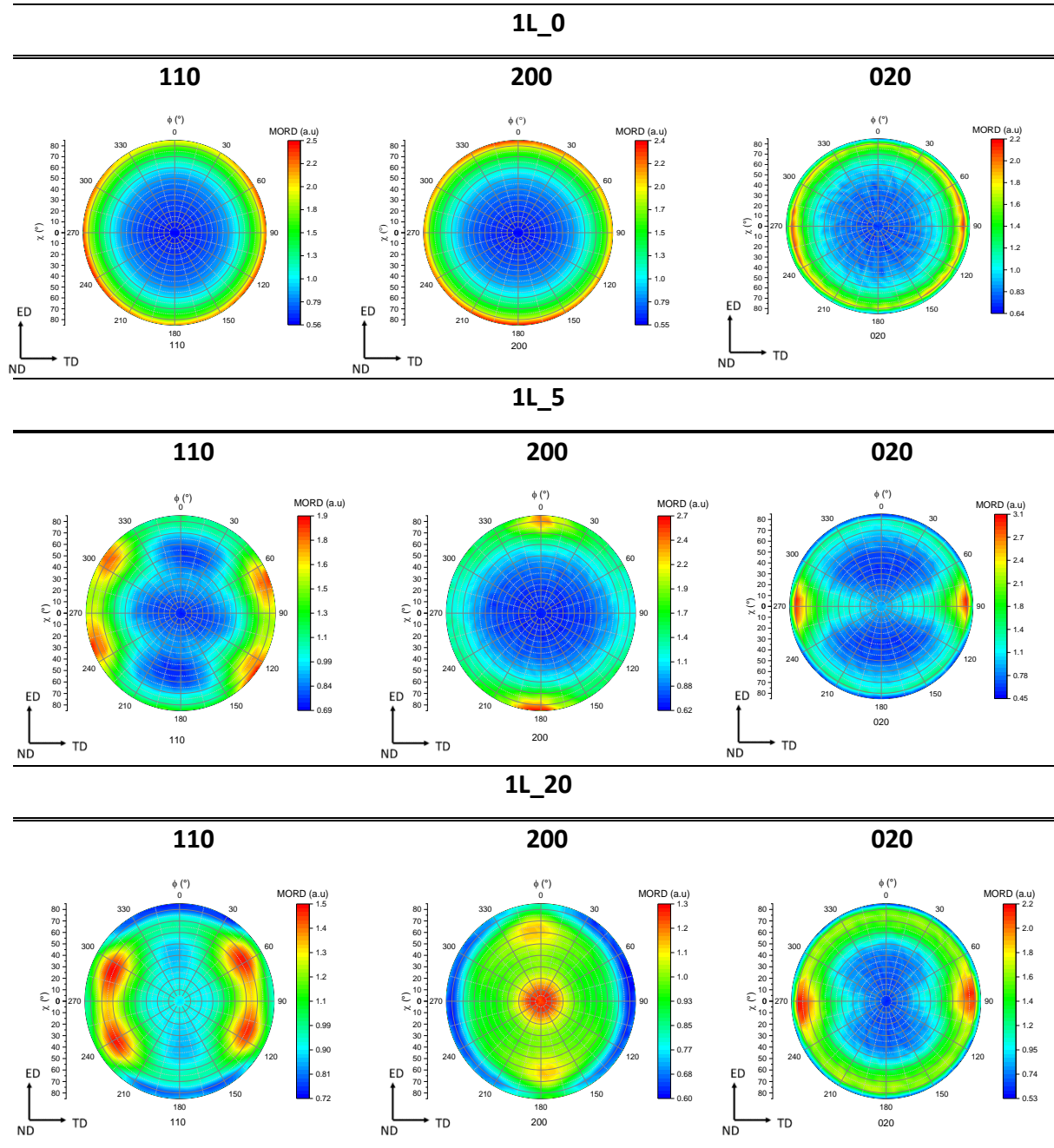
Figure 6-1: Pole figures of the LLDPE (110), (200) and (020) lattice planes of monolayer samples with different concentrations of MMT (0, 5 and 20wt%).

Nevertheless, when 5wt% of MMT (1L_5) is added (**Figure 6-1**), we observe that the maximum diffraction intensity on the pole figure of the (200) lattice plane is localized in the extrusion direction. Meanwhile, the diffraction intensity for the (020) lattice plane is localized more in the transverse direction of the film. In relation to the orientation of the (110) lattice plane, four symmetric diffraction poles are detected within the ED-TD plane. These poles are positioned roughly at ± 33° in φ relative to TD and ± 57° in φ relative to ED. This indicates that

the crystallographic $\vec{a}$ and $\vec{b}$ axes are located in a plane perpendicular to the normal of the film. However, the crystallographic $\vec{a}$ axis shows a tendency to preferentially orient in the ED direction, while the crystallographic $\vec{b}$ axis follows the TD direction. These observations may be indicative of early stages of the Keller-Machin crystallization models detailed in the appendix **Figure A-2-1** (**Keller & Machin., 1967**) (to be discussed in more details later in this chapter).

Furthermore, with the addition of 20wt% MMT (1L_20) (**Figure 6-1**), a textured morphology is still observed in LLDPE compared to a film without MMT. However, the texture observed is slightly different from those observed at 5wt% MMT. Specifically, on the 200 pole figure, the maximum diffraction is centered on the pole, with some signal still diffracting in the ED direction of the sample. The orientation of the (020) lattice plane remains similar to that of the 5wt% sample. Finally, the diffraction poles of the (110) lattice plane are located at an angle χ of about 70° and at ± 30° in ϕ relative to TD and ± 60° in ϕ with respect to ED. At first glance, it appears that the crystallographic $\vec{a}$ axis is predominantly oriented in the direction of the film normal, while the crystallographic $\vec{b}$ axis remains oriented relative to the TD. These observations suggest either a change in the orientation of the crystalline lamellae compared to a film containing 5wt% fillers or a Keller-Machin I model with the presence of twisted lamellae and random orientation of the crystallographic $\vec{a}$ axis in the ND-TD plane (**Keller & Machin., 1967; Nagasawa et al., 1973**) (**Figure A-2-1**).

In order to reach a conclusive assessment of the observed morphologies, it is essential to quantify the identified to obtained orientations of the crystallographic $\vec{a}$, $\vec{b}$, and $\vec{c}$ axes. This can be done by extracting the orientation factors of the crystallographic $\vec{a}$, $\vec{b}$, and $\vec{c}$ axes relative to the ED, TD, and ND directions from the pole figures, as explained in the experimental part.

It is important to note that the presence of 2D nano-fillers promotes a preferential orientation of LLDPE. According to studies conducted by **Wang et al., 2005** and **Jain et al., 2013,** montmorillonite induces an increase in local shear on polymer chains, particularly in the case of intercalated morphologies. This increase leads to chain disentanglement, which

contributes to slow down their relaxation, allowing polymers to crystallize with a preferential orientation. This phenomenon was observed with the incorporation of only 1wt% of montmorillonite.

6.1.2 Quantification of the crystallinity

The objective of this study was to quantify the impact of MMT on the crystallization of LLDPE and determine whether it increases crystallinity in the samples or not.

The first heating cycle curves in DSC for films containing 0, 5, and 20wt% of MMT are plotted in **Figure 6-2** below. The first heating cycle is selected because it enables to get information about the direct effects of the film forming process.

Figure 6-2 : First heating DSC thermogram of the monolayer films containing 0, 5 and 20wt% of MMT. The positive value of the heat flow is for endothermic peaks.

When the film contains 5wt% of MMT, two melting peaks are observed, indicating the formation of two distinct lamellar populations. In fact, in the case of DOWLEX 2645 LLDPE it shows two melting peaks (**Cabrera., 2020**) and the first peak is associated to the crystallization of LLDPE short chains. Conversely, in the other two cases, only a single broad melting peak is formed. This suggests that both the filler content and the presence of nano-fillers influence the size and distribution of the lamellae. Furthermore, the incorporation of 20wt% of MMT results in a shift of the main melting temperature from 120°C to 118°C. The fusion enthalpy was derived from these curves to calculate the crystallinity percentage in the sample. Additionally, the melting temperature of the peaks was used to estimate the lamellar size with the **equation 3.8** detailed in the experimental chapter. All extracted information is summarized in **Table 6-1**.

Table 6-1 : Percentage of crystallinity (χ_c) and LLDPE lamellas size (l) determined from DSC thermogram from Figure 6-2

SAMPLE	OMMT concentration (wt%)	χ_c (%)	T_{f1} (°C)	T_{f2} (°C)	l_1 (nm)	l_2 (nm)
1L_0	0	27	/	120.16	/	10.26
1L_5	5	27	114.91	120.06	8.51	10.22
1L_20	20	19	/	118.41	/	9.61

The percentage of crystallinity remains constant between a film with 0 and 5wt% of MMT (**Table 6-1**). However, the addition of 20wt% of montmorillonite results in a decrease in this percentage, dropping from 27% to 19%. According to **Piorkowska., 2013**, an excessive presence of nano-fillers may reduce the crystallinity. Beyond a 5wt% nano-filler content, there may be a decrease in crystallinity, due to the presence of fillers that prevent the polymer chains to organize. Upon examining the calculated lamellar size in the samples, one can note that the addition of 5wt% of MMT generated two distinct populations of lamellae, measuring 8.51nm and 10.22nm, respectively. In contrast, the film without fillers contained a single population of lamellae with a size of 10.26nm. When 20wt% of montmorillonite was added, a single population of lamellae is present, with a slightly smaller size estimated at 9.61nm. The observation may be linked to decrease in crystallinity or steric hindrance caused by the fillers,

which affects the growth of LLDPE lamellae (**Piorkowska., 2013**). In literature, the size of LLDPE lamellae is typically between 10 and 12 nm (**Peacok., 2000**), but in the present case with 20wt% of MMT, the global lamellar size is reduced to 9.61 nm, which is below. This suggests that the presence of MMT can lead to shorter lamellae and reduced crystallinity.

6.1.3 Quantification of the crystallographic $\vec{a}$, $\vec{b}$ and $\vec{c}$ axes orientation

The presence of MMT fillers does not significantly affect the crystallinity of the films. However, it is suspected that the morphology of LLDPE crystallization is affected. Therefore, it is important to quantify the observed orientation in the films to determine the induced LLDPE crystallization mechanism by the presence of MMT.

Figure 6-1 presents pole figures where orientation factors were calculated to determine the positions of the crystallographic $\vec{a}$, $\vec{b}$ and $\vec{c}$ axes of the LLDPE crystal system relative to the reference axes of the film, ND, TD, and ED, respectively. The calculated $\cos^2_{j,i}$ for each direction 'i' (ND, TD, ED) and each crystallographic $\vec{j}$ axis ($\vec{a}$, $\vec{b}$, $\vec{c}$) are consolidated in **Table 6-2**. As a reminder, $\cos^2_{j,i}$ = 0 when the orientation of the crystallographic $\vec{j}$ axis is perpendicular to the direction 'i'; $\cos^2_{j,i}$ = 1/3 when the orientation of the crystallographic $\vec{j}$ is random along the 'i' direction, and $\cos^2_{j,i}$ = 1 when the orientation of the crystallographic $\vec{j}$ is parallel to the 'i' direction.

Table 6-2 : Orientation factors of monolayer films with different amount of MMT. Calculated from poles figures displayed in Figure 6-1.

SAMPLE	$\cos^2_a$			$\cos^2_b$			$\cos^2_c$		
	ED	TD	ND	ED	TD	ND	ED	TD	ND
1L_0	0.38	0.38	0.24	0.34	0.37	0.29	0.28	0.25	0.47
1L_5	0.41	0.32	0.27	0.30	0.40	0.30	0.29	0.28	0.43
1L_20	0.33	0.29	0.38	0.35	0.37	0.28	0.32	0.34	0.34

The values extracted from the sample were plotted on a Desper-Stein triangle to compare the positions of the crystallographic $\vec{a}$, $\vec{b}$ and $\vec{c}$ axes (**Figure 6-3**). X represents the ED of the sample, Y represents the TD, and Z represents the ND.

Figure 6-3 : Desper-Stein triangle of monolayer films with different amount of MMT, where the orientation factors of the crystallographic $\vec{a}$, $\vec{b}$ and $\vec{c}$ axes of LLDPE crystal system are displayed. Symbols: cross is for the crystallographic $\vec{a}$ axis, full is for the crystallographic $\vec{b}$ axis and empty is for the crystallographic $\vec{c}$ axis.

For the monolayer sample with 0wt% of MMT, the points corresponding to the crystallographic $\vec{a}$, $\vec{b}$ and $\vec{c}$ axes are primarily located along the Z-direction of the Desper-Stein triangle (**Figure 6-3**). The point corresponding to the crystallographic $\vec{c}$ axis tends towards orientation in the ND direction, while the points corresponding to the crystallographic $\vec{a}$ and $\vec{b}$ axes tend towards orientation perpendicular to the ND axis. These positions confirm the

hypothesis of a uniaxial orientation along the film normal (**Desper., 1969**). This orientation could also be associated with the presence of flattened spherulites (**Haudin., 2015b**).

Upon adding 5wt% of MMT, the crystallographic $\vec{c}$ axis point remains aligned with the Z-direction in the ND direction. However, the crystallographic $\vec{a}$ axis point shows a tendency to orient in the extrusion direction with a $\cos^2{}_{a,ED}$ value of 0.41. Meanwhile, the crystallographic $\vec{b}$ axis point indicates a transverse orientation to the extrusion with a $\cos^2{}_{b,TD}$ value of 0.40. These measurements align with the orientations obtained from the pole figure. The well-defined crystallographic axes orientations in relation to the film's three directions suggest a crystallization model associated with thin film crystallization (**Adams et al., 1986**) and tend towards a KMII-type crystallization model as the positions of the crystallographic $\vec{a}$ and $\vec{c}$ axes are not identical (**Figure A-2-4** ; **Figure A-2-5**). If they had been, this would have been consistent with a mode of lamellar growth in the form of twists (**Nagasawa et al., 1973**). Furthermore, it appears that the lamellar orientation is not 'edge-on' with a crystallographic $\vec{c}$ axis orientation in the extrusion direction. Instead, it is 'in-plane' with the chain crystallographic $\vec{c}$ axis oriented in the normal direction. However, determining the nature of the crystallization model conclusively is challenging since the cosine squared values of crystallographic $\vec{a}$, $\vec{b}$, and $\vec{c}$ axes relative to the corresponding ED, ND and TD directions are still far from 1.

The addition of 20wt% of MMT results in the crystallographic $\vec{a}$, $\vec{b}$, and $\vec{c}$ axes points being relatively close to the Z-direction. The crystallographic $\vec{c}$ axis orientation point is located at the isotropic orientation point (crossing point of X, Y, and Z axes). The crystallographic $\vec{a}$ axis orientation point tends to move slightly towards the ND direction with a $\cos^2{}_{a,ND}$ value of around 0.48, while the crystallographic $\vec{b}$ axis point tends to be perpendicular to the ND with a $\cos^2{}_{b,ND}$ value of 0.28. The results of the orientation factor are consistent with the pole figures shown in **Figure 6-1**. The 200 pole figure of the 1L_20 sample shows that most of the diffraction occurs along the ED-ND direction. Likewise, a diffraction circle is observed for all ϕ values beyond $\chi > 70°$ in the pole figure of the lattice plane (020), although a small part of the signal diffracts more along the ED. It is difficult to determine a specific orientation model in this case due to the predominant isotropic orientation of the crystallographic axes.

Thus, this section identifies that, under equivalent process conditions, the presence of MMT promotes a preferential orientation of LLDPE crystals along the three film axes: ND, ED, and TD. Without nano-fillers, LLDPE primarily crystallizes parallel to the film surface, but without any preferred orientation according to the ED or TD (**Figure 6-4a)**. The effect of fillers is similar to an increase in local shear rate experienced by the polymer chains, thus encouraging their crystallization within the flowing material. Based on our initial observations on monolayer films, it appears that LLDPE alone crystallizes in the form of flattened spherulites (**Figure 6-4a**). Meanwhile, in the presence of 5wt% of MMT, it tends to crystallize in the form of a thin film according to a KMII-type morphological model with an 'in-plane' lamellar orientation (**Figure 6-4b**).
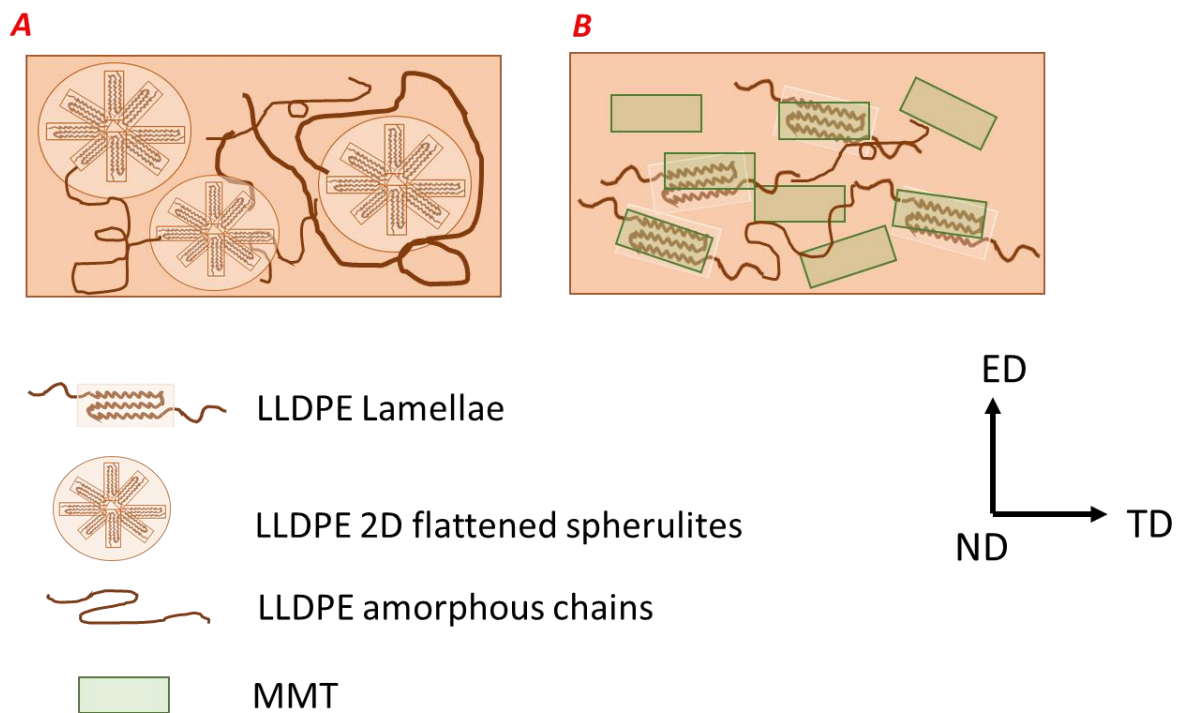
Figure 6-4 : Scheme of films top view to illustrate the crystallization morphologies of the LLDPE. A) Monolayer film without MMT, B) Monolayer film with 5wt% MMT.

6.2   IMPACT OF THE ARCHITECTURE

After studying the influence of nano-fillers on the crystallization of LLDPE, the analysis focused on the impact of multi-nano layer architecture on the orientation of LLDPE crystals. To achieve this, Multi-Nano Layer films comprising 1025 layers with equivalent draw ratios were examined. One of these films was devoid of MMT, allowing for the assessment of the unique effect of the MNL architecture. The two remaining films contained MMT, with one having an architecture A ≠ B, and the other having an architecture A = B. The architectures are shown in **Figure 6-5**.
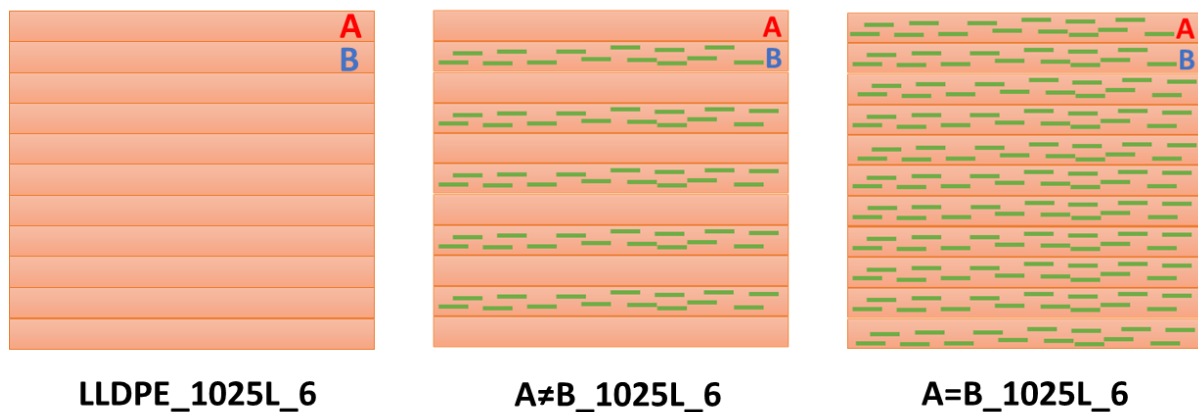
Figure 6-5 : Scheme of the architectures of the films. From left to right: film without MMT, film with the alternation of filled and unfilled MMT layers and film with all layers filled with MMT.

6.2.1   XRD texture analysis of 1025 layers MNL films

Texture analysis on the 1025-layer MNL films with a draw ratio of 6 (it corresponds to a 100µm thick film, which is the reference thickness in this work) were measured and plotted on the pole figures. Results are displayed in the **Figure 6-6.**

The pole figures of the MNL sample without MMT fillers indicate diffraction primarily concentrated at angles χ greater than 65° across all values of ϕ from 0 to 360°. This distribution implies that the crystallographic $\vec{a}$ and $\vec{b}$ axes of the LLDPE crystal system are randomly

oriented, aligned along the transverse direction and extrusion direction, but perpendicular to the film's normal.

Upon initial examination, the MMT-free MNL structure does not seem to exhibit a preferential orientation of the LLDPE relative to the TD and ED axes, and no additional effect is observed compared to the MMT-free monolayer film in **Figure 6-1**.
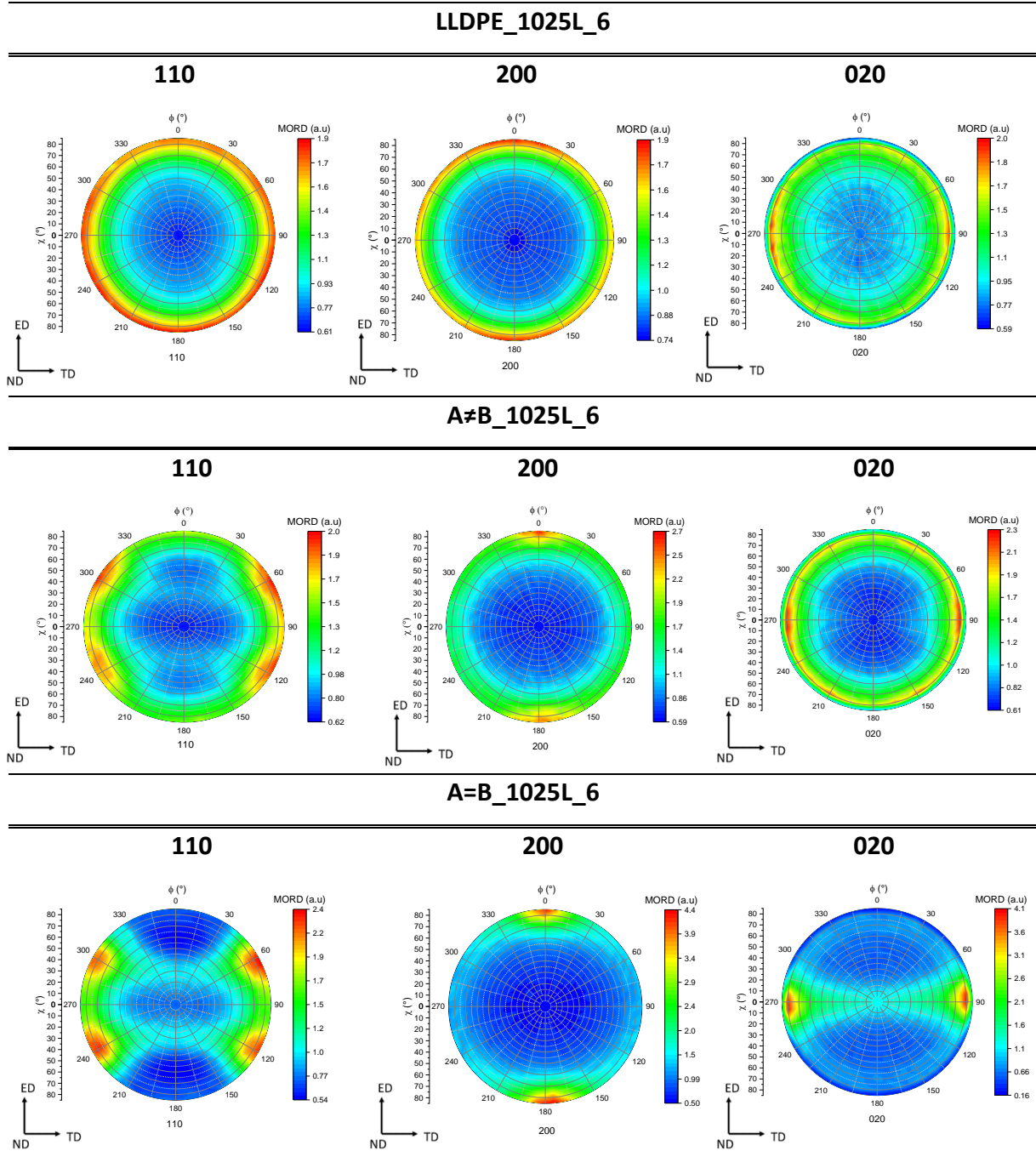
Figure 6-6: Pole figures of the LLDPE (110), (200) and (020) lattice planes of 1025 layers films with different architectures.

In the A≠B architecture, all pole figures exhibit a diffraction circle at χ values greater than 65-70° and across all values of ϕ. However, more intense diffraction poles are observed at certain ϕ values. For the (110) lattice plane, the poles are located at an angle of approximately ± 30° in ϕ relative to the TD and around ± 60° in ϕ with respect to the ED. The (200) lattice plane has its high-density diffraction poles in the ED direction, while the (020) lattice plane has its maximum in the TD direction. These orientations are similar to those observed in the monolayer film with 5wt% of fillers (**Figure 6-1**; 1L_5). The pole figures suggest that the presence of MMT nano-fillers promotes the preferential orientation of LLDPE in an MNL architecture. However, it can be assumed that the diffraction circles stem from the layers without montmorillonite, while the diffraction poles arise from the induced crystallization in layers containing fillers.

Finally, for the film with an A=B architecture, no diffraction circles are observed, but highly localized diffraction poles appear. The position of the diffraction poles on the pole figures suggests a KMI crystallization model (**Keller & Machin., 1967**) (**Figure A-2-1**). The position of these poles for the lattice planes (110), (200), and (020) is similar to that mentioned for the A≠B architecture, but they are more intense and strongly localized. Thus, the preferential orientation is more advanced in the case of an MNL film than for a monolayer film with 5wt% MMT (**Figure 6-1**), even with equivalent filler content in the film. Since both films were stretched with a DR of 6 and thus have the same thickness, this shows that the MNL provides a better organization in the film, leading to the development of more advanced crystal morphologies.

Several hypotheses can be considered regarding the effect of montmorillonite on the orientation of LLDPE chains. In all cases, it appears that montmorillonite increases local shear, promoting chain orientation. However, the passage of material through MNL multiplier elements generates even more shear, which repetitively affects the material. LLDPE tends to crystallize better under shear and form superstructures (such as shish-kebab) depending on shear intensity (**Keller & Kolnaar., 2006**). This could enhance LLDPE orientation compared to a monolayer film that only experiences increased local shear induced by filler presence during passage through the flat die (**Silagi., 2005; Jain et al., 2023**). One additional hypothesis proposes that the distribution of these nano-fillers might be more uniform throughout the thickness of the material. This uniform distribution could result in a more consistent shear

effect generated by the fillers within the molten polymer flow. As a consequence of this more uniform shear, there may be a greater degree of molecular orientation within the material.

6.2.2 Quantification of the crystallinity

Our objective here in this section was to quantify the crystallinity in the previous films (MMT-free 1025 layers film, A≠B and A=B architectures) and determine whether the observed orientations of film architectures increase crystallinity.

Figure 6-7 below shows the DSC curves for the MNL films studied during the first heating cycles. The first heating cycle is selected because it enables to get information about the direct effects of the MNL process on the LLDPE crystallinity or lamellas sizes.
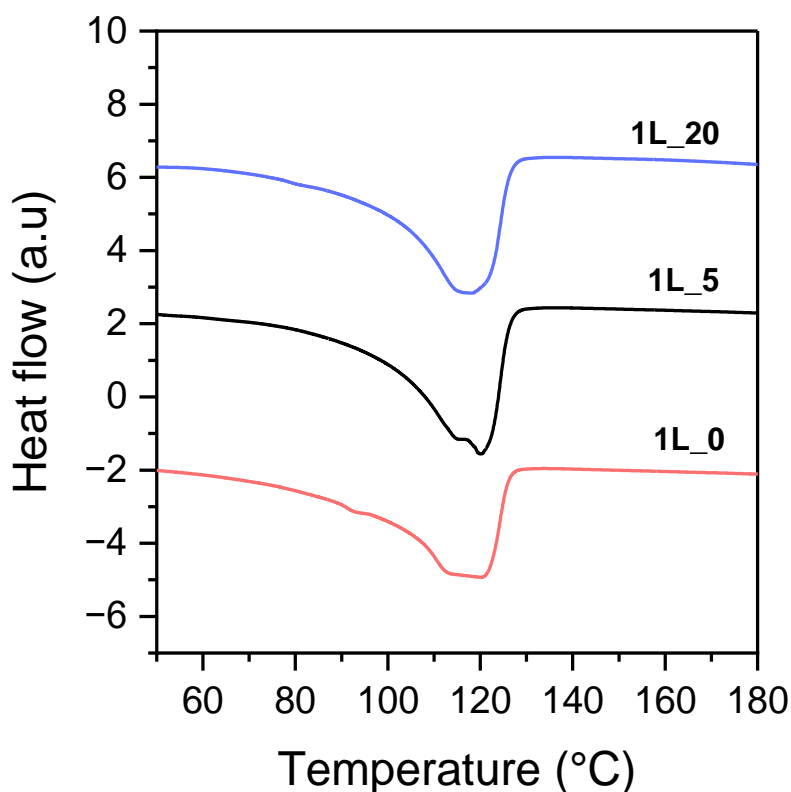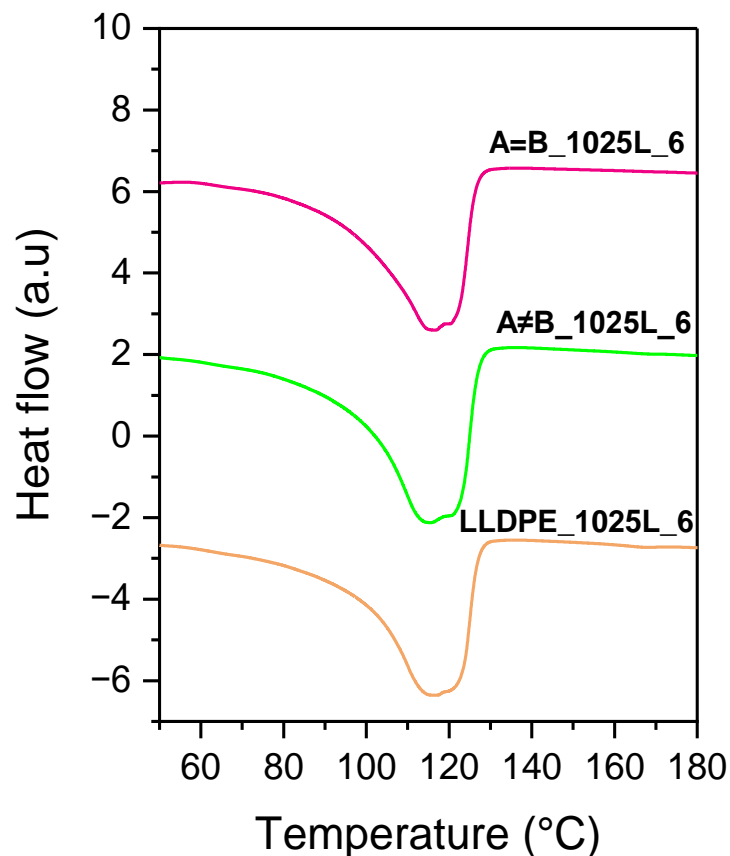

Figure 6-7 : First heating DSC thermograms of the 1025 layers films with different architectures. The positive value of the heat flow is for endothermic peaks.

All samples exhibit a broad melting peak consisting of two slightly distinct peaks, suggesting the presence of two populations of crystalline lamellae.

Table 6-3 : Percentage of crystallinity (χ_c) and LLDPE lamellas size (l) determined from DSC thermogram from Figure 6-7.

SAMPLE	OMMT concentration (wt%)	χ_c (%)	T_{f1} (°C)	T_{f2} (°C)	l_1 (nm)	l_2 (nm)
LLDPE_1025L_6	0	32	117.51	121.38	9.02	10.78
A≠B_1025L_6	2.5	28	115.46	122.42	8.67	10.61
A=B_1025L_6	5	27	116.26	120.72	8.90	10.52

After analyzing the data from **Figure 6-7** and **Table 6-3**, it is obvious that the Multi-Nano Layer film without MMT has a higher level of crystallinity compared to films with MMT. The crystallinity rates are 32% for the MNL film without MMT, and 28% and 27% for configurations A≠B and A=B, respectively. There is no significant difference in crystallinity between the two architectural variations. Generally, the crystallinity percentage are comparable to those observed in monolayer films (**Table 6-1**), except for the MNL film without MMT, which exhibits higher crystallinity than its monolayer counterpart without fillers (32 % versus 27% respectively).

The size of the crystal lamellae shows a noticeable similarity between the two size populations, with an average of 9nm for the smaller and 10.5nm for the longer lamellae. The use of fillers, whether in partial or in all layers, appears to have a similar effect, slightly reducing the size of the lamellae. The size of the lamellae obtained is comparable to that observed in monolayer films with equivalent MMT filler content.

The higher crystallinity in the MNL film without MMT, compared to films with fillers, can be attributed to the fact that the MNL, passing through the multiplier elements, enhances chain elongation and orientation through flow and shear dynamics. This results in the formation of more oriented structures, which promotes faster crystallization at the die exit and ultimately increases the final crystallinity of the films compared to monolayer films. However, when fillers are added, MNL only affects the morphology of crystallization without influencing the increase in the crystallinity within the films. **Jain et al., 2023** observed no

increase in crystallinity in films with filler addition either. However, they did notice a change in the orientation of crystalline lamellae, which is also the case in this work.

6.2.3 Quantification of the crystallographic $\vec{a}, \vec{b}$ and $\vec{c}$ axes orientation

The main goal of this part is to quantify the orientation of the crystallographic $\vec{a}, \vec{b}$ and $\vec{c}$ axes of the LLDPE crystal system in relation to the film processing directions (ED, TD, ND). **Figure 6-6** presents the pole figures, from which we extracted the orientation factors and determined the position of the crystallographic $\vec{a}, \vec{b}$ and $\vec{c}$ axes of the LLDPE crystal system relative to the reference directions of the film, ND, TD, and ED. The calculated $\cos^2_{i,j}$ values for each crystallographic $\vec{j}$ axis and direction 'i' are compiled in **Table 6-4**.

Table 6-4 : Orientation factors of 1025 layers films with different architectures. Calculated from poles figures displayed in Figure 6-6.

SAMPLE	$\cos^2_a$			$\cos^2_b$			$\cos^2_c$		
	ED	TD	ND	ED	TD	ND	ED	TD	ND
LLDPE_1025L_6	0.36	0.36	0.28	0.34	0.36	0.30	0.30	0.28	0.42
A≠B_1025L_6	0.39	0.35	0.26	0.35	0.38	0.27	0.26	0.27	0.47
A=B_1025L_6	0.45	0.31	0.24	0.22	0.44	0.34	0.33	0.25	0.42

The extracted $\cos^2_{i,j}$ have been displayed on the Desper-Stein triangle (**Figure 6-8**)

For the MMT-free MNL film (orange), the positions of the crystallographic $\vec{a}, \vec{b}$ and $\vec{c}$ axes are close to the Z-direction of the Desper-Stein triangle. The crystallographic $\vec{c}$ axis tends to orient towards the sample's normal direction with a $\cos^2_{c,ND}$ of approximately 0.42. The crystallographic $\vec{a}$ and $\vec{b}$ axes are located at a $\cos^2_{a,ND}$ and $\cos^2_{b,ND}$ values ND of about 0.3 and tend to be perpendicular to ND. The crystallographic axis orientation is consistent with the

MMT-free monolayer film (**Figure 6-3**). The film still exhibits uniaxial orientation along the normal direction, resulting in flattened spherulite crystallization.
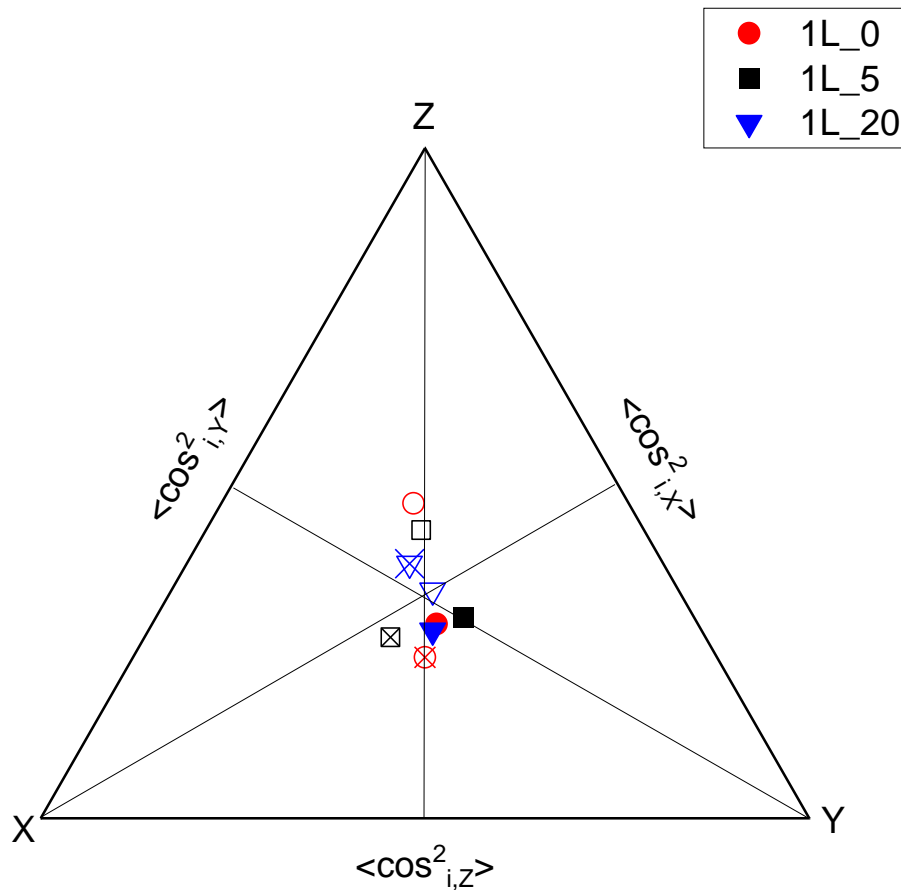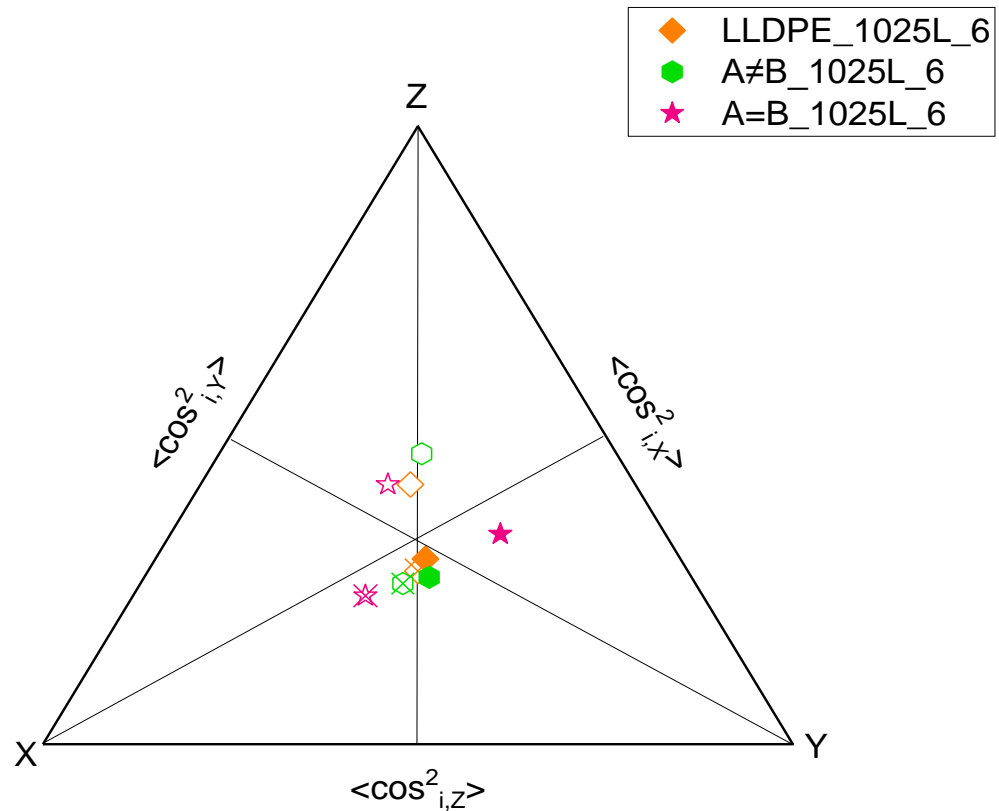

Figure 6-8 : Desper-Stein triangle of 1025 layers films with different architectures, where orientation factors of crystallographic $\vec{a}, \vec{b}$ and $\vec{c}$ axes of LLDPE crystal system are displayed. Symbol: cross is for crystallographic $\vec{a}$ axis, full is for crystallographic $\vec{b}$ axis and empty is for crystallographic $\vec{c}$ axis.

Regarding the film with the A≠B architecture, represented in green, the crystallographic $\vec{c}$ axis maintains an orientation towards the normal direction with a $\cos^2_{c,ND}$ of 0.47. Points for crystallographic $\vec{a}$ and $\vec{b}$ axes generally remain close to the Z-direction of the triangle. However, the crystallographic $\vec{b}$ axis shows a slight tendency to orient towards the TD, with a $\cos^2_{b,TD}$ of 0.38, while the crystallographic $\vec{a}$ axis tends to orient towards the ED, with a $\cos^2_{a,ED}$ of 0.39.

Based on the orientation factor values, the crystallographic $\vec{a}$ and $\vec{b}$ axes remain close to the Z-direction, suggesting a uniaxial orientation along the Z-direction. However, this does

not correspond to what is observed in the pole figure, which shows maximum diffraction in the ED and TD for the (200) and (020) lattice planes. It is important to note that the calculation of $\cos^2_{i,j}$ values takes into account diffraction intensities over all ϕ values. Previous observations in pole figures showed diffraction for all χ values, with some diffraction peaks more pronounced than in the ED and TD directions. Therefore, in this calculation, orientations are averaged, resulting in a more uniaxial orientation. This is consistent with the hypothesis that MMT-free layers crystallize with a uniaxial orientation along ND, while layers containing MMT promote a preferential orientation in the ED and TD directions.

The orientation of crystallographic $\vec{a}$, $\vec{b}$ and $\vec{c}$ axes in the A=B architecture does not exhibit a uniaxial orientation around the Z-direction. Instead, there is an orientation of the crystallographic axes in the three X, Y, and Z directions. The orientation of this sample is similar to that of the monolayer film containing 5wt% of MMT. Specifically, the crystallographic $\vec{a}$ axis is oriented in the extrusion direction with a $\cos^2_{a,ED}$ of 0.45, compared to 0.41 for the monolayer film. The crystallographic $\vec{b}$ axis is oriented in the TD direction with a $\cos^2_{b,TD}$ of 0.44, compared to 0.40 in the monolayer. The crystallographic $\vec{c}$ axis remains in a direction close to ND with a $\cos^2_{c,ND}$ of 0.42, compared to 0.43 for the monolayer film. Thus, in this case, the positions of crystallographic $\vec{a}$, $\vec{b}$ and $\vec{c}$ axes are more clearly defined in relation to the film directions. It is observed that the MNL A=B configuration promotes a more pronounced orientation of crystallographic $\vec{a}$ and $\vec{b}$ axes in the ED and TD directions, respectively, compared to a monolayer film containing the same percentage of MMT nano-fillers.

The observations of the MNL architecture with a 5wt% MMT concentration in an A=B configuration are consistently associated with a crystallization model that is considered as a thin film (**Adams et al., 1986**). The axes are aligned along the three film directions based on the KMII morphological model (**Figure A-2-4** ; **Figure A-2-5**). The pole figures initially suggested a KMI-type orientation with twisted lamellae. Despite the extraction of orientation factors, it was found that the crystallographic $\vec{a}$ and $\vec{c}$ axes did not show a random orientation along a particular direction. In the presence of twisted lamellae, one would expect to observe a coincidence of orientation between the crystallographic $\vec{a}$ and $\vec{c}$ axes around the Y-direction of the Desper-Stein triangle (**Figure A-2-3**). However, this expected alignment is not observed in this study. When considering the arrangement of crystallographic $\vec{a}$, $\vec{b}$ and $\vec{c}$ axes, a trend

towards an 'in-plane' lamellar orientation emerges. Specifically, crystallographic $\vec{a}$ axis is aligned in the extrusion direction, and the crystallographic $\vec{c}$ axis of the chains is parallel to the film's normal. This orientation is atypical for LLDPE and differs from most studies that describe an 'edge-on' orientation of lamellae. This observation is not yet well-understood and could be due to the significant influence of MMT on the crystallization process. It suggests that the presence of MMT could hinder the growth and orientation of LLDPE towards its most stable configuration, which is characterized by an 'edge-on' orientation.

To conclude this part, we observed that the MNL architecture of the films did not affect the crystallization morphology of LLDPE in the absence of fillers, compared to a monolayer film without fillers (**Figure 6-9**). However, the addition of fillers to some of the films resulted in two distinct crystallization modes: one for the layers without fillers and another for the layers with fillers (**Figure 6-9**).
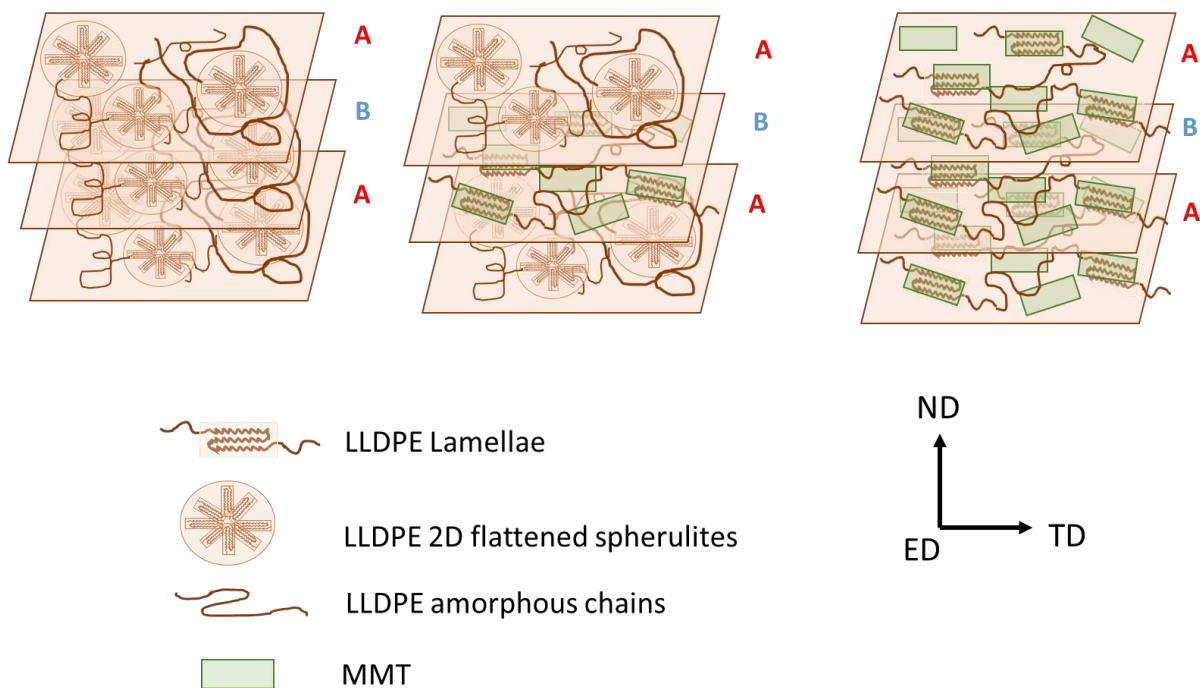
Figure 6-9 : Scheme of films top / side view to illustrate the crystallization morphologies of the LLDPE. From left to the right: LLDPE_1025L_6; A≠B_1025L_6; A=B_1025L_6.

Thus, when all layers are filled, an induced preferential orientation is observed throughout the film, which is more pronounced than in a monolayer film (**Figure 6-10**). As a result, the presence of MMT in MNL leads to an improved orientation of LLDPE compared to a monolayer film. However, no increase in crystallinity was observed.
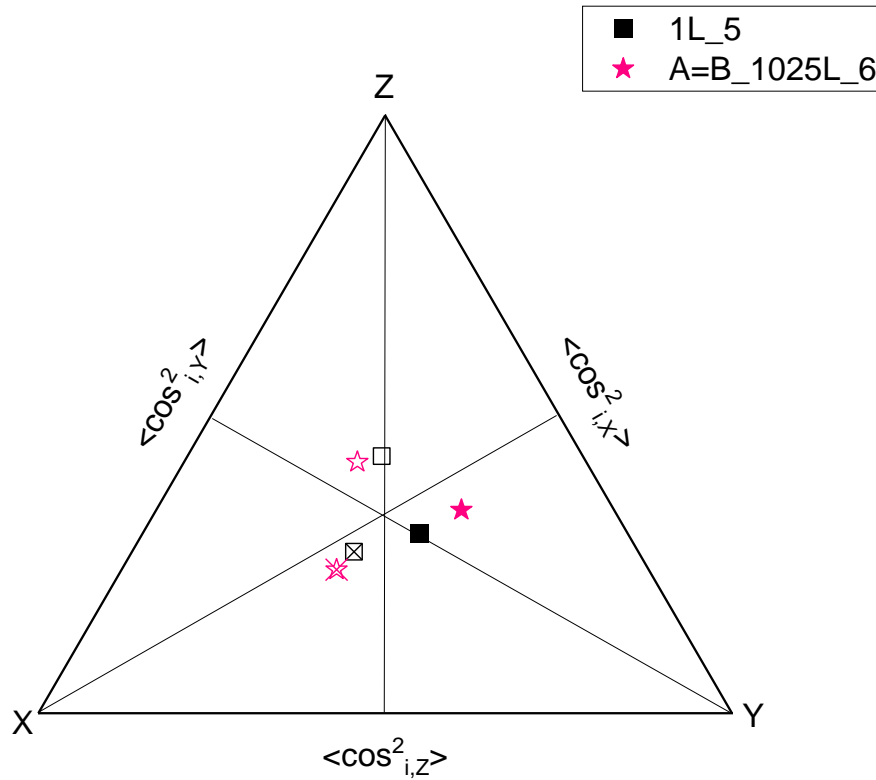
Figure 6-10 : Desper-Stein triangle of 1 layer versus 1025 layers films with 5wt% MMT, where orientation factors of crystallographic $\vec{a}$, $\vec{b}$ and $\vec{c}$ axes of LLDPE crystal system are displayed. Symbol: cross is for crystallographic $\vec{a}$ axis, full is for crystallographic $\vec{b}$ axis and empty is for crystallographic $\vec{c}$ axis.

6.3   IMPACT OF THE STRETCHING ON THE CRYSTALLIZATION OF LINEAR LOW-DENSITY POLY(ETHYLENE)

As observed in the previous section, the architecture of the films appears to have a critical effect on the crystallization of LLDPE. The MNL manufacturing process induces increased shear and elongation of the polymer chains due to the presence of multiplier elements that are repeated before the molten material passes through the flat die. According to **Haudin., 2015**, stretching LLDPE chains between the exit of the flat die and their cooling on the chill-roll can affect chain orientation and elongation. This section examines the effect of variable tensions applied on the film to reduce the nominal thickness of layers in the MNL film, corresponding to more or less significant draw ratios. The combined effect of film architecture and draw ratio on the crystallization of LLDPE is explored. It is important to note that drawing results in the confinement of LLDPE chains in progressively thinner layers.

6.3.1   XRD texture analysis on stretched monolayer and MNL films

Texture analyses were performed on monolayer and multi-nano layer films without fillers at draw ratios ranging from 6 to 23, as well as on films with A≠B and A=B architecture comprising 1025 layers, this time with a draw ratio ranging from 0 to 23. The pole figures exhibit the very same symmetry than before. Therefore, only one quarter of the pole figure will be displayed in **Figure 6-11**, **Figure 6-12** and **Figure 6-13**.
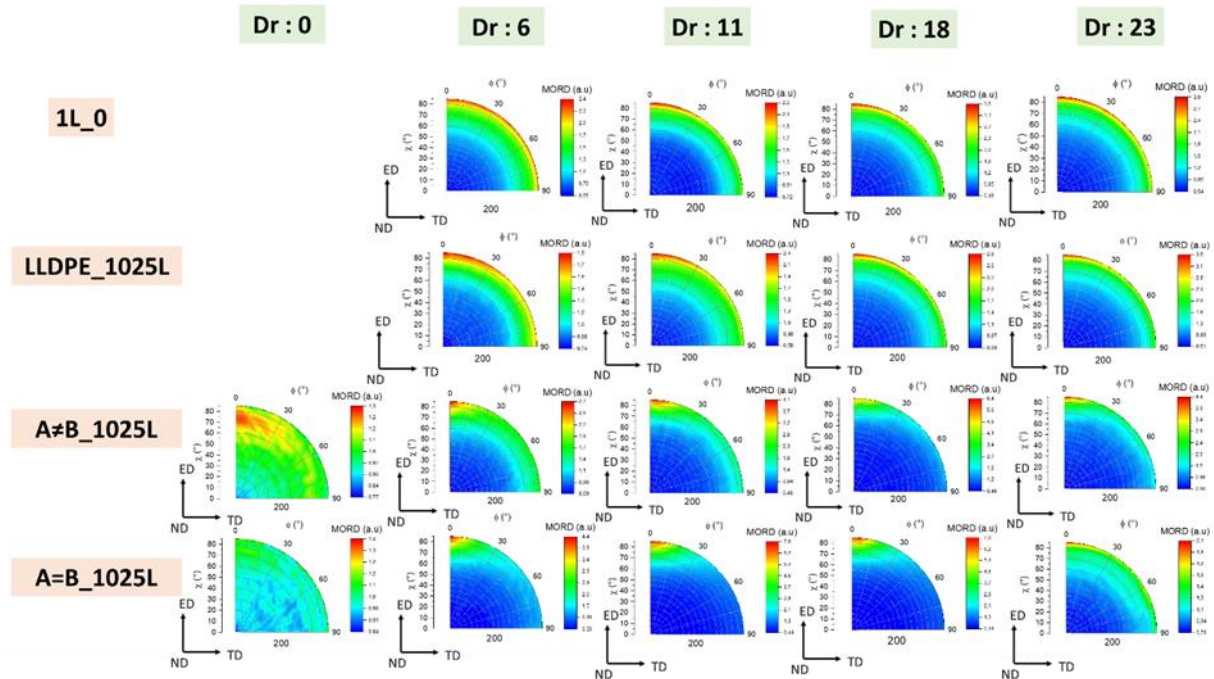
Figure 6-11 : Pole figures of the LLDPE (200) lattice plane of 1025 layers films with different architectures and draw ratios.

It is important to note that for the 200 pole figure, the highest diffraction peak is always located at the poles in the extrusion direction, regardless of the film configuration. Additionally, increasing the draw ratio intensifies and localizes the diffraction signal, regardless of the architecture or the presence of MMT. As the draw ratio increases, the diffraction circle becomes more defined. For films without MMT fillers, the optimal orientation begins at a χ angle of 60° when DR is 6 and at 70-75° when DR is 23. However, for MNL films with MMT fillers, the drawing results in increased localization of the diffraction signal at precise poles in the direction of extrusion.

In both architectures, the optimal orientation is achieved at a DR of 18. However, at a DR of 23, the orientation is less well-defined. In the A≠B architecture, the diffraction circle decreases for all values of ϕ. Due to an increase in DR, the total film thickness decreased, resulting in a reduction in nominal layer thickness. For the A≠B architecture, the MMT-free layers measure 40 nm thick at a DR of 18. This reduction may promote an increased proximity between the filled and unfilled layers, which may induce an effect of the MMT filler on the MMT-free layers, favoring their crystallization along a preferential orientation. Indeed, the diffraction circle of the MMT-free phase weakens as the DR increase and, eventually becoming

a single high density diffraction pole. Furthermore, this trend is not observed in monolayer films and MNL without fillers. Thus, the attenuation may be due to the effect of MMT fillers, and therefore MMT layers, on the MMT-free layers.
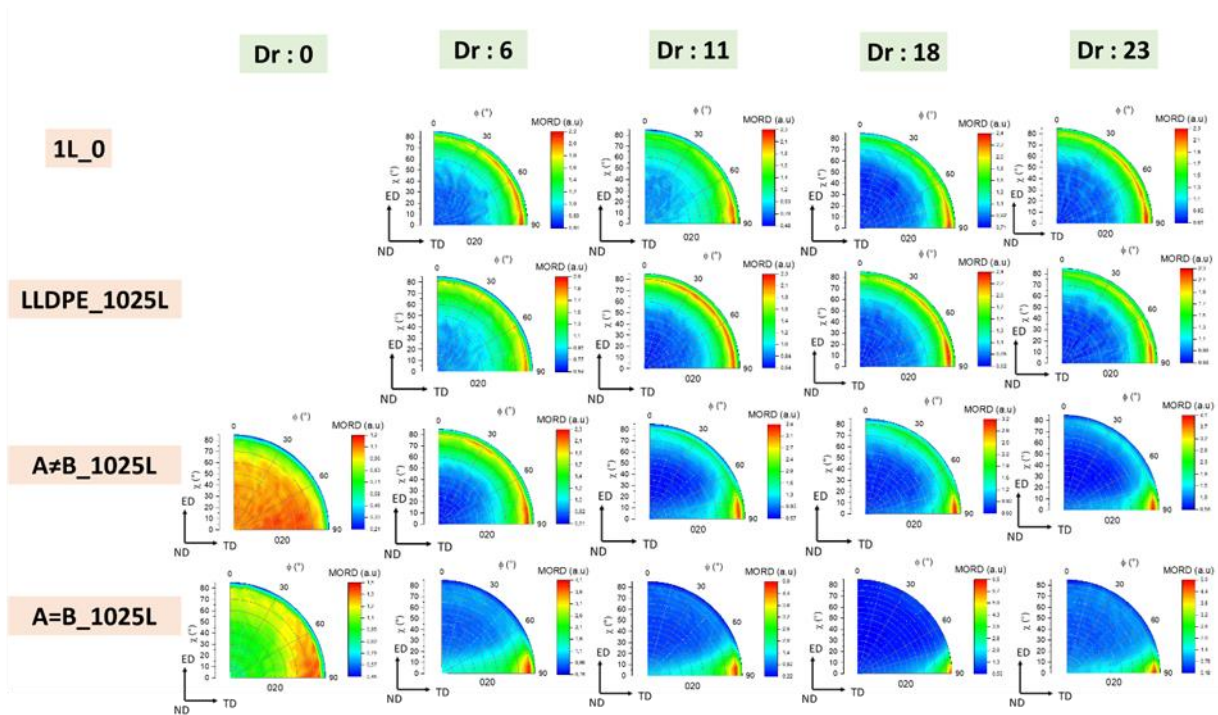
Figure 6-12 : Pole figures of the LLDPE (020) lattice plane of 1025 layers films with different architectures and draw ratios.

The pole figures of the (020) lattice planes confirm the previous observations regarding the evolution of diffraction spots based on drawing conditions and film architecture. The position of the diffraction poles highlights the tendency of the (020) lattice plane to orient perpendicular to the extrusion direction.
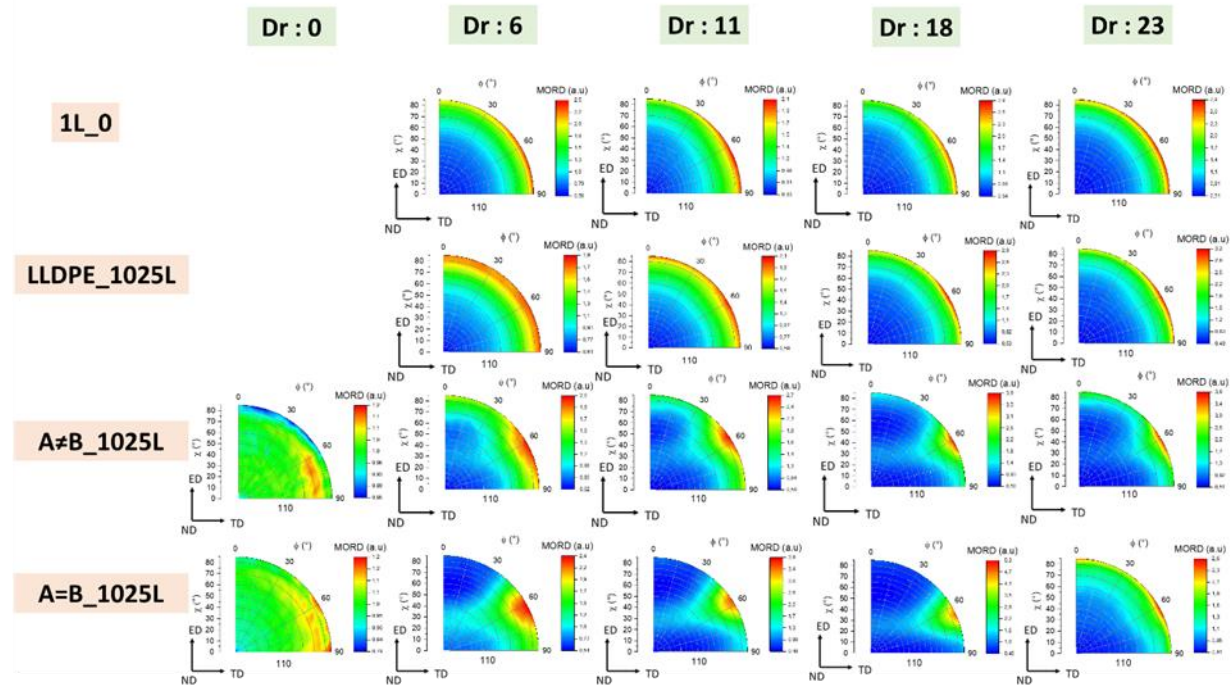
Figure 6-13 : Pole figures of the LLDPE (110) lattice planes of 1025 layers films with different architectures and draw ratios.

Finally, the pole figures of the (110) lattice planes exhibit the same texture evolution as the other two lattice planes as the draw ratio increases. Diffraction poles remain located at approximately 30° TD and 60° ED.

Drawing generally improves orientation, as shown by the pole figures, due to increased tensile strength, which causes the polymer chains to disentangle and align in the direction of the forces applied. This phenomenon was previously observed in poly(ethylene) by **Yoda & Kuriyama., 1977** with an 'edge-on' orientation. However, a drastic change in orientation occurs at a draw ratio of 23. Drawing in air accelerates crystallization kinetics on the chill-roll, as noted by **Haudin., 2015b**. At very high draw ratios, crystallization kinetics may be too fast and cooling too quick to allow an optimal crystallization, orientation and growth. To confirm this hypothesis, we used a thermal infrared camera to measure the temperature profile of the polymer melt during the drawing and cooling stages on the chill-roll. **Figure 6-15** displays the temperature profile extracted from IR images as represented in **Figure 6-14**. Only A=B films with 1025 layers and varying draw ratios were measured.
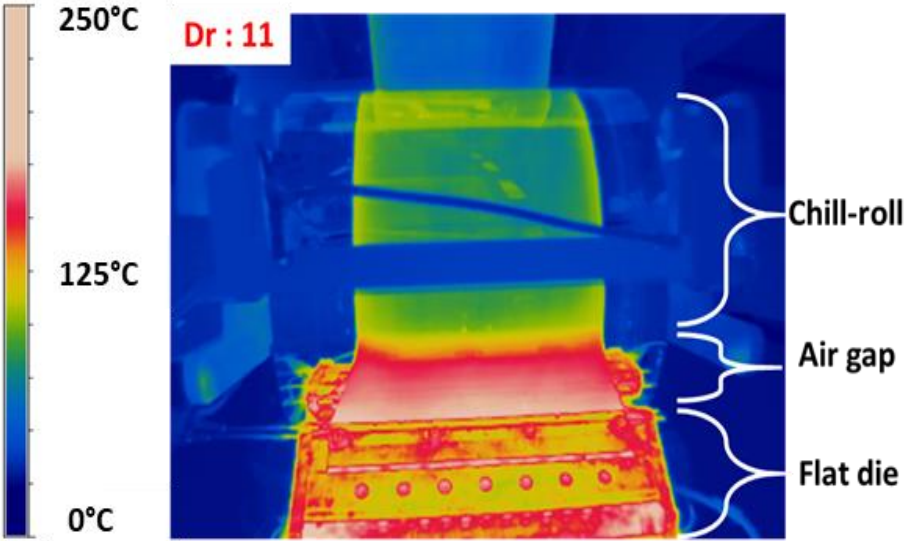
Figure 6-14 : IR thermal image of the A=B_1025L_11 film during the drawing and cooling step on the chill-roll.
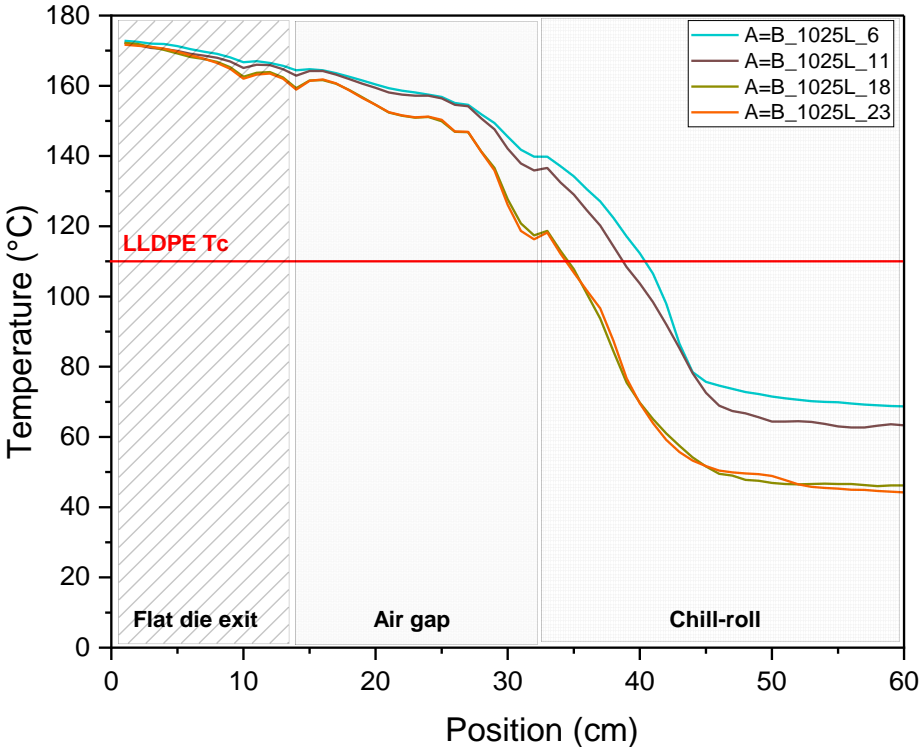
Figure 6-15 : Temperature profile versus the position on the image like Figure 6-14 extracted by IR thermal camera of the A=B_1025L film for different draw ratios (6, 11, 18, 23) from the die exit to the chill-roll.

The **Figure 6-15** illustrates that cooling and crystallization take place mainly on the chill-roll. Indeed, the crystallization temperature of LLDPE in the molten state is achieved on the chill-roll. It appears that the crystallization temperature (T_c) of LLDPE is reached more quickly as the DR increases. To confirm this, we plotted the temperature profile over time on **Figure 6-16**.
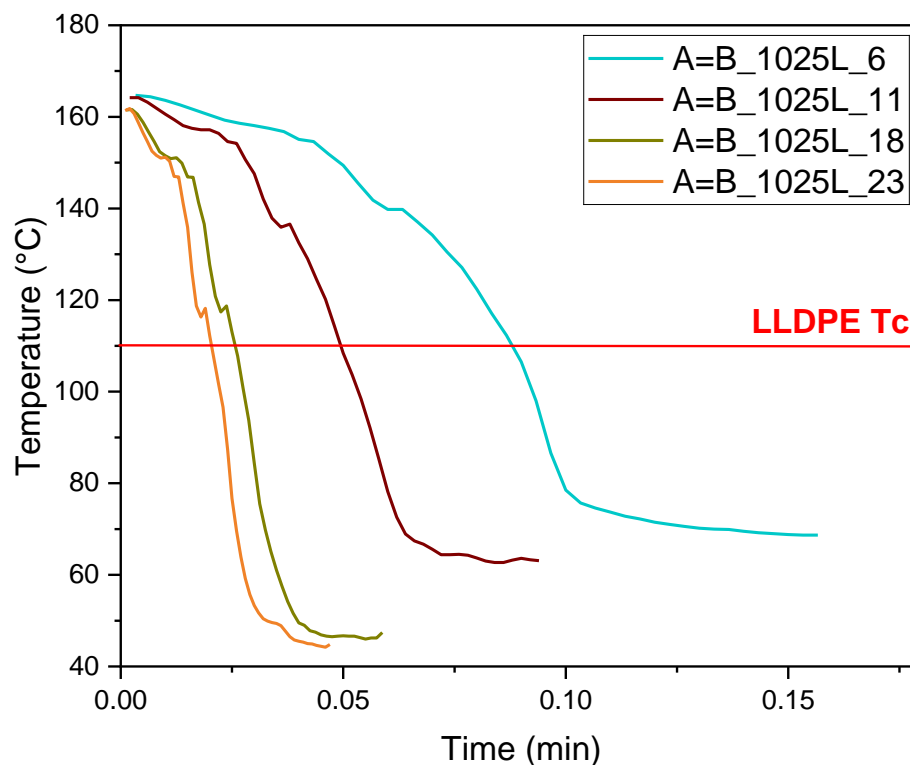
Figure 6-16 : Temperature profile from Figure 6-15 versus the time for A=B_1025L film for different draw ratios (6, 11, 18, 23).

In our case, an increase in draw ratio corresponds with an increase in chill-roll speed, so we divided the distance by the chill-roll speed. **Figure 6-16** indicates that films with higher DR reach the crystallization temperature of LLDPE faster and also cool faster compared to those with lower DR. For instance, at a DR of 23, T_c is reached in 0.021 min, which is 4 times faster than at a DR of 6, where T_c is reached in 0.09 min. The loss of orientation for a DR of 23 may be due to crystallization occurring too fast, leaving insufficient time for the chains to orient themselves optimally.

206

6.3.2 Quantification of the crystallinity of linear low-density poly(ethylene) in stretched films

The objective is to quantify the film's crystallinity characterized above and determine whether the observed orientations of the film architectures contribute to an increase in crystallinity.

Figure 6-17 displays the thermograms for all previously characterized samples.
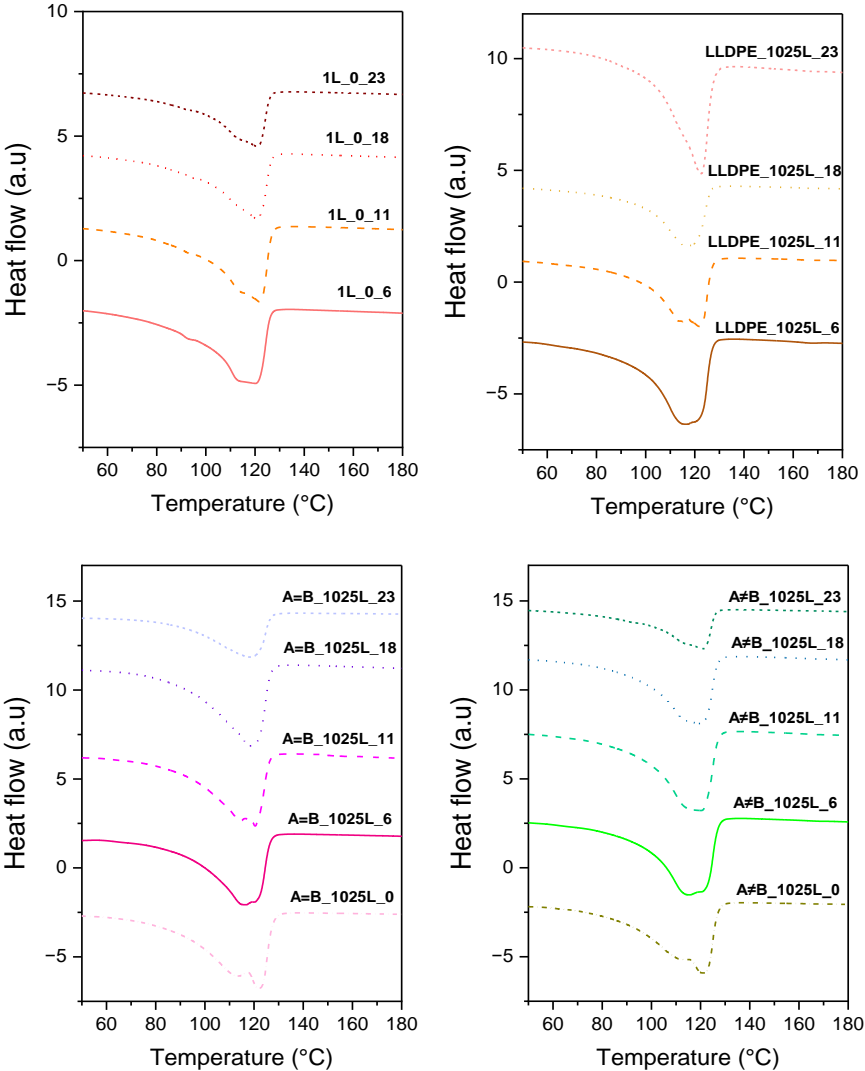
Figure 6-17 : First heating DSC thermograms of the different architectures (1L_0; LLDPE_1025L; A≠B_1025L and A=B_ 1025L) at different draw ratios. Each graph corresponds to a set of films. The positive value of the heat flow is for endothermic peaks.

The degree of crystallinity and the size of the LLDPE crystalline lamellae were calculated by extracting respectively the enthalpy of fusion values and the position of the melting peaks. Results are displayed in the **Table 6-5** and **Figure 6-18** respectively.

Table 6-5 : Percentage of crystallinity (χ_c) and LLDPE lamellas size (l) determined from DSC thermograms from Figure 6-17.

SAMPLE	χ_c (%)				
	DR: 0	DR: 6	DR: 11	DR: 18	DR: 23
1L_0	/	27	31	32	26
LLDPE_1025L_6	/	32	30	30	22
A≠B_1025L_6	32	28	31	30	29
A=B_1025L_6	31	27	28	29	21

Table 6-5 shows that, in most cases, the crystallinity of LLDPE are similar as a function of draw ratio and film architecture, except for a decrease observed at high draw ratios. When comparing MMT-free configurations, a crystallinity of around 30-32% is noted, dropping to 22-26% at a draw ratio of 23. The addition of MMT fillers results in crystallinity of 28-30% for A≠B and 27-29% for A=B, with a decrease at the maximum draw ratio. The data indicates that the presence of MMT fillers and the film architecture does not increase the crystallinity. On the contrary, an increased amount of fillers appears to slightly reduce it. This trend could be linked to the slowing down of crystallization in the presence of fillers (**Piorkowska., 2013**). Furthermore, the decrease in crystallinity at a DR of 23 is consistent with the quenching phenomena mentioned previously. In summary, the drawing process primarily affects the orientation of LLDPE. There is no significant impact on the increase in crystallinity, except at excessively high drawing ratios.

The melting behavior of films architectures without fillers is characterized by a broad peak made of two more or less well defined peaks in most cases, as observed in the identified melting peaks (**Figure 6-17**). The values of the melting peaks show a slight variation between MNL and monolayer architectures. For MNL films, the melting peaks are located around 115-117°C and 122°C, while for monolayer films, they are around 111-113°C and 120-122°C. When

MMT fillers are added and films are drawn, two distinct melting peaks are observed, particularly in an A=B architecture. However, in the case of A≠B architecture, a single broad melting peak is still present, with an increase in draw ratio. For the A≠B architecture, two melting peaks are present at DRs of 0 and 6, with a T_f value of 114-115°C and 120-122°C. As the draw ratio increases to a DR of 23, the single melting peak shifts to a maximum of 120°C for the DR 18 and 116°C for a DR of 23. In the A=B architecture, the position of the two melting peaks moves towards lower T_f as the DR increases, compared to other films under equivalent conditions. The peak positions at 113 and 123°C are reduced to 112°C and 118°C with increasing drawdown.
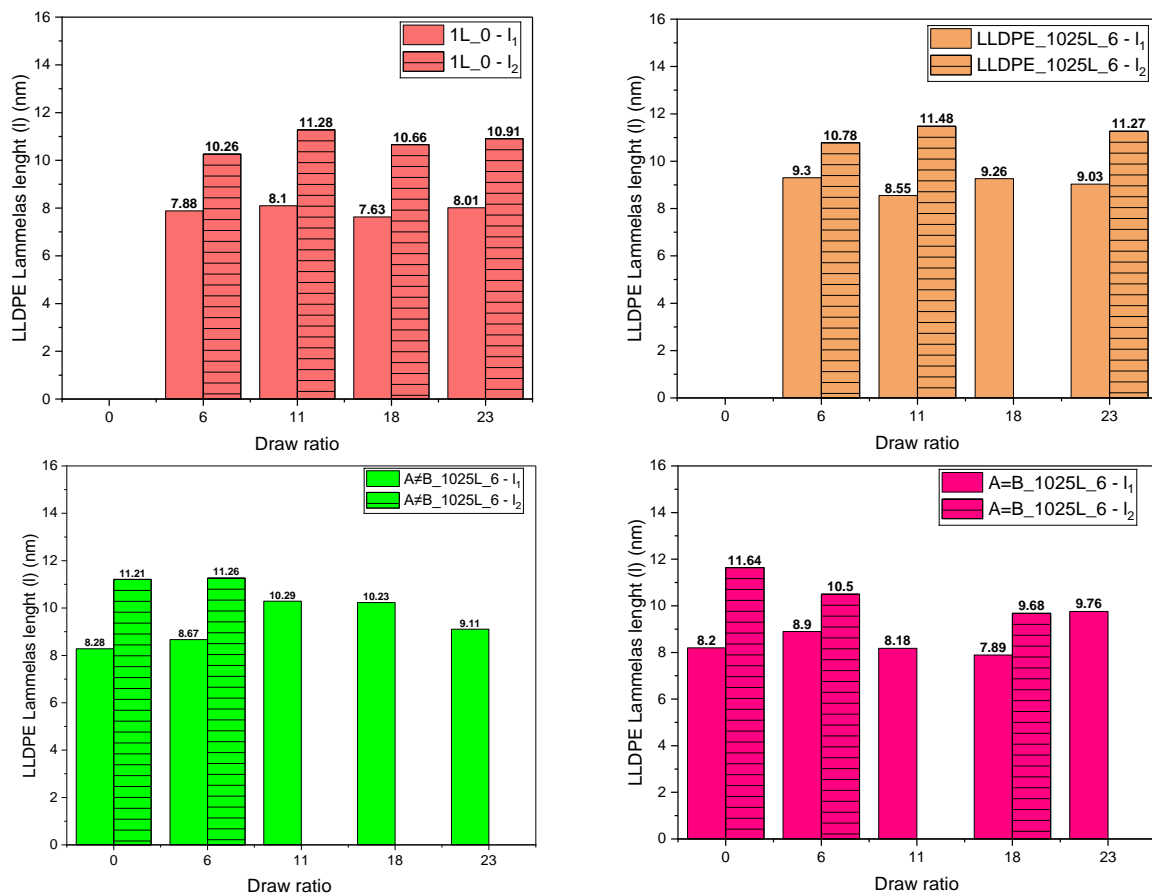
Figure 6-18 : LLDPE lamellas sizes (l) calculated from the DSC thermograms shown in Figure 6-17. Each graph represents one specific film architecture (1L_0; LLDPE_1025L; A≠B_1025L and A=B_ 1025L) at different draw ratios.

In **Figure 6-18**, for some draw ratio there is only one column meaning there is only one population of crystals which have been identified with the DSC measurements.

Figure 6-18 shows that the size of the lamella remains stable with increasing draw ratio for all films without MMT fillers. However, the lamella size in the MMT-free MNL films is slightly larger than that of the monolayer film. When MMT fillers are added to the different MNL architectures, the size of the crystalline lamellae tends to decrease with increasing draw ratio. This observation supports the notion that a higher draw ratio results in faster crystallization and cooling of LLDPE (as shown in **Figure 6-16**). As a result, there is less time for the growth of crystalline lamellae, leading to smaller lamellae compared to films with a lower draw ratio.

6.3.3 Quantification of the crystallographic $\vec{a}, \vec{b}$ and $\vec{c}$ axes orientation

The pole figures in **Figure 6-11**, **Figure 6-12** and **Figure 6-13** were used to calculate the orientation factors for the crystallographic $\vec{a}$, $\vec{b}$, and $\vec{c}$ axes of the LLDPE crystal system relatively to the film reference directions, ND, TD, and ED. The resulting $\cos^2_{i,j}$ for each axis and direction are presented in **Table 6-6**, **Table 6-7**, **Table 6-8** and **Table 6-9**. These values were then plotted in a Desper-Stein triangle (**Figure 6-19**, **Figure 6-20**, **Figure 6-21** and **Figure 6-22**).

Table 6-6 : Orientation factors of monolayer films without MMT (1L_0) at different draw ratios. Calculated from poles figures displayed in Figure 6-11, Figure 6-12 and Figure 6-13.

SAMPLE	$\cos^2_a$			$\cos^2_b$			$\cos^2_c$		
	ED	TD	ND	ED	TD	ND	ED	TD	ND
1L_0_6	0.38	0.38	0.24	0.34	0.37	0.29	0.28	0.25	0.47
1L_0_11	0.37	0.35	0.28	0.33	0.38	0.29	0.30	0.27	0.43
1L_0_18	0.41	0.37	0.22	0.33	0.38	0.29	0.26	0.25	0.49
1L_0_23	0.39	0.37	0.24	0.35	0.38	0.27	0.26	0.25	0.49
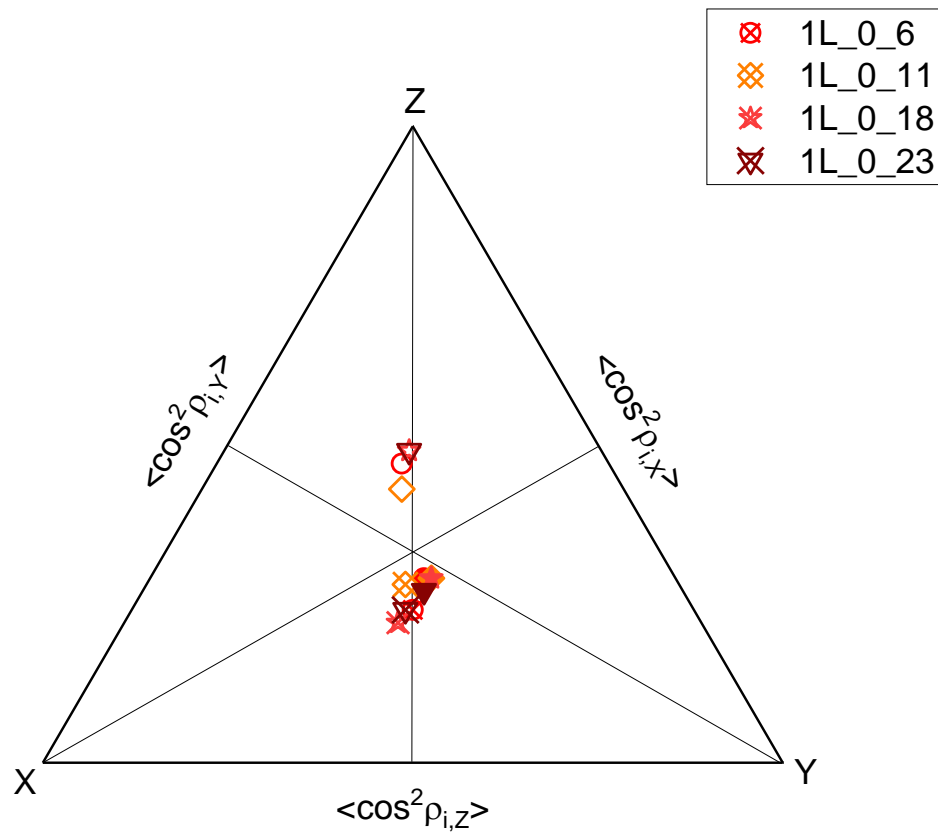
Figure 6-19 : Desper-Stein triangles of monolayer films without MMT (1L_0) at different draw ratios, where orientation factors of crystallographic $\vec{a}$, $\vec{b}$ and $\vec{c}$ axes of LLDPE crystal system are displayed. Symbol: cross is for crystallographic $\vec{a}$ axis, full is for crystallographic $\vec{b}$ axis and empty is for crystallographic $\vec{c}$ axis.

For the monolayer film without MMT, it is observed that despite the draw ratio increasing from 6 to 23, the positions of the crystallographic $\vec{a}$, $\vec{b}$, and $\vec{c}$ axes remained close to the Z-direction of the triangle. This indicates a uniaxial orientation along the normal direction of the film. The crystallographic $\vec{c}$ axis remain aligned in the normal direction with $\cos^2_{c,ND}$ values ranging from 0.43 to 0.49. Crystallographic $\vec{a}$ and $\vec{b}$ axes are usually oriented perpendicular to the normal, with $\cos^2_{a,ND}$ values ranging from 0.22 to 0.28, and $\cos^2_{b,ND}$ ranging from 0.27 to 0.28. Therefore, the orientation factors confirm that increasing the draw ratio does not enhance the orientation of crystalline LLDPE lamellae in all three film directions. Crystallization persists in the form of flattened spherulites.

Table 6-7 : Orientation factors of MMT free MNL films with 1025 layers (LLDPE_1025L) at different draw ratios. Calculated from poles figures displayed in Figure 6-11, Figure 6-12 and Figure 6-13.

SAMPLE	$\cos^2_a$			$\cos^2_b$			$\cos^2_c$		
	ED	TD	ND	ED	TD	ND	ED	TD	ND
LLDPE_1025L_6	0.36	0.36	0.28	0.34	0.36	0.30	0.30	0.28	0.42
LLDPE_1025L_11	0.38	0.36	0.26	0.37	0.35	0.28	0.25	0.29	0.46
LLDPE_1025L_18	0.39	0.36	0.25	0.35	0.38	0.27	0.26	0.26	0.48
LLDPE_1025L_23	0.41	0.36	0.23	0.34	0.38	0.28	0.25	0.26	0.49
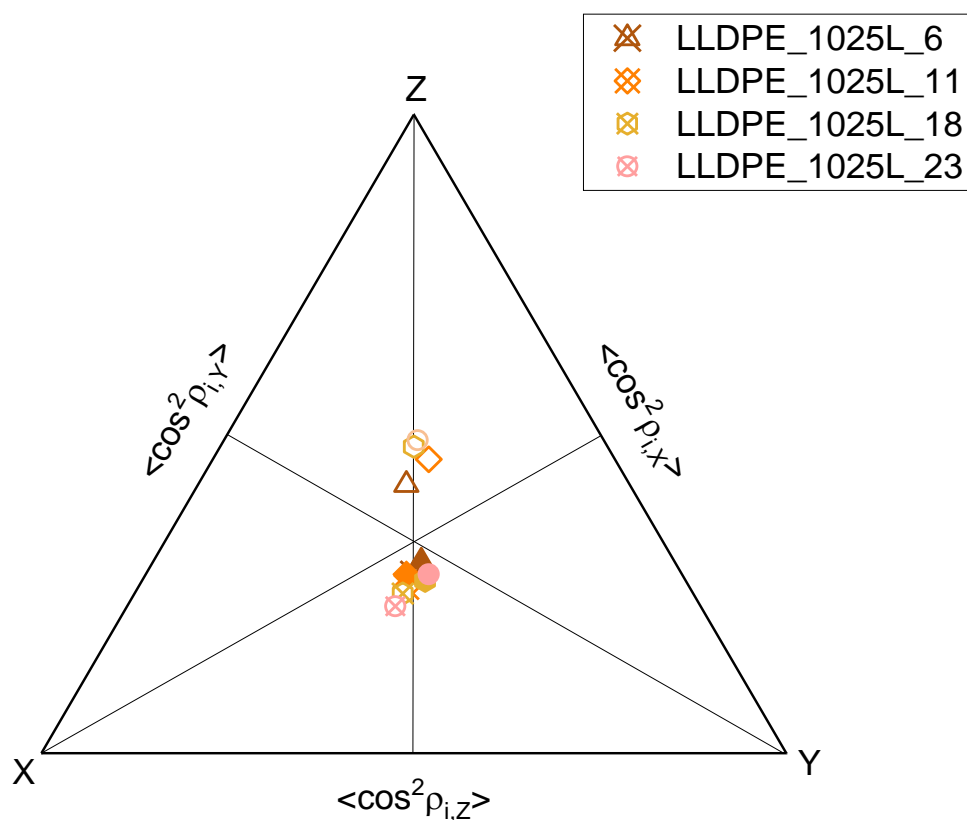
Figure 6-20 : Desper-Stein triangles of MMT free MNL films with 1025 (LLDPE_1025L) at different draw ratios, where orientation factors of crystallographic $\vec{a}$, $\vec{b}$ and $\vec{c}$ axes of LLDPE crystal system are displayed. Symbol: cross is for crystallographic $\vec{a}$ axis, full is for crystallographic $\vec{b}$ axis and empty is for crystallographic $\vec{c}$ axis.

A similar situation is observed in the MNL configuration without MMT fillers in response to an increase in draw ratio compared to monolayer films without fillers. A uniaxial orientation of the crystallographic axes along the ND is still present, with $\cos^2_{c,ND}$ values remain between 0.42 and 0.49. The crystallographic $\vec{a}$ and $\vec{b}$ axes still tend to orient perpendicularly to the normal direction, with $\cos^2_{a,ND}$ values ranging from 0.23 to 0.28 and $\cos^2_{b,ND}$ between 0.27 and 0.30. Thus, the orientation factors indicate that MMT-free MNL films do not significantly improve the orientation of the LLDPE crystals compared to monolayer films without fillers. The crystallization occurs still in the form of flattened spherulites.

Table 6-8 : Orientation factors of A≠B MNL films architectures with 1025 layers (A≠B_1025L) at different draw ratios. Calculated from poles figures displayed in Figure 6-11, Figure 6-12 and Figure 6-13.

SAMPLE	$\cos^2_a$			$\cos^2_b$			$\cos^2_c$		
	ED	TD	ND	ED	TD	ND	ED	TD	ND
A≠B_1025L_0	0.34	0.33	0.33	0.29	0.33	0.38	0.37	0.34	0.29
A≠B_1025L_6	0.39	0.35	0.29	0.35	0.38	0.27	0.26	0.27	0.47
A≠B_1025L_11	0.35	0.42	0.23	0.32	0.40	0.28	0.33	0.18	0.49
A≠B_1025L _18	0.47	0.31	0.22	0.33	0.40	0.27	0.20	0.29	0.51
A≠B_1025L _23	0.42	0.35	0.23	0.32	0.40	0.28	0.26	0.25	0.49
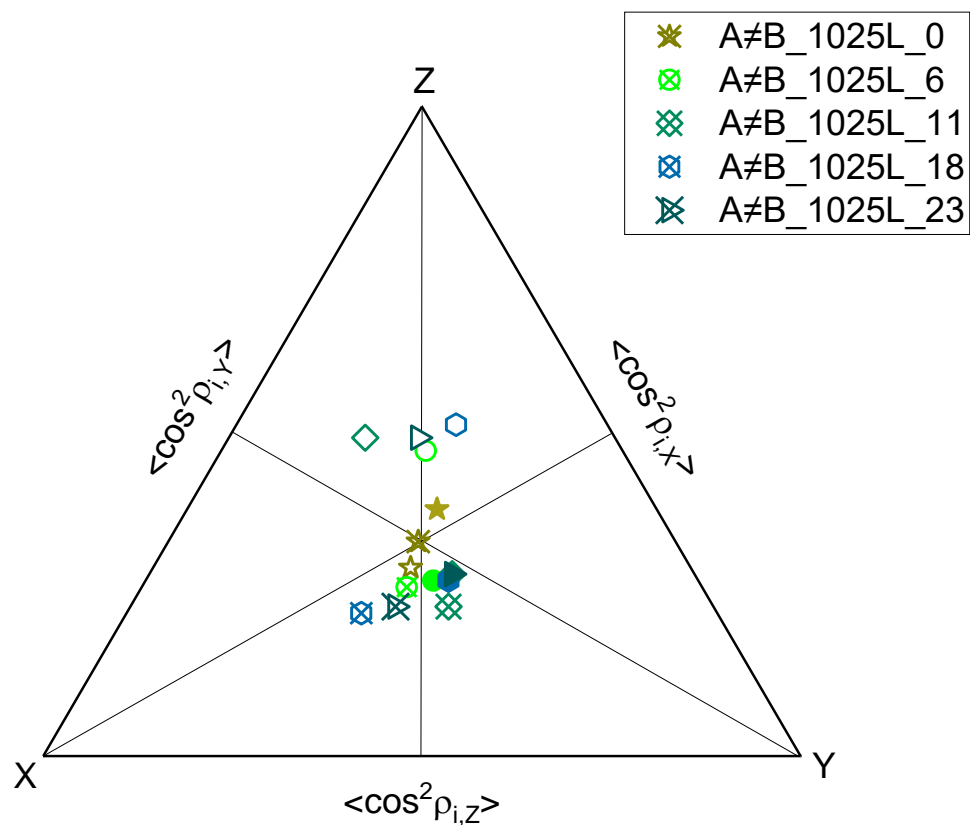
Figure 6-21 : Desper-Stein triangle of A≠B MNL films architecture with 1025 layers (A≠B_1025L) at different draw ratios, where orientation factors of crystallographic $\vec{a}$, $\vec{b}$ and $\vec{c}$ axes of LLDPE crystal system are displayed. Symbol: cross is for crystallographic $\vec{a}$ axis, full is for crystallographic $\vec{b}$ axis and empty is for crystallographic $\vec{c}$ axis.

In the MNL A≠B configuration with no drawing applied (DR of 0), the crystallographic $\vec{a}$ axis is located at the isotropic point. The crystallographic $\vec{b}$ axis tends to orient towards TD, while crystallographic $\vec{c}$ axis tends to orient towards ED. As the draw ratio increases to 6, the crystallographic axes become uniaxially oriented along the ND as explained in section 6.2. For DR values greater than 6, the positions of crystallographic $\vec{a}$, $\vec{b}$, and $\vec{c}$ axes become more clearly defined relative to the three directions of the film.

However, an increase in the draw ratio results in a variation in the position of crystallographic $\vec{a}$ and $\vec{c}$ axes relative to the TD and ED directions, while crystallographic $\vec{b}$ axis remains oriented in the TD direction. At a DR of 11, crystallographic $\vec{a}$ axis tends to orient in the TD-ED plane, with a random orientation relative to the ED direction ($\cos^2_{a,ED}$ of 0.35) and the TD direction ($\cos^2_{a,TD}$ of 0.42). Similarly, crystallographic $\vec{c}$ axis exhibits a random orientation along the ED in the ND-ED plane, with $\cos^2_{c,ED}$ values of 0.33 and $\cos^2_{c,ND}$ of 0.49.

However, at a DR of 18, the random orientations of the crystallographic $\vec{a}$ and $\vec{c}$ axes relatively to the ED direction are lost. Crystallographic $\vec{a}$ axis indicates an orientation in the ED direction with a $\cos^2_{a,ED}$ value of 0.47, while crystallographic $\vec{c}$ axis tends to orient perpendicular to the ED direction in the TD-ND plane with a $\cos^2_{c,ED}$ value of 0.20. A draw ratio of 23 results in a slight decrease in $\cos^2$ values compared to a DR of 18, but no significant loss of orientation is noted. This decrease is consistent with a quenching phenomenon that may occur at excessively high draw ratios, leading to a loss of preferred orientation. The A≠B architecture shows a significant orientation of crystallographic $\vec{a}$, $\vec{b}$, and $\vec{c}$ axes in the three film directions. This phenomenon evolves with the increasing draw ratio and correlates with the pole figures results (**Figure 6-11**, **Figure 6-12** and **Figure 6-13**). As the DR increases, the diffraction signal tends to resemble that observed in films containing 5wt% MMT (A=B_1025L). We can thereby conclude that the orientation of LLDPE crystal lamellae tend to be 'in-plane' oriented in all the cases, with an increase of the preferred orientation according to the ED, TD and ND when the DR increase.

Table 6-9 : Orientation factors of A=B MNL films architectures with 1025 layers (A≠B_1025L) at different draw ratios. Calculated from poles figures displayed in Figure 6-11, Figure 6-12 and Figure 6-13.

SAMPLE	$\cos^2_a$			$\cos^2_b$			$\cos^2_c$		
	ED	TD	ND	ED	TD	ND	ED	TD	ND
A=B_1025L_0	0.33	0.33	0.34	0.31	0.35	0.34	0.36	0.32	0.32
A=B_1025L_6	0.45	0.31	0.24	0.22	0.44	0.34	0.33	0.25	0.42
A=B_1025L_11	0.52	0.28	0.20	0.23	0.45	0.32	0.25	0.27	0.48
A=B_1025L _18	0.52	0.27	0.21	0.25	0.45	0.30	0.23	0.28	0.49
A=B_1025L _23	0.36	0.35	0.29	0.24	0.43	0.33	0.40	0.22	0.38
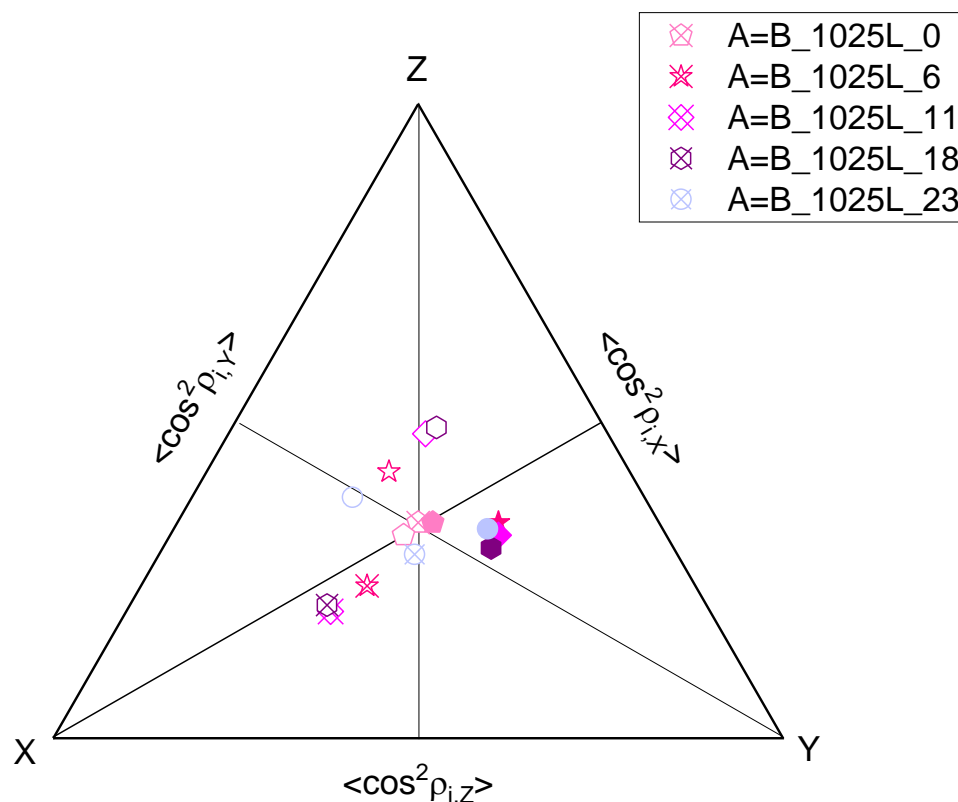
Figure 6-22 : Desper-Stein triangle of A=B MNL films architecture with 1025 layers (A=B_1025L) at different draw ratios, where orientation factors of crystallographic $\vec{a}$, $\vec{b}$ and $\vec{c}$ axes of LLDPE crystal system are displayed. Symbol: cross is for crystallographic $\vec{a}$ axis, full is for crystallographic $\vec{b}$ axis and empty is for crystallographic $\vec{c}$ axis.

In the MNL A=B configuration, it is observed that if the film is not drawn during cooling (DR 0), the orientation of crystallographic $\vec{a}$, $\vec{b}$, and $\vec{c}$ axes is close to the isotropic orientation point. Therefore, no direction is favored for the growth of LLDPE crystals, and crystal growth can occur in the form of spherulites due to the absence of constraints during cooling. When stress is applied during cooling, an orientation of crystallographic $\vec{a}$, $\vec{b}$, and $\vec{c}$ axes is observed in all three film directions.

As the draw ratio increases from 6 to 18, the points corresponding to the orientation of crystallographic $\vec{a}$ axis approach the extrusion direction, with a $\cos^2_{a,ED}$ value increasing from 0.45 to 0.52. Similarly, for the points corresponding to the orientation of crystallographic $\vec{b}$ axis in the TD, $\cos^2_{b,TD}$ values increase from 0.35 to 0.45 for DR values ranging from 6 to 18. Finally, the orientation of crystallographic $\vec{c}$ axis in the ND direction is determined by its corresponding point, with $\cos^2_{c,ND}$ values ranging from 0.42 to 0.49 for DR values from 6 to 18. Thus, distinct crystallographic axes orientations are observed towards X, Y and Z vertices of the triangle. This means that crystallographic $\vec{a}$, $\vec{b}$ and $\vec{c}$ axes tend to orient respectively in the ED, TD, and ND directions to reach a KMII thin film crystallization model (**Figure A-2-5**).

These observations support previous works on the crystallization models of LLDPE in films. These studies describe the formation of a thin film with lamellae aligned in the plane of the film, which resembles a presumed 'KMII' type of orientation. However, it is important to note that the observed orientation is 'in-plane'. This is surprising as many studies on poly(ethylene) and its crystallization, as well as the literature on multi-nano layer co-extrusion technology, tend to report 'edge-on' orientations when LLDPE is confined in layers of a few nanometers, as observed in the works of **Zhang et al., 2014a, b, and c**.

Our study on drawing conditions shows that we can effectively control the crystallization of LLDPE, forming oriented 2D crystals similar to those observed in the literature on MNL. However, in the literature, authors achieve these orientations by inducing confinement crystallization through the combination of an amorphous and a semi-crystalline phase, and by reducing the layer thickness, as reported by **Bernal-Lara et al. in 2005 and 2006**. In our work, these preferential orientations do not appear to be induced by a reduction in nominal layer thickness, as no change in orientation was observed in MNL films without MMT. However, these orientations are mainly caused by the addition of two-dimensional nano-

fillers. These nano-fillers promote shear and local confinement on the LLDPE chains, resulting in the observed orientations. Additionally, stretching improves polymer chain orientation. Therefore, incorporating 2D fillers into a monomaterial multi-nanolayer film system is a promising approach to achieve 2D crystalline lamellar orientation of LLDPE similar to that obtained in cases of confinement-induced crystallization.

6.4 CORRELATION OF ALL PARAMETERS

The purpose of this section is to establish a correlation between the morphologies identified in the previous three sections, the orientation of montmorillonite achieved, and the barrier properties of the films. The goal is to draw conclusions about potential synergies among these parameters and the morphologies of the systems obtained.

6.4.1 Correlation of linear low-density poly(ethylene) crystallization and orientation with the MMT 'in-plane' orientation

As previously observed, given the lack of significant impact of layer thickness reduction on MMT orientation in the previous chapter, the aim here is to identify potential correlations between MMT and LLDPE crystallization. We aim at determining whether the matrix affects this orientation or whether additional factors are involved. All conclusions regarding LLDPE crystallization and MMT orientation are summarized in **Table 6-10** below.

Table 6-10 : Compilation of all parameters investigated in this chapter and their influence on the crystallization of LLDPE and the orientation of MMT.

PARAMETER	LLDPE CRYSTALLIZATION MODELS	MMT ORIENTATION
MMT Concentration	The presence of MMT leads to a preferred orientation of LLDPE toward the ND, ED and TD. LLDPE Lamellas tend to be oriented 'in-plane'.	The increase of MMT concentration improves the 'in-plane' orientation.
Film architecture	The addition of MMT in the MNL architecture leads to a better 'in-plane' orientation of LLDPE compared to monolayer films.	The presence of MMT in all the layers gives a better 'in-plane' orientation.
Drawing ratio	The increase of the draw ratio leads to the best 'in-plane' orientation achieved in those set of samples.	The increase of the stretching slightly improves the 'in-plane' orientation

The study suggests that the presence of montmorillonite promotes a preferential orientation of LLDPE crystals, indicating that crystallization occurs in close proximity to the fillers. Additionally, it is plausible that LLDPE influences the orientation of montmorillonite during the crystallization process. We can also conclude that an improvement in LLDPE orientation occurs with increasing draw ratio, as well as a slight enhancement in montmorillonite orientation. This suggests that LLDPE crystallizes around montmorillonite, which may limit the orientation of the latter to conform to the morphology of LLDPE crystals rather than being confined due to a decrease in the size of individual layers.

6.4.2 Correlation of linear low-density poly(ethylene) crystallization and orientation with the H_2O barrier properties

As the previous chapter did not demonstrate any significant impact from the 'in-plane' orientation of the MMT fillers on barrier properties, we have shifted our focus to exploring the potential impact at the polymer matrix level. The polymer matrix constitutes 95% of the sample in our 5% MMT samples. Therefore, this chapter analyzes the orientation and crystallization of LLDPE in our samples to better understand their evolution.

On **Table 6-11**, when observing the variation of parameters such as MMT concentration or film architecture, a lamellar structure slightly more oriented compared to a MMT-free film emerges in both cases. However, there is a modest decrease in barrier properties of about 13% at best when the concentration of MMT is 20wt%, rather than 5wt%. It is worth noting that this decrease is observed only at a concentration of 20wt% of MMT.

Table 6-11 : Compilation of all parameters investigated and their influence on the LLDPE crystallization and the H_2O barrier properties.

PARAMETER	LLDPE CRYSTALLIZATION MODELS	H_2O BARRIER PROPERTIES
MMT Concentration	The presence of MMT leads to a preferred orientation of LLDPE toward the ND, ED and TD. LLDPE Lamellas tend to be oriented 'in-plane'.	-13% H_2O permeability at the maximum.
Film architecture	The addition of MMT in the MNL architecture leads to a better 'in-plane' orientation of LLDPE compares to a monolayer film.	-13% H_2O permeability with MMT in all the layers.
Drawing ratio	The increase of the draw ratio leads to the best 'in-plane' orientation achieved in those set of samples.	+ 38% H_2O permeability at the maximum DR.

The presence of MMT fillers or crystal conformation may be linked to the observed improvement. Upon examining the film stretching parameter, a significant improvement in the preferential orientation of LLDPE is observed. However, this improvement does not necessarily correspond with an increase in crystallinity and only slightly orients the MMT. As a result, there is an increase in permeability of about 38%.

In this context, it seems that the highly oriented crystallization of LLDPE does not improve H_2O barrier properties. Previous work by **Zhang et al., 2014b** demonstrated that in an HDPE/HP0 (Cyclic olefin polymer) MNL system, reducing the nominal layer thickness from 800 to 300 nm resulted in a 50% reduction in HDPE O_2 permeability compared to a HDPE reference film. This change in thickness lead to obtained 2D flattened spherulites. When the nominal layer thickness was reduced to 100nm, oriented 2D lamellas were obtained.

However, the permeability increased by 45% compared to what was observed at a thickness of 300nm. Moreover, as crystallization appears to be localized around the fillers, there is no additive or complementary effect of the two elements that can block gas diffusion (crystalline lamellae and MMT nano-sheets).

7. CHAPTER 7: BI-AXIAL STRETCHING: EFFECT ON MONTMORILLONITE AND LINEAR LOW-DENSITY POLY(ETHYLENE) CRYSTALS ORIENTATION

INTRODUCTION

In the previous chapters, we observed that the 'in-plane' orientation of MMT was limited during processing in both monolayer and multi-nano-layer configurations with 5wt% of MMT. Despite reducing the nominal layer thickness in the MNL film, the orientation only slightly improved. The integral breadth decreased from 53° to 42° with a reduction in nominal layer thickness from 100μm to 29nm. Therefore, we attempted to understand the underlying phenomena and identify a relationship between MMT and LLDPE crystals. It has been found that the presence of MMT affects the crystallization of LLDPE. Without MMT, LLDPE tends to crystallize uniaxially in accordance with the film normal. However, in the presence of MMT, it crystallizes with a preferential orientation along the ED, TD, and ND of the films. This suggests that LLDPE crystallizes in the vicinity of the MMT charges, which may affect the orientation of the MMT. In order to further improve the orientation of the MMT, we explored whether a post-processing treatment could have any beneficial effect.

Thus, in this chapter we investigated the effect of bi-axial stretching below the melting temperature of the films on MMT orientation. For that purpose, several films and configurations were analyzed, including a monolayer film with 5wt% MMT, a multi-nano layer film consisting of 1025 layers with 5wt% MMT, and a monolayer film with 20wt% MMT. Bi-axial stretching was also applied to films without fillers for comparison and to better understand the mechanisms involved. It should be noted that the tests were stopped just before the samples reached their breaking point. We present here a thorough review of the results obtained from bi-axial stretching of various films and their correlation with the final barrier properties of the films.

7.1 THE BI-AXIAL STRETCHING TRIALS

This section analyzes experimental parameters, focusing on the temperature used for bi-axial stretching of both filled and unfilled LLDPE films. It also details the engineering stress over strain curves recorded during the bi-axial stretching to provide an overview of what happened to the film microstructure in the process.

7.1.1 Bi-axial stretching conditions

To prepare for the bi-axial stretching measurement, we measured the DSC curves of the samples. The first heating cycle is particularly important as it provides information on the film's characteristics in the initial state of the process. The goal here is to determine the optimal temperature for conducting the bi-axial stretching tests. **Figure 7-1** displays the results of the first heating curves obtained by DSC.
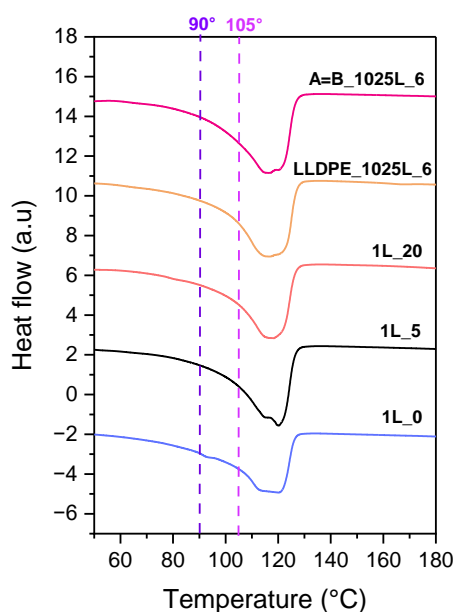
Figure 7-1 : DSC thermograms of the first heating cycle of the samples before-bi-axial stretching. The positive value of the heat flow is for endothermic peaks.

CHAPTER 7: BI-AXIAL STRETCHING: EFFECT ON MONTMORILLONITE ORIENTATION AND LINEAR LOW-DENSITY POLY(ETHYLENE) CRYSTALS

As shown in **Table 7-1**, the samples chosen have a crystallinity ranging from 27% to 32% and a LLDPE crystal lamella size between 8nm and 10.8nm. These values are influenced both by the architecture of the sample and the presence or absence of MMT as concluded in the previous chapter.

Table 7-1 : Percentage of crystallinity (χ_c) and LLDPE lamellas size (l_1 and l_2) determined from the DSC thermogram shown in Figure 7-1.

SAMPLE	OMMT concentration (wt%)	χ_c (%)	T_{f1} (°C)	T_{f2} (°C)	l_1 (nm)	l_2 (nm)
1L_0	0	27	/	120.16	/	10.26
1L_5	5	27	114.91	120.06	8.51	10.22
1L_20	20	19	/	118.41	/	9.61
LLDPE_1025L_6	0	32	117.51	121.38	9.02	10.78
A=B_1025L_6	5	27	116.26	120.73	8.90	10.52

The bi-axial stretching tests were conducted at temperatures below the point of complete melting of LLDPE. This decision was made to preserve polymer crystals and investigate their impact on the orientation of MMT. Additionally, it was made also to maintain the mechanical strength of the sample in order to be able to stretch it.

Two temperatures were chosen for the tests: a first temperature of 90 °C was selected as it is close to the onset of the melting peak: the mobility of the polymer chains is increased with a partial melting the LLDPE crystals. The second temperature of 105 °C was chosen as it is close to the maximum melting peak (**Figure 7-1**), representing a more advanced stage of LLDPE lamellar melting.

7.1.2 Mechanical follow-up during bi-axial stretching

During bi-axial stretching, force transducers placed on the motorized arms continuously recorded the force applied to the samples. This enables dynamic monitoring of the mechanical strength of the sample as a function of the deformation and the degree of bi-axial stretching, what facilitates the detection of any formation of more oriented structures and consequent changes in microstructures.

7.1.2.1 Monolayer films

Overall most of the curves show an increase in engineering stress at low engineering strain, which corresponds to the elastic deformation of the material (**Figure 7-2**). This slope is used to calculate the Young modulus (**Figure 3-24**). The point between the end of the elastic deformation and the plateau is known as the yield point, which corresponds to the beginning of the plastic deformation of the material (refer to **Chapter 3**). The plateau corresponds to the necking propagation step, where crystal slips or fragmentation can occur. After the plateau, in some cases, there is an increase in engineering stress (also called strain-hardening), which is associated with the reorganization of polymer crystals into fibrillary crystals. It is important to note that the bi-axial stretching trials were stopped just before the films broke. As a result, some samples may not have the same level of deformation (engineering strain).

Figure 7-2 below shows the engineering stress over strain curves, in the transverse direction of the monolayer films (the one from the extrusion direction of the film is the same).
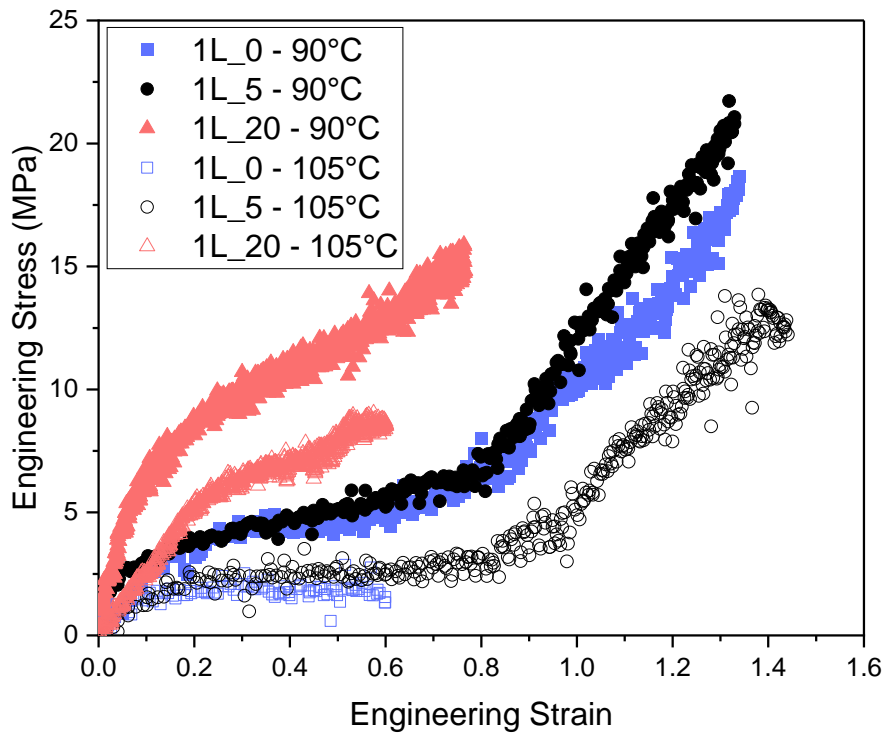
Figure 7-2 : Engineering stress over strain values recorded during bi-axial stretching of monolayer samples with different amount of MMT inside (0, 5 and 20wt%).

In **Figure 7-2**, in the case of monolayer films, we observed an increase of Young's modulus with increasing content of MMT in the samples compared to the sample without MMT (1L_0). As a reminder the Young Modulus correspond to the material stiffness and is calculated from the slope of the engineering stress over strain at low deformation. The values increase from 21 MPa at 0wt% MMT to 33 MPa for 5wt% MMT, and 54 MPa for 20wt% MMT at a temperature of 90°C. At 105°C, the measured modulus are about 17.5 MPa at 0wt% MMT, 12.9 MPa at 5wt% MMT, and 24 MPa at 20wt% MMT. These results are consistent with the literature on nanocomposites. Indeed, the presence of nano-fillers increases the number of interactions between polymers and fillers, resulting in an increase in the Young's modulus (**Ji et al., 2012**). The temperature increases the chain mobility in the samples, which leads to a decrease of material stiffness and thus to a decrease of their modulus which is the case at 105°C (**Matsuo & Sawatari., 1998**).

CHAPTER 7: BI-AXIAL STRETCHING: EFFECT ON MONTMORILLONITE ORIENTATION AND LINEAR LOW-DENSITY POLY(ETHYLENE) CRYSTALS

For stretching carried out at 90°C and 105°C, a plateau is observed at an engineering strain level between 0.2 and 0.8 for samples containing 0 and 5wt% MMT. This corresponds to the onset of the yield point and the propagation of necking, which indicates a disentanglement of the polymer chains in the amorphous region. This can also result from crystal fragmentation, sliding, and interlamellar shear (**Xu et al., 2023**). The engineering stress value at the plateau is higher for stretching at 90°C than at 105°C due to the presence of more LLDPE crystal lamellae. After the plateau, the engineering stress increases noticeably at higher strain levels. This phenomenon resembles strain-hardening. It is commonly attributed to a reorganization of the polymer chain and a change in morphology from crystals to highly oriented fibril structures (**Xu et al., 2023**). This strain-hardening is observed in samples containing 5wt% of MMT at both 90°C and 105°C, as well as in the MMT-free sample (yet only at 90°C). This suggests that MMT fillers have an impact on this transformation. At 105°C, more LLDPE crystals melt, what results in a decrease in mechanical toughness and more disentanglement of the polymer chains and are thus prone to break at low deformation. However, the presence of fillers and LLDPE crystals forms a network-like configuration that maintains the structure during high deformation.

Finally, at high deformation, the ultimate engineering stress (value at the end of the curve) is higher at 90°C than at 105°C, reaching approximately 20 MPa at 90°C compared to 12 MPa at 105°C. This suggests potentially different levels of orientation and textures, possibly due to a lower proportion of crystal lamellae at 105°C compared to 90°C. However, this does not affect the deformation level right before break.

For the sample containing 20wt% MMT, the yield point is less pronounced and the presence of a necking propagation plateau is not clearly identifiable. As the structure reorganizes and the modulus increases towards strain levels of 0.5, fast rupture is observed. The increased concentration of MMT fillers leads to an increase in polymer/MMT interfaces, which can cause cavitation phenomena (creation of voids in the polymer matrix). According to **Rahmanian et al., 2024**, the material rupture may occur at an advanced strain level due to cavitation phenomena resulting from the presence of adhesion sites that are more susceptible to losing their adhesion.

7.1.2.2 Multi-nano layer films

Figure 7-3 below show the engineering stress over strain curves, in the transverse direction of the multi-nano layer films (the one from the extrusion direction of the film is the same).
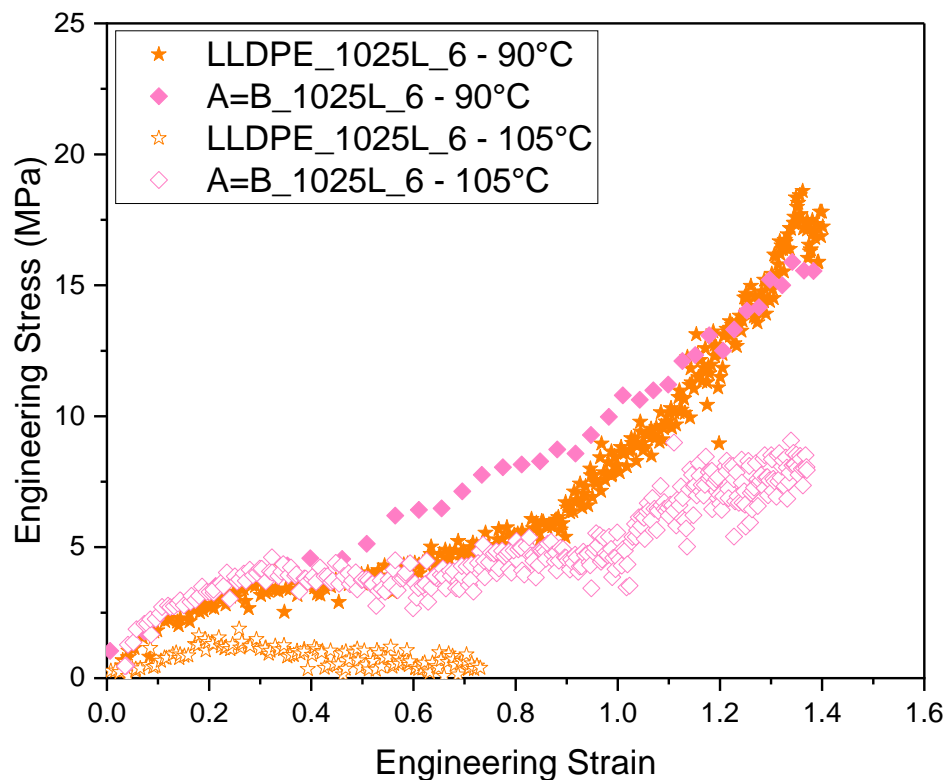
Figure 7-3 : Engineering stress over strain values recorded during bi-axial stretching of multi-nano layer samples with 0 and 5wt% of MMT.

The value of Young modulus of multi-nano-layer films containing 5wt% of MMT is about 12 MPa at both 90°C and 105°C. In contrast, the MMT-free film reaches 11 MPa at 90°C and 8 MPa at 105°C. The plateau of the necking propagation appears at an intermediate strain level, typically between 0.2 and 0.8. However, the plateau is less pronounced for bi-axial stretching at 90°C rather than at 105°C. This might suggest that samples are prone to less crystallographic transformations and goes directly to a fibrillary structure reorganization. At

105°C, the film without filler exhibits a notably lower yield stress and an early rupture at a strain level of 0.7, compared to 1.3 for the other films. These results are consistent with those obtained for the MMT-free monolayer film at the same temperature. Finally, at higher strain levels (0.8 to 0.9), a strain-hardening is also observed as a result of reorganization phenomena and the formation of more oriented structures, as previously mentioned for monolayer films.

7.1.2.3 Monolayer vs Multi-nano layer films

Figure 7-4 and **Figure 7-5** compare the engineering stress over strain curves obtained for MNL films and the monolayer films with 0wt% of MMT and 5wt% of MMT respectively.
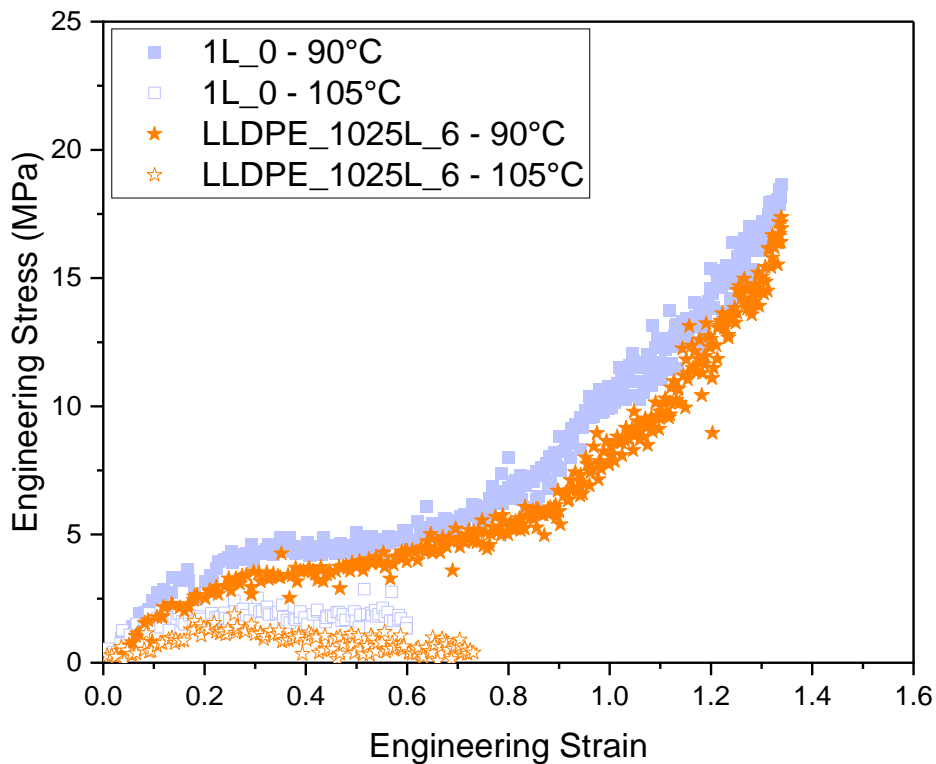
Figure 7-4 : Engineering stress over strain values recorded during bi-axial stretching of monolayer and multi-nano layer samples without MMT.

At both temperatures, the Young modulus of the MNL film is lower than the one of the monolayer film. At 90°C the Young modulus is about 21 MPa for the monolayer film against 11 MPa for the MNL film and at 105°C of 17.5 MPa versus 8 MPa respectively. This means MNL are softer than the monolayer films. This observation is surprising because in some cases MNL is used to increase films stiffness (**Li et al., 2024**). At higher engineering strain, both film architectures have the same behavior. At 90°C, the necking propagation plateau occurs at roughly the same engineering strain values to go strain-hardening. At 105°C, both film architectures lead to a break at low deformation, during the necking propagation plateau. The MNL film goes to a higher deformation value (0.7 versus 0.6 for the monolayer film). It may be due to the architecture, which provides a better chains organization leading to a slightly better resistance to the deformation.
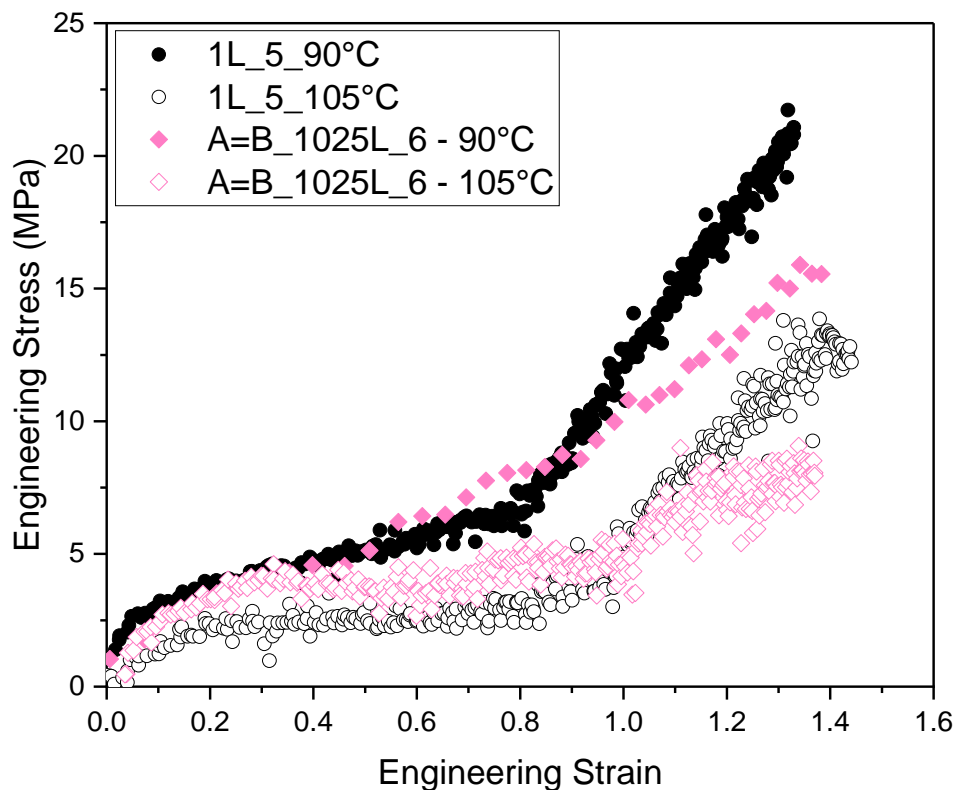
Figure 7-5 : Engineering stress over strain values recorded during bi-axial stretching of monolayer and multi-nano layer samples with 5wt% of MMT.

In **Figure 7-5**, the addition of 5wt% of MMT, at both temperatures, the Young modulus of the MNL film is lower than the one of the monolayer film. At 90°C the Young modulus is about 33 MPa for the monolayer film against 12 MPa for the MNL film and at 105°C of 12.9 MPa versus 12 MPa respectively. The effect of fillers addition and temperature on modulus variations are less pronounced in multi-nano layer films compared to monolayer films. At higher engineering strain, both film architectures have the same behavior, a necking propagation plateau and then a strain-hardening. The strain-hardening appears at higher engineering strain at 105°C. Indeed, at 105°C polymer chains have more mobility than at 90°C leading to more disentangling and a delayed strain-hardening. All the samples goes to the same level of deformation at 90°C and 105°C which is not the case of MMT free films at 105°C. This means, the presence of MMT allows for higher deformations at 105°C by creating a network-like structure with LLDPE crystals and it is not due to the film architecture. Finally, the engineering stress value of the film before the break is different in all the films. It may suggest different level of organization or fibrillary structure.

The bi-axial stretching trials yielded valuable information about the morphological changes in the films. It is now necessary to characterize the MMT orientation to identify any improvements and determine if the microstructural changes identified from the engineering stress over strain curves have an impact on it. The crystallinity will also be evaluated to determine if the observed strain-hardening is partially due to a reorganization of the amorphous phase. In this case, it would increase the crystallinity. Additionally, the texture of the LLDPE crystals must also be characterized to identify any textural changes that may indicate the presence of a fibrillary structure and explain the observed strain-hardening.

7.2 THE ORIENTATION OF THE MMT NANO-FILLERS AND CORRELATION TO THE H$_2$O BARRIER PROPERTIES

In this part, the objective is to measure the 002 pole figures of MMT of all the bi-axially stretched films in order to extract the integral breadth to identify any MMT 'in-plane' orientation improvement. Then the MMT H$_2$O barrier properties of the films will be investigated in order to establish any potential correlations with the MMT 'in-plane' orientation.

7.2.1 Orientation of the MMT nano-fillers

The orientation of montmorillonite was analyzed in monolayer samples with 5 and 20wt% MMT concentrations (1L_5 and 1L_20), as well as in multi-nano layer samples with 5wt% MMT (A=B_1025L_6). Texture analysis were conducted in order to assess the orientation of the (002) montmorillonite lattice plane, and the results were presented in pole figures.

The pole figures for the 90°C and 105°C bi-axial stretching are shown in **Figure 7-6**. The integral breadth values extracted from the pole figures are compiled in **Table 7-2**, along with the IB calculated for the samples before bi-axial stretching.

002 POLE FIGURE AFTER BI-AXIAL STRETCHING

90°C | **105°C**

1L_5 | **1L_5**

1L_20 | **1L_20**

A=B_1025L_6 | **A=B_1025L_6**
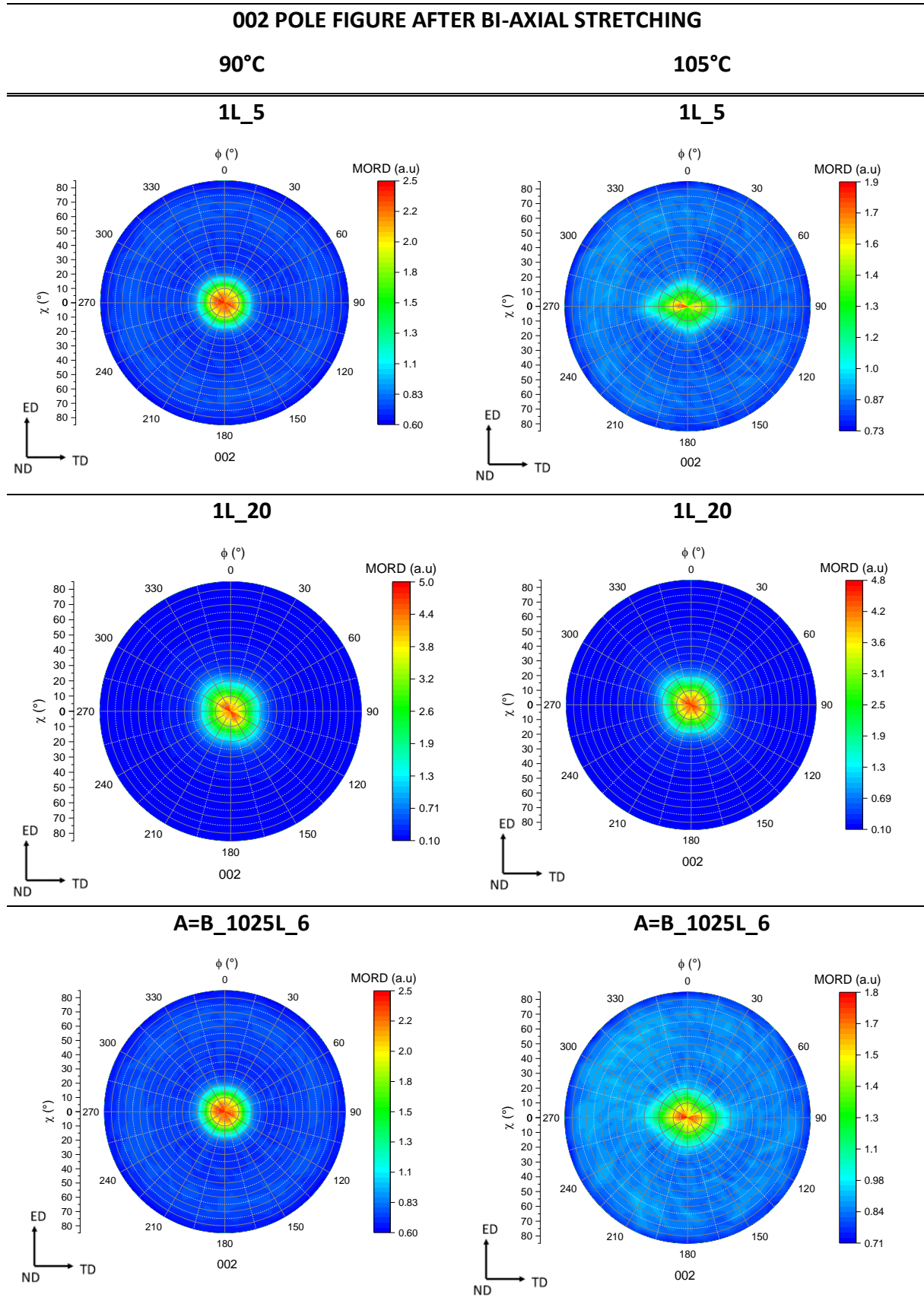
Figure 7-6 : Pole figures of the MMT (002) lattice planes of bi-axially stretched samples at 90°C and 105°C.

234

CHAPTER 7: BI-AXIAL STRETCHING: EFFECT ON MONTMORILLONITE ORIENTATION AND LINEAR LOW-DENSITY POLY(ETHYLENE) CRYSTALS

In most cases, the pole figures are similar, with a significant diffraction intensity at their center, localized for χ values between 0 and 20°. However, when stretched at 105°C, the diffraction signal slightly elongates in the TD direction while ED and TD are stretched simultaneously.

Table 7-2 : Integral breadth values extracted from 002 MMT pole figures displayed in Figure 7-6.

SAMPLE	INTEGRAL BREADTH (°)		
	BEFORE BI-AXIAL STRETCHING	AFTER BI-AXIAL STRETCHING AT 90°C	AFTER BI-AXIAL STRETCHING AT 105°C
1L_5	52 ± 1	30 ± 0.2	34 ± 0.8
1L_20	42 ± 0.5	31 ± 0.2	32 ± 0.8
A=B_1025L_6	53 ± 1	32 ± 0.2	31 ± 0.8

An improvement in the 'in-plane' orientation of the MMT nano-fillers is evident. For samples containing 5wt% MMT, the integral breadth decreases from 52-53° ± 1° to values ranging from 30° ± 0.2° to 34° ± 0.8°, depending on the bi-axial stretching temperature. Similarly, for samples with 20wt% MMT, the integral breadth decreases from 42° ± 0.5° to 31° ± 0.2° -32° ± 0.8° after bi-axial stretching. It is worth noting that neither the MMT concentration nor the film architecture affects the IB achieved after bi-axial stretching.

In **Chapter 5**, we analyzed the effect of MMT on the crystallization and orientation of LLDPE crystals. Our proposal is that LLDPE crystallization initiates at the edges of MMT loadings. Therefore, during bi-axial stretching conducted below the melting temperature of LLDPE, LLDPE crystals remain in lamellar form near these fillers. These LLDPE crystals may act as rigid points during bi-axial stretching, facilitating stress transfer and inducing greater shear on the MMT fillers. This would improve the local orientation of MMT fillers. Studies have shown that stress transfer affects the orientation of montmorillonite. **Tabatabaei & Ajji., 2011** observed that MMT orientation is more favorable in a poly(lactic acid) matrix than in a poly(propylene) matrix under equivalent process conditions. This was attributed to the higher viscosity of PLA, which enhances stress transfer and promotes MMT orientation. **Ren et al.,**

2015 showed that PE crystalline domains act as nodes, forming a network-like structure between montmorillonite and PE. This facilitates the orientation of MMT during stretching in a PE-MMT system.

Therefore, our findings indicate that the presence of LLDPE crystals, which act as hard points and facilitate stress transfer onto the MMT, favors their 'in-plane' orientation.

Finally, if we contrast the values of orientation with the engineering stress-strain curves in **Figure 7-2** and **Figure 7-3**, we can observe that whether the level of deformation achieved (engineering strain) or the engineering stress reached right before the break, the orientation of the MMT remain similar. This means that all the samples seem to have different levels of organization at the end of the bi-axial stretching, but they all have the same 'in-plane' orientation. However, all the samples have reached the necking propagation plateau (more or less identifiable according to the samples). Therefore, we can hypothesize that the improvement in the 'in-plane' orientation of the MMT may occur at this stage. To verify this hypothesis, a pole figure should be recorded at each stage of the bi-axial stretching trials to track the MMT orientation.

7.2.2 Correlation of the MMT orientation with the H_2O barrier properties

We aim here at determining whether the MMT orientation improvements observed after bi-axial stretching below the melting temperature result in enhanced barrier properties in film

Figure 7-7 presents the water permeability values measured on samples before and after bi-axial stretching at 90°C and 105°C.
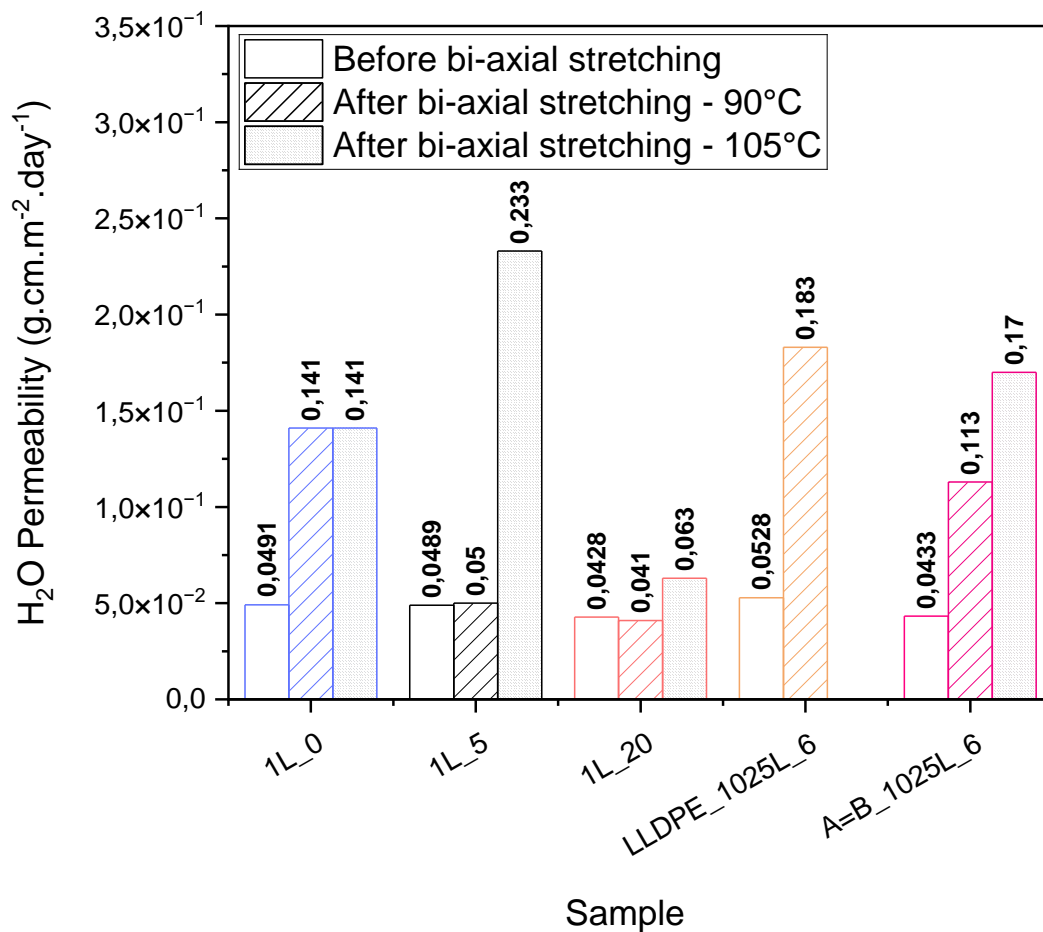
Figure 7-7 : H_2O permeability values versus the temperature at which the bi-axial stretching was performed for all the samples studied.

All permeability values of the films were similar before bi-axial stretching. However, after the bi-axial stretching, significant variations were observed between samples. Surprisingly, in most cases, water permeability was not reduced after the bi-axial stretching process, while the 'in-plane' orientation of MMT was significantly improved (**Table 7-2**).

After bi-axial stretching at 90°C, the film without MMT fillers showed a significant increase of 187% in water permeability compared to the situation before bi-axial stretching. However, films with fillers showed only a slight increase in H_2O permeability. The addition of 5wt% MMT resulted in a 2% increase, while the addition of 20wt% MMT resulted in a 3% decrease. At 105°C, samples with MMT showed a greater increase in permeability, with increases of 376% and 47% for 5% and 20% MMT, respectively.

237

The MNL configuration followed a similar trend. After being stretched in two directions at 90°C, the film without MMT showed a 246% increase from the initial measurement. The film with 5wt% MMT showed a 160% increase. At 105°C, the increase became even more significant, reaching 292% with 5wt% MMT. It is important to note that the film without any filler could not be measured at 105°C due to a hole that appeared during stretching.

Despite the improvement in the 'in-plane' orientation of the MMT, we did not observe a decrease in water permeability. In fact, the values have more than doubled.

However, the increase is most significant at 105°C. This intensification could result from i) a more pronounced melting of the LLDPE lamellae, leading to a reduction in the crystallinity, or ii) a textural change. As shown in the previous chapter, the orientation of LLDPE appears to be a crucial factor in determining the barrier properties of the film. LLDPE crystallized with a preferred orientation when the films were uniaxial stretched above the melting temperature, resulting in a slight improvement in the MMT 'in-plane' orientation but a 38% increase in water permeability.

Furthermore, intense deformation may cause the formation of fibrillar structures, resulting in cavities due to decohesion phenomena and morphological changes (**Pawlak et al., 2014**). However, in our case, we observed strain-hardening, indicating a potential fibrillary organization of LLDPE crystals. Therefore, our structure is susceptible to cavity formation, which could explain the significant increase in water permeability of the films, despite the improvement in MMT 'in-plane' orientation.

7.3 LINEAR LOW-DENSITY POLY(ETHYLENE) CRYSTALLIZATION AND TEXTURE INVESTIGATION

This section aims to clarify and describe any microstructural modifications that occur in the films during the bi-axial stretching process. The investigation aims to explain the significant increase in water permeability, despite the improved 'in-plane' orientation of montmorillonite. To achieve this goal, we analyzed DSC to evaluate the potential increase in crystallinity, which may be associated with reorganizations within the amorphous phase.

Finally, texture measurements were conducted on LLDPE to identify any alterations in lamella morphology. As well as any correlation of LLDPE crystallization changes with the strain-hardening observed on engineering stress-strain curves.

7.3.1 Investigation of crystallinity changes: DSC measurements

The question at hand is whether strain hardening increases crystallinity by organizing the amorphous chains between the LLDPE crystals or simply modifies the orientation of the crystals without increasing their amount.

To investigate this, we conducted DSC measurements on the samples after bi-axial stretching. **Figure 7-8** displays the portion of the first heating cycle that contains the sample melting peak. The first heating cycle of the films before bi-axial stretching are displayed in **Figure 7-1**.

After bi-axial stretching at 90°C and 105°C, various melting peak morphologies were observed depending on the samples and specific biaxial stretching conditions. In most cases, a single melting peak is observed, which may vary in width depending on the samples and bi-axial stretching conditions.
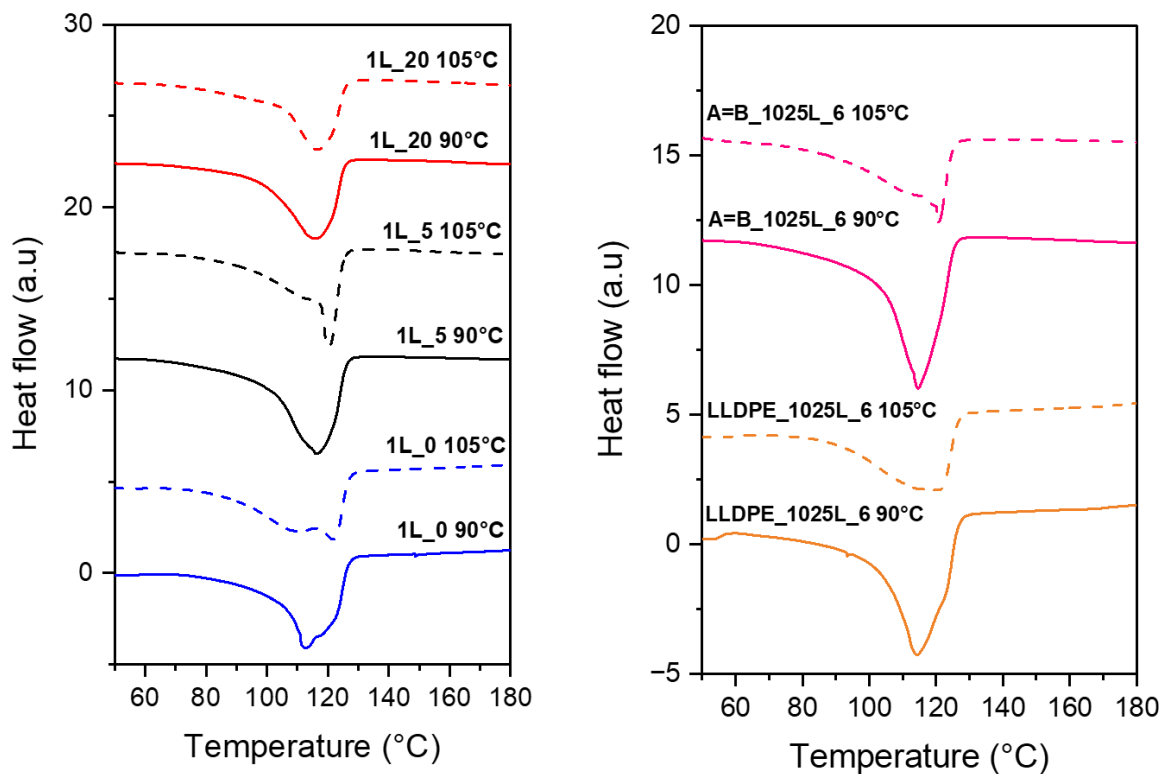
Figure 7-8 : DSC thermograms of the first heating cycle of the samples after bi-axial stretching at 90°C and 105°C. On the left, monolayer samples and on the right multi-nano layer samples. The positive value of the heat flow is for endothermic peaks.

Upon examining the monolayer films, it is observed that the MMT-free film has two closely spaced melting peaks. The first peak, which is more pronounced, occurs at around 116°C for the sample stretched at 90°C. Conversely, for the sample bi-axially stretched at 105°C, the second peak located at around 120°C is more prominent. The film with 5wt% MMT, on the other hand, has a single wide peak with a maximum at 116°C for the sample stretched at 90°C. The melting peak for the equivalent sample stretched at 105°C is narrower and located at 120°C. When 20wt% MMT is present, a single wide peak remains with a maximum at 116°C, regardless of the bi-axial stretching temperature. This analysis suggests that bi-axial stretching at 105°C generally results in narrower melting peaks at higher temperatures, indicating the presence of more homogeneous and thinner-sized lamellae. Increasing the filler concentration appears to limit these changes.

240

Figure 7-8 shows that films with a multi-nano-layer architecture exhibit a single, narrow melting peak, especially when stretched at 90°C. The peak maximum temperature is around 114°C for films with 0wt% and 5wt% of MMT. When stretched at 105°C, the film without MMT shows a wide peak, while the film containing 5wt% of MMT shows a narrow peak with a maximum at 120°C. These observations suggest that the MNL architecture leads to narrower peaks, indicating a more homogeneous population of lamellar sizes. The broad peak at 105°C without MMT can be explained by the fact that the film reached lower levels of deformation than the film with fillers.

The stretching stopped during necking mechanisms, where crystal fragmentation occurs, whereas in the other cases (with 5wt% MMT), stretching went as far as strain hardening, which favors more oriented and regular structures, which explains the presence of fine peaks.

Therefore, the thermograms reflect changes in crystal size resulting from biaxial stretching, as evidenced by variations in the melting peak maxima and shapes.

The lamellar sizes were calculated from the DSC measurements and are listed in **Table 7-3**.

Table 7-3 : LLDPE lamella size (l) after bi-axial stretching at 90°C and 105°C determined from DSC thermograms from Figure 7-8.

SAMPLE	BI-AXIAL STRETCHING TEMPERATURE	T_{f1} (°C)	T_{f2} (°C)	l_1 (nm)	l_2 (nm)
1L_0	90°C	112.82	116.48	7.97	8.97
	105°C	110.81	121.77	7.51	10.95
1L_5	90°C	116.12	/	8.86	/
	105°C	120.51	/	10.40	/
1L_20	90°C	116.06	/	8.84	/
	105°C	116.53	/	8.99	/
LLDPE_1025L_6	90°C	114.33	/	8.35	/
	105°C	119.51	/	10.01	/
A=B_1025L_6	90°C	114.52	/	8.41	/
	105°C	120.71	/	10.49	/

CHAPTER 7: BI-AXIAL STRETCHING: EFFECT ON MONTMORILLONITE ORIENTATION AND LINEAR LOW-DENSITY POLY(ETHYLENE) CRYSTALS

After bi-axial stretching, the monolayer MMT-free film exhibits a significant reduction in lamellar size compared to the initial sample (refer to **Table 7-1**). This reduction leads to the emergence of two distinct lamella populations: a first population of shorter lamellae that decreases in size from approximately 10 nm to 7-9 nm, and a second population of larger lamellae that remains the same. The reduction in size can be attributed to crystal fragmentation or defibrillation (**Bowden & Young., 1974; Peterlin, 1967**). **Chen et al., 2020** also observed a decrease in crystalline lamellae size due to fragmentation during biaxial stretching of LLDPE.

The addition of 5wt% of MMT resulted in the disappearance of the two distinct lamellar populations after bi-axial stretching at 90°C and 105°C. Shorter lamellae persisted at 90°C while longer lamellae were preserved at 105°C. After bi-axial stretching, both cases with 20wt% MMT showed a reduction in lamellar size from 9.6 nm to approximately 8.8 nm, indicating possible defibrillation. Similar observations were made in the context of the MNL architecture, regardless of the presence of MMT, compared to the monolayer sample with 5wt% MMT.

The values of fusion enthalpy were extracted from the peaks obtained by DSC, and the resulting crystallinity percentages are shown in **Figure 7-9**.

The bi-axial stretching process enhances the film's crystallinity regardless of its architecture. However, the extent of this enhancement is for most cases affected by the test temperature. A more significant increase is observed at 90°C compared to 105°C. This may be due to fewer LLDPE crystals initially melting when the sample is heated to 90°C, unlike at 105°C where complete melting is approached. However, the increase in crystallinity may also be due to the reorganization of the amorphous phase, which is typically observed in bi-axial stretching processes. This phenomenon contributes to a more ordered structure. Stress is applied to both crystals and amorphous polymer chains, resulting in deformation in the rubbery state. This triggers various mechanisms within the crystalline lamellae, such as fine slip, coarse slip, or interlamellar slip. These processes elongate the amorphous phase between the lamellae, promoting better organization (**Xu et al., 2023**).
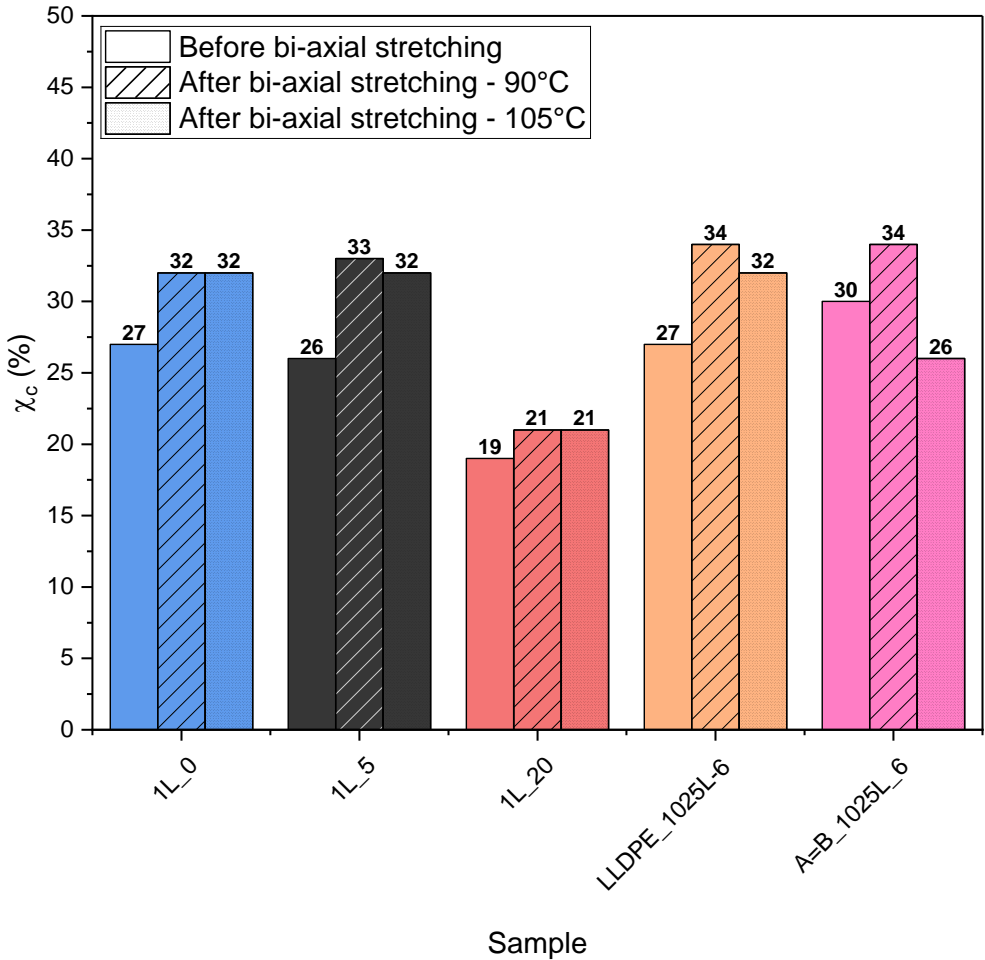
Figure 7-9 : Percentage of crystallinity (χ_c) in the samples before and after bi-axial stretching at 90°C and 105°C determined from the DSC thermograms shown in Figure 7-8.

Biaxial stretching consistently increases crystallinity, but it also affects lamellar size. Additionally, defibrillation and morphological changes that promote cavitation may contribute to the paradox between increased crystallinity and increased water permeability.

7.3.2 Investigation of linear low-density poly(ethylene) texture changes: XRD pole figures

XRD texture analysis was performed on the samples after bi-axial stretching at temperatures of 90°C and 105°C to characterize induced morphologies. Samples analyzed included monolayer films with 0, 5, and 20wt% MMT and multi-nano layer films with 0 and 5wt% MMT. Results are presented in pole figures and summarized in **Figure 7-10**, **Figure 7-11**, **Figure 7-16** and **Figure 7-17**.

The pole figures obtained from monolayer samples stretched bi-axially at 90°C exhibit distinct characteristics. At 0 and 5wt% MMT, the structures are similar. Specifically, for the lattice planes (200), a peak of maximum diffraction is observed at the center of the pole figure, indicating that the crystallographic $\vec{a}$ axis of the LLDPE lamellae is oriented parallel to the film normal direction. The lattice plane (020) shows weak diffraction intensity throughout the pole figure (at all χ and ϕ values). However, there are two poles of maximum diffraction at the TD at χ angles greater than 75°, indicating a preferential orientation of the crystallographic $\vec{b}$ axis in the transverse direction. These observations suggest a change in the orientation of the LLDPE lamellae, from an 'in-plane' orientation before bi-axial stretching to an 'edge-on' orientation after bi-axial stretching. In the previous chapter, it was noted that the orientation of LLDPE lamellae was predominantly 'in-plane'. The 'edge-on' orientation obtained is consistent with the orientation found in the study of biaxial stretching of polyethylene by **Aiji et al., 2015**.

1L_0 – 90°C

110   200   020

1L_5 – 90°C

110   200   020

1L_20 – 90°C

110   200   020

Figure 7-10 : Pole figures of the (110), (200) and (020) LLDPE lattice planes of monolayer bi-axially stretched samples at 90°C.

For the (110) lattice plane orientation, three diffraction poles appear in the TD, aligned with the TD-ND axis. Two symmetrical high density diffraction poles appear at an angle χ of about 60° to the ND and about 30° to the TD, corresponding to the orientation of the (110)

245

lattice plane for an 'edge-on' arrangement. Additionally, a central diffraction pole is observed in the ND direction, but it is not associated with the (110) lattice plane.

The orientations obtained for the 20wt% MMT film are similar to those for the 0 and 5wt% MMT monolayer films. However, the pole figure of the lattice plane (020) shows a diffraction circle at angles χ greater than 50° and at all values of ϕ, with more pronounced diffraction in the direction transverse to the extrusion. Similarly, the pole figure (110) exhibits diffraction poles at an angle of approximately 60° to ND and 30° to TD. The diffraction pattern of these poles is strongest in the TD-ND direction (at ϕ = 90° and 270°) and slightly weaker in the ED-ND direction (at ϕ = 0 and 180°). This indicates that the LLDPE lamellae are oriented 'edge-on', but with a partially random distribution in relation to the normal and the film surface.

Figure 7-11 : Pole figures of the (110), (200) and (020) LLDPE lattice planes of multi-nano layer bi-axially stretched samples at 90°C.

CHAPTER 7: BI-AXIAL STRETCHING: EFFECT ON MONTMORILLONITE ORIENTATION AND LINEAR LOW-DENSITY POLY(ETHYLENE) CRYSTALS

The MNL samples that underwent bi-axial stretching at 90°C exhibit a texture similar to the previous monolayer films. In both cases, with and without MMT, the diffraction maximum at the center of the pole figure for the lattice plane (200) indicates a predominant orientation of the crystallographic $\vec{a}$ axis in the normal direction. The pole figures for the lattice plane (020) show a maximum in the TD, indicating that the crystallographic $\vec{b}$ axis is perpendicular to the film normal and in the TD direction. Films without MMT exhibit a diffraction circle at all φ values between χ values of 50° and 80°, indicating an isotropic orientation of the crystallographic $\vec{b}$ axis with respect to the film normal. However, in the presence of MMT, the diffraction pole maxima are concentrated only in the TD, resulting in the loss of this isotropic crystallographic $\vec{b}$ axis orientation.

In both configurations, a diffraction signal is still observed at the center of the pole figure for the (110) lattice plane, although it does not belong to the plane itself. However, its contribution is less significant than in the case of monolayer samples.

To clarify the presence of the central point in the pole figure of the lattice plane (110), we analyzed the 2θ scans recorded prior to the texture measurements. It was noticed that certain X-ray diffraction patterns indicate the potential emergence of a secondary crystalline phase in LLDPE.
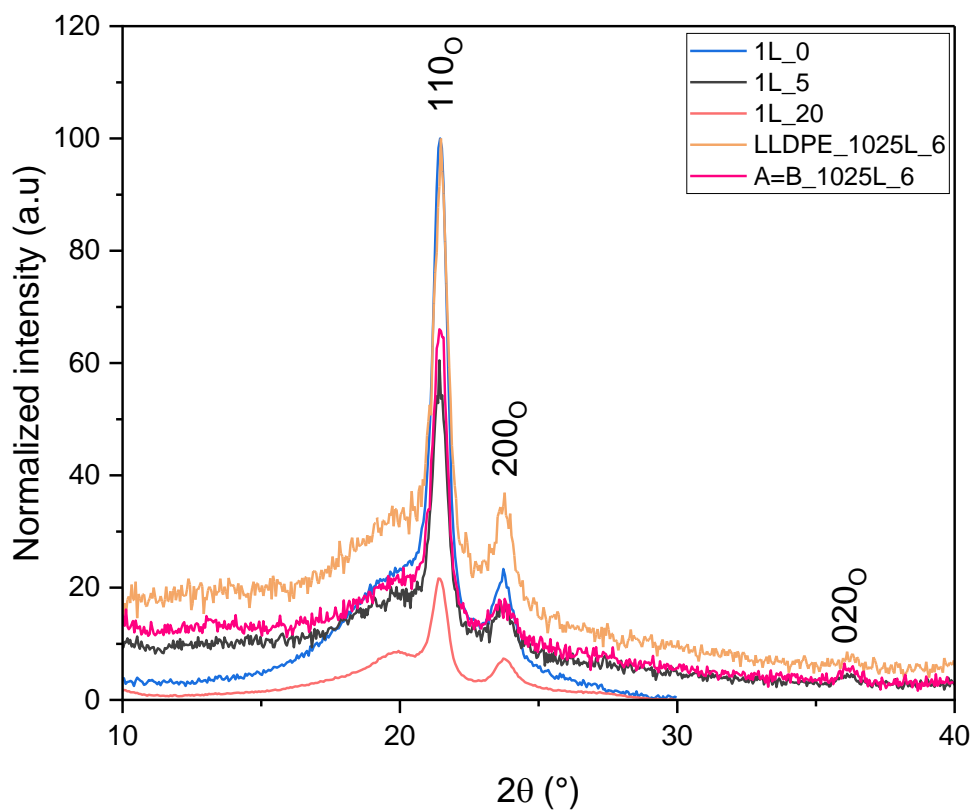
Figure 7-12 : XRD patterns measured on the samples studied before bi-axial stretching.

Before bi-axial stretching, the XRD pattern of the film in **Figure 7-12** shows 110, 200, and 020 Bragg peaks, all belonging to the orthorhombic phase of the LLDPE. At a 2θ angle of 20°, there is a broad halo, which varies in intensity depending on the sample. This halo is typically associated with the contribution of the amorphous phase.

Figure 7-13 and **Figure 7-14** show the XRD pattern of the film after bi-axial stretching at 90°C and 105°C, respectively.
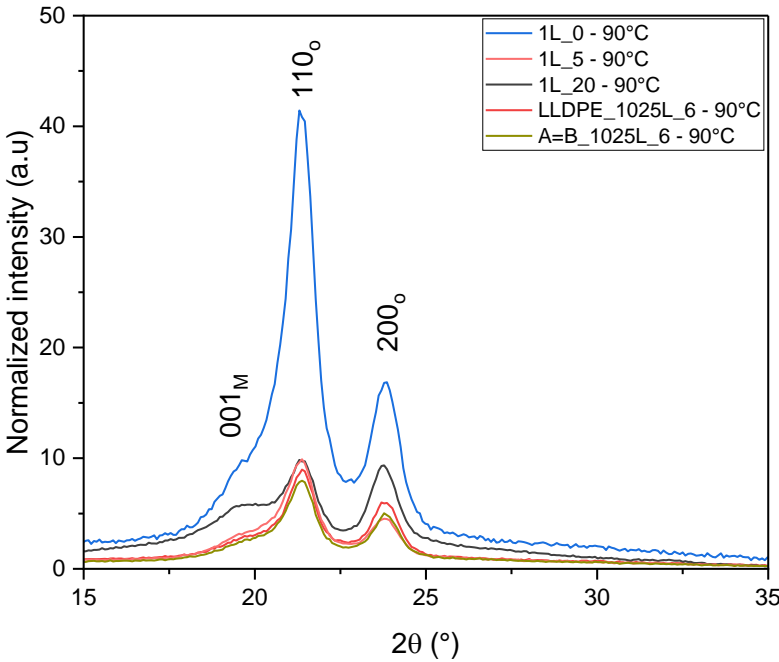
Figure 7-13 : XRD patterns measured on the samples studied, identification of the 001 monoclinic Bragg peak after bi-axial stretching at 90°C.
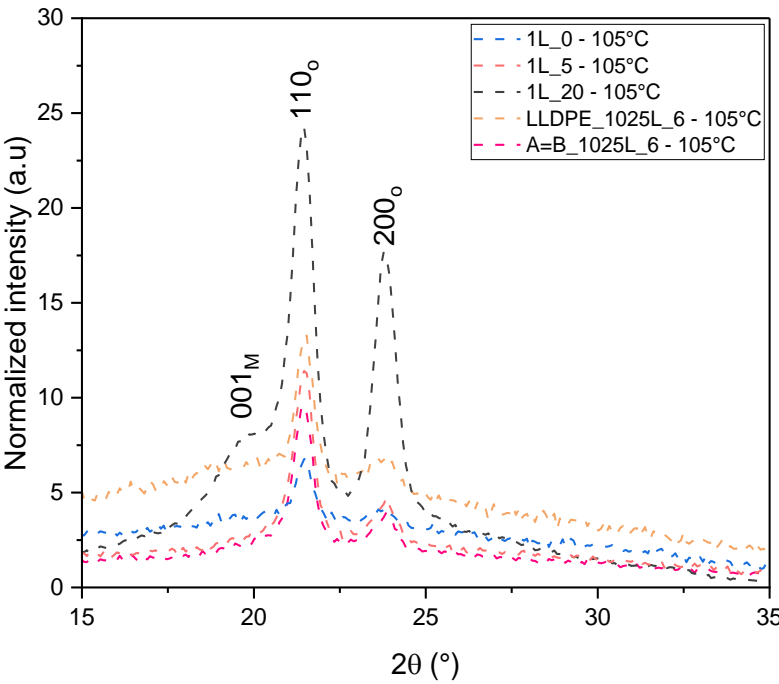
Figure 7-14 : XRD patterns measured on the samples studied, identification of the 001 monoclinic Bragg peak after bi-axial stretching at 105°C.

XRD patterns of samples bi-axially stretched at 90°C in **Figure 7-13** display an enlargement of the 110 LLDPE Bragg peak compared to the pattern shown in **Figure 7-12** before bi-axial stretching. On the contrary at 105°C, in **Figure 7-14**, the 110 Bragg peaks does not seem to present an enlargement, except for the film containing 20wt% of MMT. This enlargement suggests an overlapping of several Bragg peaks. It is unclear whether the observed shoulder is due to the contribution of the amorphous phase or the appearance of a new phase. As mentioned in **Chapter 2**, stretching at temperatures below 110°C can lead to martensite deformation, resulting in the presence of two phases in LLDPE: an orthorhombic unit cell and a monoclinic phase. This transformation results in a change in the β angle of the lattice cell from 90° to 107.9° (**Peacock., 2000**), and a change in the lattice parameter b from about 4.95 to 4.79 Å (**Peacock., 2000**), although these variations remain very close. Thus, several peaks of the monoclinic phase may appear.

Figure 7-15, displays the pole figure obtained at a 2θ = 19° on sample 1L_0 without MMT stretched at 90°C. This 2θ position corresponds to the 110 Bragg peak enlargement identified in **Figure 7-13**.
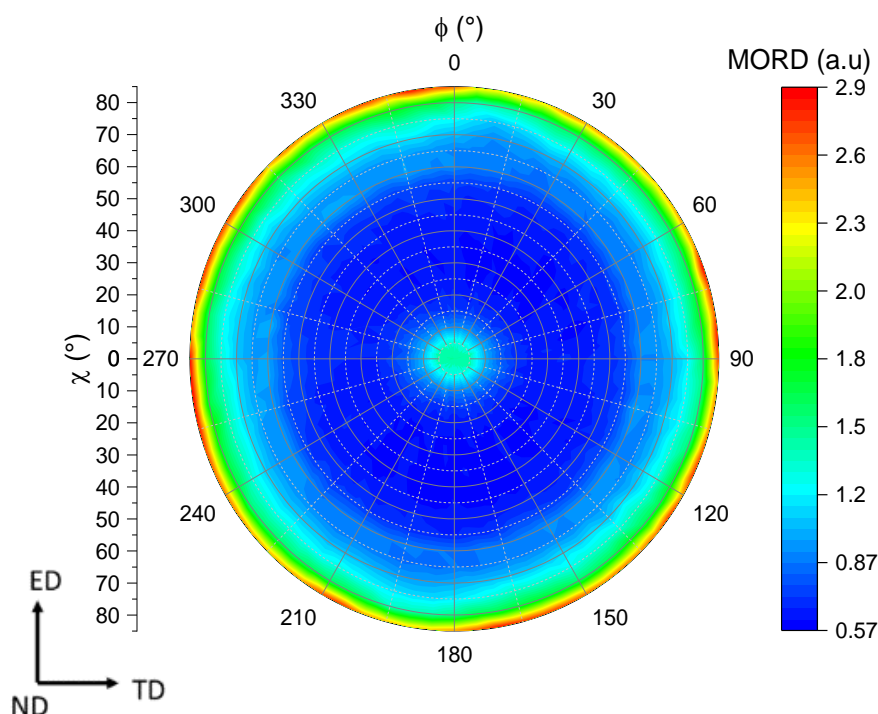
Figure 7-15 : Pole figure of the Bragg peak located at 2θ = 19° from the monolayer sample without MMT bi-axially stretched at 90°C.

CHAPTER 7: BI-AXIAL STRETCHING: EFFECT ON MONTMORILLONITE ORIENTATION AND LINEAR LOW-DENSITY POLY(ETHYLENE) CRYSTALS

A circle-shaped maximum diffraction intensity is observed for all values of ϕ at angles of χ greater than 75°, with the maximum located at 85°. This indicates that this part can be attributed to the (001) lattice plane of the monoclinic phase. The lamellae in this sample are oriented in the 'edge-on' configuration with the crystallographic $\vec{a}$ axis perpendicular to the ND and the crystallographic $\vec{b}$ axis in the TD direction. The crystallographic $\vec{c}$ axis is placed perpendicular to the ND, which is identified by the highest diffraction intensity located at χ angles higher than 85°. The diffraction pole at the center is most likely a contribution from the (200) lattice plane of the monoclinic phase of LLDPE formed following the martensitic deformation. In **Wang et al., 2019** work, the Bragg peaks for the (001), (200), and (201) lattice planes of the monoclinic phase were found to be very close to the 110 and 200 peaks of the orthorhombic phase. **Wang et al., 2019** used a high-energy X-ray source with good resolution, while our work's resolution is comparable to that of **Butler et al., 1995** or **Feng et al., 2011**. **Figure 7-10** and **Figure 7-11** identify the contribution of the overlapping 001_M, 110_O, 200_M, 200_O, and 201_M Bragg peaks in the region of 2θ angles from 19 to 25°, on pole figures.

Martensitic deformations can be identified consistently since they occur in PE at temperatures below 110°C. Additionally, these transformations align with the slip mechanism between lamellae that occurs during plastic deformation induced by bi-axial stretching, as described by **Xu et al., 2023** and **Peterlin., 1967**.

Figure 7-16 illustrates the impact of biaxial stretching at 105°C on pole figures.

The texture obtained after bi-axial stretching at 105°C differs slightly from that obtained at 90°C. Notably, films without MMT filler exhibit a difference that is absent at 90°C. Specifically, without MMT filler, there is no observed change in LLDPE lamellae orientation from 'in-plane' to 'edge-on'. Instead, diffraction poles are observed on both TD and ED for the (110) and (200) lattice planes. The lamellae orientation is distributed along both the ED and TD axes, with a tendency to be perpendicular to the ND of the film. When MMT fillers are present, the behavior is similar to that observed on the same samples bi-axially stretched at 90°C.
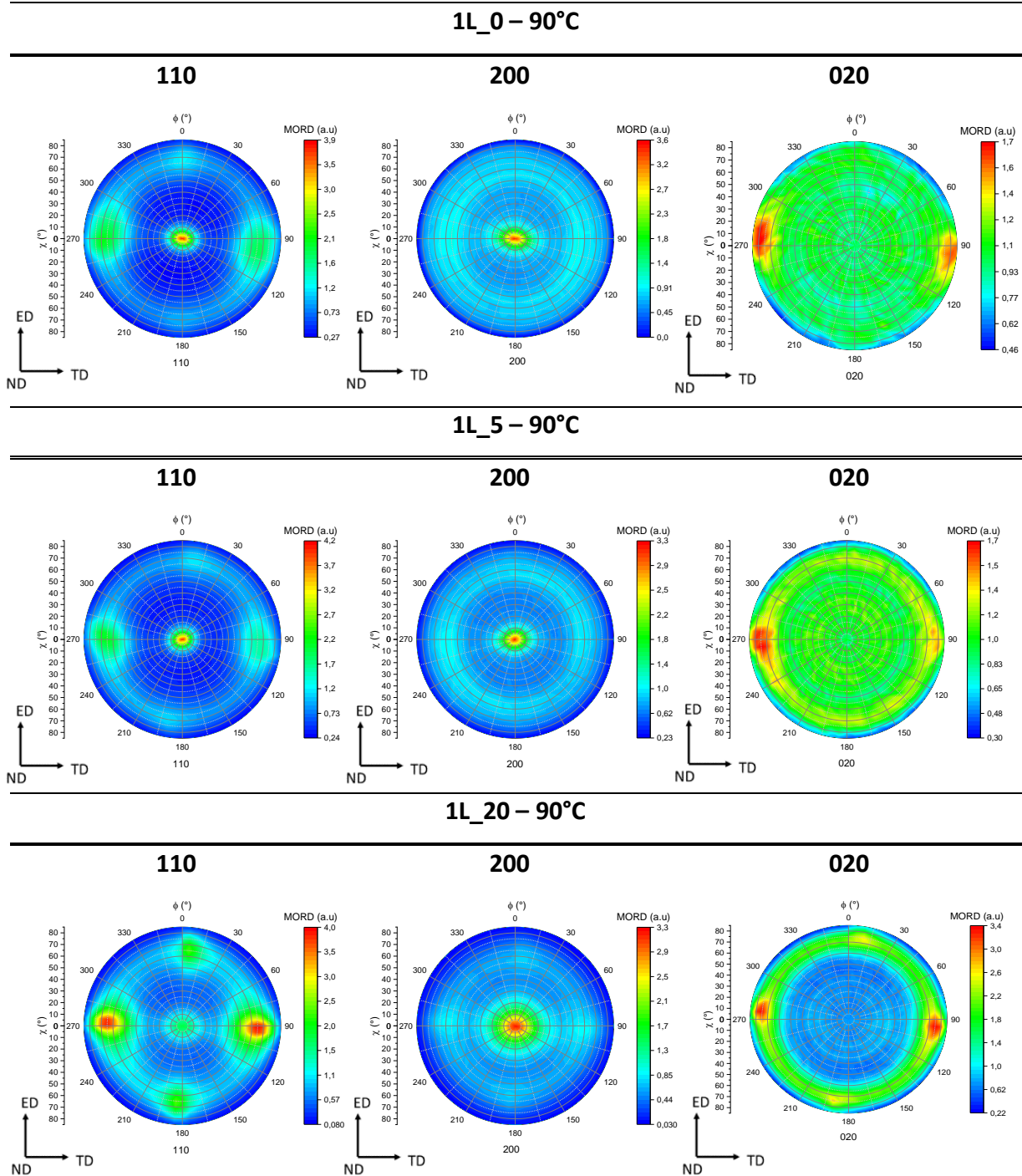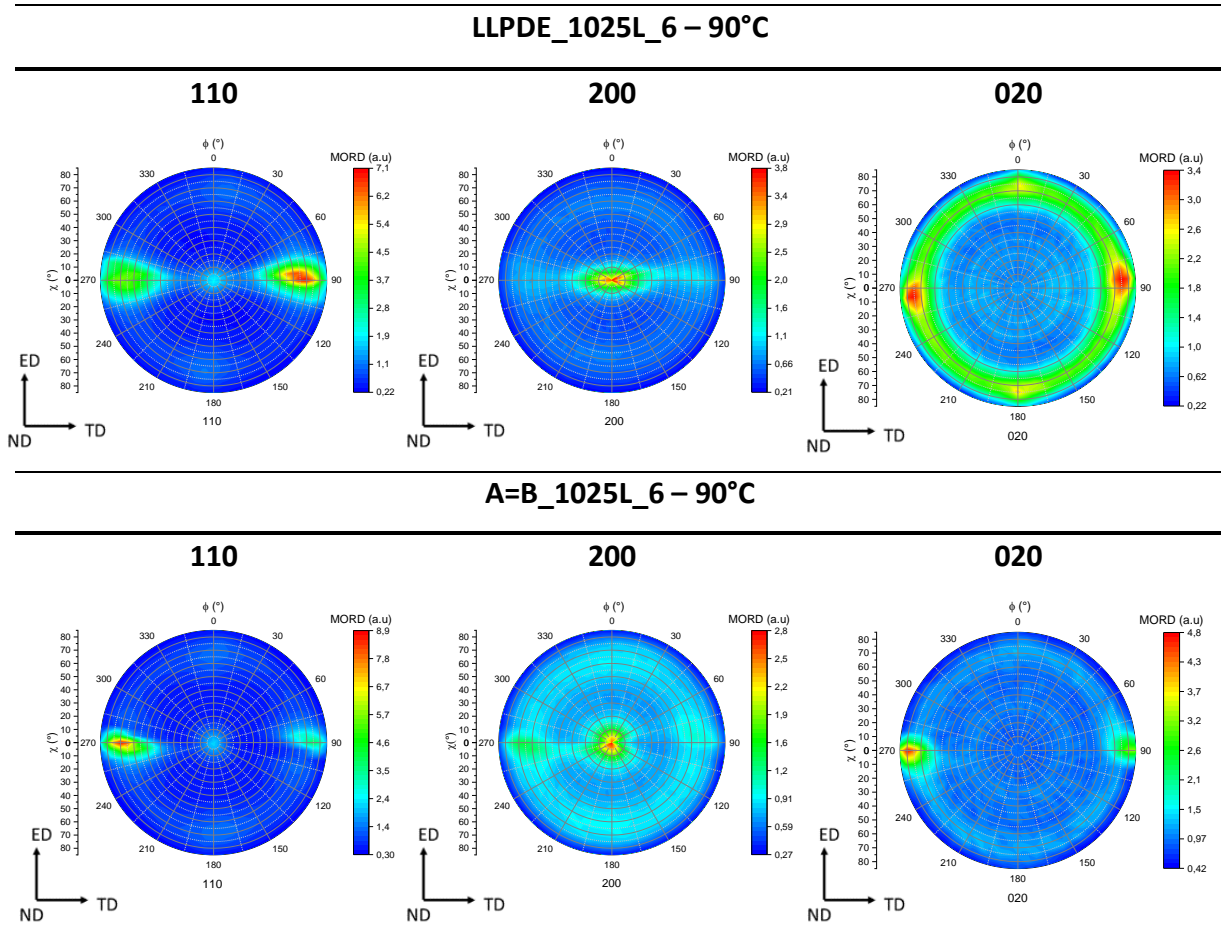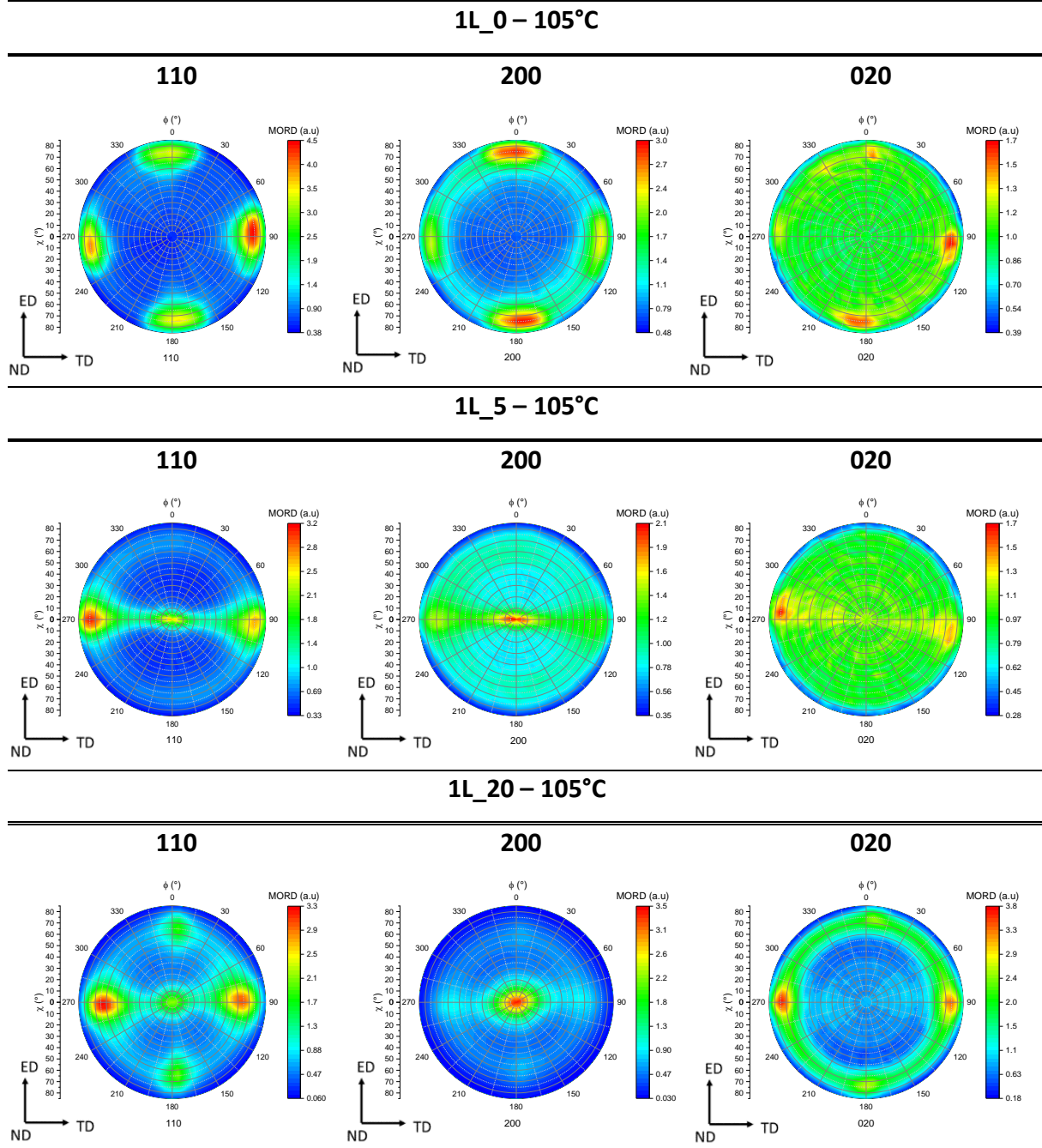
Figure 7-16 : Pole figures of the (110), (200) and (020) LLDPE lattice planes of monolayer bi-axially stretched samples at 105°C.

At 5wt% MMT content, diffraction is observed on the entire pole figures (χ and ϕ values) for the (200) and (020) planes. The maximum pole diffraction is localized at the center of the pole figure, towards the ND for the (200) plane and in the TD direction for the (020) lattice plane. However, for the (110) lattice plane, diffraction is observed on the TD-ND axis

252

with two maxima still localized around 60° from the TD and at 30° from the ND, as well as diffraction at the center.

Upon initial inspection, the diffraction at the center does not appear to stem from the monoclinic phase as it is not discernible in the 2θ scans (**Figure 7-14**). However, it is important to note that this phase can form at 105°C and remains metastable up to 110°C. Therefore, it can be assumed that the monoclinic phase persists during the bi-axial stretching process at 105°C, and the diffraction pole at the center of the 110 pole figure belongs to the monoclinic phase.

At a concentration of 20wt% MMT, the behavior and orientation remain the same as what was observed at 90°C.
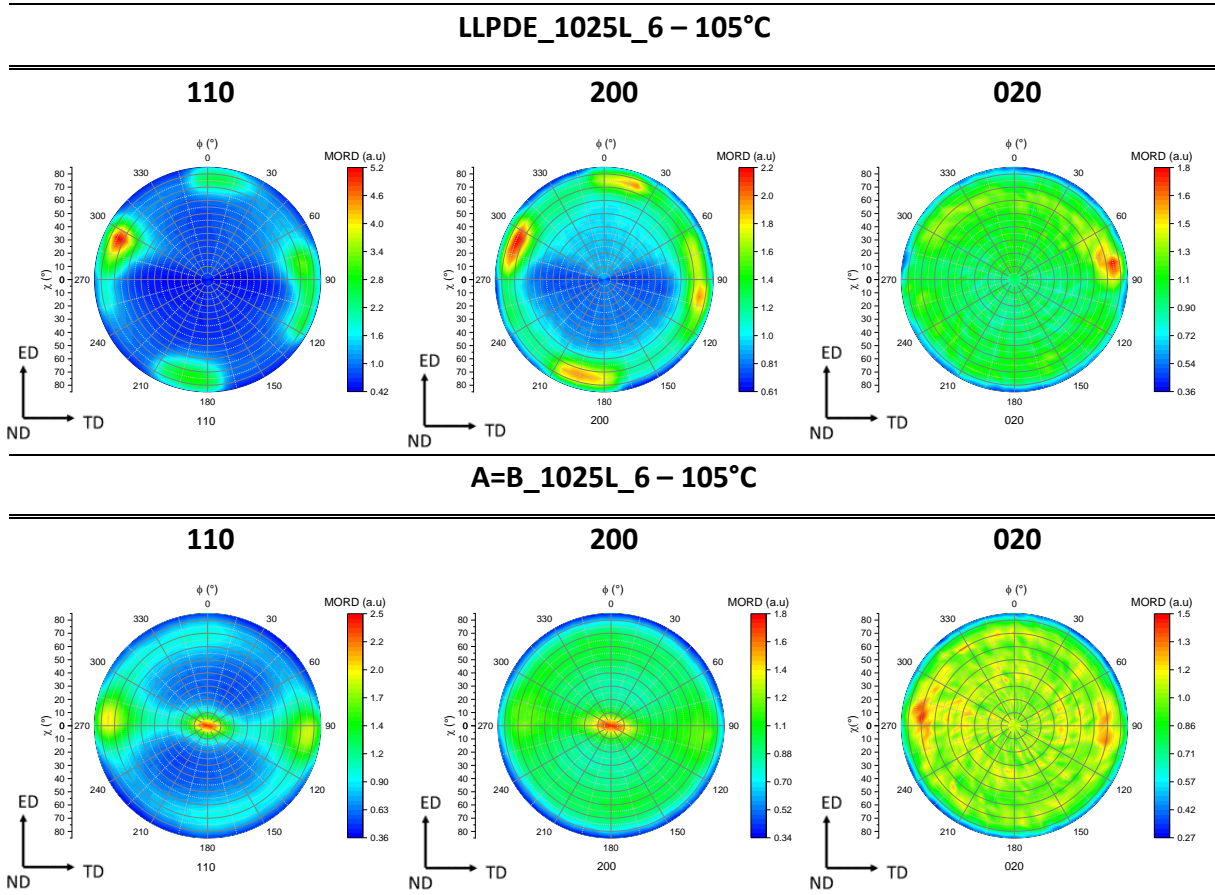
Figure 7-17 : Pole figures of the (110), (200) and (020) LLDPE lattice planes of multi-nano layer bi-axially stretched samples at 105°C.

In **Figure 7-17,** the MNL architecture films without fillers exhibit a comparable behavior to that of the MMT free monolayer film at 105°C. This involves a state of lamellar reorganization in the ED and ND directions, but no transition from 'in-plane' to 'on-edge' orientation is detected.

From the engineering stress-strain curves (**Figure 7-3**), it can be inferred that the strain-hardening phase at high deformation values is accompanied by a transition in lamellar orientation from 'in-plane' to 'edge-on'. This is suggested by the fact that no texture transition is observed in these two precedent cases without MMT filler at 105°C. In fact, they reach a strain value of 0.6 and 0.7 right before fracture, at the necking propagation plateau, while all the samples showing a transition from 'in-plane' to 'edge-on' show a strain-hardening behavior during bi-axial stretching.

On the other hand, in the case where fillers are present in the MNL structure, the behavior is similar to that was observed in the monolayer film with 5wt% of MMT subjected to bi-axial stretching at 105°C (**Figure 7-16**). Diffraction is observed on the entire pole figures for the (200) and (020) planes, with the maximum diffraction pole localized at the center of the pole figure towards the ND for the (200) plane in the TD direction for the (020) lattice plane. For the (110) lattice plane, diffraction is observed on the TD-ND axis with two maxima still localized around 60° from the TD and at 30° from the ND, as well as diffraction at the center.

In summary, bi-axial stretching at temperatures below the melting point causes deformation of the orthorhombic phase of LLDPE, resulting in the formation of a dual-phase population consisting of the monoclinic and orthorhombic phases. These observations highlight the presence of lamellar deformations in the form of slipping, particularly at 90°C (**Peterlin., 1967**).

For all samples, except for the one without MMT bi-axially stretched at 105°C, the final orientations remain similar regardless of the initial orientation. This includes the fiber texture along the normal of the film or a preferential orientation of the lamellae in all three directions of the film. After bi-axial stretching, a transition of the lamellae from an 'in-plane' to an 'edge-on' orientation is observed. The stretching process aligns the amorphous chains with the lamellae of LLDPE, creating a network between them and the crystals (**Keller & Kolnaar.,**

1993). This stretching acts like a spring, promoting the orientation of LLDPE crystals towards their most stable conformation, which is 'edge-on'. Changes in crystal orientation have been observed following bi-axial stretching tests on PE, as reported by **Chen et al., 2020**.

The orientation factor could not be quantified due to the presence of two phases. Additionally, when bi-axially stretched, the presence of MMT does not impact the production of highly oriented texture with lamellae that have an 'edge-on' orientation. As demonstrated in the previous chapter, highly oriented structures with 'in-plane' oriented LLDPE lamellae were consistently achieved in the presence of MMT. In this case, we can achieve highly oriented textures with 'edge-on' lamellae even without MMT present at 90°C. Additionally, the presence of MMT helps maintaining a specific texture that allows for greater deformation at temperatures near the complete melting point of LLDPE.

7.4 CONCLUSIONS

A comprehensive analysis was conducted to establish links between all observations made in this chapter. The bi-axial stretching resulted in various changes that simultaneously enhanced the orientation of montmorillonite and altered the barrier properties.

7.4.1 Morphological changes

This section focuses on the morphological changes induced by biaxial stretching, which are illustrated in **Figure 7-18**.

The hypotheses regarding the morphology and organization of the system have been derived from the conclusions of the previous chapters. It is assumed that the presence of MMT influences the orientation of LLDPE lamellae parallel to the film surface. These lamellae are located in close proximity to the fillers, as shown in **Figure 7-18a**. Upon bi-axial stretching, heating the samples increases the mobility of the LLDPE chains, making them more likely to orient under the effect of deformation.
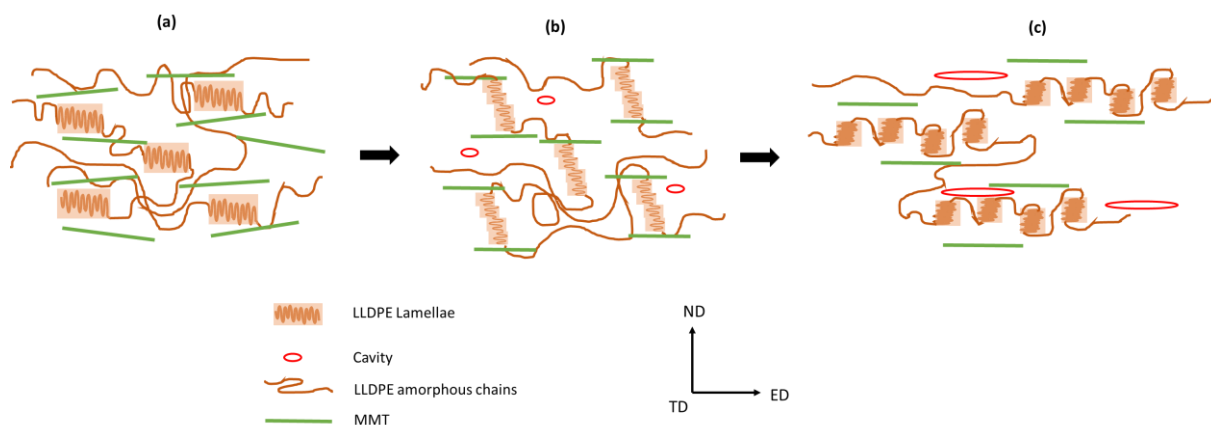
Figure 7-18 : Scheme of hypothesis of the morphological change induced during the bi-axial stretching.

During bi-axial stretching, the lamellae near the MMT fillers act as hard points, allowing for stress transfer between the crystals and the MMT fillers. This promotes 'in-plane' orientation of the MMT. Stretching also affects the amorphous chains that contribute to the organization and orientation of the stiffer lamellae. Under the influence of crystallographic slip mechanisms induced by the strain, there is a change in crystals orientation from 'in-plane' to 'on-edge' (**Figure 7-18b**). At higher strain levels, a secondary phase is formed due to martensitic deformation. This transformation is characterized by the distortion of the initial mesh, indicating lamellar fragmentation and coarse sliding phenomena.

DSC analyses support the proposed hypothesis, showing changes in lamellae distribution and size after bi-axial stretching. However, at higher levels of deformation, lamellae may reorganize into oriented macrostructures, such as fibrils. The mechanisms behind these reorganizations are not yet fully understood. To gain a better understanding of these changes and identify their precise onset, a comprehensive study of morphologies at various levels of deformation would be necessary.

Deformations in the rubbery state promote the formation of cavities, which tend to occur in semi-crystalline materials under local three-dimensional tensile stress. This phenomenon is especially noticeable during bi-axial stretching, where deformation is applied in the length and width directions, inducing compression in the thickness direction (**Pawlak et al., 2014**). The size of the cavities is likely to increase with the level of deformation (**Figure 7-18c**).

7.4.2 H_2O barrier properties

The changes resulting from biaxial stretching cause cavities to form within the samples. This is consistent with the significant increase in water permeability, despite the improved orientation of montmorillonite and the overall increase in crystallinity rate of LLDPE in the films.

Further tests would be beneficial to enhance our understanding of the induced transformations and determine the optimal timing to achieve the desired MMT 'in-plane' orientation without compromising the final properties. Here are some recommendations:

i)   The tests were stopped just before the samples reached their breaking point, which is typically an engineering strain of 1.3-1.4. This resulted in significant instability. To prevent cavity propagation before complete rupture, it may be recommended to stop the stretching earlier, around an engineering strain of 1, at the beginning of the strain-hardening stage.

ii)   Texture analyses could be conducted on the LLDPE and MMT orientation at various points along the stress-strain curve. Analyses near the yield point, necking propagation, and beginning of the strain-hardening phase would provide insights into the transformation mechanisms of LLDPE and optimal MMT orientation. Additionally, measuring the barrier properties of these samples to identify any shifts during deformation could be insightful.

iii)   It could also be interesting to perform the very same tests yet on thicker samples. The initial samples had a thickness of 100μm and reached thicknesses of a few tens of micrometers by the end of the experiment. This decrease in thickness makes the sample much more fragile and potentially more prone to defect formation. Testing thicker samples would allow for a more thorough evaluation of the influence of thickness on cavity formation and, consequently, on permeability increase.

8. CHAPTER 8: CONCLUSION & PERSPECTIVES

8.1   GENERAL CONCLUSION

This study has examined the mechanisms that govern the nano-structuring of Multi-Nano Layered films and their impact on water barrier properties.

Various parameters that influence the 'in-plane' orientation of montmorillonite in polymer films were identified, ranging from film composition to processing conditions. Factors such as MMT concentration, flow, and shear forces favor this orientation. Reducing the size of layers to a few tens of nanometers in a multi-nano layer film configuration did not significantly improve orientation of MMT compared to a monolayer film.

However, bi-axial stretching experiments carried out at temperatures below the melting temperature of LLDPE and in its rubbery state demonstrated a clear improvement in MMT orientation. The presence of LLDPE lamellae was found to facilitate stress transfer during deformation, resulting in improved MMT orientation. Although we observed an improvement in MMT orientation parallel to the film surface, there was no corresponding improvement in water permeability. In fact, in some cases, we even measured an increase in permeability. This led us to investigate more thoroughly the interaction between the polymer matrix, specifically LLDPE, and the MMT nano-fillers. The presence of MMT promotes a preferential orientation of LLDPE in the form of 2D lamellae aligned parallel to the film surface. This orientation is improved by the MNL structure. This improves the distribution of fillers in the film thickness and facilitates the elongation of polymer chains during processing, promoting better film organization. Although LLDPE crystal orientation and the formation of highly oriented superstructures have improved, we still measured a 38% increase in permeability.

Although the orientation has been improved, the film still remains mostly amorphous, which limits its barrier effectiveness. These results emphasize the crucial role of the polymer matrix in the performance of barrier films and underscore the importance of selecting appropriate materials to optimize these properties. Thus, this is recommended to use a polymer matrix with an initial crystallinity of at least 60%. This would provide a crystalline

phase that limits gas diffusion, while also incorporating and orienting 2D nano-fillers to further reduce permeability.

The goal of achieving a WVTR of $1 \cdot 10^{-5}$ $g \cdot m^{-2} \cdot day^{-1}$ was not met. However, we have identified the factors that may have contributed to the stagnation of barrier properties. Therefore, we have explored various ways to improve the systems used to confirm whether the identified obstacles are indeed responsible for the failure to enhance barrier properties. Furthermore, we have learned valuable lessons from the crystallization process that occurs in the presence of MMT and have investigated the potential for applying this knowledge to other areas. These considerations are explained in detail below.

8.2   PERSPECTIVES

As a result of this work, a number of perspectives can be envisaged. These can be grouped into two main application areas.

8.2.1 Validation of assumptions regarding barrier properties

Several strategies can be used to achieve the desired permeability values and even more understand what happens in our films.

Permeability can be measured using equipment that provides more data points during transient regimes, when water vapor flux increases and reaches a stabilization plateau. This allows for determination of a diffusion coefficient that provides more information on gas diffusion through the film. Unfortunately, we were unable to obtain these points with our equipment.

Performing X-ray tomography on the samples would help identify and quantify the cavities formed in the films after bi-axial stretching. Additionally, it would provide an overview of the MMT repartition in the films before and after bi-axial stretching, which would provide valuable information to understand the diffusion in our films.

To address the issues related to crystallinity, it is recommended to use a matrix with higher initial crystallinity, such as HDPE, which has a crystallinity of around 50-70%. This approach allows investigating the effect of matrix crystallinity on barrier properties while maintaining an equivalent level of MMT fillers orientation.

After verifying the effect of the degree of crystallinity, one can adjust the orientation of the fillers to determine whether this adjustment has a greater impact on reducing permeability in a matrix with a higher degree of crystallinity (such as HDPE).

Furthermore, to improve MMT orientation by using bi-axial stretching, it would be crucial to confirm when MMT filler orientation improves (from our investigation it should be during the necking propagation stage) and when cavities form. This would prevent any deterioration in film structure that could lead to a degradation of barrier properties. By understanding these processes, one could utilize MMT orientation without compromising film quality.

8.2.2 Application of the knowledge generated to other fields and uses

In this study, several elements were highlighted in terms of the crystallization of LLDPE in a controlled manner, according to a preferential orientation and not in the form of spherulites. The organization within the films was also examined. All those observations were initiated by the presence of MMT in the polymer films.

The exfoliated state of MMT enhances oriented crystallization by increasing local shear on the polymer chains. This effect, combined with confinement-induced crystallization in MNL films, may yield interesting outcomes. Indeed, combining an amorphous polymer 'A' with a semi-crystalline polymer 'B', or two semi-crystalline polymers 'A' and 'B' with distinct crystallization temperatures ($T_{c(A)} > T_{c(B)}$), can induce confinement-induced crystallization phenomena on polymer 'B', resulting in a controlled orientation of polymer crystals 'B'. Adding MMT to the 'confining' phase 'A' would also result in oriented crystallization in that phase.

Thus, an MNL film with A-B-A architecture would have 2D crystalline lamellae oriented in both phase A and B.

Additionally, the results of the LLDPE crystallization experiment in **Chapter 6** suggest that a 1025 layer sample with 5wt% of MMT has a more advanced LLDPE orientation compared to its equivalent with only 1 layer. This leads us to hypothesize that multi-nano-layer co-extrusion improves the organization of MMT nano-filler distribution throughout the film thickness. It appears also to promote better organization of polymer chains, resulting in more oriented crystallization of LLDPE. Given these findings, it may be advantageous to employ MNL co-extrusion with MMT for piezoelectric film applications. The piezoelectricity of a material is determined by its ability to crystallize in a specific form that lacks a center of symmetry and inversion symmetry. PVDF is a polymer that exhibits these characteristics, specifically in its β-form (space group Cm2m), which displays piezoelectric properties (**Xie et al., 2021**). However, obtaining this form is complex. Nonetheless, **Zhang et al. 2012,** demonstrated that the β-form is favored in the presence of MMT. Additionally, this form typically develops under draw-induced elongation. Indeed, we have studied some of these conditions in our work using LLDPE and it gives promising effect for piezoelectric application. Therefore, it would be beneficial to investigate the impact of MNL co-extrusion of PVDF with MMT on PVDF crystallization and its influence on its piezoelectric properties.

REFERENCES

Adams, W. W.; Yang, D.; Thomas, E. L. Direct Visualization of Microstructural Deformation Processes in Polyethylene. *J Mater Sci* **1986**, *21* (7), 2239–2253. https://doi.org/10.1007/BF01114262.

Agassant, J.-F.; Demay, Y. Investigation of the Polymer Coextrusion Process: A Review. *Polymers* **2022**, *14* (7), 1309. https://doi.org/10.3390/polym14071309.

Ahmad, J.; Bazaka, K.; Anderson, L. J.; White, R. D.; Jacob, M. V. Materials and Methods for Encapsulation of OPV: A Review. *Renewable and Sustainable Energy Reviews* **2013**, *27*, 104–117. https://doi.org/10.1016/j.rser.2013.06.027.

Ajji, A.; Zhang, X.; Elkoun, S. Biaxial Orientation in HDPE Films: Comparison of Infrared Spectroscopy, X-Ray Pole Figures and Birefringence Techniques. *Polymer* **2005**, *46* (11), 3838–3846. https://doi.org/10.1016/j.polymer.2005.03.002.

Akelah, A.; Moet, A. Polymer-Clay Nanocomposites: Free-Radical Grafting of Polystyrene on to Organophilic Montmorillonite Interlayers. *JOURNAL OF MATERIALS SCIENCE* **1996**, *31* (13), 3589–3596. https://doi.org/10.1007/BF00360767.

Alexander, L. X-ray diffraction methods in polymer science. *J Mater Sci* **6**, 93 (1971). https://doi.org/10.1007/BF00550300

Alexandre, M.; Dubois, P. Polymer-Layered Silicate Nanocomposites: Preparation, Properties and Uses of a New Class of Materials. *Materials Science and Engineering: R: Reports* **2000**, *28* (1–2), 1–63. https://doi.org/10.1016/S0927-796X(00)00012-7.

Alix, S.; Follain, N.; Tenn, N.; Alexandre, B.; Bourbigot, S.; Soulestin, J.; Marais, S. Effect of Highly Exfoliated and Oriented Organoclays on the Barrier Properties of Polyamide 6 Based Nanocomposites. *J. Phys. Chem. C* **2012**, *116* (8), 4937–4947. https://doi.org/10.1021/jp2052344.

Althues, H.; Henle, J.; Kaskel, S. Functional Inorganic Nanofillers for Transparent Polymers. *Chem. Soc. Rev.* **2007**, *36* (9), 1454. https://doi.org/10.1039/b608177k.

Bartczak, Z.; Rozanski, A.; Richert, J. Characterization of Clay Platelet Orientation in Polylactide–Montmorillonite Nanocomposite Films by X-Ray Pole Figures. *European Polymer Journal* **2014**, *61*, 274–284. https://doi.org/10.1016/j.eurpolymj.2014.10.020.

REFERENCES

Bernal-Lara, T. E.; Liu, R. Y. F.; Hiltner, A.; Baer, E. Structure and Thermal Stability of Polyethylene Nanolayers. *Polymer* **2005**, *46* (9), 3043–3055. https://doi.org/10.1016/j.polymer.2005.01.055.

Bernal-Lara, T. E.; Masirek, R.; Hiltner, A.; Baer, E.; Piorkowska, E.; Galeski, A. Morphology Studies of Multilayered HDPE/PS Systems. *J of Applied Polymer Sci* **2006**, *99* (2), 597–612. https://doi.org/10.1002/app.22178.

Bharadwaj, R. K. Modeling the Barrier Properties of Polymer-Layered Silicate Nanocomposites. *Macromolecules* **2001**, *34* (26), 9189–9192. https://doi.org/10.1021/ma010780b.

Bironeau, A.; Salez, T.; Miquelard-Garnier, G.; Sollogoub, C. Existence of a Critical Layer Thickness in PS/PMMA Nanolayered Films. *Macromolecules* **2017**, *50* (10), 4064–4073. https://doi.org/10.1021/acs.macromol.7b00176.

Biswas, M.; Ray, S. S. Recent Progress in Synthesis and Evaluation of Polymer-Montmorillonite Nanocomposites. In New Polymerization Techniques and Synthetic Methodologies; Abe, A., Albertsson, A.-C., Cantow, H.-J., Dušek, K., Edwards, S., Höcker, H., Joanny, J.-F., Kausch, H.-H., Kobayashi, T., Lee, K.-S., McGrath, J. E., Monnerie, L., Stupp, S. I., Suter, U. W., Wegner, G., Young, R. J., Series Eds.; Advances in Polymer Science; Springer Berlin Heidelberg: Berlin, Heidelberg, 2001; Vol. 155, pp 167–221. https://doi.org/10.1007/3-540-44473-4_3.

Bowden, P. B. ; Young, R. J, Deformation Mechanisms in Crystalline Polymers. *Journal of materials science* **1974,** 9, 2034-2051. https://doi.org/10.1007/BF00540553.

Bouich, A.; Pradas, I. G.; Khan, M. A.; Khattak, Y. H. Opportunities, Challenges, and Future Prospects of the Solar Cell Market. *Sustainability* **2023**, *15* (21), 15445. https://doi.org/10.3390/su152115445.

Bourg, V.; Ienny, P.; Caro-Bretelle, A. S.; Le Moigne, N.; Guillard, V.; Bergeret, A. Modeling of Internal Residual Stress in Linear and Branched Polyethylene Films during Cast Film Extrusion: Towards a Prediction of Heat-Shrinkability. *Journal of Materials Processing Technology* **2019**, *271*, 599–608. https://doi.org/10.1016/j.jmatprotec.2019.04.002.

Bumbudsanpharoke, N.; Lee, W.; Choi, J. C.; Park, S.-J.; Kim, M.; Ko, S. Influence of Montmorillonite Nanoclay Content on the Optical, Thermal, Mechanical, and Barrier

REFERENCES

Properties of Low-Density Polyethylene. *clays clay miner* **2017**, *65* (6), 387–397. https://doi.org/10.1346/CCMN.2017.064071.

Burt, T. M.; Jordan, A. M.; Korley, L. T. J. Toward Anisotropic Materials via Forced Assembly Coextrusion. *ACS Appl. Mater. Interfaces* **2012**, *4* (10), 5155–5161. https://doi.org/10.1021/am301072s.

Bustos, F. Cristallisation sous cisaillement du polyéthylène : effets de l'architecture moleculaire. PhD Thesis, Universit2 Claude Bernard, Lyon, France, **2004**.

Bustos, F.; Cassagnau, P.; Fulchiron, R. Effect of Molecular Architecture on Quiescent and Shear-induced Crystallization of Polyethylene. *J Polym Sci B Polym Phys* **2006**, *44* (11), 1597–1607. https://doi.org/10.1002/polb.20820.

Butler, M. F.; Donald, A. M.; Bras, W.; Mant, G. R.; Derbyshire, G. E.; Ryan, A. J. A Real-Time Simultaneous Small- and Wide-Angle X-Ray Scattering Study of In-Situ Deformation of Isotropic Polyethylene. *Macromolecules* **1995**, *28* (19), 6383–6393. https://doi.org/10.1021/ma00123a001.

Cabrera, G. Eco-Design and Processing of recycled multilayer/multiphase polymer materials: Structure-properties-process relationship. PhD Thesis**, 2020.**

Cabrera, G.; Touil, I.; Masghouni, E.; Maazouz, A.; Lamnawar, K. Multi-Micro/Nanolayer Films Based on Polyolefins: New Approaches from Eco-Design to Recycling. *Polymers* **2021**, *13* (3), 413. https://doi.org/10.3390/polym13030413.

Caillere, S.; Henin, S.; Rautureau, M. Mineralogie des argiles. 1. Structure et proprietes physico-chimiques [definition, structure des mineraux des argiles, etudes par les techniques de diffusion, d'interference et de spectroscopie d'emission et d'absorption, methodes thermiques, etude chimique]. Actualites Scientifiques et Agronomiques (France) **1982**, (8).

Carr, J. M.; Langhe, D. S.; Ponting, M. T.; Hiltner, A.; Baer, E. Confined Crystallization in Polymer Nanolayered Films: A Review. *J. Mater. Res.* **2012**, *27* (10), 1326–1350. https://doi.org/10.1557/jmr.2012.17.

Cassagnau, Ph. Melt Rheology of Organoclay and Fumed Silica Nanocomposites. *Polymer* **2008**, *49* (9), 2183–2196. https://doi.org/10.1016/j.polymer.2007.12.035.

Chandrasekhar, S. Liquid Crystals; Cambridge monographs on physics; Cambridge University Press, **1992**.

REFERENCES

Chawla, K. K. *Composite Materials*; Springer New York: New York, NY, **2012**. https://doi.org/10.1007/978-0-387-74365-3.

Chen, H. Y.; Bishop, M. T.; Landes, B. G.; Chum, S. P. Orientation and Property Correlations for LLDPE Blown Films. *J of Applied Polymer Sci* **2006**, *101* (2), 898–907. https://doi.org/10.1002/app.23583.

Chen, Q.; Wang, Z.; Zhang, S.; Cao, Y.; Chen, J. Structure Evolution and Deformation Behavior of Polyethylene Film during Biaxial Stretching. *ACS Omega* **2020**, *5* (1), 655–666. https://doi.org/10.1021/acsomega.9b03250.

Cui, Y.; Kumar, S.; Rao Kona, B.; Van Houcke, D. Gas Barrier Properties of Polymer/Clay Nanocomposites. *RSC Adv.* **2015**, *5* (78), 63669–63690. https://doi.org/10.1039/C5RA10333A.

Dada, M.; Popoola, P. Recent Advances in Solar Photovoltaic Materials and Systems for Energy Storage Applications: A Review. *Beni-Suef Univ J Basic Appl Sci* **2023**, *12* (1), 66. https://doi.org/10.1186/s43088-023-00405-5.

Dai, X.; Hou, C.; Xu, Z.; Yang, Y.; Zhu, G.; Chen, P.; Huang, Z.; Yan, L.-T. Entropic Effects in Polymer Nanocomposites. *Entropy* **2019**, *21* (2), 186. https://doi.org/10.3390/e21020186.

Decker, J. J.; Meyers, K. P.; Paul, D. R.; Schiraldi, D. A.; Hiltner, A.; Nazarenko, S. Polyethylene-Based Nanocomposites Containing Organoclay: A New Approach to Enhance Gas Barrier via Multilayer Coextrusion and Interdiffusion. *Polymer* **2015**, *61*, 42–54. https://doi.org/10.1016/j.polymer.2015.01.061.

Desper, C. R. Structure and Properties of Extruded Polyethylene Film. *J of Applied Polymer Sci* **1969**, *13* (1), 169–191. https://doi.org/10.1002/app.1969.070130117.

Desper, C. R.; Stein, R. S. Measurement of Pole Figures and Orientation Functions for Polyethylene Films Prepared by Unidirectional and Oriented Crystallization. *Journal of Applied Physics* **1966**, *37* (11), 3990–4002. https://doi.org/10.1063/1.1707966

Doh, J. G.; Cho, I. Synthesis and Properties of Polystyrene-Organoammonium Montmorillonite Hybrid. *Polymer Bulletin* **1998**, *41* (5), 511–518. https://doi.org/10.1007/s002890050395.

Domenech, T. Structure et Propriétés de Nanocomposites Polypropylène/Argile Lamellaire Préparés Par Mélange à l'état Fondu. PhD. Thesis, Ecole Nationale Supérieure des Mines de Paris, Paris, France, 2012.

REFERENCES

Domenech, T.; Peuvrel-Disdier, E.; Vergnes, B. Influence of Twin-Screw Processing Conditions on Structure and Properties of Polypropylene – Organoclay Nanocomposites. *International Polymer Processing* **2012**, *27* (5), 517–526. https://doi.org/10.3139/217.2591.

Domenech, T.; Peuvrel-Disdier, E.; Vergnes, B. The Importance of Specific Mechanical Energy during Twin Screw Extrusion of Organoclay Based Polypropylene Nanocomposites. *Composites Science and Technology* **2013**, *75*, 7–14. https://doi.org/10.1016/j.compscitech.2012.11.016.

European commission, "Communication from the Commission to the European Parliament, the Council, the European Economic and Social Committee and the Committee of the Regions on the 2017 list of Critical Raw Materials for the EU", **2017**. http://eur-lex.europa.eu/legal-content/EN/ALL/?uri=COM:2017:0490:FIN.

Fawcett, E. W.; Gibson, R. O.; Perrin, M. W. UNITED STATES PATENT OFFICE, 2,153,553.

Feng, L. Melting and Crystallization Behavior of Linear Low-Density Polyethylene; Library and Archives Canada = Bibliothèque et Archives Canada: Ottawa, 2007.

Feng, S.; Lin, Y.; Yu, W.; Iqbal, O.; Habumugisha, J. C.; Chen, W.; Meng, L.; Lu, A.; Li, L. Stretch-Induced Structural Transition of Linear Low-Density Polyethylene during Uniaxial Stretching under Different Strain Rates. *Polymer* **2021**, *226*, 123795. https://doi.org/10.1016/j.polymer.2021.123795.

Fu, S.; Sun, Z.; Huang, P.; Li, Y.; Hu, N. Some Basic Aspects of Polymer Nanocomposites: A Critical Review. *Nano Materials Science* **2019**, *1* (1), 2–30. https://doi.org/10.1016/j.nanoms.2019.02.006.

Fujiwara, S.; Sakamoto, T. Method for manufacturing a clay-polyamide composite. Kokai Patent Application 109998, **1976**.

Gaddam, S. K.; Pothu, R.; Boddula, R. Advanced Polymer Encapsulates for Photovoltaic Devices – A Review. *Journal of Materiomics* **2021**, *7* (5), 920–928. https://doi.org/10.1016/j.jmat.2021.04.004.

Gao, Y.; Picot, O. T.; Tu, W.; Bilotti, E.; Peijs, T. Multilayer Coextrusion of Graphene Polymer Nanocomposites with Enhanced Structural Organization and Properties. *J of Applied Polymer Sci* **2018**, *135* (13), 46041. https://doi.org/10.1002/app.46041.

REFERENCES

Gilman, J. W. Flammability and Thermal Stability Studies of Polymer Layered-Silicate clay/ Nanocomposites. *Applied Clay Science* **1999**, 15, 31-49. https://doi.org/10.1016/S0169-1317(99)00019-8.

Gilman, J. W.; Jackson, C. L.; Morgan, A. B.; Harris, R.; Manias, E.; Giannelis, E. P.; Wuthenow, M.; Hilton, D.; Phillips, S. H. Flammability Properties of Polymer–Layered-Silicate Nanocomposites. Polypropylene and Polystyrene Nanocomposites. *Chem. Mater.* **2000**, *12* (7), 1866–1873. https://doi.org/10.1021/cm0001760.

Giraldo, S.; Jehl, Z.; Placidi, M.; Izquierdo-Roca, V.; Pérez-Rodríguez, A.; Saucedo, E. Progress and Perspectives of Thin Film Kesterite Photovoltaic Technology: A Critical Review. *Advanced Materials* **2019**, *31* (16), 1806692. https://doi.org/10.1002/adma.201806692.

Gloaguen, J.-M.; Lefebvre, J.-M. Nanocomposites polymères/silicates en feuillets. *Techniques de l'ingénieur* **2007**.

Gopakumar, T. G.; Lee, J. A.; Kontopoulou, M.; Parent, J. S. Influence of Clay Exfoliation on the Physical Properties of Montmorillonite/Polyethylene Composites. *Polymer* **2002**, *43* (20), 5483–5491. https://doi.org/10.1016/S0032-3861(02)00403-2.

Green, M. A.; Dunlop, E. D.; Yoshita, M.; Kopidakis, N.; Bothe, K.; Siefer, G.; Hao, X. Solar Cell Efficiency Tables (Version 62). *Progress in Photovoltaics* **2023**, *31* (7), 651–663. https://doi.org/10.1002/pip.3726.

Greenland, D. J. Adsorption of Polyvinyl Alcohols by Montmorillonite. *Journal of Colloid Science* **1963**, *18* (7), 647–664. https://doi.org/10.1016/0095-8522(63)90058-8.

Gupta, R. K.; Pasanovic-Zujo, V.; Bhattacharya, S. N. Shear and Extensional Rheology of EVA/Layered Silicate-Nanocomposites. *Journal of Non-Newtonian Fluid Mechanics* **2005**, *128* (2–3), 116–125. https://doi.org/10.1016/j.jnnfm.2005.05.002.

Haudin, J.-M. Crystallization in Processing Conditions. In Handbook of Polymer Crystallization (eds E. Piorkowska and G.C. Rutledge). **2013**. https://doi.org/10.1002/9781118541838.ch15

Haudin, J.-M. Développement de structures dans les polymères - Concepts généraux. *Plastiques et composites* **2015**. https://doi.org/10.51257/a-v1-am3120.

REFERENCES

Hobbs, J. K.; Humphris, A. D. L.; Miles, M. J. In-Situ Atomic Force Microscopy of Polyethylene Crystallization. 1. Crystallization from an Oriented Backbone. *Macromolecules* **2001**, *34* (16), 5508–5519. https://doi.org/10.1021/ma0104478.

Höhne, G. W. H. Another Approach to the Gibbs–Thomson Equation and the Melting Point of Polymers and Oligomers. *Polymer* **2002**, *43* (17), 4689–4698. https://doi.org/10.1016/S0032-3861(02)00305-1.

Hyvärinen, M.; Jabeen, R.; Kärki, T. The Modelling of Extrusion Processes for Polymers—A Review. *Polymers* **2020**, *12* (6), 1306. https://doi.org/10.3390/polym12061306.

Hyun, Y. H.; Lim, S. T.; Choi, H. J.; Jhon, M. S. Rheology of Poly(Ethylene Oxide)/Organoclay Nanocomposites. *Macromolecules* **2001**, *34* (23), 8084–8093. https://doi.org/10.1021/ma002191w.

IEA, *Share of renewable electricity generation by technology, 2000-2028*, IEA, Paris https://www.iea.org/data-and-statistics/charts/share-of-renewable-electricity-generation-by-technology-2000-2028 , IEA. Licence: CC BY 4.0

Jain, M.; Mutlu, Z.; Mao, J.; Zhou, J.; Zhou, P.; Wu, C.; Isik, T.; Cao, Y.; Ortalan, V.; Cakmak, M. Shear Amplification of Orientation in Nylon 11/Clay Nanocomposites during Melt Casting and Resulting Electrical Properties. *Polymer Engineering & Sci* **2023**, *63* (3), 863–879. https://doi.org/10.1002/pen.26250.

Jamnig, A. "Thin Metal Films on Weakly-Interacting Substrates: Nanoscale Growth Dynamics, Stress Generation, and Morphology Manipulation." Linköping Studies in Science and Technology. Dissertations; Linköping University Electronic Press: Linköping, **2020**; Vol. 2084. https://doi.org/10.3384/diss.diva-168458.

Ji, X. L.; Jing, J. K.; Jiang, W.; Jiang, B. Z. Tensile Modulus of Polymer Nanocomposites. *Polymer Engineering & Sci* **2002**, *42* (5), 983–993. https://doi.org/10.1002/pen.11007.

Jin, Y.; Rogunova, M.; Hiltner, A.; Baer, E.; Nowacki, R.; Galeski, A.; Piorkowska, E. Structure of Polypropylene Crystallized in Confined Nanolayers. *J Polym Sci B Polym Phys* **2004**, *42* (18), 3380–3396. https://doi.org/10.1002/polb.20211.

Keith, H. D.; Padden, F. J. A Phenomenological Theory of Spherulitic Crystallization. *Journal of Applied Physics* **1963**, *34* (8), 2409–2421. https://doi.org/10.1063/1.1702757.

REFERENCES

Keller, A.; Kolnaar, J. W. H. Chain Extension and Orientation: Fundamentals and Relevance to Processing and Products. *Progress in Colloid & Polymer Science* **1993**, 92, 81–102. https://doi.org/10.1007/BFb0115450.

Keller, A.; Kolnaar, H. W. H. Flow-Induced Orientation and Structure Formation. In *Materials Science and Technology*; Cahn, R. W., Haasen, P., Kramer, E. J., Eds.; Wiley, **2006**. https://doi.org/10.1002/9783527603978.mst0210.

Keller, A.; Machin, M. J. Oriented Crystallization in Polymers. *Journal of Macromolecular Science, Part B* **1967**, *1* (1), 41–91. https://doi.org/10.1080/00222346708212739.

Kestenbach, H.-J.; Loos, J.; Petermann, J. Transcrystallization at the Interface of Polyethylene Single-Polymer Composites. *Mat. Res.* **1999**, *2* (4), 261–269. https://doi.org/10.1590/S1516-14391999000400005.

Khosrokhavar, R.; Naderi, G.; Bakhshandeh, G. R.; Ghoreishy, M. H. R. Effect of Processing Parameters on PP/EPDM/Organoclay Nanocomposites Using Taguchi Analysis Method. *Iranian Polymer Journal* **2016**, 2, 179-191. https://doi.org/10.1007/s13726-015-0412-6

Kojima, Y.; Usuki, A.; Kawasumi, M.; Okada, A.; Fukushima, Y.; Kurauchi, T.; Kamigaito, O. Mechanical Properties of Nylon 6-Clay Hybrid. *J. Mater. Res.* **1993**, *8* (5), 1185–1189. https://doi.org/10.1557/JMR.1993.1185. (a)

Kojima, Y.; Usuki, A.; Kawasumi, M.; Okada, A.; Kurauchi, T.; Kamigaito, O. Synthesis of Nylon 6–Clay Hybrid by Montmorillonite Intercalated with E-caprolactam. *J. Polym. Sci. A Polym. Chem.* **1993**, *31* (4), 983–986. https://doi.org/10.1002/pola.1993.080310418. (b)

Lagasse, R. R.; Maxwell, B. An Experimental Study of the Kinetics of Polymer Crystallization during Shear Flow. *Polymer Engineering & Sci* **1976**, *16* (3), 189–199. https://doi.org/10.1002/pen.760160312.

Langhe, D. ; Ponting, M. 2 - Coextrusion Processing of Multilayered Films, Manufacturing and Novel Applications of Multilayer Polymer Films, *William Andrew Publishing* **2016**, 16-45. https://doi.org/10.1016/B978-0-323-37125-4.00002-2.

Lertwimolnun, W.; Vergnes, B. Influence of Compatibilizer and Processing Conditions on the Dispersion of Nanoclay in a Polypropylene Matrix. *Polymer* **2005**, *46* (10), 3462–3471. https://doi.org/10.1016/j.polymer.2005.02.018.

REFERENCES

Lertwimolnun, W.; Vergnes, B. Effect of Processing Conditions on the Formation of Polypropylene/Organoclay Nanocomposites in a Twin Screw Extruder. *Polym. Eng. Sci.* **2006**, *46* (3), 314–323. https://doi.org/10.1002/pen.20458.

Lewis, J. S.; Weaver, M. S. Thin-Film Permeation-Barrier Technology for Flexible Organic Light-Emitting Devices. *IEEE J. Select. Topics Quantum Electron.* **2004**, *10* (1), 45–57. https://doi.org/10.1109/JSTQE.2004.824072.

Li, J.; Lai, L.; Wu, L.; Severtson, S. J.; Wang, W.-J. Enhancement of Water Vapor Barrier Properties of Biodegradable Poly(Butylene Adipate- *Co* -Terephthalate) Films with Highly Oriented Organomontmorillonite. *ACS Sustainable Chem. Eng.* **2018**, *6* (5), 6654–6662. https://doi.org/10.1021/acssuschemeng.8b00430.

Li, J.; Touil, I.; Sudre, G.; Yousfi, M.; Lu, B.; Zhang, H.; Shen, J.; Morelle, X.; Maazouz, A.; Lamnawar, K. Fabrication of Architectured Multilayers with Mismatched Rheological Behaviors: Layer Stability, Structure, and Confinement Dictate Polyethylene-Based Film Properties. *Ind. Eng. Chem. Res.* **2024**, *63* (4), 1953–1964. https://doi.org/10.1021/acs.iecr.3c03923.

Li, X.; McKenna, G. B.; Miquelard-Garnier, G.; Guinault, A.; Sollogoub, C.; Regnier, G.; Rozanski, A. Forced Assembly by Multilayer Coextrusion to Create Oriented Graphene Reinforced Polymer Nanocomposites. *Polymer* **2014**, *55* (1), 248–257. https://doi.org/10.1016/j.polymer.2013.11.025.

Lindenmeyer, P. H.; Lustig, S. Crystallite Orientation in Extruded Polyethylene Film. *J. Appl. Polym. Sci.* **1965**, *9* (1), 227–240. https://doi.org/10.1002/app.1965.070090121.

Lozay, Q. Conception et caractérisation de matériaux composites nanostructurés à hautes propriétés barrières. Etude de films multinanocouches de PE et PA6 chargés de montmorillonite. PhD Thesis, **2020.**

Lozay, Q.; Beuguel, Q.; Follain, N.; Lebrun, L.; Guinault, A.; Miquelard-Garnier, G.; Tencé-Girault, S.; Sollogoub, C.; Dargent, E.; Marais, S. Structural and Barrier Properties of Compatibilized PE/PA6 Multinanolayer Films. *Membranes* **2021**, *11* (2), 75. https://doi.org/10.3390/membranes11020075.

Lu, B.; Alcouffe, P.; Sudre, G.; Pruvost, S.; Serghei, A.; Liu, C.; Maazouz, A.; Lamnawar, K. Unveiling the Effects of In Situ Layer–Layer Interfacial Reaction in Multilayer Polymer Films

via Multilayered Assembly: From Microlayers to Nanolayers. *Macro Materials & Eng* **2020**, *305* (5), 2000076. https://doi.org/10.1002/mame.202000076.

Lu, B.; Zhang, H.; Maazouz, A.; Lamnawar, K. Interfacial Phenomena in Multi-Micro-/Nanolayered Polymer Coextrusion: A Review of Fundamental and Engineering Aspects. *Polymers* **2021**, *13* (3), 417. https://doi.org/10.3390/polym13030417.

Ma, J.; Qi, Z.; Hu, Y. Synthesis and Characterization of Polypropylene/Clay Nanocomposites. *J of Applied Polymer Sci* **2001**, *82* (14), 3611–3617. https://doi.org/10.1002/app.2223.

Mackey, M.; Flandin, L.; Hiltner, A.; Baer, E. Confined Crystallization of PVDF and a PVDF-TFE Copolymer in Nanolayered Films. *J. Polym. Sci. B Polym. Phys.* **2011**, *49* (24), 1750–1761. https://doi.org/10.1002/polb.22375.

Manas-Zloczower, I.; Feke, D. L. Dispersive Mixing of Solid Additives. In *Mixing and Compounding of Polymers*; Manas-Zloczower, I., Ed.; Carl Hanser Verlag GmbH & Co. KG: München, **2009**; pp 183–215. https://doi.org/10.3139/9783446433717.004.

Matsuo, M.; Sawatari, C. Temperature Dependence of the Crystal Lattice Modulus and the Young's Modulus of Polyethylene. *Macromolecules* **1988**, *21* (6), 1653–1658. https://doi.org/10.1021/ma00184a022.

McKeen, L. W. Fluorinated coatings and finishes handbook: The definitive user's guide. *William Andrew* **2015**.

Messin, T.; Follain, N.; Lozay, Q.; Guinault, A.; Delpouve, N.; Soulestin, J.; Sollogoub, C.; Marais, S. Biodegradable PLA/PBSA Multinanolayer Nanocomposites: Effect of Nanoclays Incorporation in Multinanolayered Structure on Mechanical and Water Barrier Properties. *Nanomaterials* **2020**, *10* (12), 2561. https://doi.org/10.3390/nano10122561. a)

Messin, T.; Marais, S.; Follain, N.; Guinault, A.; Gaucher, V.; Delpouve, N.; Sollogoub, C. Biodegradable PLA/PBS Multinanolayer Membrane with Enhanced Barrier Performances. *Journal of Membrane Science* **2020**, *598*, 117777. https://doi.org/10.1016/j.memsci.2019.117777. b)

Modesti, M.; Lorenzetti, A.; Bon, D.; Besco, S. Effect of Processing Conditions on Morphology and Mechanical Properties of Compatibilized Polypropylene Nanocomposites. *Polymer* **2005**, *46* (23), 10237–10245. https://doi.org/10.1016/j.polymer.2005.08.035.

REFERENCES

Moisan, C.; Gholamvand, Z.; Monge, G.; Inal, K.; Dennler, G. Control and Characterization of the Preferential Crystalline Orientation of MoS2 2D Flakes in Printed Layers; 2017. https://doi.org/10.48550/arXiv.1708.02870.

Monasse, B. Nucleation and Anisotropic Crystalline Growth of Polyethylene under Shear. *J Mater Sci* **1995**, *30* (19), 5002–5012. https://doi.org/10.1007/BF01154515.

Morgan, A. B., Guilman, J. W. Characterization of Polymer-Layered Silicate (Clay) Nanocomposites by Transmission Electron Microscopy and X-Ray Diffraction: A Comparative Study.*Journal of Applied Polymer Science* **2003**, 87, 1329 –1338. https://doi.org/10.1002/app.11884.

Nagasawa, T.; Matsumura, T.; Hoshino, S. Film forming of crystalline polymer -2. Microstructure. *Applied Polymer Symposium* **1973**, 20, 295-313.

Nicolosi, V.; Chhowalla, M.; Kanatzidis, M. G.; Strano, M. S.; Coleman, J. N. Liquid Exfoliation of Layered Materials. *Science* **2013**, *340* (6139), 1226419. https://doi.org/10.1126/science.1226419.

Nielsen, L. E. Models for the Permeability of Filled Polymer Systems. *Journal of Macromolecular Science: Part A - Chemistry* **1967**, *1* (5), 929–942. https://doi.org/10.1080/10601326708053745.

Nissel, F. R. Method and apparatus for multilayer coextrusion of sheet or film. US Patent, 3,884,265, **1976.**

Normand, G.; Peuvrel-Disdier, E.; Vergnes, B. Attempts to Optimize the Dispersion State during Twin-Screw Extrusion of Polypropylene/Clay Nanocomposites. *International Polymer Processing* **2017**, *32* (1), 129–137. https://doi.org/10.3139/217.3318.

NREL's Best Research-Cell Efficiency Chart **2023**, https://www.nrel.gov/pv/assets/pdfs/best-research-cell-efficiencies.pdf.

Pawlak, A.; Galeski, A.; Rozanski, A. Cavitation during Deformation of Semicrystalline Polymers. *Progress in Polymer Science* **2014**, *39* (5), 921–958. https://doi.org/10.1016/j.progpolymsci.2013.10.007.

Pazur, R. J.; Prud'homme, R. E. X-Ray Pole Figure and Small Angle Scattering Measurements on Tubular Blown Low-Density Poly(Ethylene) Films. *Macromolecules* **1996**, *29* (1), 119–128. https://doi.org/10.1021/ma9464229.

REFERENCES

Peacock, A. J. Handbook of Polyethylene: Structures, Properties, and Applications; *Plastics engineering; Dekker: New York*, **2000**.

Peterlin, A. Plastic Deformation of Polyethylene. Mechanism and Properties. *J. polym. sci., C Polym. symp.* **1967**, 15 (1), 427–443. https://doi.org/10.1002/polc.5070150137.

Peters, G.W.M; Balzano, L.; Steenbakkers, R. J. A. Flow induced crystallization. *Handbook of polymer crystalliza*tion; **2013**, 399 – 432.

Pham, H. D.; Yang, T. C.; Jain, S. M.; Wilson, G. J.; Sonar, P. Development of Dopant-Free Organic Hole Transporting Materials for Perovskite Solar Cells. *Advanced Energy Materials* **2020**, *10* (13), 1903326. https://doi.org/10.1002/aenm.201903326.

Ponting, M.; Hiltner, A.; Baer, E. Polymer Nanostructures by Forced Assembly: Process, Structure, and Properties. *Macromolecular Symposia* **2010**, *294* (1), 19–32. https://doi.org/10.1002/masy.201050803.

Ponting, M. Gradient mutilayered films & confined crystallization of polymer nanolayers by forced assembly coextrusion. PhD Thesis, **2010.**

Porter, D., E. Metcalfe, and M. J. K. Thomas. Nanocomposite fire retardants-a review. *Fire and Materials 24.1* **2000**, 45-52.

Pople, J. A.; Mitchell, G. R.; Sutton, S. J.; Vaughan, A. S.; Chai, C. K. The Development of Organized Structures in Polyethylene Crystallized from a Sheared Melt, Analyzed by WAXS and TEM. *Polymer* **1999**, *40* (10), 2769–2777. https://doi.org/10.1016/S0032-3861(98)00202-X.

Pusch, R.; Karnland, O. "Physicochemical stability of smectite clays." Eng. Geol. **1996**, 41, 73–85. https://doi.org/10.1016/0013-7952(95)00027-5.

Rahmanian, V.; Galeski, A.; Rozanski, A. Polyethylene Nanocomposites with Carbon Nanofillers: Similarities and Differences and New Insight on Cavitation in Tensile Drawing. *Macromolecules* **2024**. https://doi.org/10.1021/acs.macromol.3c01755.

Ren, C.; Jiang, Z.; Du, X.; Men, Y.; Tang, T. Microstructure and Deformation Behavior of Polyethylene/Montmorillonite Nanocomposites with Strong Interfacial Interaction. *J. Phys. Chem. B* **2009**, *113* (43), 14118–14127. https://doi.org/10.1021/jp9063164.

Ren, J.; Silva, A. S.; Krishnamoorti, R. Linear Viscoelasticity of Disordered Polystyrene–Polyisoprene Block Copolymer Based Layered-Silicate Nanocomposites. *Macromolecules* **2000**, *33* (10), 3739–3746. https://doi.org/10.1021/ma992091u.

REFERENCES

Renewable Energy Market Update - June 2023, International Energy Agency, **2023**.

Rits, V. A. D.; Plançon, A.; Sakharov, B. A.; Besson, G.; Tsipursky, S. I.; Tchoubar, C. Diffraction Effects Calculated for Structural Models of K-Saturated Montmorillonite Containing Different Types of Defects. *Clay miner.* **1984**, *19* (4), 541–561. https://doi.org/10.1180/claymin.1984.019.4.03.

Rivollier, N.; Schwiddessen, R.; Cabrera, G.; Combeaud, C.; Schorr, S.; Dennler, G. Montmorillonite Exfoliation in LLDPE and Factors Affecting Its Orientation: From Monolayer to Multi-Nano-Layer Polymer Films. *Polymers* **2024**, *16* (2), 200. https://doi.org/10.3390/polym16020200.

Ryu, S. H.; Chang, Y.-W. Factors Affecting the Dispersion of Montmorillonite in LLDPE Nanocomposite. *Polym. Bull.* **2005**, *55* (5), 385–392. https://doi.org/10.1007/s00289-005-0437-7.

Schiessl, S.; Kucukpinar, E.; Rivollier, N.; Langowski, H.-C.; Eisner, P. A Comparative Study on the Roll-to-Roll Processing of a Silicate–Polyvinyl Alcohol Composite Barrier Lacquer Using Slot-Die and Reverse Gravure Coating Techniques. *Polymers* **2023**, *15* (13), 2761. https://doi.org/10.3390/polym15132761.

Schrenk W.J. Apparatus for multilayer coextrusion of sheet or film. US patent 3,884,606, **1975**.

Schrenk W.J. Chisholm D.S. Cleereman K.J. Alfrey T.Jr Method of preparing multilayer plastic articles. US Patent 3,565,985, **1971**.

Seto, T.; Hara, T.; Tanaka, K. Phase Transformation and Deformation Processes in Oriented Polyethylene. *Jpn. J. Appl. Phys.* **1968**, *7* (1), 31. https://doi.org/10.1143/JJAP.7.31.

Shah, R. K.; Paul, D. R. Nylon 6 Nanocomposites Prepared by a Melt Mixing Masterbatch Process. *Polymer* **2004**, *45* (9), 2991–3000. https://doi.org/10.1016/j.polymer.2004.02.058.

Shen, X.; Zheng, Q.; Kim, J.-K. Rational Design of Two-Dimensional Nanofillers for Polymer Nanocomposites toward Multifunctional Applications. *Progress in Materials Science* **2021**, *115*, 100708. https://doi.org/10.1016/j.pmatsci.2020.100708.

Shi, M.; Yang, W.; Cheng, L.; Zhen, X.; Jiao, Z. Confinement Effects on the Orientation of Graphene in Multilayer Polymer Nanocomposites during Lamination: A Molecular Dynamics

REFERENCES

Simulation. *Journal of Applied Physics* **2019**, *126* (4), 045103. https://doi.org/10.1063/1.5099409.

Shi, M., Yang, W., Zhang, Y., Tan, J., Cheng, L., Jiao, Z., Zhen, X. Mechanical and dielectric properties and crystalline behavior of multilayer graphite-filled polyethylene composites. *J. Appl. Polym. Sci.* **2019**, 136, 48131. https://doi.org/10.1002/app.48131

Shi, Y.; Ye, W.; Hua, D.; Zhou, Q.; Huang, Z.; Liu, Y.; Li, S.; Guo, T.; Chen, Y.; Eder, S. J.; Wang, H. Interfacial Engineering for Enhanced Mechanical Performance: High-Entropy Alloy/Graphene Nanocomposites. *Materials Today Physics* **2023**, *38*, 101220. https://doi.org/10.1016/j.mtphys.2023.101220.

Silagy, D. Extrusion de film à plat : cast film. *Plastiques et composites* **2005**. https://doi.org/10.51257/a-v1-am3707.

Small, C. M.; Mcnally, G. M.; Murphy, W. R.; Marks, A. The Manufacture and Performance of Polyethylene-Polyisobutylene Films for Cling Applications. *Dev. Chem. Eng. Mineral Process.* **2003**, *11* (1–2), 169–184. https://doi.org/10.1002/apj.5500110217.

Sobamawo, M. G. ; Yinusa, A. A. Insight into the Boundary Layer Flows of Free Convection and Heat Transfer of Nanofluids Over a Vertical Plate using Multi-Step Differential Transformation Method. *Iranian Journal of Mechanical Engineering Transactions of the ISME* **2019**, 20(1), 5-45.

Sollogoub, C. Procédé de coextrusion multi-nanocouche - Principe et potentialités. *Plastiques et composites* **2018**. https://doi.org/10.51257/a-v1-am3662.

Solomon, M. J.; Almusallam, A. S.; Seefeldt, K. F.; Somwangthanaroj, A.; Varadan, P. Rheology of Polypropylene/Clay Hybrid Materials. *Macromolecules* **2001**, *34* (6), 1864–1872. https://doi.org/10.1021/ma001122e.

Suwas, S.; Ray, R. K. *Crystallographic Texture of Materials*; Engineering Materials and Processes; Springer London: London, 2014. https://doi.org/10.1007/978-1-4471-6314-5.

Tabatabaei, S. H.; Ajji, A. Crystal Structure and Orientation of Uniaxially and Biaxially Oriented PLA and PP Nanoclay Composite Films. *J. Appl. Polym. Sci.* **2011**, n/a-n/a. https://doi.org/10.1002/app.35563.

REFERENCES

Tan, B.; Thomas, N. L. A Review of the Water Barrier Properties of Polymer/Clay and Polymer/Graphene Nanocomposites. *Journal of Membrane Science* **2016**, *514*, 595–612. https://doi.org/10.1016/j.memsci.2016.05.026.

Tenn, N.; Follain, N.; Soulestin, J.; Crétois, R.; Bourbigot, S.; Marais, S. Effect of Nanoclay Hydration on Barrier Properties of PLA/Montmorillonite Based Nanocomposites. *J. Phys. Chem. C* **2013**, *117* (23), 12117–12135. https://doi.org/10.1021/jp401546t.

Tjong, S. C. Structural and Mechanical Properties of Polymer Nanocomposites. *Materials Science and Engineering: R: Reports* **2006**, *53* (3–4), 73–197. https://doi.org/10.1016/j.mser.2006.06.001.

Tollar, J.E, U.S. Patent 3 3239 197 **1966**.

Tribout, C.; Monasse, B.; Haudin, J. M. Experimental Study of Shear-Induced Crystallization of an Impact Polypropylene Copolymer. *Colloid Polym Sci* **1996**, *274* (3), 197–208. https://doi.org/10.1007/BF00665636.

Tsipursky, S.I.; Drits, V.A. The distribution of octahedral cations in the 2:1 layers of dioctahedral smectites studied by oblique-texture electron diffraction. *Clay Minerals* **1984**, 19(2), 177–193. https://doi.org/10.1180/claymin.1984.019.2.05.

Vaia, R. A.; Jandt, K. D.; Kramer, E. J.; Giannelis, E. P. Kinetics of Polymer Melt Intercalation. *Macromolecules* **1995**, *28* (24), 8080–8085. https://doi.org/10.1021/ma00128a016.

Vergnes, B. The Use of Apparent Yield Stress to Characterize Exfoliation in Polymer Nanocomposites. *International Polymer Processing* **2011**, *26* (2), 229–232. https://doi.org/10.3139/217.2462.

Vergnes, B. Influence of Processing Conditions on the Preparation of Clay-Based Nanocomposites by Twin-Screw Extrusion. *International Polymer Processing* **2019**, *34* (5), 482–501. https://doi.org/10.3139/217.3827.

Wang, H.; Keum, J. K.; Hiltner, A.; Baer, E.; Freeman, B.; Rozanski, A.; Galeski, A. Confined Crystallization of Polyethylene Oxide in Nanolayer Assemblies. *Science* **2009**, *323* (5915), 757–760. https://doi.org/10.1126/science.1164601. a)

Wang, H.; Keum, J. K.; Hiltner, A.; Baer, E. Confined Crystallization of PEO in Nanolayered Films Impacting Structure and Oxygen Permeability. *Macromolecules* **2009**, *42* (18), 7055–7066. https://doi.org/10.1021/ma901379f. b)

REFERENCES

Wang, H.; Keum, J. K.; Hiltner, A.; Baer, E. Crystallization Kinetics of Poly(Ethylene Oxide) in Confined Nanolayers. *Macromolecules* **2010**, *43* (7), 3359–3364. https://doi.org/10.1021/ma902780p.

Wang, K.; Xiao, Y.; Na, B.; Tan, H.; Zhang, Q.; Fu, Q. Shear Amplification and Re-Crystallization of Isotactic Polypropylene from an Oriented Melt in Presence of Oriented Clay Platelets. *Polymer* **2005**, *46* (21), 9022–9032. https://doi.org/10.1016/j.polymer.2005.07.025.

Wang, Z.; Liu, Y.; Liu, C.; Yang, J.; Li, L. Understanding Structure-Mechanics Relationship of High Density Polyethylene Based on Stress Induced Lattice Distortion. *Polymer* **2019**, *160*, 170–180. https://doi.org/10.1016/j.polymer.2018.11.054.

Watzeels, N., Van Durme, K., Miltner, H. E., Block, C., Van Assche, G., Van Mele, B., Bogdanov, B. and Rahier, H. Optimization of Extrusion Parameters for Preparing PCL-Layered Silicate Nanocomposites Supported by Modeling of Twin-Screw Extrusion. *Macromol. Mater. Eng.* **2013**, 298, 210 – 220. https://doi.org/10.1002/mame.201100419.

White, J. L.; Spruiell, J. E. Specification of Biaxial Orientation in Amorphous and Crystalline Polymers. *Polymer Engineering & Sci* **1981**, *21* (13), 859–868. https://doi.org/10.1002/pen.760211309.

Xie, L.; Wang, G.; Jiang, C.; Yu, F.; Zhao, X. Properties and Applications of Flexible Poly(Vinylidene Fluoride)-Based Piezoelectric Materials. *Crystals* **2021**, *11* (6), 644. https://doi.org/10.3390/cryst11060644.

Xie, S.; Istrate, O. M.; May, P.; Barwich, S.; Bell, A. P.; Khan, U.; Coleman, J. N. Boron Nitride Nanosheets as Barrier Enhancing Fillers in Melt Processed Composites. *Nanoscale* **2015**, *7* (10), 4443–4450. https://doi.org/10.1039/C4NR07228F.

Xu, J.-T.; Wang, Q.; Fan, Z.-Q. Non-Isothermal Crystallization Kinetics of Exfoliated and Intercalated Polyethylene/Montmorillonite Nanocomposites Prepared by in Situ Polymerization. *European Polymer Journal* **2005**, *41* (12), 3011–3017. https://doi.org/10.1016/j.eurpolymj.2005.04.042.

Xu, S.; Zhou, J.; Pan, P. Strain-Induced Multiscale Structural Evolutions of Crystallized Polymers: From Fundamental Studies to Recent Progresses. *Progress in Polymer Science* **2023**, *140*, 101676. https://doi.org/10.1016/j.progpolymsci.2023.101676.

REFERENCES

Yano, K.; Usuki, A.; Okada, A.; Kurauchi, T.; Kamigaito, O. Synthesis and properties of polyimide–clay hybrid. J. Polym. Sci. A Polym. Chem. **1993**, 31: 2493-2498. https://doi.org/10.1002/pola.1993.080311009.

Yapar, S.; Torres Sánchez, R. M.; Emreol, M.; Weidler, P.; Emmerich, K. Microwave Irradiation Used for All Steps of Pre-Pillaring Al-Montmorillonite. *Clay miner.* **2009**, *44* (2), 267–278. https://doi.org/10.1180/claymin.2009.044.2.267.

Yeun, J.; Bang, G.; Park, B. J.; Ham, S. K.; Chang, J. Poly(Vinyl Alcohol) Nanocomposite Films: Thermooptical Properties, Morphology, and Gas Permeability. *J of Applied Polymer Sci* **2006**, *101* (1), 591–596. https://doi.org/10.1002/app.23372.

Yoda, O.; Kuriyama, I. Structural Changes on Hot-rolling of Polyethylene. I. Crystallite Orientation and Lamellar Deformation. *J. Polym. Sci. Polym. Phys. Ed.* **1977**, *15* (5), 773–786. https://doi.org/10.1002/pol.1977.180150502.

Zeng, B.; Yang, L.; Qin, J.; Zheng, Y.; Guo, S. Nacre-Inspired Polymeric Materials with Body Heat-Responsive Shape-Memory Effect, High Optical Transparence, and Balanced Mechanical Properties. *ACS Appl. Mater. Interfaces* **2020**, *12* (46), 52008–52017. https://doi.org/10.1021/acsami.0c15871.

Zhang, C.; Shi, M.; Zhang, Y.; Yang, W.; Jiao, Z.; Yang, L. EG/TPU Composites with Enhanced Flame Retardancy and Mechanical Properties Prepared by Microlayer Coextrusion Technology. *RSC Adv.* **2019**, *9* (41), 23944–23956. https://doi.org/10.1039/C9RA03653A.

Zhang, G.; Lee, P. C.; Jenkins, S.; Dooley, J.; Baer, E. The Effect of Confined Crystallization on High-Density Poly(Ethylene) Lamellar Morphology. *Polymer* **2014**, *55* (2), 663–672. https://doi.org/10.1016/j.polymer.2013.12.027. (a)

Zhang, G.; Lee, P. C.; Jenkins, S.; Dooley, J.; Baer, E. The Effect of Confined Spherulite Morphology of High-Density Polyethylene and Polypropylene on Their Gas Barrier Properties in Multilayered Film Systems. *Polymer* **2014**, *55* (17), 4521–4530. https://doi.org/10.1016/j.polymer.2014.07.009. (b)

Zhang, G.; Xu, H.; MacInnis, K.; Baer, E. Crystallization of Linear Low Density Polyethylene under Two-Dimensional Confinement in High Barrier Blend Systems. *Polymer* **2014**, *55* (26), 6853–6860. https://doi.org/10.1016/j.polymer.2014.10.040. C)

Zhang, X.; Xu, Y.; Zhang, X.; Wu, H.; Shen, J.; Chen, R.; Xiong, Y.; Li, J.; Guo, S. Progress on the Layer-by-Layer Assembly of Multilayered Polymer Composites: Strategy, Structural

REFERENCES

Control and Applications. *Progress in Polymer Science* **2019**, *89*, 76–107. https://doi.org/10.1016/j.progpolymsci.2018.10.002.

Zhang, X. M.; Elkoun, S.; Ajji, A.; Huneault, M. A. Oriented Structure and Anisotropy Properties of Polymer Blown Films: HDPE, LLDPE and LDPE. *Polymer* **2004**, *45* (1), 217–229. https://doi.org/10.1016/j.polymer.2003.10.057.

Zhang, Y.Y., Jiang, S.L., Yu, Y., Xiong, G., Zhang, Q.F. and Guang, G.Z, Phase transformation mechanisms and piezoelectric properties of poly(vinylidene fluoride)/montmorillonite composite. J. Appl. Polym. Sci., *2012*, 123: 2595-2600. https://doi.org/10.1002/app.34431

Zhao, X.; Urano, K.; Ogasawara, S. Adsorption of Polyethylene Glycol from Aqueous Solution on Montmorillonite Clays. *Colloid & Polymer Sci* **1989**, *267* (10), 899–906. https://doi.org/10.1007/BF01410338.

Zhu, T. T.; Zhou, C. H.; Kabwe, F. B.; Wu, Q. Q.; Li, C. S.; Zhang, J. R. Exfoliation of Montmorillonite and Related Properties of Clay/Polymer Nanocomposites. *Applied Clay Science* **2019**, *169*, 48–66. https://doi.org/10.1016/j.clay.2018.12.006.

3M™ Ultra Barrier Solar Film 512, Technical data sheet, **2018**.

ACKNOWLEDGMENT

Firstly, I thank my supervisor at IPC, Gilles Dennler, for his constant support, availability, and commitment throughout my thesis. I am grateful for his benevolence and the enriching exchanges we had together.

Secondly, I thank my second supervisor, Professor Susan Schorr, for her guidance at the HZB and for welcoming me to her team. I am thankful to her for teaching me crystallography.

I would also like to express my gratitude to René Schwiddessen for his help and guidance at HZB, particularly in the practical part of my tests and in the technical follow-up of my results. I also warmly thank him for welcoming me into his office.

Additionally, I extend my thanks to Lionel Tenchine for our collaboration on the Custom-Art project, and to Géraldine Cabrera with whom I had the pleasure of working on this project. I am grateful to Géraldine for her support throughout my thesis, for the good times I had in Alençon and Oyonnax, and for being my travel partner.

I would also like to express my sincere gratitude to Christelle Combeaud for opening her doors to me at CEMEF, where I was able to carry out bi-axial stretching. Her comments on my thesis work and our scientific exchanges were invaluable, helping me to progress in my research.

I would like to express my gratitude to Professors Bruno Vergnes and Jean-Marc Haudin for taking the time to discuss their respective research on montmorillonite exfoliation and LLDPE crystallization.

I am grateful to Alex, Christophe, Michael, Corentin, and Quentin for their help in films processing. Additionally, I would like to thank the SE-ASD team in Berlin for their hospitality and training on their equipment.

APPENDIX

A.1 CARREAU-YASUDA FIT – CHAPTER 4

Table A-1-1 : Parameters extracted from the Carreau-Yasuda fit in Figure 4-5.

SAMPLE	σ_0	η_0	λ	a	m
CNa_20_5	1,659	137,207	0.06	0.21	0.04
CNa_5_0.5	899	535,034	3.10	0.18	0.26
CNa_5_1	633	332,724	2.34	0.19	0.28
CNa_5_3	725	48,656	0.30	0.30	0.27
CNa_5_5	281	24,429	0.11	0.35	0.25
CNa_5_10	231	19,057	0.04	0.33	0.13
LLDPE_LLDPE-g-MA	253	27,582	0.03	0.30	0.08

Table A-1-2 : Parameters extracted from the Carreau-Yasuda fit in Figure 4-6

SAMPLE	σ_0	η_0	λ	a	m
C20A_20_5	107,980	3,554,219	87.90	0.96	0.33
C20A_5_0.5	1,530	133,471	0.21	0.22	0.19
C20A_5_1	1,890	50,328	3.05	0.52	0.48
C20A_5_3	1,741	75,466	6.01	0.52	0.48
C20A_5_5	1,823	137,731	0.15	0.21	0.20
C20A_5_10	1,612	36,852	0.91	0.56	0.42
LLDPE_LLDPE-g-MA	253	27,582	0.03	0.30	0.08

A.2 LLDPRE CRYSTALLIZATION MODELS – CHAPTER 6

This appendix details the expected pole figures and Desper-Stein triangles in case of a perfect LLDPE crystallization in Keller-Machin models in bulk and in thin films.

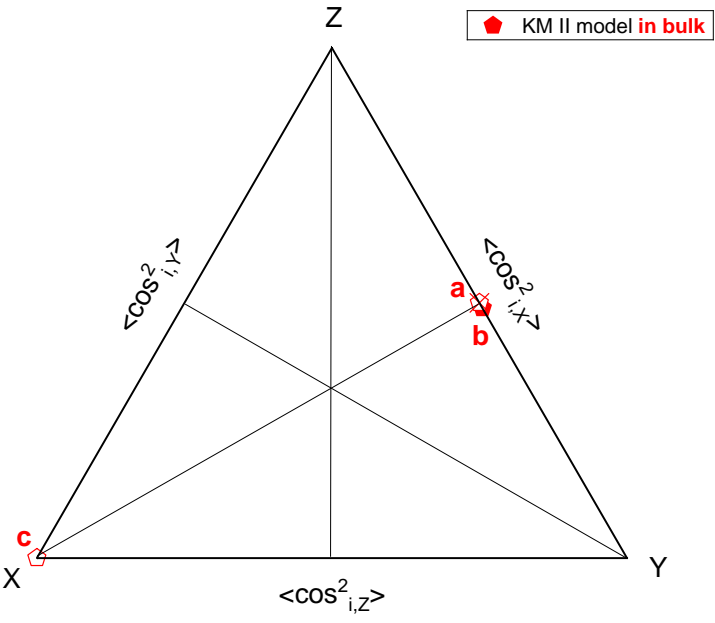***Keller – Machin I in bulk (KMI) – twisted lamellas***

Figure A-2-1 : Scheme of KMI crystallization model in bulk and its corresponding pole figures and Desper-Stein triangle.

Keller – Machin II in bulk (KMII) – 'edge-on' lamellas

Crystal axis

Pole figures

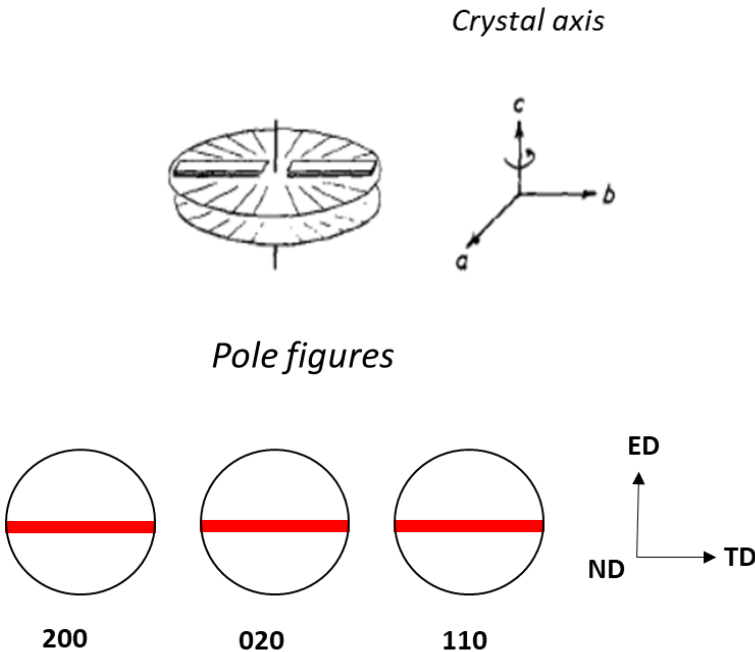**200**   **020**   **110**

Figure A-2-2 : Scheme of KMII crystallization model in bulk and its corresponding pole figures and Desper-Stein triangle.

285

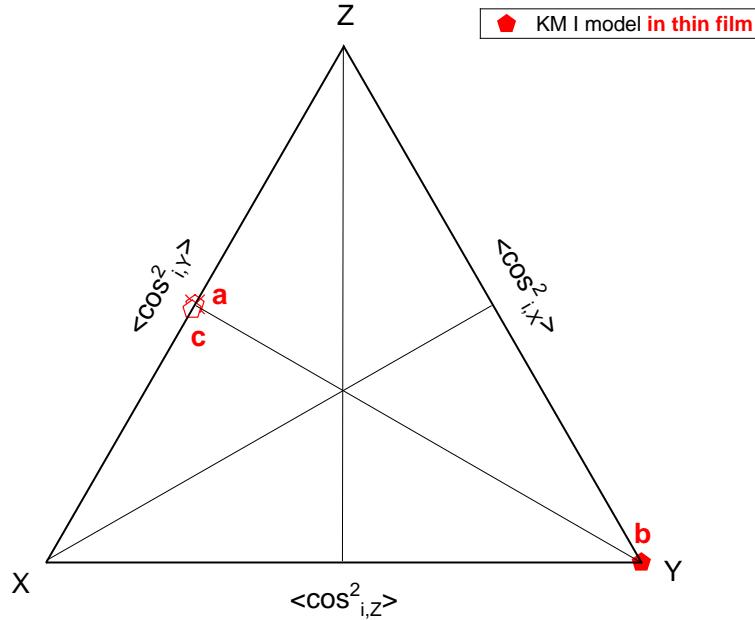***Keller – Machin I in thin films (KMI) – twisted lamellas***
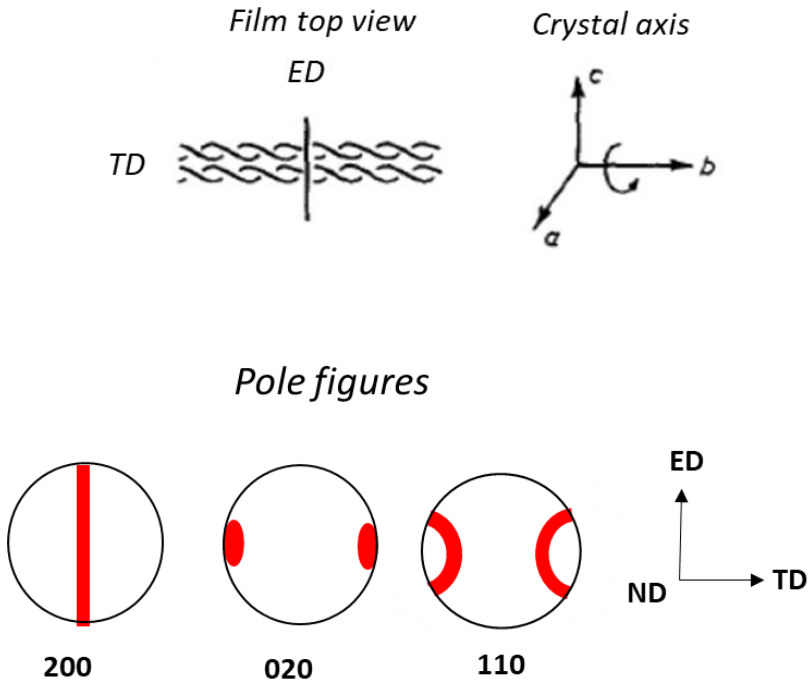

Figure A-2-3 : Scheme of KMI crystallization model in thin film and its corresponding pole figures and Desper-Stein triangle.

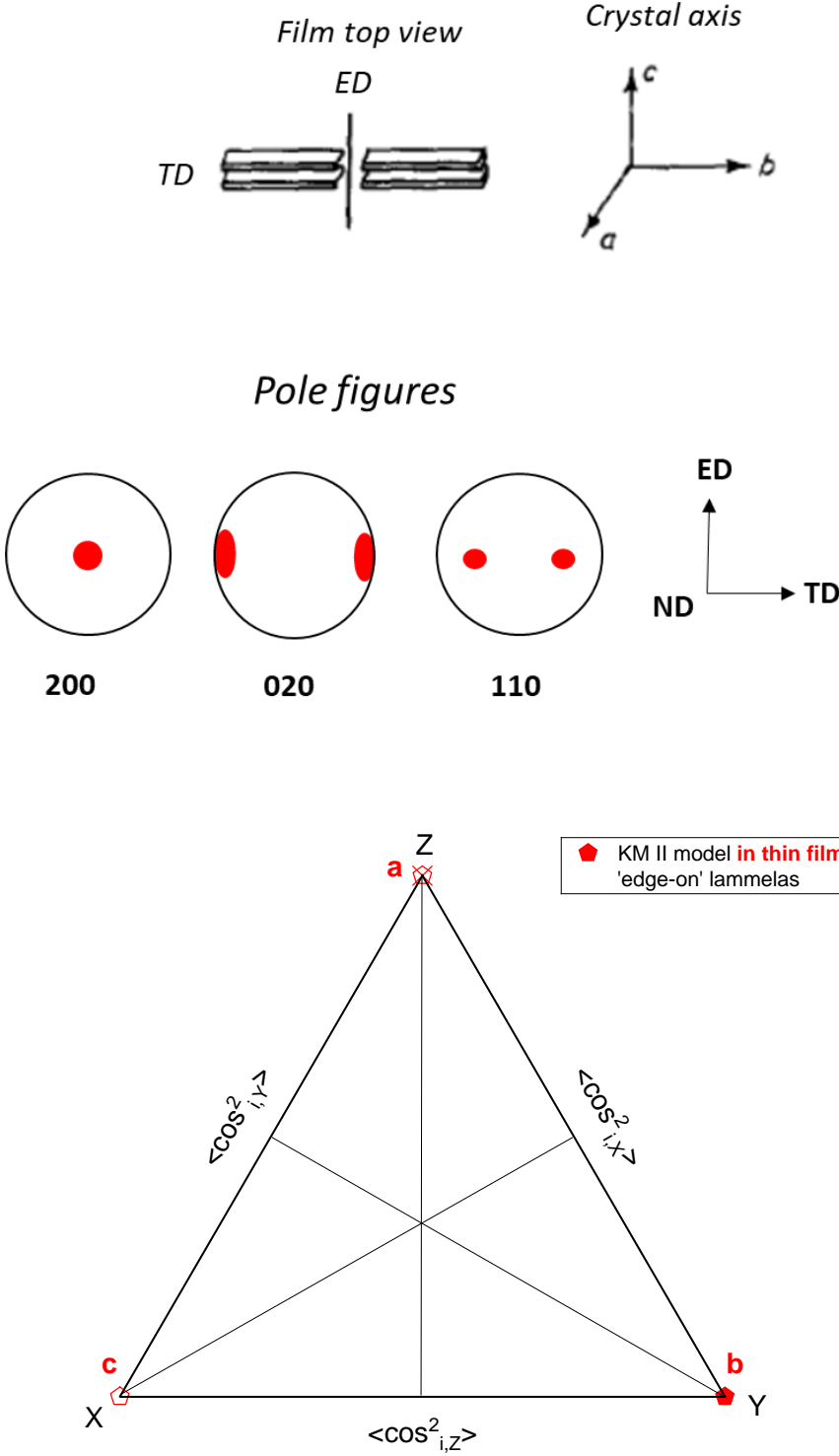**Keller – Machin II in thin films (KMII) – 'edge-on' lamellas**

Figure A-2-4 : Scheme of KMII crystallization model in thin film, with 'edge-on' lamellas and its corresponding pole figures and Desper-Stein triangle.

Keller – Machin II in *thin films* (KMII) – 'in-plane' lamellas

Film top view

ED

TD

Crystal axis

a

b

c

Pole figures

ED

ND → TD

200   **020**   **110**

Z

c

KM II model in thin film 'in-plane' lammelas

$<\cos^2_{i,Y}>$

$<\cos^2_{i,X}>$
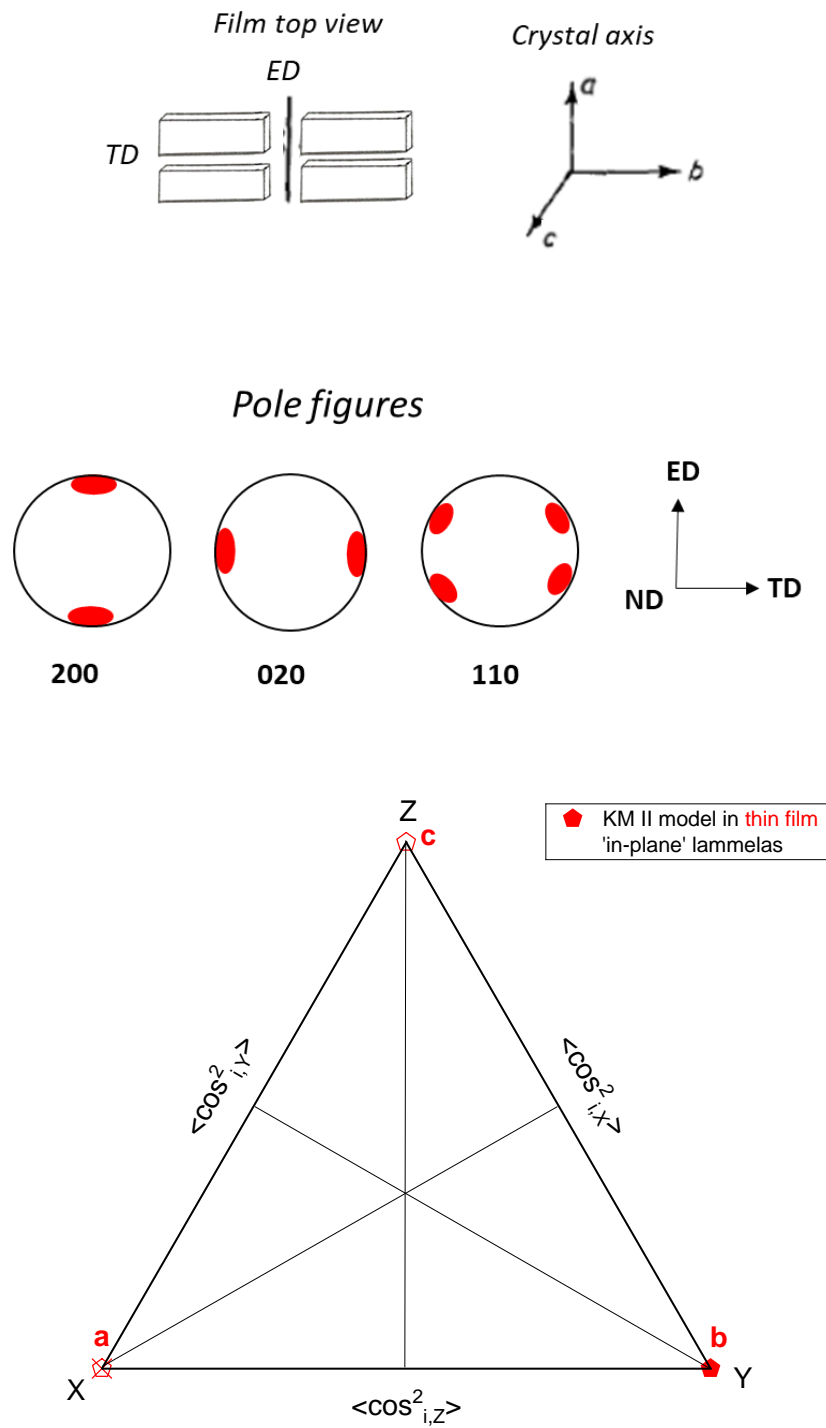
a

b

X

Y

$<\cos^2_{i,Z}>$

Figure A-2-5 : Scheme of KMII crystallization model in thin film, with 'in-plane' lamellas and its corresponding pole figures and Desper-Stein triangle.

EIDESTATTLICHE ERKLÄRUNG

Ich erkläre hiermit, dass ich die vorgelegte Dissertation mit dem Titel

A comprehensive study of the orientation mechanisms of montmorillonite in an LLDPE polymer matrix using multi-nano-layer polymer co-extrusion: from orientation quantification to polymer-filler structure-property relationships

selbständig verfasst und keine anderen als die angegeben Hilfsmittel und Quellen verwendet habe. Ferner wird hiermit erklärt, dass die Dissertation weder in der vorgelegten noch in einer ähnlichen Fassung zu einem früheren Zeitpunkt an der Freien Universität oder einer anderen Hochschule als Dissertation eingereicht worden ist.

Ein Teil meiner Ergebnisse aus den Kapiteln 4 und 5 meiner Dissertation, die in einem Artikel unter folgender Referenz veröffentlicht wurde:

Rivollier, N.; Schwiddessen, R.; Cabrera, G.; Combeaud, C.; Schorr, S.; Dennler, G. Montmorillonite Exfoliation in LLDPE and Factors Affecting Its Orientation: From Monolayer to Multi-Nano-Layer Polymer Films. *Polymers* **2024**, *16* (2), 200. https://doi.org/10.3390/polym16020200.

Dies ist ein Open-Access-Artikel, der unter den Bedingungen der Creative Commons Attribution 4.0 International licence Lizenz verteilt wird.

Die Beiträge der Autoren lauten wie folgt:

Methodik, N.R., R.S., G.C., C.C. und G.D.; Validierung, G.D., R.S. und S.S.; Formale Analyse, N.R.; Untersuchung, N.R.; Schreiben - Erstellung des ursprünglichen Entwurfs, N.R.; Schreiben - Überprüfung und Bearbeitung, N.R. Alle Autoren haben die veröffentlichte Version des Manuskripts gelesen und ihr zugestimmt.

Schließlich wird ein Teil der bislang unveröffentlichten Arbeiten zu einem späteren Zeitpunkt in Form von Artikeln veröffentlicht werden.

Berlin, 24.10.2024

Noémie RIVOLLIER